THE MECHANISM OF RADIATION-INDUCED SEGREGATION IN FERRITIC-MARTENSITIC STEELS

by

Janelle J. Penisten

A dissertation submitted in partial fulfillment
of the requirements for the degree of
Doctor of Philosophy
(Nuclear Engineering and Radiological Sciences)
in The University of Michigan
2012

Doctoral Committee:
- Professor Gary S. Was, Chair
- Professor Michael Atzmon
- Professor Lumin Wang
- Assistant Professor Emmanuelle Marquis
- Associate Research Scientist Kai Sun

For my grandparents, Richard & Sumako Taniguchi

ACKNOWLEDGEMENTS

First and foremost, I would like to thank my advisor, Dr. Gary Was, for his immeasurable assistance throughout my doctoral program. His guidance, support, constructive criticism, and patience have helped me push through the challenges of my research and have made me a better scientist.

My fellow research group members have provided endless encouragement, discussed research problems and ideas, and assisted me in the laboratory: Anne Cambpell, Cheng Xu, Mike McMurtrey, Micah Hackett, Pantip Ampornrat, Elaine West, Deepak Kumar, Vani Shankar, Tyler Moss, Kale Stephenson, Gokce Gulsoy, Yugo Ashida, Stephen Raiman, Shyam Dwaraknath, Liz Beckett, Alex Cusick, and Peng Wang. I am exceedingly grateful to Zhijie (George) Jiao, for his assistance with microscopy, irradiations, and FIB, as well as for our many technical discussions about microstructure, precipitation, RIS, and dose rate effects in F-M alloys. I am also forever indebted to Ovidiu Toader and Fabian Naab, of the Michigan Ion Beam Laboratory, for their countless hours of assistance with proton and ion irradiations, and for their patience with me, even after 3:00 a.m. phone calls. I am also thankful for the assistance of Alex Flick and Rob Blackburn, without whom numerous problems in the laboratory would have remained unresolved.

The staff at the SHaRE user facility at Oak Ridge National Laboratory has assisted me with RIS measurement techniques, microscope troubleshooting, and FIB: Chad Parish, Jim Bentley, and Ed Kenik. Special thanks go to Jeremy Busby, also of Oak Ridge National Laboratory, for teaching me how to collect RIS measurements, for answering my many technical questions, and for all of the excellent general advice about research and grad school.

To Kevin Field, Yina Huang, Leland Barnard, and Dane Morgan of the University of Wisconsin and Brian Wirth of the University of Tennessee, thank you for the many technical conversations over the years—I am confident that our collaborative efforts to understand the phenomenon of RIS in F-M alloys will make a significant contribution to our field.

To the Shipman Scholars Program, thank you for bringing me to the University of Michigan more than ten years ago. To Mark Kloetzel and Jamil Ahmadia, thank you for igniting my passion for science and inspiring me to pursue this career path—I wish every child could have such wonderful teachers.

To my family—mom, dad, Joey & Steve, Myra & John—thank you for your love, encouragement, and for believing in me, not only during my doctoral studies, but throughout my life. To my husband, Thomas Wharry, thank you for your support, compassion, for challenging me, for bearing with me through grad school, and for making me a better person.

And finally, to Grandma and Grandpa, thank you for teaching me the value of hard work, integrity, humility, and determination, and for encouraging me to achieve. You have provided me with the means to have so many opportunities throughout my life, and you have inspired me to always make the most of those opportunities. This thesis is dedicated to you and your legacy.

This research was supported by the U.S. Department of Energy awards DE-FG07-07ID14828 and DE-FG07-07ID14894.

TABLE OF CONTENTS

LIST OF FIGURES

LIST OF TABLES

LIST OF APPENDICES

CHAPTER 1 INTRODUCTION

The rapidly growing global demand for energy and resources, coupled with the increasing importance of homeland security and reduction of nuclear waste volumes has sparked interest in new Generation IV nuclear technologies. Many of these reactor concepts are designed to consume existing nuclear waste in the production of electricity, and extract a greater energy yield from the same fuel volume, thereby shortening the lifespan of nuclear waste. However, with the promise of Generation IV designs comes the challenge of finding suitable materials that will withstand the harsh operating conditions in-reactor. Structural components of Generation IV reactors will be subject to high temperatures up to 600°C, corrosive environments, cyclic loading, and radiation damage up to several hundred displacements per atom (dpa). Ensuring the integrity of these materials under such extreme conditions is paramount to the safety, performance, and long-term success of the Generation IV nuclear fleet.

Ferritic-martensitic (F-M) steels are leading candidates for cladding and structural components in many Generation IV designs because of their excellent material properties. Typical F-M alloys have high strength at elevated temperatures, and their thermal expansion coefficient and thermal conductivity provide excellent resistance to thermal stresses [1], [2]. F-M alloys are dimensionally-stable and have low activation. Furthermore, they have adequate creep strength up to 550-600°C, and have even been used in fossil fuel-fired power plant components operating at 500-750°C [1], [2].

These F-M steels are binary Fe-Cr alloys with a body centered cubic (b.c.c.) crystal structure. Their Cr concentration ranges from approximately 7at% to 15at%. Typical alloying elements include W, V, Mn, Ta, and Ti, which aid in reducing the activation of the steel under irradiation [1]. Chromium and these alloying elements play a critical role in forming precipitates and carbides within the F-M microstructure. Under irradiation, these precipitates and carbides can grow, nucleate, or dissolve, thus significantly altering the desirable mechanical properties of the alloy. The Cr-rich ferrite α' phase, for example, is of particular concern because of its potential to embrittle the alloy. Precipitates and carbides that are detrimental to the mechanical properties of the alloy, can form when the alloy undergoes highly localized changes in bulk concentration at sinks, a phenomenon known radiation-induced segregation (RIS).

Very little is known about RIS in F-M alloys. Only a few experimental studies have been performed, and all of them have been conducted with different alloys, irradiating particles, dose rates, temperatures, and doses. Furthermore, the results of these studies are inconclusive, and do not point toward any clear trends or patterns in the behavior of RIS.

Studies of RIS in F-M alloys began in the early 1980s, with high-dose-rate electron and C^+ ion irradiation experiments on b.c.c. Fe-Cr model alloys with Cr concentrations in the range 5-13at% Cr and various solute additions [3–5]. Those studies reveal a variety of Cr RIS behaviors, from Cr enrichment by a magnitude of ~17at%, to Cr depletion by a magnitude of ~4at%.

The first neutron irradiation experiments on F-M alloys showed Cr enrichment in both a commercial and model alloy (HT9 and Fe-12CrMoVNb, respectively) [6], [7]. Proton and ion irradiation studies reported Cr depletion in commercial HT9 and F82H, as well as in model Fe-13Cr alloys [8–10].

The most recent studies on RIS in F-M alloys are that of Gupta, *et al.* [11] and Lu, *et al.* [12], both in 2006, and those of Marquis, *et al.* in 2011 [13], [14]. Gupta, *et al.* report Cr enrichment in proton-irradiated T91, while Lu, *et al.* report Cr depletion in Ni^+ ion-irradiated E911 steel. The Marquis studies observe both Cr enrichment and Cr depletion in Fe^+ ion-irradiated model alloys.

These inconclusive, and oftentimes contradictory, experimental results underscore the need for a greater understanding of RIS in F-M alloys. Comparisons can be made with RIS in austenitic alloys, for which there exists a significant body of literature and understanding. Studies on a wide range of ternary Fe-Cr-Ni austenitic alloys have demonstrated consistent and predictable Cr depletion, Ni enrichment, and a balance change in Fe concentration [15], [16]. The mechanism for RIS in austenitic alloys has been identified as inverse Kirkendall, in which segregation results from differences in atom-vacancy jump rates of constituent atoms [17], [18]. Predictive models, based on the inverse Kirkendall mechanism, have been developed and have proven successful for Fe, Ni, and Cr RIS in austenitic steels. Although RIS in F-M alloys does not follow the same behavior as in austenitic alloys, the knowledge of RIS in austenitic alloys may be able to assist in understanding RIS in F-M alloys.

The objective of this thesis is to determine the mechanism of RIS in F-M alloys. The second chapter of this work covers all relevant background literature; experimental results of RIS in F-M alloys from literature are covered in greater detail than presented in this Introduction, and the development of RIS mechanisms and computational tools are also be discussed. Chapter 3 presents the detailed objective of this work. Chapter 4 covers the experimental approach and procedures applied while performing this research work. Experimental results, including RIS measurements and relevant sink density measurements, are presented in Chapter 5. Chapter 6 details the computational modeling component of this thesis, including a description of the model and its inputs, as well as model results. Chapter 7 discusses the experimental results and compares them to model predictions, in order to demonstrate consistency with the proposed RIS mechanism. Lastly, Chapter 8 presents the conclusions of this thesis and future suggested work.

CHAPTER 2 BACKGROUND

Steel structural components in a nuclear reactor are subject to considerable fluences of fast neutrons, the damage from which can induce substantial microstructural and microchemical changes in the steel. In the structural components of the existing fleet of nuclear reactors, irradiation-induced changes such as the creation of composition gradients at grain boundaries, the nucleation and growth of dislocation loops and voids, phase formation and embrittlement, and irradiation-enhanced creep, have all been observed. These changes can have severe adverse consequences on the mechanical properties and corrosion resistance of the steel.

A new and exciting class of steels—high-Cr F-M alloys—are being investigated for future nuclear applications because of their promising material properties, which suggest improved resistance to irradiation-induced changes. Little is understood, however, about RIS in F-M alloys. Specifically, RIS of Cr is of particular concern, as it may lead to the precipitation of brittle phases at grain boundaries.

This chapter will provide further context to the issue of RIS in F-M alloys, and the ensuing experimental and modeling work contained within this thesis. The concept of RIS will first be introduced, and proposed RIS mechanisms will be explained. The body of literature covering experimental measurements of RIS in F-M alloys will be critically analyzed. And lastly, the development and general properties of F-M alloys will be discussed.

2.1 Mechanisms of Radiation-Induced Segregation

Radiation-induced segregation (RIS) is a non-equilibrium process in which a coupling between point defect fluxes and alloying element fluxes gives rise to microchemical concentration gradients at point defect sinks. Over the years, a number of theories and computational models for RIS have been suggested, which have led to the evolution of two mechanisms by which RIS is proposed to occur: the inverse Kirkendall mechanism, and the solute drag mechanism. This section will introduce the phenomenon of RIS, then progress through the development of RIS mechanisms. The discussion on RIS mechanisms will begin with early RIS theories and work up to thorough descriptions of the inverse Kirkendall and solute drag mechanisms, with modeling details covered for each mechanism. Lastly, a section shall be spent on the mechanism of RIS in austenitic stainless steels, which has been extensively researched and demonstrated.

2.1.1 An Introduction to RIS

The phenomenon of RIS occurs under irradiation, when point defect diffusion induces the formation of an alloying element concentration gradient at a point defect sink, such as a grain boundary. Energetic irradiation produces Frenkel pairs of vacancies and interstitials within a crystalline lattice. Many of these point defects recombine with one another. But at elevated temperatures, typically between $0.3T_m$ and $0.5T_m$ [15], point defects can be sufficiently mobile so as to escape recombination, and instead diffuse to point defect sinks. The vacancy flux to sinks is offset by an equal flux of atoms in the opposite direction, while the interstitial flux to sinks is composed of a flux of atoms. At sinks, the point defects will become re-incorporated into the crystalline lattice.

Point defects may be preferentially associated with a particular alloying component, in which case the defect flux toward sinks will be coupled with a net flux of that particular alloying element. Alloying element fluxes cause that element to either build up or deplete away at defect sinks, introducing a concentration gradient in what was otherwise an initially homogeneous alloy. In order to achieve a lower-energy configuration, the elemental concentration gradients will tend to re-homogenize by inducing back diffusion of the segregated elements. With back diffusion working against the continued flux of point defects to sinks, the result is a quasi-steady state under continued irradiation, as the defect-driven alloying element fluxes are counterbalanced by diffusion-driven back diffusion [19].

A simple schematic of RIS is shown in Figure 2.1 for a binary 50%A-50%B system. Here, the defect and solute atom fluxes are represented as vectors, drawn to scale, alongside the point defect concentrations. In Figure 2.1(a), there is a vacancy flux toward a grain boundary, where there exists a vacancy concentration gradient. The vacancy flux is opposed by an atomic flux, made up of A and B atoms. But given a vacancy-A atom coupling, the flux of A away from the boundary is greater than the flux of B away from the boundary. Thus arises an atomic concentration gradient, in which atom A is depleted at the boundary. Similarly, Figure 2.1(b) examines the interstitial flux to a grain boundary having an interstitial concentration gradient. The interstitial flux is composed of a flux of A atoms and B atoms, although interstitial-B atom coupling causes the flux of B atoms toward the boundary to exceed the flux of A atoms toward the boundary. Thus, the interstitial flux results in the enrichment of B atoms at the boundary. Putting the vacancy and interstitial flux contributions together, one observes an atomic concentration gradient at the boundary, enriched in B and depleted in A, as shown in Figure 2.1(c). Note that the solute-defect coupling in this schematic can be attributed to any potential RIS mechanism; the schematic does not imply a specific mechanism.

Because RIS is a diffusion-driven process, it is highly sensitive to irradiation conditions, and will only occur within a specific temperature range at a given dose rate [20], [21]. The interplay of temperature and dose rate controls the amount of segregation, and the effect of these two experimental parameters on RIS is illustrated in Figure 2.2. At low temperatures, defects are somewhat immobile and require more time to diffuse to sinks. In such a situation, a low dose rate will allow defects more time to diffuse to sinks and generate RIS, before the next damage cascade impacts. A high dose rate at low temperatures limits all point defects to recombination within the cascade volume, since the defect mobilities are so low that they cannot escape the cascade and diffuse to sinks to produce RIS. Conversely, at extremely high temperatures, point defect mobility is so large that RIS can easily be reduced by back diffusion if the dose rate is too low. High temperatures and high dose rates, on the other hand, can produce RIS very quickly, without allowing enough time for back diffusion, such that RIS can be maximized. Ultimately, the amount of RIS in an alloy is extremely sensitive to temperature and dose rate, the two experimental parameters which control the level of recombination in the matrix, the diffusion of point defects to sinks, and the back diffusion of segregated elements.

RIS is an extremely complex diffusion-driven process, highly dependent upon many different variables and experimental parameters. The coupling between atoms and point defects, which causes RIS, has been proposed to occur by multiple mechanisms. These mechanisms will the studied in the following sections.

2.1.2 Early Development of RIS Mechanisms

Theories of RIS mechanisms actually originated from experiments on unirradiated metals, in which diffusion of thermal vacancies generated sufficient solute segregation. In due time, these mechanisms were of course extended to irradiated specimens containing a far greater concentration of point defects. Simple models of these phenomena were then developed. These formative works in RIS mechanics shall be described in this section, which will provide a historical perspective to our current understanding of RIS.

The early 1960s discovery of vacancy gradients at grain boundaries, interfaces, dislocations, and other sinks [22–24] was the precursor to the development of modern RIS mechanisms. These initial studies were performed on as-fabricated, unirradiated specimens, which were typically of high purity and composed of either a single- or bi-crystal. In early experiments, high-temperature annealing generated a homogenous, equilibrium concentration of vacancies throughout the specimen. Upon rapid quenching, however, the vacancy concentration became supersaturated, and these excess vacancies tended to migrate toward strong sinks such as grain boundaries, where they gave rise to a vacancy concentration gradient. These early studies also revealed microhardness gradients at grain boundaries, which correlated very strongly with the vacancy concentration gradients. Further pursuit of those results by Aust, *et al.*, [25] suggested that the hardness gradients were the direct result of solute clustering based on a solute-vacancy coupling interaction mechanism. It was proposed, then, that if a positive solute-vacancy binding energy existed, excess vacancies diffusing to grain boundaries would essentially "drag" certain solute atoms with them to the boundaries [25].

Aust's vacancy-solute drag mechanism can explain solute enrichment at a grain boundary, but around the same time it was proposed, Howard and Lidiard [26] suggested an alternative theory to explain solute depletion at grain boundaries. Their solute depletion mechanism states that the atomic flux away from grain boundaries, which opposes the vacancy flux toward grain boundaries, will be disproportionately composed of the most mobile atomic species in a substitutional solute. Thus, solute atoms having higher diffusion coefficients than solvent atoms, and having low solute-vacancy binding energies, will diffuse opposite the direction of the vacancy flux, and therefore become depleted at grain boundaries.

Soon afterward, Anthony, *et al.*, [27–29] proposed that solute segregation was the combined outcome of both the Aust vacancy-solute drag mechanism and the Howard-Lidiard mechanism of preferential solute diffusion opposite the vacancy flux. Anthony suggested that these two mechanisms either oppose or supplement one another in producing solute segregation. But heretofore, thermally-generated vacancies were the only point defect specie considered in the mechanistic theories of solute segregation, primarily because interstitial formation energies are so insurmountably large that the equilibrium interstitial concentration in a metal is essentially negligible.

At this point in mechanism development, however, Okamoto and Wiedersich [30] made the jump from a quench-driven solute segregation to irradiation-assisted solute segregation. Knowing that irradiation produces a high concentration of interstitials, far in excess of that found in equilibrium, Okamoto and Wiedersich added a third mechanism to Anthony's two mechanisms: that in which interstitials can also produce segregation. Okamoto and Wiedersich theorized that undersized atoms are more easily, and more frequently, accommodated in interstitial sites than are oversized atoms. This results in the ratio of undersized to oversized solutes comprising the interstitial flux to exceed the ratio of their bulk concentrations, leading to enrichment of undersized solutes and depletion of oversized solutes at grain boundaries.

Complementary to their work in identifying an interstitial mechanism, Okamoto and Wiedersich [30] also formulate one of the first quantitative models of RIS, based upon a dilute binary alloy. Their model is based upon the assumption that the defect-induced flux of solute atoms to sinks, J_s^d, is proportional to the instantaneous flux of the point defect specie causing solute segregation, J_d:

$$J_s^d = \beta_s^d J_d . \qquad (2.1)$$

The proportionality factor β_s^d is a measure of the drag efficiency. Next, the model asserts that steady-state RIS is reached when the reverse solute flux, J_s, induced by the developing solute gradient, is large enough to just balance J_s^d. This allows the authors to express the steady-state condition as

$$J_s^d = -\beta_s^d D_d \nabla C_d = D_s \nabla C_s = -J_s , \qquad (2.2)$$

where D_s and D_d are diffusion coefficients of the solute and defects, respectively. Equation 2.2 can be solved for the steady-state solute concentration, C_s, in terms of the steady-state irradiation-produced point defect concentration, C_d. This model from Okamoto and Wiedersich is perhaps too simple for the very complex process of RIS, however. It does not allow for study of transient effects, nor does it account for the dependence of RIS on temperature and dose rate.

In an attempt to improve upon the shortcomings of the Okamoto and Wiedersich model, Johnson and Lam [31] develop a RIS model to include interstitial-impurity interactions, vacancy-impurity interactions, and the migration of bound vacancy-impurity complexes. Their model is based upon a dilute binary alloy having the f.c.c. (face centered cubic) crystal structure, in which the self-interstitial takes the form of a <100> dumbbell that migrates to nearest-neighbor positions via orthogonal jumps. The authors define two types of interstitial-impurity complexes, both of which are illustrated in Figure 2.3. Type-*a* complexes are those in which a <100> split interstitial dumbbell is located in the second-nearest-neighbor position to the impurity; these complexes can cause impurity migration. Type-*b* complexes, on the other hand, have the <100> split interstitial located in the first nearest-neighbor position to the impurity, and cannot cause impurity migration because the dumbbell can only migrate around the impurity.

Johnson and Lam identify ten different reactions involving point defects, impurities, defect-impurity complexes, and sinks, which must be considered in their model of solute segregation. Each of these reactions has a rate constant, denoted as K_n, where n is an arbitrary numerical designation for the reaction. Concentrations are designated as C_x, where x can denote free interstitials or vacancies (i, v), impurities (I), type-*a* or type-*b* interstitial-impurity complexes (iIa, iIb), vacancy-impurity complexes (vI), or effective interstitial or vacancy sink concentrations (is, vs). The ten reactions are:

$$Irradiation \xrightarrow{K_0} C_i + C_v$$

$$C_i + C_v \xrightarrow{K_1} 0$$

$$C_i + C_I \xleftrightarrow{K_2, K_2'} C_{iIa}$$

$$C_i + C_I \xleftrightarrow{K_3, K_3'} C_{iIb}$$

$$C_v + C_I \xleftrightarrow{K_4, K_4'} C_{vI}$$

$$C_i + C_{vI} \xrightarrow{K_5} C_I$$

$$C_v + C_{iIa} \xrightarrow{K_6} C_I$$

$$C_v + C_{iIb} \xrightarrow{K_7} C_I$$

$$C_i + C_{is} \xrightarrow{K_8} C_{is}$$

$$C_v + C_{vs} \xrightarrow{K_9} C_{vs}$$

The first reaction (rate constant K_0) represents the creation of a Frenkel pair of point defects by irradiation. The second reaction (K_1) represents recombination. The third and fourth reactions (K_2, K_3) represent the formation of the two types of interstitial-impurity complexes, while the fifth reaction (K_4) represents the formation of a vacancy-impurity complex. The reactions governed by K_5, K_6, and K_7 represent the annihilation of a complex with a freely-migrating point defect, leaving an impurity. The final two reactions (K_8, K_9) deal with the annihilation of a point defect at a sink.

Considering the complexity of the reactions studied in the Johnson and Lam model, it is not surprising that they lead to an extremely complicated problem with an equally complicated solution, from which very little insight can actually be garnered. The rate constants of the ten reactions, and the diffusion coefficients of each type of migrating specie, are dependent upon a number of physical parameters, none of which are known with very much certainty. Furthermore, an extremely complex system of six different differential rate equations emerges from the ten reactions included in the model.

The numerical solution to this system of equations yields a convoluted set of concentration profiles (an example is shown in Figure 2.4), from which the implications on segregation of each diffusing specie—or each mechanism, rather—are impossible to extract. So although the Johnson and Lam model provides a more detailed description of RIS than the Okamoto and Wiedersich model does, its cumbersome setup and non-insightful results render this model quite impractical.

Despite the limitations of these early RIS theories and models, they introduced the ideas upon which all later work in RIS mechanics has been built. From these early perspectives, theories on RIS mechanisms have developed into what are now two overarching classifications [32]: one in which solute segregation is attributed to the formation of mobile defect-solute complexes, and another in which solute segregation is attributed to differences in defect-solute exchange rates, characterized as a rate theory-type approach or the inverse Kirkendall mechanism. Both of these classes of mechanisms shall be described in detail in the forthcoming sections.

2.1.3 Inverse Kirkendall Mechanism

The Kirkendall effect [33] is at first glance, the exact opposite—or inverse—of the phenomenon of RIS. In Kirkendall experiments, a material with an initially uniform vacancy distribution will experience a net vacancy flux across a lattice plane or some "marker" plane. This vacancy flux is the direct result of the composition gradient, which arises when alloying components diffuse via vacancies at different rates. An effective way to understand the Kirkendall effect is to picture a diffusion couple, as shown in Figure 2.5, in which diffusion occurs by atom-vacancy exchange. Atomic mixing by the interpenetration of the two halves of the diffusion couple induces a concentration gradient proportional to the difference in the diffusion coefficients of the two components of the couple. Since the red-colored atoms in Figure 2.5 exchange with vacancies more readily than do the blue-colored atoms, a net flux of vacancies is generated in a reference frame fixed at the free ends of the diffusion couple. Under irradiation, the inverse sequence occurs—a defect flux gives rise to a concentration gradient—explaining the reasoning behind the name "inverse Kirkendall" mechanism.

The Kirkendall effect assumes a sufficient vacancy concentration exists in a metal at thermal equilibrium. Irradiation, however, imposes a far-from-equilibrium state in a metal, in which considerable fluxes of vacancies and interstitials are generated in the bulk and diffuse to sinks. The inverse Kirkendall mechanism accounts for these point defect fluxes by introducing a defect gradient to the traditional Kirkendall mechanism, thereby allowing for calculation of the atom fluxes comprising the defect fluxes.

Essential to the Kirkendall theory is the underlying simplification of neglecting any binding between vacancies and particular atomic species, thereby ignoring the effects of vacancies "dragging" solutes with which they have positive binding energy, to the grain boundary. This is a reasonable simplification in a random concentrated alloy, since any vacancy will have representatives of all alloying components amongst its nearest neighbors [34]. In dilute alloys, however, vacancies will not necessarily find all alloying components amongst its nearest neighbors, and so neglecting vacancy binding in such a case would be egregious.

Much of the early work in theoretical RIS mechanisms focused on dilute binary systems [26], [30], [31]. It was not until 1978, when Marwick [34] proposed a quantitative model of the inverse Kirkendall mechanism that the treatment of RIS mechanisms became extended to random concentrated alloys. Soon afterward, significant developments in rate theory RIS models were made by Wiedersich, *et al.* [35] in concentrated binary alloys, Lam, *et al.* [36] extended the Wiedersich approach to concentrated ternary alloys, and Perks, *et al.* [17], [37] further refined the model. Collectively, these references comprise the commonly-accepted rate theory-based, inverse Kirkendall RIS model, which has been used by researchers such as Watanabe, *et al.* [38], [39], Allen, *et al.* [15], [18], [21], and Hackett [40], [41].

The ensuing derivation will establish a model for the inverse Kirkendall mechanism, as developed by Marwick [34], Wiedersich, *et al.* [35], Lam, *et al.* [36], and Perks, *et al.* [17], [37]. The derivation will be performed using the variable x to represent the constituent elements of the alloy, where x = A, B, or C for an A-B-C ternary alloy, say. This derivation holds, then, for binary, ternary, quaternary, or any other alloy system. For the sake of illustration, the final flux expressions and kinetic rate equations will be written for a ternary alloy, but it should be noted that similar sets of equations can be written for an alloy with any number of constituent elements.

Since segregation is attributed to point defect diffusion, one begins with the point defect rate equations:

$$\frac{\partial C_v}{\partial t} = -\nabla J_v + K_0 - R - S_v \ , \qquad (2.3)$$

$$\frac{\partial C_i}{\partial t} = -\nabla J_i + K_0 - R - S_i \ , \qquad (2.4)$$

where C_v and C_i are the vacancy and interstitial concentrations, $-\nabla J_v$ and $-\nabla J_i$ are the divergences of the vacancy and interstitial fluxes, K_0 is the defect production rate, R is the recombination rate, and S_v and S_i are the rate of defect annihilation at sinks. The recombination rate can be expressed as:

$$R = K_{iv} C_i C_v \ , \qquad (2.5)$$

where K_{iv} is the recombination rate constant. Likewise, the vacancy annihilation rate at sinks can be written as $S_v = K_{vs} C_v Cs$, with a similar expression for interstitials. Similar to the point defect rate equations, the atom species conservation equations can be written as:

$$\frac{\partial C_x}{\partial t} = -\nabla J_x \ . \qquad (2.6)$$

Since all vacancy and interstitial diffusion is assumed to occur through the x constituent atoms, the point defect fluxes can be partitioned between the x atom types:

$$J_i = \sum_x J_i^x \ , \qquad (2.7)$$

$$J_v = \sum_x J_v^x \ . \qquad (2.8)$$

The flux of atoms diffusing through interstitials moves in the same direction as the flux of interstitials, whereas the flux of atoms diffusing through vacancies moves opposite the direction of the flux of vacancies. Thus, the partial defect fluxes can be related to the partial atomic fluxes, as follows:

$$J_i^x = J_x^i \ , \qquad (2.9)$$

$$J_v^x = -J_x^v \ . \qquad (2.10)$$

Combining Equations 2.7-2.10:

$$J_i = \sum_x J_x^i \ , \tag{2.11}$$

$$J_v = \sum_x J_x^v \ . \tag{2.12}$$

Likewise, atomic fluxes can be written as the sum of partial defect fluxes:

$$J_x = J_x^v + J_x^i \ . \tag{2.13}$$

The partial defect fluxes are functions of the concentration gradients of solute atoms, and can be expressed as follows:

$$J_x^i = -D_x^i \alpha \nabla C_x - D_i^x \nabla C_i \ , \tag{2.14}$$

$$J_x^v = -D_x^v \alpha \nabla C_x - D_v^x \nabla C_v \ , \tag{2.15}$$

where D_x^i and D_x^v are the partial diffusion coefficients of the *x* atomic species through interstitials and vacancies, and D_i^x and D_v^x are the partial diffusion coefficients of interstitials and vacancies through *x* atoms. These partial diffusion coefficients all take the form:

$$D_x^j = d_{xj} N_j \ , \tag{2.16}$$

$$D_j^x = d_{xj} N_x \ , \tag{2.17}$$

where *j* represents either vacancies or interstitials, d_{xj} is the diffusivity coefficient of the various possible atom-defect pairs, and N_j and N_x are the atomic fractions of defects and solute atoms, respectively. The diffusivities have a form following Manning's random alloy theory [42]:

$$d_{xj} = \frac{1}{6} \lambda_x^2 Z_x f_x^j \omega_{xj} \ , \tag{2.18}$$

where λ_x is the jump distance, Z_x is the number of nearest-neighbor atoms to atom *x*, f_x^j is the correlation factor, and ω_{xj} is the jump frequency of the *x*-*j* atom-defect pair. The jump frequency can be expressed as:

$$\omega_{xj} = \nu \exp\left(\frac{\Delta S_{mj}^x}{k}\right) \exp\left(\frac{-E_{mj}^x}{kT}\right) \ , \tag{2.19}$$

where ν is the deBye frequency, ΔS_{mj}^{x} is the entropy of migration of an *x-j* solute-defect pair, E_{mj}^{x} is the migration energy of an *x-j* atom-defect pair, *k* is the Boltzmann constant, and *T* is the temperature. The atomic fractions can be expressed as:

$$N_j = \Omega C_j \ , \qquad (2.20)$$

$$N_x = \Omega C_x \ , \qquad (2.21)$$

where *Ω* is the average atomic volume of the alloy.

It follows, then, that the total diffusion coefficients for interstitials, vacancies, and atomic species are:

$$D_i = \sum_x d_{xi} N_x \ , \qquad (2.22)$$

$$D_v = \sum_x d_{xv} N_x \ , \qquad (2.23)$$

$$D_x = d_{xi} N_i + d_{xv} N_v \ . \qquad (2.24)$$

Now, having determined the diffusivities and diffusion coefficients, they can be incorporated into the fluxes, and a new set of flux expressions can be written. Taking *α* as the thermodynamic factor, which describes the difference between the chemical potential gradient and the concentration gradient,

$$\alpha = \left(1 + \frac{\partial \ln \gamma_A}{\partial \ln N_A}\right) = \left(1 + \frac{\partial \ln \gamma_B}{\partial \ln N_B}\right), \qquad (2.25)$$

the flux expressions are written as follows for an A-B-C ternary alloy:

$$J_A = -D_A \alpha \nabla C_A + d_{Av} N_A \nabla C_v - d_{Ai} N_A \nabla C_i \ , \qquad (2.26)$$

$$J_B = -D_B \alpha \nabla C_B + d_{Bv} N_B \nabla C_v - d_{Bi} N_B \nabla C_i \ , \qquad (2.27)$$

$$J_C = -D_C \alpha \nabla C_C + d_{Cv} N_C \nabla C_v - d_{Ci} N_C \nabla C_i \ , \qquad (2.28)$$

$$J_i = -\left(d_{Ai} - d_{Ci}\right) N_i \alpha \nabla C_A - \left(d_{Bi} - d_{Ci}\right) N_i \alpha \nabla C_B - D_i \nabla C_i \ , \qquad (2.29)$$

$$J_v = -\left(d_{Av} - d_{Cv}\right) N_v \alpha \nabla C_A - \left(d_{Bv} - d_{Cv}\right) N_v \alpha \nabla C_B - D_v \nabla C_v \ , \qquad (2.30)$$

These flux equations (Equations 2.26-2.30) are a simplified description of atom and defect motion. It is important to note that the flux of A atoms can be influenced by the gradient of B and C atoms, which can be represented by terms of the form $D_{AB} \nabla C_B$ and

$D_{AC}\nabla C_C$ in Equation 2.26, and similar terms in Equations 2.27-2.28. However, these so-called "cross coefficients" are neglected in inverse Kirkendall RIS models because their values are generally unknown in the temperature range over which RIS occurs. One can then recognize that the first terms of Equations 2.26-2.28 are essentially Fick's law; the second and third terms represent the implementation of a point defect concentration gradient, which characterizes the inverse Kirkendall methodology.

Assuming that $C_A + C_B + C_C = 1$ and $\nabla C_C = -(\nabla C_A + \nabla C_B)$, then of the three solute atom flux expressions and two defect flux expressions, only four of them are independent, since

$$J_A + J_B + J_C = -J_v + J_i \ . \tag{2.31}$$

The new flux terms as determined in Equations 2.26-2.30 can be incorporated into the kinetic rate equations of atom and defect concentrations. Although independence rules state that only four of these kinetic rate equations are needed, all six equations are written below:

$$\frac{\partial C_A}{\partial t} = \nabla\left[D_A \alpha \nabla C_A + N_A\left(d_{Av}\nabla C_v - d_{Ai}\nabla C_i\right)\right] \ , \tag{2.32}$$

$$\frac{\partial C_B}{\partial t} = \nabla\left[D_B \alpha \nabla C_B + N_B\left(d_{Bv}\nabla C_v - d_{Bi}\nabla C_i\right)\right] \ , \tag{2.33}$$

$$\frac{\partial C_C}{\partial t} = \nabla\left[D_C \alpha \nabla C_C + N_C\left(d_{Cv}\nabla C_v - d_{Ci}\nabla C_i\right)\right] \ , \tag{2.34}$$

$$\frac{\partial C_i}{\partial t} = \nabla\left[-\left(d_{Ai} - d_{Ci}\right)N_i \alpha \nabla C_A - \left(d_{Bi} - d_{Ci}\right)N_i \alpha \nabla C_B + D_i \nabla C_i\right] + K_0 - R - S_i \ , \tag{2.35}$$

$$\frac{\partial C_v}{\partial t} = \nabla\left[-\left(d_{Av} - d_{Cv}\right)N_v \alpha \nabla C_A - \left(d_{Bv} - d_{Cv}\right)N_v \alpha \nabla C_B + D_v \nabla C_v\right] + K_0 - R - S_v \ . \tag{2.36}$$

The above derivation of the atom and defect kinetic rate theory equations forms the backbone of all published and peer-reviewed models of the inverse Kirkendall RIS mechanism. The first extensive benchmarking of this model against experimental data was performed by Perks [17], [37], which is why this model is often referred to as the "Perks model". Both Perks [17], [37] and Allen [15], [18] showed that the inverse Kirkendall mechanism, as modeled using the approach outlined above, can accurately predict the magnitude and direction of RIS in austenitic stainless steels. A number of researchers [17], [18], [34–37] have utilized this inverse Kirkendall model, the notable differences between their studies being alternative treatments of diffusivities and the thermodynamic factor. For example, Wiedersich, *et al*. [35], set all correlation factors, f_x^j, to unity, but otherwise used the inverse Kirkendall model as derived above. Marwick's modeling effort [34] implemented thermodynamic factors inconsistently, but it also considered grain boundary migration by including an additional flux of $\delta N_x J_v$ in the atomic flux expressions.

Using the approach outlined above, Wiedersich, *et al*. [35] determine the RIS behavior of a binary B-25%A alloy in two sets of simulations. In the first set of simulations, A atoms preferentially migrate via vacancies, by assigning E_{mv}^{A}=0.77 eV, E_{mv}^{B}=1.28 eV, E_{mi}^{A}=0.10 eV, and E_{mi}^{B}=0.15 eV. These migration energies are similar to those of Cu as element A and Ni as element B. The result is depletion of A atoms down to 0 at% at moderate temperatures, with lower magnitudes of depletion at extremely low and extremely high temperatures—in other words, a bell-shaped curve of temperature dependence. When both A and B vacancy migration energies are set to 1.28 eV, and interstitial migration energies remain unchanged from the previous case, preferential transport of A atoms via interstitials occurs, leading to A enrichment. At lower dose rates, two effects are noted. First, the maximum enrichment magnitude increases with decreasing dose rate. And second, the bell-shaped temperature dependence shifts to a lower temperature range. These results are shown in Figure 2.6.

The inverse Kirkendall mechanism as discussed and derived within this section, has been approached with a very general perspective, allowing for universal applicability. That is, it is not derived or discussed specifically for, or with respect to, a particular alloy system or crystal structure. Later, in Section 2.1.5, the inverse Kirkendall mechanism will be applied to f.c.c. austenitic stainless steels.

2.1.4 Solute Drag Mechanism

The solute drag or interstitial binding mechanism is that in which defect-solute complexes form under irradiation, and are sufficiently mobile so as to undergo considerable diffusion before dissociating. The bound solutes are “dragged” to grain boundaries, where that solute specie will enrich. This mechanism has been shown to be of great importance in dilute alloys [32], where the nearest neighbors surrounding a defect do not change over very long diffusion distances. However, the same cannot be said of concentrated alloys, where nearest neighbors to defects change dramatically as the defect diffuses, leading to an ambiguous definition of a defect-solute complex. Thus, the solute drag mechanism is of little importance in concentrated alloys.

The solute drag mechanism requires the migration energy of the bound complex be less than the energy for dissociation of the complex [17]. The dissociation energy can be approximated as the sum of the binding energy of the complex and the migration energy of the point defect in the pure solvent. Solute-vacancy complexes rarely meet this condition, but solute-interstitial complexes meet the condition for alloy components having a large size mismatch, such as P, Si, and Nb in say, stainless steel [32], [43].

Progress in modeling the solute drag mechanism has predominantly been made by Faulkner, *et al*. [44–49]. These works have been focused on impurity atoms such as Si, C, B, and P, in both binary and ternary Fe systems. The model calculates the maximum segregation of impurity *z*, according to the equation:

$$C_z^{\max} = C_g \frac{E_b}{E_f} \left[\frac{C_b^z \exp\left(E_b^z / kT\right)}{\sum_z C_g^z \exp\left(E_b^z / kT\right)} \right] \left[1 + \frac{\xi K_0 F(\eta)}{A D \rho_d^2} \exp\left(E_f^z / kT\right) \right], \qquad (2.37)$$

where C_g is the total concentration of all impurities in the grain, E_b^z is the binding energy between impurity *z* and a self-interstitial, E_f^z is the interstitial formation energy, and C_g^z is the concentration of impurity *z*. Additionally, ξ is the defect production efficiency, K_0 is the defect production rate, $F(\eta)$ is the recombination term, A is the vibrational entropy surrounding the defect, D is the diffusion coefficient, and ρ_d is the sink density. This model supposes that all impurity atoms must compete for self-interstitial sites, the physics of which are represented in the denominator of the first bracketed term.

The Faulkner model of the solute drag mechanism can predict impurity segregation in good agreement with experimental measurements. In the ferritic steel used in Russian VVER reactor pressure vessels (composition by wt%: 0.25 C, 0.31 Si, 0.47 Mn, 3.30 Cr, 1.07 Ni, 0.37 Mo, 0.040 S, 0.018 P, 0.10 Cu, 0.1 V, balance Fe), Faulkner’s solute drag mechanism predicts the approximately six-fold increase in the phosphorus concentration at grain boundaries under 300°C neutron irradiation at low dose rates on the order of ~10^{-8}-10^{-10} dpa/sec, as shown in Figure 2.7. Unfortunately, the maximum dose to which Faulkner's models have been tested is 1 dpa—far below the anticipated doses in Generation IV nuclear reactor applications. Furthermore, the Faulkner models are only designed to evaluate RIS of impurity elements, and contain no information on the bulk RIS behavior of alloying components, such as Fe and Cr in F-M alloys.

Other researchers have attempted to include solute-interstitial binding effects for alloying components in a rate theory model [35], [36]. They use the following expression for the concentration of atom *x*-interstitial complexes, in which this expression can be written for each of *x* alloying components in the alloy:

$$C_{xi} = C_i \frac{C_x \exp\left(E_b^{xi}/kT\right)}{C_x \exp\left(E_b^{xi}/kT\right) + \sum\limits_{y \neq x} C_y} , \tag{2.38}$$

where the summation $\sum\limits_{y \neq x} C_y$ is computed over all alloying components except for the atomic specie for which the expression is being written, and E_b^{xi} is the binding energy of the atom *x*-interstitial complex. This model predicts that in a binary alloy, the component most strongly bound to the interstitial flux will enrich at grain boundaries.

Watanabe, *et al.* [38] also uses the inverse Kirkendall and solute drag mechanisms in combination to model RIS in austenitic Fe-Cr-Ni alloys. The inverse Kirkendall component of their model considers only interstitials and uses constant vacancy migration energies, which is opposite the treatment of researchers such as Perks [17], [37] and Allen [18]. Nickel is assigned a higher interstitial migration energy, 0.9 eV, than Cr and Fe, 0.3 eV for both elements; so contrary to conventional understanding that Ni is more likely to diffuse via interstitials due to it being undersized in the Fe-Cr-Ni system, this Watanabe model implies that Fe and Cr diffuse faster than Ni via interstitials. The Watanabe model also accounts for, however, the enrichment of Ni through the binding of Ni atoms to the interstitial flux with an energy of 0.75 eV. The Watanabe model concludes that the primary RIS mechanism is dumbbell interstitial migration, since boundary migration is observed even at low temperatures where vacancies are largely immobile [50]. However, other researchers [15], [17], [40], [51], [52] have demonstrated that RIS can occur through preferential vacancy exchange inverse Kirkendall mechanisms at these temperatures, even at dose rates as high as ~10^{-3} dpa/sec.

Although the solute drag mechanism offers an interesting perspective on RIS and may provide insight into solute-defect binding phenomena, these mechanisms may ultimately be impractical for understanding bulk RIS behaviors of alloying components in non-dilute alloys. All materials studied in this thesis are concentrated alloys, in which bound solute-interstitial complexes would be difficult to define and likely to dissociate prior to significant diffusion. Thus, the solute drag mechanism may not be of much importance in understanding RIS in F-M alloys.

2.1.5 Mechanism of RIS in Austenitic Alloys

Knowledge of RIS, thus far, is predominantly based upon f.c.c. Fe-Cr-Ni austenitic stainless steels, in which the RIS phenomenon is very well-understood. Because of the link between Cr RIS and irradiation-assisted stress corrosion cracking (IASCC) in austenitic steels, extensive experimental and modeling efforts have been devoted to RIS in Fe-Cr-Ni systems. These copious studies have provided a very good understanding of RIS behaviors and dependencies in austenitic steels, and have thus allowed for the confirmation of inverse Kirkendall as the driving mechanism of RIS. Although these observed trends and mechanisms may not hold in F-M alloys, it is nevertheless instructive to study them.

Experiments have revealed extremely consistent Cr depletion and Ni enrichment, with Fe making up the balance, over a wide range of irradiation conditions [15], [16]. A typical austenitic RIS concentration profile across a grain boundary is shown in Figure 2.8. With temperature variable, RIS profiles change in width and amplitude. At low temperatures, steady-state RIS profiles are shallow and narrow. With increasing temperature, greater defect mobility increases the magnitude of RIS. However, higher temperatures also enhance back diffusion, which causes the RIS profiles to broaden, until at extremely high temperatures, steady-state RIS profiles become so broad that nearly no segregation can be detected. Thus, temperature dependence of RIS in austenitic steels has a bell shape, attributed to the counteracting effects of limited defect mobility at low temperatures and extreme back diffusion at high temperatures; RIS is maximized at some moderate temperature. Temperature dependence of RIS in typical austenitic steel is shown in Figure 2.9. When studying dose rate functionality of RIS in austenitic stainless steels, two trends arise. First, the temperature range over which RIS occurs increases with increasing dose rate. And second, the temperature at which maximum segregation occurs increases with increasing dose rate. Both of these dose rate effects are captured in Figure 2.10.

The work of Perks [17], [37] are the hallmark studies identifying and confirming that RIS in austenitic stainless steels occurs by the inverse Kirkendall mechanism. Perks' model assumes interstitials do not contribute to RIS, and instead, generates RIS only due to differences in atom-vacancy exchange rates. Interstitial jump rates, then, are set independent of the participating atomic species. Perks performs RIS modeling of austenitic Fe-Cr-Ni alloys, and consistently predicts Cr depletion and Ni enrichment, with Fe either enriching or depleting to maintain at the grain boundary $C_{Fe} + C_{Cr} + C_{Ni} = 100$ at%. Perks validates his model against experimental measurements of Fe-20Cr-25Ni irradiated at 450°C to 1 dpa at a dose rate of 2×10^{-8} dpa/sec; the Perks model results for this irradiation condition are shown in Figure 2.11. Perks is able to successfully predict the direction of segregation for each constituent element, and can reasonably predict the magnitude of RIS. The work of Perks [17], [37] shows that it is unnecessary to account for interstitial effects, and that the vacancy-driven inverse Kirkendall mechanism alone can sufficiently describe RIS in austenitic steels.

Allen & Was [18] modify the treatment of migration energies in the Perks inverse Kirkendall model specifically for austenitic Fe-Cr-Ni alloys. Their modifications to the inverse Kirkendall model are based upon findings that, in austenitic Fe-Cr-Ni alloys, diffusivities are a function of alloy composition. Their modified inverse Kirkendall, or "MIK" model, then, calculates migration energies based on local compositions, or short-range ordering. To illustrate the concept, the MIK expression for the Cr-vacancy migration energy is as follows:

$$
\begin{aligned}
E_{vm}^{Cr} = {} & C_{Cr}\left[-\frac{3}{2}E_{coh}^{Cr}+\frac{1}{2}E_{vm}^{pureCr}-\frac{1}{2}E_{vf}^{Cr}\right] \\
& +C_{Fe}\left[-E_{coh}^{Cr}-\frac{1}{2}E_{coh}^{Fe}+\frac{1}{2}E_{vm}^{pureFe}-\frac{1}{2}E_{vf}^{Fe}-ZE_{FeCr}^{ord}\right] \\
& +C_{Ni}\left[-E_{coh}^{Cr}-\frac{1}{2}E_{coh}^{Ni}+\frac{1}{2}E_{vm}^{pureNi}-\frac{1}{2}E_{vf}^{Ni}-ZE_{NiCr}^{ord}\right] \\
& +C_{v}\left[-E_{coh}^{Cr}-E_{vf}^{Cr}\right]+\left[\frac{3}{2}E_{coh}^{Cr}+\frac{1}{2}E_{vm}^{pureCr}+\frac{1}{2}E_{vf}^{Cr}\right]
\end{aligned}
\quad , \qquad (2.39)
$$

where the subscripts *coh* represent a cohesive energy, *ord* an ordering energy, *fv* a vacancy formation energy, and *mv* a vacancy migration energy.

The Allen & Was MIK model has proven to be highly accurate as a predictive tool for RIS in f.c.c. austenitic steels over a wide range of temperatures and doses. In Figure 2.12, model predictions are plotted against measurements for Cr and Ni RIS in nine different austenitic steels irradiated with protons between 200°C and 600°C to doses from 0.1 to 3.0 dpa. Clearly, the MIK model presents a far more accurate prediction of RIS than does the Perks model.

The inverse Kirkendall mechanism is proven to be the driving force for the very consistent, predictable RIS observed in austenitic stainless steels. The vacancy contribution to the inverse Kirkendall flux can alone predict with sufficient accuracy the direction of RIS, RIS magnitudes, and RIS profile shapes. However, this is not to say that interstitials do not play a role at all. Whether the same mechanism applies in F-M alloys remains to be seen, but the well-established understanding of RIS in the simpler, austenitic alloy system, offers significant insight into the diffusion behavior of point defects in the presence of ionizing radiation.

2.1.6 Solute Size Effect

Size effects, or volume misfit, of constituent atoms, have been strongly correlated with RIS direction and magnitude [30], [43]. Although the solute size effect is not a mechanism of RIS, it is a convenient way to think about segregation. Size effects become most evident when there are dramatic differences in atomic volume between solute and solvent atoms.

It is theorized that in order to reduce lattice strain energy, undersized substitutional solutes will preferentially exchange with solvent atoms in interstitial positions, whereas oversized solutes will preferentially exchange with vacancies, or will return to or remain on substitutional sites. Thus, under irradiation, a disproportionately large amount of undersized solutes will participate in the interstitial flux, while a disproportionately large amount of oversized solutes will oppose the vacancy flux. This leads to a solute redistribution, from which develops an enrichment of undersized solutes and a depletion of oversized solutes at sinks.

In Fe-Cr-Ni austenitic stainless steels, Cr is an oversized solute by ~5% volume misfit, and is consistently observed to deplete under a wide range of irradiation conditions. Similarly, the consistent Ni depletion in austenitic stainless steels can also be correlated with the ~3% volume misfit of undersized Ni atoms in the Fe-Ni-Cr lattice. Excellent agreement between the volume misfit and the observed direction of segregation in a variety of binary alloys and stainless steels is shown in Table 2.1.

Unfortunately, the volume misfit between Fe and Cr atoms is very small in b.c.c. Fe-Cr binary alloys, leading to the size effect having a very unclear influence on RIS in F-M steels. Some have theorized that Cr acts as both an oversized and undersized solute in the Fe-Cr system. The atomic radius of Cr is slightly larger than that of Fe, suggesting that Cr is oversized. But because larger elements such as W, Nb, Mo, Ta, V, and Ti are often used as alloying components in F-M alloys, sizable concentrations of these oversized atoms may cause the lattice parameter of the alloy to increase such that Cr reverts to acting as an undersized solute. This idea is illustrated in Figure 2.13, which pre-supposes an interstitial-solute drag mechanism and thus relates the sign of interstitial binding energy to the relative solute size. Molecular dynamics (MD) simulations confirm [53–55] that Cr can be either oversized or undersized in the b.c.c. Fe-Cr system. These simulations find two different semi-empirical Finnis-Sinclair-type potential, one of which has Cr oversized and depleting, the other of which has Cr undersized and enriching.

2.2 Ferritic-Martensitic Alloys

The first high-Cr (9-12 wt% Cr) steels originated in 1912, when a 12 wt% Cr steel was alloyed with 2-5 wt% Mo, and was manufactured into steam turbine blades. Shortly thereafter, the stainless characteristics of these steels came to be understood. Around the same time, the hardness and durability of high-Cr high-C martensitic steels became known, leading to their extensive use in consumer applications. It wasn't until the 1930s, however, that these two advantageous characteristics—corrosion and oxidation resistance attributed to a high Cr content, and hardness at elevated temperatures due to a tempered martensite microstructure—were combined. The resulting alloys were 9-12 wt% Cr steels having low C, additions of Mo, W, V, Nb, and N, amongst other elements, with high creep-rupture strength and resistance to oxidation and corrosion [1]. Ever since, there has been significant advancement in understanding this class of steels, as their utility in the petrochemical, chemical processing, gas turbine, aerospace, and electric power industries has grown.

Modern F-M alloys can be quite complex. Their constitution, phase formation, and heat treatment are critical to proper microstructural development, upon which their excellent mechanical properties strongly depend. These formative metallurgical aspects of F-M alloys will be discussed in this section.

2.2.1 Physical Metallurgy

The typical laboratory heat treatment of high-Cr steels is a multi-step process. First, the steel is austenitized in the temperature range 850-1200°C. Next, either air cooling or rapid quenching induces a phase transformation from austenite to martensite. Subsequently, the steel is tempered to improve its strength, ductility, and toughness [2]. Double-austenitizing for higher-Cr martensitic steels (e.g. ~12Cr) has been shown to produce a more uniform grain structure, resulting in greater homogeneity of properties after the last tempering step [1].

At austenitizing temperatures, the steels are either fully austenitic or have a duplex austenite and δ-ferrite structure [1]. The amount of δ-ferrite present, relative to the amount of austenite present, influences strength, toughness, and the amount of martensite that will develop following cooling to ambient temperature. Ferrite-forming elements, Cr, Mo, Nb, V, W, Si, Ti, and Al, increase the tempering resistance of steels and inhibit austenite phase growth. The effect of Cr, a ferrite-forming element, on the constitution of Fe-Cr alloys containing 0.1 wt% C is illustrated in Figure 2.14. The δ-ferrite content increases by 14% per additional mass% of Cr in an alloy [1].

Formation of δ-ferrite can be suppressed by the addition of austenite-forming elements: C, N, Ni, Mn, Cu, and Co [1]. Carbon is one of the most commonly-used austenite stabilizers, although it decreases toughness and impairs corrosion resistance. In addition, carbon indubitably induces the formation of MC carbides (M = V, Nb, Ti, or Ta). Higher austenitizing temperatures are required to dissolve these carbides, resulting in coarser prior austenite grain (PAG) sizes, and thus, reduced toughness and creep ductility [1]. Since Cr is a ferrite-forming element, it is much more difficult to eliminate δ-ferrite if more Cr is present in the bulk. Therefore, limiting Cr content to ≤ 9 wt% also helps to suppress δ-ferrite formation [1].

All austenite present at the annealing (i.e. austenitizing) temperature should fully transform to martensite during cooling. However, alloying additions can lower the martensite transition start and finish temperatures, thereby increasing the likelihood of retaining austenite, especially if the martensite start temperature is near or below room temperature [1]. Retained austenite increases the toughness of the steel, but is undesirable because strength-decreasing distortions occur during the martensitic transformation. Internal stresses resulting from these distortions will be retained if both martensite and austenite are present in the final, ambient temperature form of the alloy [1]. It is critical, then, to consider the advantages gained by alloying additions, against the adverse consequences they can have on phase formation and constitution.

The Schaeffler-Schneider diagram, Figure 2.15, predicts the phases present in steels, as a function of Ni and Cr content, at ambient temperature following cooling from the austenitization temperature..

A high dislocation density arises during the martensitic transformation. Large internal stresses are generated during the transformation, and it can proceed only when in tandem with accommodation processes (e.g. lattice invariant shear processes), which introduce high dislocation densities [1]. The resultant martensite is thus hard and not easily deformed.

Continuous cooling transformation (CCT) diagrams show that martensite is formed in thick sections, or laths, due to the inhibition of the pearlite transformation and the absence of bainite, even within an extended time period. This is illustrated with an example CCT diagram in Figure 2.16 for a 12Cr-MoVNb martensitic steel. Martensite laths are typically very hard, low in carbon, and have dimensions of approximately 1 μm by ≥5 μm [56]. Hardness of the martensite laths increases linearly with interstitial C or N content, but is not significantly dependent upon Cr, W, V, or Ta content, austenitizing temperature, PAG size, or lath dimensions [1].

The hardened martensite must be tempered in order to increase toughness and improve mechanical properties. The tempering process transforms brittle martensite into bainite or ferrite. When tempering begins, the steel has retained the high dislocation density formed during the martensite transformation and post-anneal cooling. However, tempering typically decreases that dislocation density by nearly a factor of ten. Even after tempering, though, dislocation densities remain high—on the order of values observed in work-hardened alloys [1]. Precise control of time and temperature during tempering is critical to achieving the desired dislocation network and its associated mechanical properties.

To avoid reaustenitization, tempering must be performed below the temperature at which martensite begins to transform to austenite upon heating, typically in the range of 760-850°C [56]. Austenitization of the ferrite formed during tempering is also undesirable. Since the equilibrium temperature above which ferrite begins to transform to austenite is decreased in the presence of Ni [1], F-M alloys have very low Ni content as compared to typical austenitic steels.

Tempered F-M alloys have a complex microstructure. Each PAG is divided into "packets" of parallel martensite laths. Although the packets themselves can have both low angle and high angle boundaries [57], laths within a single packet occupy the same habit plane, have the same orientation, and often have very close crystallographic alignment. Laths have dislocation Burgers vectors of $\frac{1}{2}a_0\langle 111\rangle$ and a network dislocation density on the order of $\sim 10^{14}$ m^{-2} [58]. During tempering, these dislocation networks rearrange into a lower-energy configuration within each lath, forming the boundaries of small subgrains. These subgrains have small misorientation angles, due to dislocations of the same sign aligning vertically to reduce the energy of interaction. The subgrain formation process is thermally-activated, and involves dislocation climb and glide. The tempering treatment itself provides the thermal activation necessary to form the subgrains [48]. A schematic of the typical F-M microstructure following tempering is shown in Figure 2.17.

Diffusion of carbon out of the matrix is key to the tempering process, allowing for martensite to transform to ferrite. Diffused C then precipitates as carbides or carbonitrides on PAGBs (prior austenite grain boundaries), packet boundaries, lath boundaries, and subgrain boundaries. The diffusion rate along high-angle boundaries is considerably higher than along low-angle boundaries. Therefore, carbides are more easily formed—and form more coarsely—along packet boundaries and PAGBs than along lath or subgrain boundaries [56], [58], [59].

Silicon concentrations in F-M alloys are kept relatively low. Silicon is soluble in the matrix, and thus causes the lattice parameter to decrease, thereby increasing coherency strains and tempering resistance [1]. Additional effects of Si, C, and other alloying or impurity elements, will be discussed in the context of precipitation in the following sub-section.

2.2.2 Precipitates

Thermal aging of high-Cr steels, during their tempering treatments, can induce the precipitation of trace impurities and alloying elements. These precipitates can significantly alter the hardness, toughness, and cracking susceptibility of the alloys. Precipitation and its associated mechanical changes are highly sensitive to the temperature at which tempering is performed [1]. As an example, the hardness behavior of a 12Cr-0.14C steel as a function of tempering temperature is shown in Figure 2.18.

Tempering below 350°C forms a fine dispersion of M_3C (Fe_3C) precipitates. The Cr content of Fe_3C increases to ~20%, with the possibility of M_7C_3 forming *in situ* from the Cr-enriched Fe_3C [1]. Both of these effects slow the Fe_3C growth rate, thereby retarding softening. At slightly higher tempering temperatures, 350-500°C, the M_3C precipitates continue to nucleate, but additional fine needles of M_2X (mainly $Cr_2(CN)$) nucleate primarily on dislocations in martensite laths [1]. The M_2X needles also retard softening, but the precipitation itself is not sufficient to produce hardening.

Tempering above 500°C causes carbide precipitation on the tangled dislocations in remaining δ-ferrite phases [1]. Up to 550°C, the M_7C_3 and M_2X phases coarsen, resulting in a rapid decrease in hardness [1]. Above 550°C, however, those M_7C_3 and M_2X are replaced by Cr-rich $M_{23}C_6$ precipitates nucleating on PAGBs and martensite lath boundaries. The rate at which hardness is decreasing slows, and the dislocation density decreases. Subgrains consisting of low-angle boundaries and dislocation arrays begin to form within laths [1].

The dislocation density is further reduced, and sugbrain formation is further increased, when $M_{23}C_6$ precipitates grow at lath boundaries, upon tempering above 650°C [1]. At even higher temperatures, above 750°C, subgrains grow into equiaxed subgrains with little or no trace of the original martensite lath structure. The $M_{23}C_6$ precipitates continue to grow, and nearly all C is precipitated in the $M_{23}C_6$, but clearly-defined dislocation networks are still present [1].

Tempering conditions are critical to precipitation of $M_{23}C_6$, the principal and most stable carbide in F-M alloys. The $M_{23}C_6$ ($M = Cr_{16}Fe_6Mo$ or $Cr_4Fe_{12}Mo_4Si_2WV$) are coarse, face centered cubic (f.c.c.) particles found at PAGBs and lath boundaries, with finer particles found within the matrix. Typical $M_{23}C_6$ particles are ~150 nm in diameter [1], but their size can increase with increasing bulk C concentration [1], and they have even been observed as large as ~2 mm in T91 [60]. The $M_{23}C_6$ occur at number densities at least an order of magnitude larger, and have diameters at least three times greater, than that of other precipitates in typical F-M alloys [61]. Additionally, studies have found [62] that in normalized and tempered HT9 and modified 9Cr-1Mo, the majority of precipitates are $M_{23}C_6$ with a small amount of MX.

The fine MX particles are found primarily on lath boundaries, occur at diameters of 20-50 nm, and grow in the f.c.c. structure [60]. They form during prolonged thermal aging, gradually replacing the M_2X precipitates which grew during tempering. The MX particles can be carbides, nitrides, or carbonitrides with compositions NbC, NbN, VN, CrVN, NbCN, or NbVC, depending upon the bulk concentration of the constituent elements [1].

The Laves phase can also replace M_2X upon prolonged high-temperature aging, and is the primary phase formed in the temperature range 450-650°C [1], [62]. The Laves phase has the composition Fe_2Mo, Fe_2W, or $Fe_2(Mo,W)$ in steels containing Mo, W, or Mo plus W, respectively. They have a hexagonal lattice structure and nucleate on Cr_2N particles within martensite laths as well as around the $M_{23}C_6$ precipitates on PAGBs and lath boundaries [1].

The precipitate distribution, constitution, and structures are critical to the superior hardness and mechanical performance of F-M alloys. The M_2X precipitates are sources of secondary hardening and increased tempering resistance, as ferrite-formers Mo, W, and V are soluble in these particles, thereby increasing its lattice parameter and associated coherency strains. In addition, at temperatures above those at which M_2X precipitates, stable carbides, nitrides, and carbonitrides of V, Nb, Ta, and Ti can form, increasing the steel's resistance to overaging and tempering. Any soluble V, Nb, Ta, and Ti also produce solid-solution strengthening and hinder subgrain recovery and growth at the highest tempering temperatures [1]. The extent of precipitation during the tempering process depends on the content of carbon, nitrogen, and other alloying elements in the steel; significantly more precipitation is seen in higher-carbon (0.2 wt% C) steels than in lower-carbon (0.1 wt% C) steels [1]. A summary of precipitation in tempered F-M alloys is shown in Table 2.2.

2.3 RIS Experiments in Ferritic-Martensitic Alloys

Heretofore, the scientific community has had only a limited understanding of RIS in F-M alloys. Only a handful of experiments have measured RIS in F-M alloys, and their results are highly contradictory, with about half of the studies reporting Cr enrichment at grain boundaries, and the other half reporting Cr depletion. Further complicating the picture, however, is that none of the published experiments have been performed under the same conditions—they all use different alloys, irradiate at different temperatures and dose rates, to different doses, with different incident particles. Many of these studies do not report on the initial condition of the alloy, and whether or not there is any solute segregation at grain boundaries prior to irradiation. It is simply impossible to draw any conclusions about RIS in F-M alloys based on the very limited—yet very diverse—results in the body of literature. Table 2.3 presents a summary of all known, peer-reviewed experiments on RIS in F-M alloys, published up to this point in time. Each of these experiments, and their results, shall be described in this section.

2.3.1 Experiments Showing Chromium Depletion

2.3.1.1 11 MeV Protons on HT9

Hamaguchi, *et al*. [8] irradiated two different heats of HT9 and a related ferritic steel, with energetic 11 MeV protons. Although the primary intention of their work was to determine irradiation-induced hardening as a function of depth into the damage profile, they also utilized Mössbauer spectral techniques to examine Cr segregation. The experimental design of their specimens used a sectioning approach to facilitate a depth-dependence study.

The first heat of HT9 was composed of (in wt%) 12.39 Cr, 1.04 Mo, 0.68 W, 0.53 Mn, 0.49 Ni, 0.31 V, 0.22 Si, 0.20 C, and a balance of Fe. It contained a small amount of delta ferrite grains amongst the tempered martensite structure. A second heat, containing only tempered martensite laths, was fabricated by reducing the concentration of ferrite-forming elements Cr, W, and V to concentrations of 12.24, 0.48, and 0.29 wt%, respectively. A fully-ferrite steel, denoted SUS410L, was also prepared, having bulk concentration (wt%) of 12.34 Cr, 0.52 Mn, 0.51 Ni, 0.21 Si, 0.02 C, 0.01 Mo, 0.01 V, and balance Fe. The alloys were austenitized between 950°C and 1030°C for up to two hours, and the two heats of HT9 were then tempered at 700°C for two hours. The alloys were cold-rolled into thin plates, 30-50 μm thick, followed by strain relief annealing. Ten to twenty of these plates were stacked atop one another, and subjected to a 10^{22} m^{-2} flux of 11 MeV protons perpendicular to their front surface, to a final dose of approximately

0.36 dpa. The irradiation temperature was estimated to range from 497°C to 647°C, and was maintained with a combination of water and helium cooling.

Concentration changes are evaluated using Mössbauer spectroscopy. This technique measures the resonance absorption of gamma rays by a solid specimen. A Mössbauer spectrum is a plot of gamma ray intensity as a function of the velocity of the gamma ray source. At velocities corresponding to the resonance energies of the specimen, a fraction of the gamma rays are absorbed, resulting in a decrease in the measured intensity, which corresponds to a valley in the spectrum. Differences in chemical environments within the specimen can be identified by changes to the Mössbauer spectrum. To determine RIS, the spectrum from an irradiated region is compared to that from an unirradiated region. The "difference spectrum" between the irradiated and unirradiated spectra, as illustrated in Figure 2.19(a) for SUS4010L at a depth of 315 μm, indicates peaks at velocities of ±5 mm/s, which provide evidence of a change in the Cr concentration. These difference peaks at ±5 mm/s have a maximum amplitude at the damage peak, as shown in Figure 2.19(b) for the irradiated SUS410L specimen. Knowing from the Mössbauer spectra that Cr segregates under irradiation, and knowing the presence of Cr alters the ferromagnetism of a b.c.c. Fe-based alloy, changes in the magnetic field may be correlated with atomic concentration changes of Cr. The average internal magnetic fields of the SUS410L unirradiated specimen and the specimen located 315 μm into the damage peak are 285 kilo-oersteds (kOe) and 291 kOe, reespectively. This 6 kOe increase to the internal magnetic field corresponds to a 2.3 at% Cr depletion in the matrix for SUS410L at peak damage.

Unfortunately, Hamaguchi, *et al*. [8] does not provide any further results of Cr RIS, either at other depths in the SUS410L specimen, or on either of the HT9 heats. Furthermore, this technique does not provide information about RIS of the alloying elements besides Cr, nor does it reveal the shape of RIS profiles.

2.3.1.2 590 MeV Protons on F82H

Schäublin, *et al*. [10] investigated the low activation F-M steel F82H, composed of 7.65 wt% Cr, 2 wt% W, <1 wt% total of Mo, Mn, V, Ta, Ti, Si, and C, and a balance of Fe. The alloy was austenitized at 1040°C for 0.5 hour, then tempered at 740°C for 2 hours. In this austenitized-and-tempered condition, thermally-generated Fe depletion and Cr enrichment gradients had already formed at martensite lath boundaries, as observed using energy filtered transmission electron microscopy (EFTEM). Irradiations were then carried out at the PIREX facility, using 590 MeV protons, to a final dose of 0.5 dpa at 250°C. Following irradiation, EFTEM techniques analyzed the microchemistry of both lath boundaries and prior austenite grain boundaries (PAGBs).

Both Fe and Cr were found to deplete in F82H following irradiation. Element profiles across irradiated boundaries were notably noisier than the profiles collected across unirradiated boundaries. The authors report concentration profiles as the number of counts, rather than converting counts to composition. Without more information about their measurements, it is impossible to extract the quantitative magnitude of segregation. However, since the authors acquired both the unirradiated and irradiated spectra under the same experimental acquisition conditions, they argue that the number of counts can be compared between the two spectra. The EFTEM element maps and counts are shown in Figure 2.20.

A few questions arise concerning Schäublin's results. First, Cr and Fe cannot both deplete in the irradiated material, without at least one other element enriching. Unfortunately, RIS behaviors are not reported for any of the other elements present in the alloy. Furthermore, it is inappropriate to compare the irradiated spectra to the unirradiated spectra based on them being acquired under the same experimental conditions. These spectra are collected on different boundaries, located on completely different samples, and will therefore yield completely different count rates in EFTEM based on differences in specimen thickness and grain orientation relative to the analytical electron beam.

2.3.1.3 250 keV Ni^+ Ions on E911

Lu, *et al.* [12] studied RIS in F-M alloy E911 using a multi-beam high voltage electron microscope, with which both the ion irradiation and post-irradiation analytical examination were performed. The alloy was first prepared by austenitization at 1060°C for 1 hour, followed by air cooling. This heat of E911 is composed of, by wt%, 9.16 Cr, 1.00 W, 0.23 Ni, 0.68 Nb, 1.01 Mo, <1.00 total of C, N, Mn, Si, P, S, and V, and a balance of Fe. The alloy was cut into 3 mm diameter TEM (transmission electron microscope) discs, then electropolished to perforation. Some of the discs were implanted with Hf to 1 at% at room temperature. Both E911 and E911+Hf were irradiated with 250 keV Ni^+ ions, producing a dose rate of 2.36 x 10^{-5} dpa/sec, at 300°C to a final dose of 0.305 dpa.

Prior to irradiation, the authors observed pre-existing P enrichment at grain boundaries. Although the bulk concentration of P is only 0.007 wt%, grain boundaries were observed to be composed of as much as 0.17 wt% P following heat treatment. Under irradiation, P enriches even further, with grain boundary concentrations as high as 0.3 wt% in E911+Hf and 1.66 wt% in E911. The authors surmise that P, as a severely undersized solute in F-M alloys, has a positive binding energy with interstitials and will thus enrich at grain boundaries. The addition of Hf, however, suppresses the amount of P enrichment. This effect is due to Hf being an extremely oversized solute and having a positive solute-vacancy binding energy. The Hf is thus able to capture vacancies with ease, which severely reduces vacancy mobility, and thereby enhances recombination in the matrix and reduces the population of point defects available to cause RIS. The suppression of RIS by oversized solute addition has been studied extensively in austenitic stainless steels [40], [41], [63].

Chromium was also enriched at grain boundaries prior to irradiation, by 3.74 wt% above the matrix concentration. Following irradiation, Cr was found depleted by 2.04 wt% and 0.63 wt% below the matrix concentration, in E911 and E911+Hf, respectively. Again, the Hf addition suppressed the magnitude of RIS.

The 250 keV Ni+ ions incident upon the specimen have a range of <100 nm in E911, which is likely less than the specimen thickness. If so, the specimens were implanted with 8.06 x 10^{16} Ni ions/cm^2, which could sufficiently alter the bulk composition so as to skew RIS results. The thin-foil nature of the irradiated specimen, as a TEM disc, also raises a question regarding the influence of the surface as a major point defect sink. Furthermore, the types of boundaries studied (e.g. lath, PAGB) were not specified.

2.3.1.4 Cr^{3+} Ions on Fe-13Cr Alloys

Neklyudov and Voyevodin [9] irradiated several b.c.c. Fe-13Cr alloys with Cr^{3+} ions at dose rates of 0.1-0.3 dpa/sec. The alloys studied include Fe-13Cr, Fe-13Cr-2Mo, Fe-13Cr-2Mo-NbVB, and Fe-13Cr-2Mo + TiO_2. Irradiations were performed with either the ESUVI materials research heavy ion accelerator or the UTI heavy ion accelerator. ESUVI irradiations used 5 MeV Cr^{3+} ions at 350-800°C and achieved doses of 1-200 dpa; UTI irradiations used 1 MeV Cr^{3+} ions at 270-700°C and achieved doses of 0.1-100 dpa. It remains unspecified which alloys were irradiated in which accelerator, and under what specific conditions. Following irradiation, microchemistry is determined using TEM with energy dispersive x-ray spectrometry (EDS).

The authors observe Cr depletion at grain boundaries in all of the alloys, although no quantitative information about the nature of the depletion, nor the irradiation conditions, is given. The Cr depletion is attributed to it being oversized in the binary Fe-Cr system, and thus segregating away from the boundary by means of the vacancy flux in accordance with the inverse Kirkendall mechanism. However, the authors also mention that the oversized solute Ti enriches at boundaries in irradiated Fe-13Cr-2Mo + TiO_2, an observation counter to the explanation offered for the Cr depletion.

Also of note is the enrichment of Cr and Si at the boundary of a <100> dislocation loop in 13Cr-2Mo-NbVB irradiated with 1 MeV Cr^{3+} ions at 575°C to 48 dpa. The segregation profile is shown in Figure 2.21. Since the loops are of the interstitial type, it is suggested that the species enriched at the loops are preferentially coupled with the interstitial flux. And since loops are biased sinks for interstitials, there will be an excess vacancy flux toward neutral sinks such as grain boundaries, which would leave the grain boundaries depleted of the species enriching at loops. This explanation of Cr-interstitial coupling, however, does not jive with the earlier suggestion that Cr is oversized in the b.c.c. Fe-Cr lattice.

Because details on these experiments are sketchy at best, it is very difficult to assess the validity of these results. The incident Cr^{3+} ions have a range of at most 1.5 μm if 5 MeV ions are used (of course, the range will be much smaller if lower-energy ions are used), and because the irradiation configuration is not discussed, it is unknown whether the incident ions penetrate the specimen, or are implanted into the specimen. TEM specimen preparation is also not discussed. Ignoring the damage profile and implantation peak when performing irradiations and creating TEM discs, will have tremendous consequences on the measured RIS behavior. Additionally, the authors do not specify the types of boundaries studied, and they use a very poor spatial resolution in the TEM-EDS analysis.

2.3.1.5 650 kV Electrons on Fe-5Cr and Fe-13Cr

As part of a larger effort to understand void suppression in fusion reactor materials, Takahashi, *et al.* [3] examined RIS at grain boundaries in b.c.c. Fe-5Cr and Fe-13Cr binary alloys. The alloys were irradiated in a high voltage electron microscope using a 3 x 10^{23} e^{-}/m^{2}-s flux of 650 kV electrons. This flux delivered a damage rate of 4-9 x 10^{-4} dpa/sec at 400°C, and a final dose of 3 dpa. Specimens were fabricated into electron-transparent TEM foils, which were then oriented to the {110} or {111} zone axis in the area of interest, for the duration of the irradiation. The irradiation area was a focused beam ~10 μm in diameter. Following irradiation, grain boundary concentrations were analyzed using EDS with a minimum probe size of 10 nm. This probe size is very large, approximately 10 times the size of modern capabilities. Such a large probe produced a massive interaction volume, preventing points along the RIS profile from being spaced less than ~50 nm apart, and thus severely restricting the spatial resolution of the RIS measurements.

Composition analysis across a grain boundary revealed Cr depletion in both Fe-5Cr and Fe-13Cr, as shown in Figure 2.22. Although the authors reported depletion in terms of an EDS Cr:Fe count ratio, one can calculate RIS magnitudes of approximately -0.64 at% and -3.94 at% for Fe-5Cr and Fe-13Cr, respectively. The resultant concentration gradients both had a full width at half maximum (FWHM) of ~200 nm. This gradient is extremely wide, particularly as compared to more recent studies, which show RIS profiles with FWHM on the order of ~20 nm [11]. Such extremely wide RIS profiles are likely an effect of the poor spatial resolution attributed to the large EDS probe diameter. A zone slightly enriched in Cr was observed between the depleted zone and the matrix. Neither voids, nor radiation-induced precipitates, were observed in either alloy.

2.3.2 Experiments Showing Chromium Enrichment

2.3.2.1 1 MV Electrons on Fe-10Cr-*x*Mn-3Al

Kato, *et al*. [4] performed RIS measurements on a series of three ferritic alloys Fe-10Cr-*x*Mn-3Al, where $x = 5$, 10, or 15. The alloys were fabricated as TEM discs 3 mm in diameter and 0.2 mm thick, solution annealed for 30 minutes at 1150°C in a vacuum chamber maintained at $<10^{-5}$ Pa, so as to prevent oxidation. Subsequently, the specimens were twin-jet electropolished to an electron-transparent 400 nm. A single-phase ferritic structure was observed. The specimens were then electron-irradiated *in situ* in a TEM, with the irradiating electron beam centered on a grain boundary. The irradiation was performed using 1 MV electrons with a flux of 4.0×10^{23} e^{-}/m^{2}-s, corresponding to a damage rate of 1.9×10^{-3} dpa/sec; a final dose of 10 dpa was achieved, and the experiment was maintained at 450°C. Following irradiation, the specimens were required to be thinned further, with 4.2 kV Ar^{+} ions, in order for EDS analysis to be performed. TEM-EDS utilized a 10 nm electron probe, which, as previously mentioned with respect to the Takahashi, *et al*. [3] study, is considerably larger than afforded by modern capabilities, and provides a rather poor spatial resolution of the RIS profile.

Basing their RIS analyses on the solute size effect, Kato, *et al*. [4] used x-ray diffraction analysis to determine the volume size factors of the constituent elements in their alloys. They find that Mn, Cr, and Al are all oversized in the Fe-Cr-Mn-Al system, as shown in Table 2.4. The Al size factor in Fe-10Cr-5Mn-3Al is larger than in Fe-10Cr-15Mn-3Al because the increase in Mn content increases the overall alloy atomic volume and thereby reduces the relative Al atomic size.

In all three alloys, the oversized solutes Mn and Al were depleted at grain boundaries, while the oversized Cr was enriched at grain boundaries. Concentration profiles have a FWHM of ~200-300 nm, owing to the large (10 nm) EDS probe. For illustration purposes, the Mn, Al, and Cr RIS profiles in Fe-10Cr-5Mn-3Al are given in Figure 2.23. Although the direction of RIS is consistent across all three alloys, the magnitude of RIS decreases quite linearly as the bulk Mn concentration increases. This trend is shown in Figure 2.24, and can be explained by the solute size effect. Increasing the bulk Mn concentration increases the overall atomic volume and lattice parameter of the alloy. If volume misfit is encouraging segregation, then it follows that when the lattice parameter of the alloy increases and can better accommodate oversized solutes, then their level of misfit is reduced, and segregation is suppressed. It is also important to note, here, that Al segregates more strongly than does Mn, and not surprisingly, Al has a larger volume size factor than does Mn.

The solute size effect, as it applies to oversized Mn and Al depletion, is inconsistent with the observed enrichment of oversized Cr. Instead, the authors relate Cr enrichment to the formation of Cr-rich precipitates at the grain boundary. Additionally, Cr enrichment was also observed at grain boundaries outside of the irradiated area, but on the irradiated specimen. In other words, 450°C annealing generated Cr enrichment. The magnitude of Cr enrichment on annealed, unirradiated grain boundaries was about half that on irradiated grain boundaries. These observations suggest that Cr segregation occurs by a thermally-activated diffusion process, which can be enhanced in the presence of irradiation.

2.3.2.2 0.5 and 2 MeV Fe^+ Ions on Fe-14.25wt%Cr

Marquis, *et al.* [14] performed ion irradiations to study RIS in a model Fe-14.25 wt% Cr (15.1 at% Cr) alloy containing <10 weight ppm C. The alloy was produced by induction melting, then hot forged at 1150°C, vacuum annealed at 800°C for 6 hours, and finally water quenched. This heat treatment crystallized large grains, on the order of 100 μm. The material were irradiated at 350°C with two different Fe^+ ion fluxes at a net rate of ~2.5×10^{15} ions/m^2-s. A 1×10^{19} ions/m^2 flux of 2 MeV Fe^+ was implanted, after which a 5×10^{18} ions/m^2 flux of 0.5 MeV Fe^+ was implanted. The two ion energies combine to yield a relatively flat damage profile, delivering a dose of ~1.5-2.3 dpa through a depth of ~700 nm, as shown in Figure 2.25. Grain boundary microchemistry was examined both before and after irradiation using atom probe tomography (APT).

Following irradiation, complex RIS behaviors of Cr and C are measured at varying depths into the specimen. At a depth of 2 μm, which is far deeper than the irradiation-damaged region and Fe-implanted zone, Cr enriches by ~4 at% at the grain boundary and C enriches by ~2.5 at% (Figure 2.26(a)). Near the back of the damage profile, around 800 nm in depth, the dose delivered is ~0.5 dpa. Here, C is enriched at the boundary, but there is some depletion of Cr on both sides of the grain boundary (Figure 2.26(c)). However, the grain boundary Cr concentration remains enriched above matrix levels, although it is slightly lower than the grain boundary Cr concentration at 2 μm depth. Then, at the 0.5 MeV Fe^+ implantation peak (Figure 2.26(b)), located 300 nm into the specimen, the Cr concentration profile further develops a "W" shape. The grain boundary Cr concentration is decreased approximately to matrix Cr levels, and is surrounded by regions depleted of Cr. The grain boundary remains enriched in C, although it is of a slightly lower magnitude than at 800 nm depth.

The solute segregation observed at a depth of 2 μm is attributed entirely to the heat treatment, and is considered by the authors to be representative of the pre-irradiation, as-fabricated grain boundary microchemistry. The authors state that lattice and grain boundary diffusion of Cr in b.c.c. Fe at the irradiation temperature of 350°C, particularly over the short duration of the irradiation, is negligible, and thus will not affect the concentration profiles at 2 μm. At the depths of 300 nm and 800 nm, however, considerable implantation of Fe will occur, and could have significant consequences on the behavior of RIS at the specified depths.

At all depths, the Cr and C concentration profiles across grain boundaries are observed to be on the order of ~8 nm in width. The authors state, however, that this is an overestimation of the true segregation profiles, due to limitations of APT spatial resolution due to trajectory aberrations near grain boundaries and possible surface diffusion and retention effects. No evidence for M_6C or $M_{23}C_6$ type carbides is detected in this alloy, even following irradiation.

2.3.2.3 Fast Neutrons on HT9

Clausing, *et al*. [6] irradiated HT9 to approximately 13 dpa in the EBR-II fast reactor. Their heat of HT9 contained, in at%: 12.81 Cr, 0.96 C, 0.59 Mo, 0.54 Ni, 0.50 Mn, 0.41 Si, 0.16 W, 0.07 Al, 0.01 each of Si, P, and N, and a balance of Fe. The heat treatment involved a 1 hour anneal at 1035°C, followed by air cooling, and finally 1 hour tempering at 760°C. The heat-treated alloy was machined into bar specimens, 1 mm square and 10 mm long, with a central 60° notch 250 μm deep. These bars were irradiated at 410°C, 520°C, and 565°C, with the irradiation temperatures being maintained within ±20°C. The neutron fluence was 2.8 x 10^{26} n/m^2, which corresponds to a dose of ~13 dpa. Control specimens were aged at the appropriate temperatures for 15000 hours to match the irradiation time of the irradiated specimens.

Following irradiation, the specimens were fractured at liquid nitrogen temperatures in an ultra-high vacuum chamber. Fracture surfaces were analyzed using scanning Auger electron spectroscopy (AES) with a 0.2 μm diameter probe. Surface layers were removed by sputtering 5 keV Ar$^+$ ions to a depth of 120 nm at normal incidence to the fracture plane. AES was performed on the fracture surface both before and after a surface layer was removed.

Fracture surfaces on the specimens irradiated at 410°C contained a small number of large, 25-50 μm diameter, relatively smooth macro-facets, which the authors believed to be PAGBs. They observed strong enrichment of Ni, Cr, Si, and P at these macro-facet surfaces, as shown in Figure 2.27; the facet surface concentrations of Cr, Si, and P were 1.4, 10, and 100 times higher than their bulk concentrations, respectively, and decreased to approached their bulk concentrations within ~30 nm below the surface. The surface concentration of Ni was 8 times its bulk concentration, and increased to 16 times its bulk concentration deeper into the specimen, where it persisted at such a high level through the 120 nm maximum sputter depth. All concentration profiles, including that of Ni, had a FWHM ~20 nm.

Besides the macro-facets, the remainder of the fracture surfaces on the 410°C irradiated specimen contained small, 2-5 μm diameter, micro-facetted regions that were randomly oriented, and believed to be related to the martensite lath and packet microstructure. No evidence of segregation was observed on these micro-facets. The higher irradiation temperatures, 520°C and 565°C, contained very few macro-facets and very little segregation. No segregation was found in thermal controls, which were completely absent of macro-facets.

The authors suggest that RIS of P is enhanced by an interaction with Cr. Since P and Si are undersize solutes in HT9, they are expected to enrich at grain boundaries due to undersize-interstitial binding effects. But since Cr has a larger atomic volume than Fe, the solute size effect would suggest that it would rather deplete at grain boundaries. The observed Cr enrichment, then, could be explained by a Cr-P interaction, which is similar to the idea of a Cr-C-vacancy complex, as proposed by Ohnuki, *et al*. [5].

The behavior of Ni, however, is extremely puzzling, particularly because its concentration remains consistently 4-8 times above bulk levels across an entire 120 nm range of the grain boundary. The authors guess that this is caused either by complex Ni-defect or Ni-solute interactions, or is the result of the interplay between RIS and back diffusion. It should, however, be noted that the AES technique can potentially to include precipitates and carbides in the measurements, the effects of which would significantly skew experimental results and could explain the persistently high Ni levels measured in the specimen.

2.3.2.4 Fast Neutrons on Fe-12CrMoVNb

Little *et al*. [7] irradiated a 12CrMoVNb martensitic steel at 465°C to 46 dpa in a fast reactor, with the primary goal of the work being to correlate RIS with precipitation. Their alloy was a commercial FV448-grade steel containing, by wt%: 10.7 Cr, 1.0 Mn, 0.65 Ni, 0.64 Mo, 0.38 Si, 0.3 Nb, 0.16 V, 0.1 C, 0.006 P, and a balance of Fe. Heat treatment involved austenitization at 1020°C for 1 hour and tempering at 700°C for 1 hour. Microchemical analyses were performed on a field emission gun (FEG) TEM with EDS; concentration profiles traversed a 2.5-100 nm range adjacent to precipitate-free segments of lath boundaries.

The study correlated RIS with the evolution of the M_6X η-phase precipitate. Little, *et al*. [7] find that Cr, Ni, Si, Mo, P, and Mn enrich at lath boundaries, then become incorporated into M_6X precipitates. They suggest that a combination of these elements, namely P, Si, and possibly Cr or Mo, co-segregate and promote M_6X formation. Concentration profiles across several lath boundaries are averaged, revealing 4 wt% depletion of Fe, and enrichment of Cr, Ni, Si, Mo, P, and Mn; these average profiles are shown in Figure 2.28. Within ~5 nm of the boundary, Ni, Si, Mo, and P enrich by approximately 0.8, 0.2, 0.6, and 0.1 wt% over the bulk concentration, respectively. Although Cr and Mn are also concentrated at the boundary, they exhibit net depletion in an adjacent matrix zone extending 2.5-50 nm away from the boundary. The boundary Cr concentration is <0.5 wt% greater than the bulk concentration, but it is >1.0 wt% greater than the Cr concentration 5-10 nm away from the boundary.

The enrichment of undersize solutes P and Si is consistent with the undersize-interstitial binding mechanism. The enrichment of oversize solutes Cr, Mn, and Mo, however, are contrary to the solute size theory. The authors suggest the possibility of Cr-P and Mn-P co-segregation phenomena. Offering plausible explanations for Ni enrichment, the authors suggest strong vacancy binding due to electronic interactions, slow Ni diffusion rates relative to the host lattice, or dominant Si-Ni interactions. It is unknown whether any pre-existing segregation was present. If, as the authors suggest, Cr-P and Mn-P co-segregation phenomena are real, these effects may cause thermal segregation during heat treatment.

2.3.2.5 2 MeV Protons on T91

Gupta, *et al*. [11] performed 2.0 MeV proton irradiation experiments on T91. Although their study was largely focused on the microstructural evolution of T91 over a range of irradiation doses and temperatures, they addressed RIS, albeit somewhat briefly. RIS behavior was studied only at an irradiation temperature of 450°C and final dose of 10 dpa, and it is not clear how many measurements were collected.

Their heat of T91 was composed of, by wt%: 8.13 Cr, 0.98 Mo, 0.43 Mn, 0.27 Si, 0.24 V, 0.24 Nb, 0.22 Ni, 0.16 Cu, 0.09 C, 0.09 P, 0.015 Al, <0.01 Si, <0.005 N, and a balance of Fe. The alloy was austenitized at 1038°C for 1 hour, then tempered at 740°C for 45 minutes. Rectangular bar specimens 20 mm x 2 mm x 1.5 mm were irradiated at a dose rate of 2 x 10^{-5} dpa/sec. Following irradiation, the bars were back-thinned to 100 μm, from which 3 mm TEM discs were cut. Discs were then jet-electropolished to perforation. Microchemical analysis was performed with EDS in a FEG-STEM with electron probe <1.0 nm FWHM.

On PAGBs, Cr enriched by 4.7 wt%, V by 0.6 wt% (nearly 3 times bulk), Fe depleted by 5.3 wt%, but Mn and Mo showed no significant variation in concentration. These concentration profiles are shown in Figure 2.29. No segregation was observed in the unirradiated T91, nor was any RIS observed at martensite lath boundaries. The authors suggest that Cr and V enrichment may be caused by a mechanism other than the inverse Kirkendall mechanism, or attributed to a difference in migration energies in the b.c.c. lattice that dictates that Fe diffuses away from the grain boundary at a faster rate than does Cr.

2.3.3 Experiments Showing Both Chromium Enrichment and Depletion

2.3.3.1 0.5 and 2 MeV Fe^+ Ions on Fe-12Cr ODS

A reduced-activation oxide-dispersion strengthened (ODS) F-M steel was ion irradiated in the work of Marquis, *et al*. [13], and RIS was studied at various depths into the damage profile. The model Fe-12 wt% Cr steel contained a fine dispersion of nano-scale Y_2O_3 particles totaling 0.4 wt% of the alloy. It was mechanically alloyed, then processed by hot isostatic pressing (HIP), and finally annealed at 750°C for 4 hours to partially recover a martensitic lath microstructure. Two types of specimens were irradiated: electropolished APT specimens and flat planar specimens. The specimens were irradiated at 500°C with two different Fe^+ ion fluxes. A flux of 2 MeV Fe^+ ions was implanted, delivering a dose of 1 x 10^{15}/cm^2, followed by a dose of 3 x 10^{15}/cm^2 of 0.5 MeV Fe^+ ions. The two ion energies combine to yield a relatively flat damage profile over a ~750 nm depth, quite similar to that shown in Figure 2.25 from the earlier work of Marquis, *et al*. [14]. Grain boundary microchemistry of the steel, in both the irradiated and unirradiated conditions, was studied by APT.

Even prior to irradiation, a complex grain boundary microchemistry is observed. Grain boundaries in the as-HIPed specimens are enriched in C, as high as ~4 at%. Inconsistent Cr enrichment is also observed at as-HIPed grain boundaries, with some boundaries exhibiting as much as ~5 at% Cr enrichment, and other boundaries exhibiting flat Cr profiles. This variation in the annealed grain boundary microchemistry is attributed to variation in grain boundary character (i.e., grain boundary energy, which itself is dependent upon grain boundary orientation). Following the four-hour anneal at 750°C, grain boundaries remain enriched in Cr, without any segregation of C. EFTEM studies confirm these pre-existing microchemical concentration gradients.

A variety of RIS behaviors are observed following ion implantation. Both Cr depletion and Cr enrichment are observed in the APT specimens, as shown in Figure 2.30, which illustrates both three-dimensional APT reconstructions as well as one-dimensional concentration profiles traversing a grain boundary demarcated in the 3D reconstruction. Here, two boundaries are shown to be completely depleted of Cr, all the way to 0 at%. The Cr depletion profiles are 3-10 nm FWHM, and their asymmetry is thought to arise from grain boundary migraton. A third boundary, however, is enriched in Cr, by ~5 at% with ~4 nm FWHM. Unfortunately, it is unknown as to what depth into the damage profile each of the aforementioned boundaries is located. If, for example, one of the boundaries laid directly in an Fe implantation peak, the implanted Fe may significantly influence the observed segregation behaviors.

To account for depth effects of the damage profile and ion implantations, the planar specimens are also studied at depths of 60 and 600 nm into the damage profile. In these specimens, microchemical analysis was performed by electron energy loss spectroscopy (EELS). The boundary at 60 nm from the implantation surface is depleted in Cr, by ~4 at%, while the boundary at 600 nm is enriched in Cr by ~3 at%. These profiles are shown in Figure 2.31. Similar to the APT results, narrow, 3 nm FWHM Cr concentration profiles are detected.

The authors extend the argument of grain boundary character to explain the extremely diverse Cr RIS behaviors. Based on the knowledge that in austenitic stainless steels, sink strengths are dependent upon grain boundary character, and thus influence the amount of RIS, Marquis, *et al.* [13] propose that similar variations in grain boundary character in the Fe-12Cr ODS steel can explain the dramatic variety in the magnitude and direction of Cr RIS. They also suggest local concentrations of impurities, such as C, as having influence over Cr RIS.

2.3.3.2 200 keV C^+ Ions on Fe-13Cr Alloys

Related to the aforementioned work of Takahashi, *et al.* [3], in a greater effort to understand the swelling resistance of ferritic steels, Ohnuki, *et al.* [5] performed an extensive study of RIS and precipitation—and their possible interrelationship—in model b.c.c. binary Fe-13Cr alloys. Solute additions of 1 wt% of either Si or Ti were included in some of the specimens, in an attempt to clarify the influence of substitutional and interstitial solutes on RIS. Irradiations were carried out using 200 keV C^+ ions, based upon the reasoning that the implanted C atoms will provide insight into the dynamics of interstitial solutes under irradiation.

The alloys Fe-13Cr, Fe-13Cr-1Si, and Fe-13Cr-1Ti were prepared by solution heat treatment in a plasma jet furnace with Fe of 99.996 wt% purity, plus Cr, Si, and/or Ti of > 99.99 wt% purity. The alloys were then cold-rolled to a thickness of 150 μm and punched into 3 mm diameter TEM discs. The discs were annealed at 800°C for 1 hour, then jet-polished to 30 μm thicknesses. Irradiations were performed at 525°C to various doses up to 118 dpa. The incident ion flux was 5.4×10^{17} ions/m^2-s, equivalent to a displacement rate of approximately 8×10^{-3} dpa/sec. Following irradiation, specimens were back-thinned to achieve electron transparency. Microchemical analysis was performed with TEM EDS and EELS.

Extensive irradiation-induced precipitation was noted in all three alloys. The Fe-13Cr contained carbides, predominantly of the $(5Cr\text{-}1Fe)_{23}C_6$ type with an f.c.c. structure, found in the matrix and on grain boundaries. The mean size and number density of these precipitates increased with irradiation dose, growing as large as 1.0 μm and as densely as 3×10^{19} m^{-3} at 114 dpa. Two types of precipitates were identified in Fe-13Cr-1Si below 57 dpa. The larger of the two contained Cr, C, and Si, and had the same morphology as those in Fe-13Cr; the presence of C suggested that these precipitates were irradiation-induced. The smaller of the two were Cr-rich but contained no C, which led the authors to surmise that they were present prior to irradiation. By 57 dpa, however, all Fe-13Cr-1Si matrix and grain boundary precipitates had the same morphology as those in Fe-13Cr. Lastly, in Fe-13Cr-1Ti, 40 nm Ti-rich precipitates were observed to nucleate in the matrix at a number density of approximately 10^{20} m^{-3}; there was no mention of Cr- or C-rich precipitates in this alloy.

Following irradiation to 57 dpa, Cr was found to enrich at grain boundaries in Fe-13Cr and Fe-13Cr-1Si, but deplete at boundaries in Fe-13Cr-1Ti. In the two alloys exhibiting grain boundary Cr enrichment, the matrix was slightly depleted of Cr. Both Si and Ti were enriched at grain boundaries in Fe -13Cr-1Si and Fe-13Cr-1Ti, respectively. The RIS profiles of all segregated elements are shown for each of the three alloys in Figure 2.32. At doses up to 114 dpa, the authors observe Cr enrichment by up to 20% on voids in both Fe-13Cr and Fe-13Cr-1Si, suggesting that voids may be covered in a RIS-generated Cr-rich shell.

Obviously, the presence of the oversized solute Ti has a significant impact on the segregation behavior of Cr. The authors suggest that in order to reduce lattice strain, oversized Ti may form a strong bond with undersized implanted C. Ti-C binding would reduce the concentration of free C that would otherwise form Cr-C-vacancy complexes, which then explains grain boundary Ti enrichment and Cr depletion. However, Si-C binding is weak in Fe-13Cr-1Si, since both Si and the implanted C are undersized; this allows, then, the formation of Cr-C-vacancy complexes, which will give rise to grain boundary Cr enrichment. Since extensive Cr- and C-rich precipitation is also observed in the irradiated Fe-13Cr and Fe-13Cr-1Si, the authors suggest that Cr-C-vacancy complexes (or, more generally, Cr-interstitial solute-vacancy complexes) migrate toward sinks and thus generate the observed Cr enrichment both at grain boundaries and voids, as well as the observed Cr and C precipitation.

The authors assume the injected C diffuses rapidly during irradiation and distributes uniformly throughout the 30 μm-thick specimen, resulting in an implanted C concentration of 0.05 wt% at 118 dpa. However, this may be an underestimation, since the damage peak of the C^+ ions is only 160 nm deep, and the diffusivity of C at the irradiation temperature is not sufficiently high enough to yield a uniform C concentration throughout the specimen, which is >180 times as thick as the depth of the damage peak.

Alternatively, the amount of implanted C may be less than 0.05 wt% if the electron-transparent area of examination is <~160 nm thick. And furthermore, the configuration of the TEM specimens is such that the entire damage profile of C is being "seen" by the electron beam, so any dependence of RIS or precipitation upon the depth of the damage profile is completely lost in this approach.

2.3.4 RIS Sensitivities in F-M Alloys

In reviewing the experiments that have been conducted on RIS in F-M alloys, it is obvious there is a great lack of understanding of the behaviors and driving mechanisms. Although many of the authors have proposed some loose theories of mechanisms, or parts of mechanisms, to explain their experimental observations, none of their ideas offer a comprehensive explanation of bulk RIS behaviors in F-M alloys. Furthermore, many of their theories contradict one another, particularly since they attempt to explain data sets that are themselves contradictory.

The experiments reveal no obvious dependencies on dose, temperature, dose rate, or alloy composition, but a few commonalities can be extracted from the data. An interrelationship between RIS at grain boundaries and RIS at loops and voids is demonstrated [5], [9]. RIS and precipitation are also correlated [5], [7], [9].

Significantly undersized elements are always observed to enrich at grain boundaries. None of the experiments report depletion of such elements as Si, C, P, or S. But, enrichment of Si is reported at grain boundaries in C^+-irradiated Fe-13Cr-1Si [5], fast neutron-irradiated HT9 [6] and 12CrMoVNb [7], and at dislocation loops in 13Cr-2MoVNb irradiated with Cr^{3+} ions [9]. Carbon enrichment is observed by Marquis, *et al.* [14] in model Fe-14.25Cr steel, and enrichment of P is noted in E911, HT9, and 12CrMoVNb [6], [7], [12]. Nickel is also found to enrich at grain boundaries [6], [7], but there are no accounts of Ni depletion.

Experimental results also reveal that the intentional addition of oversized solutes, in order to suppress RIS magnitudes, tends to be quite effective in F-M alloys. The addition of oversized Hf to alloy E911 reduced the magnitude of Cr depletion from -2.04 at% to only -0.63 at%, following 300°C Ni^+ ion irradiation to 0.305 dpa [12]. Kato, *et al.*

[4] have also observed that increasing the bulk concentration of oversized element Mn, in Fe-Cr-Mn-Al alloys causes the magnitudes of irradiation-induced Cr enrichment and Mn and Al depletion to decrease. Oversized solute additions have also proven to be an effective technique for RIS suppression in austenitic stainless steels.

Having expected Cr to deplete as it does in austenitic stainless steels, several authors [5–7] explain their observed Cr enrichment by suggesting Cr-P (i.e.. oversized-undersized) or Cr-P-vacancy binding effects. They suggest that to relieve lattice strain, oversized Cr would have a positive binding energy with an undersized solute such as P, or with a vacancy and an undersized solute. The bound complex would then diffuse to grain boundaries. This theory, however, cannot explain the Cr enrichment in high-purity model alloys, which do not contain even trace amounts of significantly undersized impurities like P. It also does not explain the numerous accounts of Cr depletion.

Finally, RIS in F-M alloys is sensitive to grain boundary character. Marquis, *et al*. [13] suggest that this parameter might explain some of the extreme variations in RIS behavior they observe in ion-irradiated model Fe-12Cr ODS. In as of yet unpublished work by Field, *et al*. [64], a very strong correlation is found between RIS magnitude and grain misorientation. Field studied a model Fe-9Cr F-M alloy irradiated to 2 dpa at 400°C with 2.6 MeV protons. Following the collection of RIS measurements across a lath boundary, Kikuchi patterns were captured from each grain adjacent to the measured boundary. Indexing of the Kikuchi patterns provides the grain boundary misorientation angle and axis, which subsequently provides insight into the local grain boundary structure. Field observed Cr enrichment and Fe depletion in the model alloy. But as the misorientation between two grains increases, the amount of Cr RIS increases at a nearly linear rate, as shown in Figure 2.33. Although Field's correlation between RIS and grain boundary misorientation is strongly linear, its slope is very shallow, suggesting that misorientation has only a minor effect on RIS.

Although experimental measurements of RIS in F-M alloys are often contradictory and fail to paint a clear picture of the driving mechanisms, a few commonalities can be identified from the data. There seems to be consensus that RIS is, at the very least, somewhat related to, or affected by: dislocation loop and void evolution, irradiation-induced precipitation and precipitate evolution, the presence of impurities, and grain boundary character. These microstructural features of F-M alloys, along with their development and their response to irradiation, will be discussed in the following section.

2.4 Other Irradiation Effects

When irradiation is introduced, the desirable microstructural and precipitate features, as developed in Section 2.2, may be severely altered or damaged. The associated physical characteristics such as hardness, toughness, and ductility, may also be impaired. This sub-section will discuss the structural, physical, and chemical implications of irradiation typically observed in F-M alloys, including dislocation loop evolution, void swelling, hardening, and precipitation.

2.4.1 Dislocation Loops

Interstitial dislocation loops are formed in very dense networks in F-M alloys under irradiation. The vast majority of these loops have <100> Burgers vectors and {100} habit planes, and range in size from ten to a few tens of nanometers. Their very high network density, on the order of a thousand loops per cubic micron, makes a significant contribution to the irradiation-induced hardening. In the next few paragraphs, the nucleation and evolution of these loops will be discussed.

At the irradiation temperatures of interest (typically below $0.3T_m$, where T_m is the melting temperature of the alloy), interstitials are mobile as compared to vacancies, and can efficiently combine to form dislocation loops that increase strength and decrease ductility of the alloy [1]. Although vacancy loops can, in theory, be created by the collapse of depleted zones within the displacement cascade, such cascade collapse has not been observed in ferrite after self-ion irradiation [1]. Therefore, vacancy loops are not expected in irradiated F-M alloys.

Two interstitial loop types can be found in F-M alloys, both of which form from a common faulted nucleus [1]. Loop nucleation begins with split dumbbell interstitials, which initially aggregate on {110} planes to form faulted loop nuclei. Early work suggested the dumbbell aggregates were <110> with ½<110> Burgers vectors, although recent molecular dynamics simulations show that stable interstitial cluster configurations instead consist of aggregates of ½<111> split dumbbells [65]. However, due to the high stacking fault energy in high-Cr F-M alloys, these loops unfault very early in their growth by a shear in one of two directions [48]. Additionally, the habit planes of these loops rotate to achieve pure edge configurations and reduce the loop elastic energy. Resulting are two types of interstitial dislocation loops:

- Cube-edge loop on {100} habit plane with <100> Burgers vector, formed by shear in <110> direction
- Glissile edge loop on {111} habit plane with ½<111> Burgers vector, formed by shear in <100> direction

It is of interest, then, to understand what fraction of the loop network is composed of each of these two types of loops. Thermodynamics suggests that the <100> shear is of lower energy than the <110> shear, and thus predicts that the glissile ½<111> edge loop is energetically-favored to be the predominant loop specie found in the network [66]. However, experiments have observed exactly the opposite—loop networks composed almost entirely of <100> cube-edge loops [1].

One model suggests that the bias of a dislocation is highly dependent upon the magnitude of its Burgers vector [65]. The <100> loop has a Burgers vector $|\mathbf{b}| = a$, where a is the lattice parameter, whereas the ½<111> loop has only $|\mathbf{b}| = a\sqrt{3}/2$. So in a system containing both loop types, the ½<111> loops will be neutral sinks, while the <100> loops will be highly biased interstitial sinks [9], [65], [67]. Under irradiation, then, the <100> loops will grow by preferential interstitial capture, leaving a net vacancy flux to the ½<111> loops, causing them to shrink, and thus explaining the predominance of the <100> loops in an irradiation-induced loop network.

An alternative theory on the presence of the <100> loops is based upon cluster mobility [65]. It is suggested that ½<111> loops have a much larger defect capture radius, and therefore receive a greater flux of point defects, than <100> loops.

Additionally, ½<111> loops also have low migration energy for gliding toward, and thus absorbing, point defects, whereas the <100> clusters are highly immobile. At steady-state, the point defect balance equations state that the vacancy concentration is greater than the interstitial concentration. Thus, ½<111> loops eventually disappear, either by absorbing those free vacancies, or by gliding to annihilation at sinks. The <100> loops remain to grow at a rate governed by the difference in fluxes between the two point defect species, and since the mobility of interstitials is much greater than the mobility of vacancies, <100> loops are more likely to survive and grow than ½<111> loops [65], [68–70].

Molecular dynamics simulations which have shown loop aggregation beginning with ½<111> split dumbbells have also proposed a nucleation-growth relationship [71] that can explain the population of the energetically-unfavorable <100> loops. Beginning with small ½<111> clusters on the {110} plane, these clusters either rapidly migrate to sinks or interact with one another. The <100> loop nucleates when two comparably-sized ½<111> clusters interact, propagating through each other's habit planes, until the loop is transformed to <100>, while remaining on the {110} habit plane. As the loop grows to a size $n > 68$, {100} becomes a lower-energy habit plane than {110}, and thus the loop reorients itself without changing its <100> Burgers vector. The resulting <100>{100} loops are metastable and practically immobile, and will grow by absorption of other small ½<111> clusters [71].

Loops continue to nucleate and grow under continuing irradiation, until saturation is achieved. The most systematic observations of this behavior were performed by Gupta, *et al.*, and Jiao, *et al.*, on a heat of proton-irradiated T91 at 400°C, 450°C, and 500°C, to doses ranging from 2.2 dpa to 10 dpa [66]. These experiments have revealed that at each temperature, loop size and density increase as a function of irradiation dose. The only peculiarity is that the 450°C results of Gupta, *et al.*, show a considerably smaller magnitude of number density; this is attributed to a different heat of T91 being used than in all of the other experiments. Loop size and density appear to saturate by ~10 dpa for all temperatures studied.

As a function of temperature, loop size increases, while density decreases [66]. The 400°C experiments reveal loops ranging in diameter from 20 nm to 50 nm, at densities ranging from 4-14x10^{21} m^{-3}. But at higher temperatures, 500°C, the loops are no smaller than 60 nm, and occur at densities no greater than 4x10^{21} m^{-3}.

The dislocation loop measurements of Gupta, *et al.*, and Jiao, *et al.*, are comparable in magnitude to those of neutron-irradiated T91 at 400°C to 12 dpa [11], [72] and at 360°C to 11.8 dpa [11], [72]. At very high doses of several hundred dpa, very large loops, up to 100 nm in diameter, have been recorded in 500°C neutron-irradiated T91 [73]. Loop size and density measurements in F-M alloys, which have been discussed here, are summarized in Table 2.5.

Dislocation loops in F-M alloys are generally quite small (≤100 nm), yet they are found at very high densities. These tightly-formed dislocation networks are a significant microstructural feature of irradiated F-M alloys, and have the potential to act as a major sink for point defects. Their impact on mechanical properties, irradiation-induced hardening, and perhaps even on RIS, may be profound.

2.4.2 Void Swelling

Much of the interest in F-M alloys within the nuclear energy community is in part due to these alloys' excellent resistance to radiation-induced void swelling. This desirable dimensional stability is closely related to the dislocation microstructure. In the following few paragraphs, the cause of void swelling shall be described. The swelling resistance of F-M alloys will be explained, and then experimentally observed swelling shall be reviewed.

Void swelling goes hand-in-hand with irradiation-induced dislocation loop growth and microstructural evolution. At ~$0.3T_m$ and under irradiation, dislocation stress fields have greater interaction with interstitials than with vacancies [61]. Consequently, these dislocations act as biased sinks for interstitials, leaving an excess vacancy flux to neutral sinks. Furthermore, as has previously been mentioned, <100> dislocation loop growth (and ½<111> loop disappearance) is theorized to be the effect of an interstitial bias, which again leaves an excess vacancy flux to neutral sinks [67]. As neutral sinks, void embryos are the recipients of that excess vacancy flux, which then allows the embryos to grow into voids under the continued flow of interstitials to biased sinks.

Both biased and neutral sinks must be present in order for void swelling to occur. This requirement explains the suppression of void swelling in F-M alloys, particularly when discussed in the context of void swelling in austenitic alloys. Austenitic alloys have a low initial dislocation density, which allows mobile interstitials to aggregate and form interstitial dislocation loops during the early stages of irradiation [65]. These loops are biased sinks for interstitials, and result in an excess vacancy flux to neutral sinks, leading to void growth. Conversely, F-M alloys in their initial state have a very high dislocation network density, created during the martensitic transformation. Both the dislocation network and the high density of martensite lath boundaries are strong neutral sinks, at which significant point defect recombination occurs [65], [71]. Recombination inhibits the nucleation of both voids and interstitial dislocation loops, and thus delays the onset of void swelling.

When void swelling is observed in F-M alloys, its magnitude is quite small even at very high irradiation doses. Fast neutron-irradiated T91, irradiated to 200 dpa at 420°C, shows void swelling of only 1.76% [65]. Data compiled by Klueh and Harries [65], [74] show swelling in neutron-irradiated T91 to range from 0.85% to 2%, over a variety of irradiation conditions in the range 400-500°C, to doses up to 200 dpa. Such low magnitudes of void swelling, especially after hundreds of dpa, are a key advantage of F-M alloys in nuclear applications.

2.4.3 Precipitation

Precipitates are critical in strengthening the F-M microstructure. There are several precipitate types present in unirridiated F-M alloys. But irradiation can cause these existing precipitates to evolve—growing, shrinking, coarsening, or dissolving. New, non-equilibrium precipitate phases can also form under irradiation. The following few paragraphs are dedicated to irradiation-induced precipitation and precipitate evolution. A summary of the phases that have been reported in irradiated T91 and HT9 are given in Table 2.6.

Chromium-rich ferrite (α’): Neutron irradiation induces the formation of a high density, on the order of 10^{22} m^{-3}, of fine α’ particles, 2-30 nm in diameter, in F-M steels containing ≥11-13wt% Cr in the bulk [67]. This phase has also been observed following low-temperature, high-dose-rate proton irradiation in binary Fe-Cr alloys with <10wt% Cr [1]. Although this phase can form during thermal aging in ferritic steels having very high Cr contents (i.e., >15wt% Cr), irradiation decreases the critical Cr concentration necessary for α' nucleation [1], [62], [67], [75]. The α' phase tends to be stable at lower temperatures—below about 440°C in HT9, and below about 405°C in 9Cr-1Mo [1]—but increasing Cr content increases the temperature at which α' forms and can stabilize [62]. The α' phase is a b.c.c. structure composed of Cr, Mo, Fe, and Si [60].

M_6X (η-phase): The η-phase is diamond cubic and rich in Si, Cr, Ni, and P. Although it can be found in some thermally-aged high-Cr steels, it most frequently occurs as irradiation-induced precipitates in steels containing ≥0.3wt% Ni [60], [75]. It is speculated that the η-phase replaces some of the coarse "as-tempered" $M_{23}C_6$ particles and any M_2X remaining from the tempering process, both of which can dissolve upon irradiation [1]. However, neutron irradiation studies on T91 and other ~9Cr F-M alloys have suggested that M_2X actually forms at low irradiation doses, and then the η-phase replaces it at higher doses [1].

Chi (χ) phase: This b.c.c. intermetallic forms heterogeneously in many high-Cr steels; the particle distribution differs in the tempered martensite and δ-ferrite regions of a single steel [1]. This phase is either irradiation-induced (i.e., the equilibrium phase under irradiation conditions), or a metastable phase favored by kinetic considerations, which will eventually be replaced by the Laves phase [73]. The χ-phase has been identified in 420°C, 35 dpa, fast neutron-irradiated T91 and HT9, at number densities on the order of 10^{20} m^{-3} with diameters on the order of 10 nm [1], [60]. While the typical χ-phase particle is rich in Fe, Si, and Ni, the χ-phases identified in neutron-irradiated T91 are also Mo-rich, owing to the elevated bulk Mo content in T91 and/or an excess of Mo from irradiation-decomposed $M_{23}C_6$ carbides [60]. Steels containing higher bulk Mo concentrations tend to form larger χ-phase particles [62], but some researchers have not even observed χ-phases in alloys containing <2wt% Mo [1], [62].

Laves phase: The Laves phase in F-M alloys has the composition Fe_2M, where M is either Mo or W. The Fe_2Mo type is formed extensively during thermal aging, but its formation is suppressed in most F-M steels under 300-615°C irradiation [1]. There is only one recorded instance of irradiation-induced Fe_2Mo precipitation below 600°C: in fast neutron-irradiated 10Cr-2MoVNb at 500°C to 34 and 57 dpa, for which the Laves composition was significantly different than the thermally-induced Laves [75]. Grain boundary and matrix precipitation of Fe_2W Laves has been observed in F82H and reduced-activation F-M steels [1], [60].

G-phase: Early investigations showed extensive precipitation of this complex f.c.c. silicide ($Mn_7Ni_{16}Si_{17}$) in neutron-irradiated HT9 at temperatures in the range of 300-425°C at doses of 10-60 dpa [1]. However, G-phase particles were only found infrequently, if at all, in later studies in neutron-irradiated HT9 and T91 in the temperature ranges 300-600°C to doses up to 47 dpa [1]. Only one recent study [1] has observed G-phase particles in HT9, but only after extremely high doses (200 dpa at 420°C); the G-phases grew to 10 nm in diameter within laths, and larger on PAGB and packet boundaries.

Minor phases: The sigma phase is a Fe-Cr phase enriched in Si, Ni, and P. It has been observed as large sheets and thin ribbons surrounding $M_{23}C_6$ particles in 9-13% Cr steels following neutron irradiation at 420-460°C [1] and in a 17.3wt% Cr steel following 100 dpa neutron irradiation at 540°C [67]. Trace amounts of M_2X produced during tempering may persist through irradiation, but there is evidence that this phase forms within δ-ferrite grains, on dislocations in tempered martensite laths, and at PAGBs of some duplex steels under 330-550°C irradiation [1]. Lastly, Cr_3P needles and (Fe,Cr,Mo)P particles have been observed in some steels with ≥13wt% Cr following neutron irradiation at 420-460°C and 460-615°C, respectively [60].

$M_{23}C_6$ and MX phases: The $M_{23}C_6$ and MX precipitates, which comprise the majority of the unirradiated precipitate distribution, remain, for the most part, unchanged in size and number density under irradiation [1]. Kai and Klueh [1] also reported only small increases in the diameter and small decreases in number density, of $M_{23}C_6$ and MX precipitates following 420°C irradiation. One studies, however, reports an increase in the amount of $M_{23}C_6$ precipitation on lath boundaries following 530°C neutron irradiation, especially in HT9, which has ~0.2wt% C in bulk and only one tempering treatment [7], [11], [62], [73], [75]. Others suggest that "as-tempered" $M_{23}C_6$ particles will coarsen under irradiation at temperatures in excess of 450°C [62], and that coarsening kinetics

increase with temperature, explaining the observation of larger precipitates following higher-temperature irradiations [75]. Conversely, at very low irradiation temperatures, 110-205°C, amorphisation of $M_{23}C_6$ precipitates in T91 has been reported [1]. Partial dissolution of Cr-rich precipitates such as $M_{23}C_6$ during irradiation may lead to grain boundary Cr enrichment, which may, in turn, increase the local Cr supersaturation and thus, the observed nucleation of M_6X on $M_{23}C_6$ particles [60].

2.4.4 Hardening

All of the aforementioned irradiation-induced microstructural and microchemical changes contribute to the macroscopic effect of irradiation-induced hardening. Hardening increases the yield stress and ultimate tensile strength of the material, while decreasing the uniform and total elongation. These hardening effects are apparent when comparing the stress-strain curves of an alloy in its unirradiated and irradiated states. As an instructive example, stress-strain curves for unirradiated T91 are compared against those of spallation proton- and neutron-irradiated T91 in Figure 2.34, from [61]. These stress-strain curves show that hardening effects are amplified with increasing dose.

Irradiation-induced hardening is attributed to the formation of defect clusters, voids, precipitates, and/or dislocation loops that impede the motion of dislocation lines [1]. As discussed earlier, <100> dislocation loops on the {100} plane form at very high densities under irradiation. But since the {100} plane is not a close-packed slip plane in the b.c.c. lattice, these dislocation loops are immobile contribute immensely to the observed irradiation hardening. The magnitude of irradiation-induced hardening is strongly temperature-dependent, decreasing with increasing temperature, until hardening essentially disappears between 400°C and 500°C for most alloys [76]. As a function of dose, hardening typically saturates between 5 and 10 dpa for most F-M alloys [77].

Hardening, ΔH_v, is related to the change in yield strength, $\Delta\sigma_y$, according to the following expression for F-M alloys [1], [78], [79]:

$$\Delta\sigma_y = 3.06\,\Delta H_V\,. \qquad (2.40)$$

The irradiation-induced hardening mechanisms in F-M alloys vary depending upon the irradiation temperature. At temperatures $< 0.35T_m$, where T_m is the melting temperature of the alloy, small interstitial and vacancy loops contribute to hardening. Between $0.35T_m$ and $0.4T_m$, hardening is caused by dislocation loops and the dislocation structure that develops from the loops with increasing temperature. In this temperature range, irradiation-induced or irradiation-accelerated precipitates also contribute to hardening. At very high irradiation temperatures, $\geq 0.4T_m$, diffusion anneals irradiation-induced defects, preventing them from causing any hardening, although irradiation-induced precipitates will coarsen rapidly and can cause some hardening.

Irradiation introduces important changes in F-M alloys, which have been discussed in this chapter. Dislocation loops nucleate and grow; their very high number densities allow for them to act as strong point defect sinks and contribute a great deal to irradiation-induced hardening. Void nucleation and growth, while very much suppressed in F-M alloys, can also contribute to hardening and serve as point defect sinks. Precipitates are present prior to irradiation, and contribute to the high yield stress of unirradiated F-M alloys; but under irradiation, existing precipitates can coarsen or dissolve, and new precipitates can nucleate, thus changing the contribution of the precipitate distribution to the yield stress of the alloy. Alloying components segregate to sinks through the phenomenon of RIS, creating concentration gradients at point defect sinks such as grain boundaries. These complex, and often interrelated, irradiation effects have a profound impact on the microstructure and mechanical properties of F-M alloys. The mechanism of RIS in F-M alloys will be the focus through the remainder of this thesis, and the associated microstructural effects will be shown to have a critical role.

Table 2.1. Volume misfit of various binary alloys and stainless steels, the predicted direction of solute segregation based on the solute size effect, and correlation with observed direction of segregation, from [19].

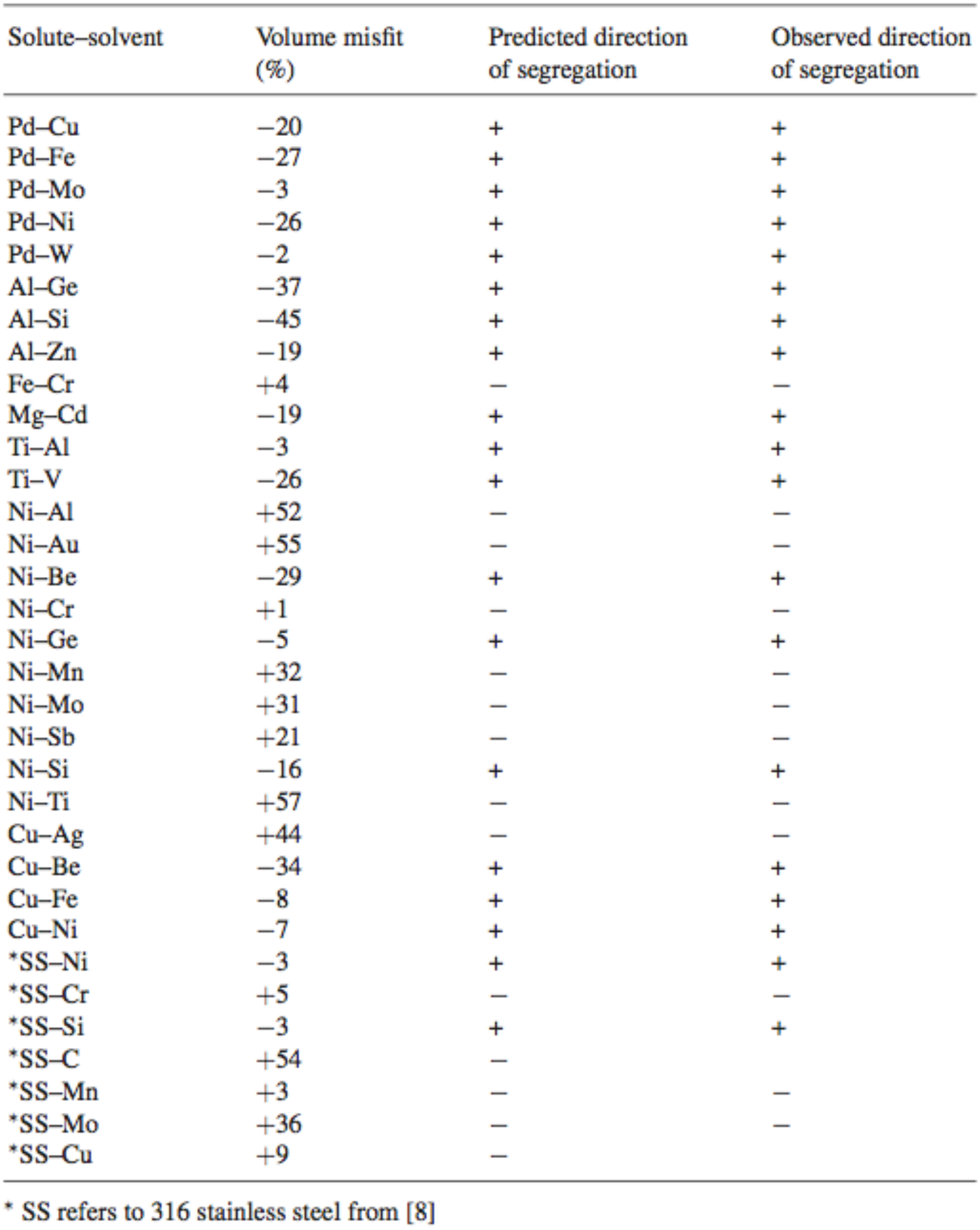

Solute–solvent	Volume misfit (%)	Predicted direction of segregation	Observed direction of segregation
Pd–Cu	−20	+	+
Pd–Fe	−27	+	+
Pd–Mo	−3	+	+
Pd–Ni	−26	+	+
Pd–W	−2	+	+
Al–Ge	−37	+	+
Al–Si	−45	+	+
Al–Zn	−19	+	+
Fe–Cr	+4	−	−
Mg–Cd	−19	+	+
Ti–Al	−3	+	+
Ti–V	−26	+	+
Ni–Al	+52	−	−
Ni–Au	+55	−	−
Ni–Be	−29	+	+
Ni–Cr	+1	−	−
Ni–Ge	−5	+	+
Ni–Mn	+32	−	−
Ni–Mo	+31	−	−
Ni–Sb	+21	−	−
Ni–Si	−16	+	+
Ni–Ti	+57	−	−
Cu–Ag	+44	−	−
Cu–Be	−34	+	+
Cu–Fe	−8	+	+
Cu–Ni	−7	+	+
*SS–Ni	−3	+	+
*SS–Cr	+5	−	−
*SS–Si	−3	+	+
*SS–C	+54	−	
*SS–Mn	+3	−	−
*SS–Mo	+36	−	−
*SS–Cu	+9	−	

* SS refers to 316 stainless steel from [8]

Table 2.2. Summary of precipitation observed in austenitized then tempered F-M alloys, from [1].

Phase	**Crystal structure, lattice parameter**	**Typical composition**	**Distribution**
$M_{23}C_6$	f.c.c. a = 1.066 nm	$(Cr_{16}Fe_6Mo)C_6$ and $(Cr_4Fe_{12}Mo_4Si_2WV)C_6$	Coarse particles at PAGBs and lath boundaries (50-150 nm) and fine intra-lath particles
MX	f.c.c. a = 0.444-0.447 nm	NbC, NbN, VN, (CrV)N, Nb(CN), and (NbV)C	Undissolved particles and fine precipitates at lath boundaries (20-50 nm)
M_2X	Hexagonal a = 0.478 nm c = 0.444 nm	Cr_2N, Mo_2C, and W_2C	Lath boundaries (Cr_2N and Mo_2C); PAGBs (Mo_2C); intra-lath (Mo_2C and W_2C; δ-ferrite in duplex steels (Cr(CN) and $(CrMo)_2(CN)$)
η-carbide	Diamond cubic a = 1.07-1.22 nm	M_6C and $(Fe_{39}Cr_6Mo_4Si_{10})C$	PAGBs, lath boundaries, and intra-lath
V carbide	f.c.c. a = 0.420 nm	V_4C_3	Low number density in matrix
Laves	Hexagonal a = 0.4744 nm c = 0.7725 nm	Fe_2Mo, Fe_2W, and $Fe_2(MoW)$	PAGBs, lath boundaries, and intra-lath; δ-ferrite in duplex steels
χ-phase	b.c.c. a = 0.892 nm	$M_{18}C$ or $Fe_{35}Cr_{12}Mo_{10}C$	Intra-lath; δ-ferrite in duplex steels

Table 2.3. Summary of all experimental measurements of RIS in F-M alloys.

Particle	Alloy	Heat Treat.	Dose (dpa)	Dose Rate (dpa/s)	Temp. (°C)	RIS Analysis Method	PPTs Before Irrad.	PPTs After Irrad.	Irrad. Damage	GB Cr Before Irrad.	GB Cr After Irrad. (at%)	Other RIS	Ref.
650 kV e^-	Fe-5Cr		3	$4\text{-}9\text{x}10^{-4}$	400	TEM-EDS		no RIP	no voids		∨ -0.64		[3]
650 kV e^-	Fe-13Cr		3	$4\text{-}9\text{x}10^{-4}$	400	TEM-EDS		no RIP	no voids		∨ -3.94		"
1 MV e^-	Fe-10Cr-5Mn-3Al	1150°C/0.5h sol anneal	10	$1.9\text{x}10^{-3}$	450	TEM-EDS	plate-like & blk. dots	Cr-rich; larger blk. dots	loops; no voids		∧ 5	Al, Mn depl	[4]
1 MV e^-	Fe-10Cr-10Mn-3Al	1150°C/0.5h sol anneal	10	$1.9\text{x}10^{-3}$	450	TEM-EDS	plate-like & blk. dots	Cr-rich; larger blk. dots	loops; no voids		∧ 4.1	"	"
1 MV e^-	Fe-10Cr-15Mn-3Al	1150°C/0.5h sol anneal	10	$1.9\text{x}10^{-3}$	450	TEM-EDS	plate-like & blk. dots	Cr-rich; larger blk. dots	loops; no voids		∧ 1.1	"	"
200 keV C^+	Fe-13Cr	solution heat treatment	57	$8\text{x}10^{-3}$	525	TEM-EDS		$M_{23}C_6$	loops, voids		∧ 17.55		[5]
200 keV C^+	Fe-13Cr-1Si	solution heat treatment	57	$8\text{x}10^{-3}$	525	TEM-EDS		$M_{23}C_6$	loops, voids		∧ 9.41	Si enr	"
200 keV C^+	Fe-13Cr-1Ti	solution heat treatment	57	$8\text{x}10^{-3}$	525	TEM-EDS		Ti carbides (matrix)	loops, voids		∨ -0.67	Ti depl	"
0.5, 2 MeV Fe^+	Fe-14.25Cr	1150°C + 800°C/6h	~2		350	APT	none	none		∧	∧ <4	C enr	[14]
0.5, 2 MeV Fe^+	Fe-14.25Cr	1150°C + 800°C/6h	~0.5		350	APT	none	none		∧	**FLAT**	C enr	"

Table 2.3 - continued

Particle	**Alloy**	**Heat Treat.**	**Dose (dpa)**	**Dose Rate (dpa/s)**	**Temp. (°C)**	**RIS Analysis Method**	**PPTs Before Irrad.**	**PPTs After Irrad.**	**Irrad. Damage**	**GB Cr Before Irrad.**	**GB Cr After Irrad. (at%)**	**Other RIS**	**Ref.**
0.5, 2 MeV Fe^+	Fe-12Cr ODS	HIP + 750°C/4h	~2		500	APT	Y_2O_3 ODS	Y_2O_3 ODS		∧	∧ ∨ +5, -10		[13]
250 keV Ni^+	E911	1060°C/1h AC	0.305	$2.4x10^{-5}$	300	TEM-EDS				∧	∨ -2.04	P enr	[12]
250 keV Ni^+	E911 + Hf	1060°C/1h AC	0.305	$2.4x10^{-5}$	300	TEM-EDS				∧	∨ -0.63	P enr	"
Fast neutron	HT9	1035°C/1h + 760°C/1h	13		410	AES	$M_{23}C_6$	more $M_{23}C_6$			∧ 4.5	Si, P, Ni enr	[6]
Fast neutron	12CrMoVNb	1020°C/1h + 700°C/1h	46		465	TEM-EDS	$M_{23}C_6$	$M_{23}C_6$, M_6X	loops, no voids		∧ 1.5	Ni, Si, Mo, P, Mn enr; Fe depl	[7]
2 MeV p^+	T91	1038°C/1h + 740°C/45m	10	$2x10^{-5}$	450	FEG STEM		No change	loops	**FLAT**	∧ 4.7	Fe depl, V enr	[11]
11 MeV p^+	SUS410L	950°C/1h	0.36	$1x10^{-4}$	497-647	Mossbauer					∨ -2.3		[8]
590 MeV p^+	F82H	1040°C/0.5h + 740°C/2h	0.5	n/a	250	EFTEM	$M_{23}C_6$	carbides	no loops or voids	∧	∨	Fe depl	[10]
1 MeV Cr^{3+}	13Cr-2Mo-VNbB	1050°C	48	0.1-0.3	575	TEM-EDS		oriented M_2X	dense small loops		∨	Cr, Si enr at loops	[9]
1-5 MeV Cr^{3+}	13Cr-2Mo + TiO_2		0.1-200	0.1-0.3	270-800	TEM-EDS			"		∨	Ti enr	"

Table 2.4. Volume size factors of Mn, Cr, and Al in ferritic Fe-Cr-Mn-Al alloy systems, as calculated by x-ray diffraction analysis by Kato, *et al*. [4].

Solute atoms	**Volume size factor (%)**	**Solid solution systems**
Mn	+ 6.45	Fe-10Cr-*x*Mn-3Al
Cr	+ 11.8	Fe-*y*Cr-15Mn-3Al
Al	+ 47	Fe-10Cr-5Mn-*z*Al
Al	+ 29	Fe-10Cr-15Mn-*z*Al

Table 2.5. Summary of dislocation loop size and density measurements in F-M alloys, from literature.

Alloy	Temperature (°C)	Dose (dpa)	Particle	Loop Density ($x10^{21}$ m^{-3})	Loop Size (nm)	Reference
T91	360	11.8	neutron	13	8.9	[61]
T91	400	3	proton	9.10	28.5	[61]
T91	400	7	proton	13.93	31.8	[61]
T91	400	10	proton	14.00	49.0	[61]
9Cr-1MoVNb (T91)	400	12	neutron	5, <100> 4, ½<111>	21, <100> 25, ½<111>	[61]
T91	450	2.2	proton	5.4	12	[61]
T91	450	3	proton	1.30	10.5	[61]
T91	450	7	proton	8.2	13.7	[61]
T91	450	9.2	proton	9.0	n/a	[11]
T91	450	10	proton	1.73	12.8	[11]
T91	500	3	proton	3.60	60.0	[11]
T91	500	7	proton	4.10	64.5	[73]
T91	500	200	neutron	n/a	up to 100	[72]

Table 2.6. Summary of precipitates observed in irradiated HT9 and T91, from [72].

Precipitate Phase	**Alloy/Steel**	**Reactor/Facility**	**Irradiation Temperature (°C)**	**Dose (dpa)**
Cr-rich Ferrite (α’)	12Cr-1MoVW (HT9)	EBR II FFTF 14 MeV Ni ions Phénix FFTF/MOTA	400, 425 420 300-600 400-530 420	25-60 35 200 30-116 200
M_6X (η)	9Cr-1MoVNb + 2Ni	HFIR	400	37
	12Cr-1MoVW (HT9)	FFTF Phénix Phénix	407 419 420, 460	47 79 110
	12Cr-1MoVW + 2Ni	HFIR	400	37
Chi (χ)	9Cr-1MoVNb (T91)	FFTF	≈420	≈35
	9Cr-1MoVNb + 2Ni	HFIR	400, 500	36-39
	12Cr-1MoVW (HT9)	EBR II FFTF 14 MeV Ni ions	425, 510, 450-540 ≈420 500	26-60 ≈35 200
	12Cr-1MoVW + Ni	HFIR	400, 500	36-39
G	12Cr-1MoVW (HT9)	EBR II HFIR FFTF/MOTA HFIR	400, 425 300, 400 420 500	25-60 10-12 200 38

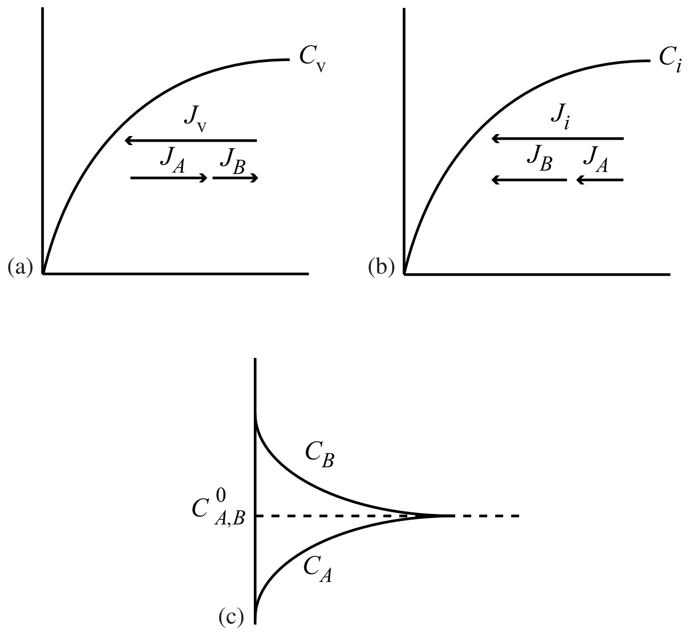

Figure 2.1. Schematic of the inverse Kirkendall RIS mechanism in a 50%A-50%B alloy, showing (a) the flux of vacancies to the grain boundary, balanced by an opposite flux of constituent atoms, with a vacancy-A atom coupling, and the resultant vacancy concentration profile; (b) the flux of interstitials to the grain boundary, composed of a flux of A and B atoms, with an interstitial-B atom coupling, and the resultant interstitial concentration profile; (c) the resultant A and B atom concentration profiles at the grain boundary, from [1].

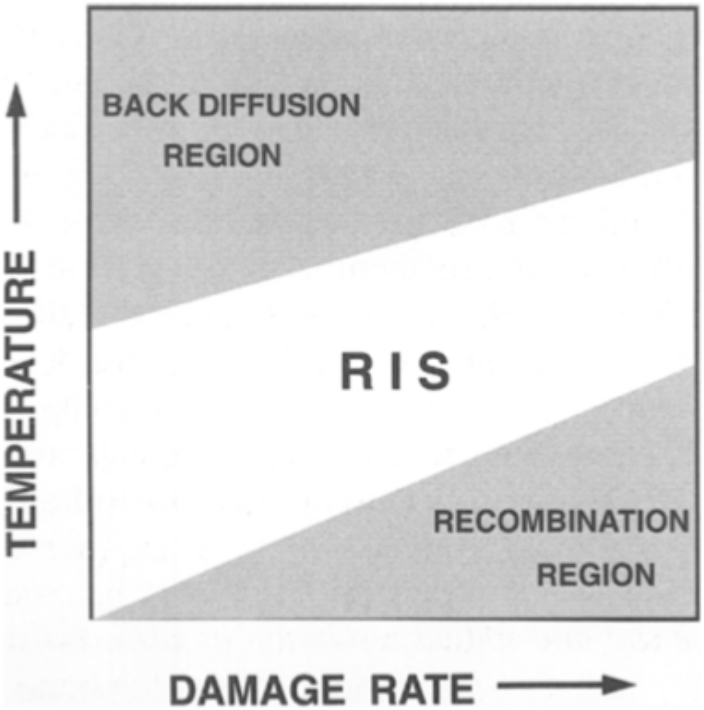

Figure 2.2. Dependence of RIS on temperature and dose rate, from [38].

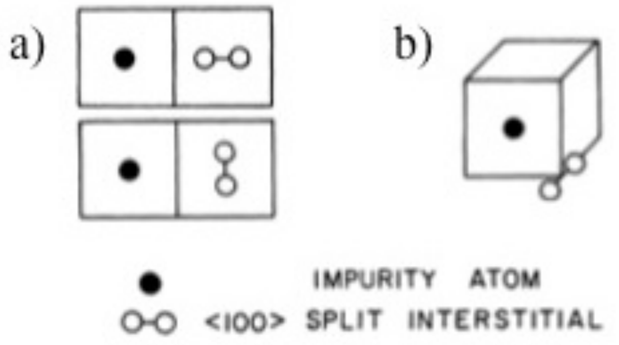

Figure 2.3. Interstitial-impurity complexes, a) type-*a*, and b) type-*b*, as defined in the Johnson and Lam RIS model, from [31].

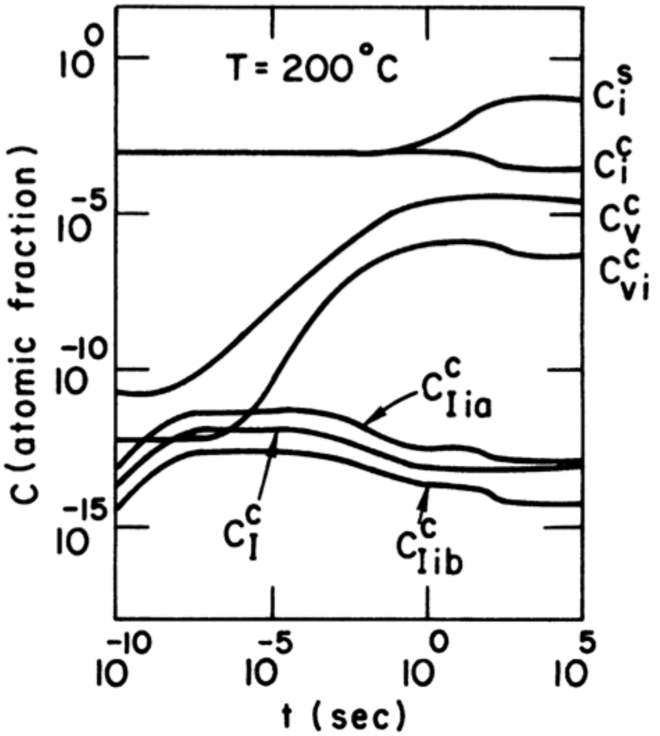

Figure 2.4. The concentrations of point defects (C_I^c, C_v^c), defect-solute complexes (C_{vi}^c, C_{Iia}^c, C_{Iib}^c), and solute atoms (C_i^c), as a function of time, at the center of a foil irradiated at 200°C, as solved by the Johnson and Lam RIS model. Surface solute concentration (C_i^S) is also shown. Taken from [31].

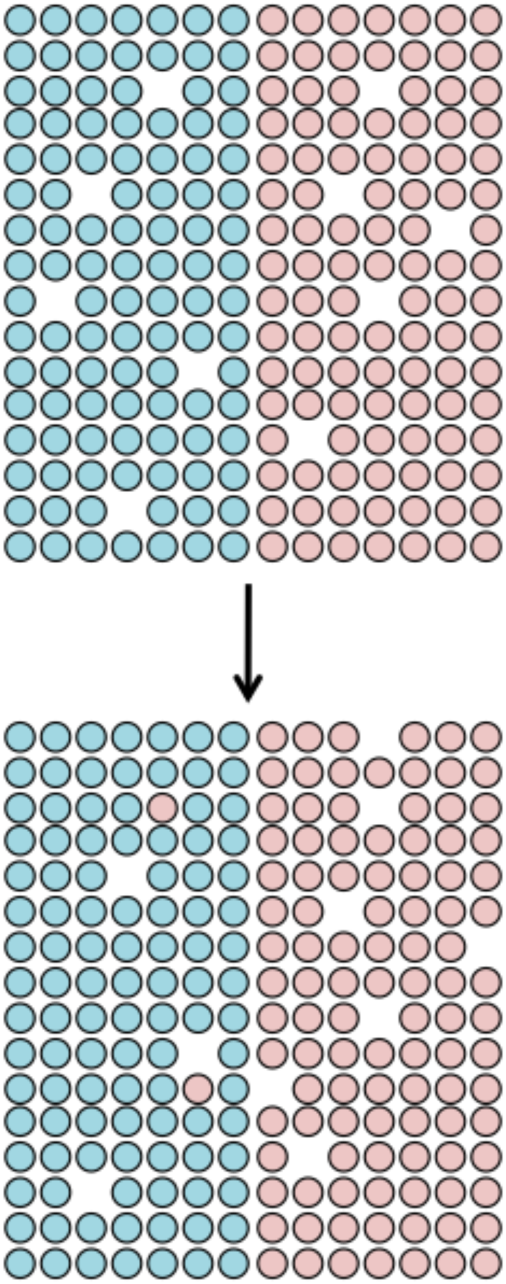

Figure 2.5. Pictorial illustration of the Kirkendall effect, in which a vacancy flux across the interface is generated in a material having an initially uniform vacancy distribution, due to a concentration gradient arising from differences in vacancy diffusivity for different atomic species.

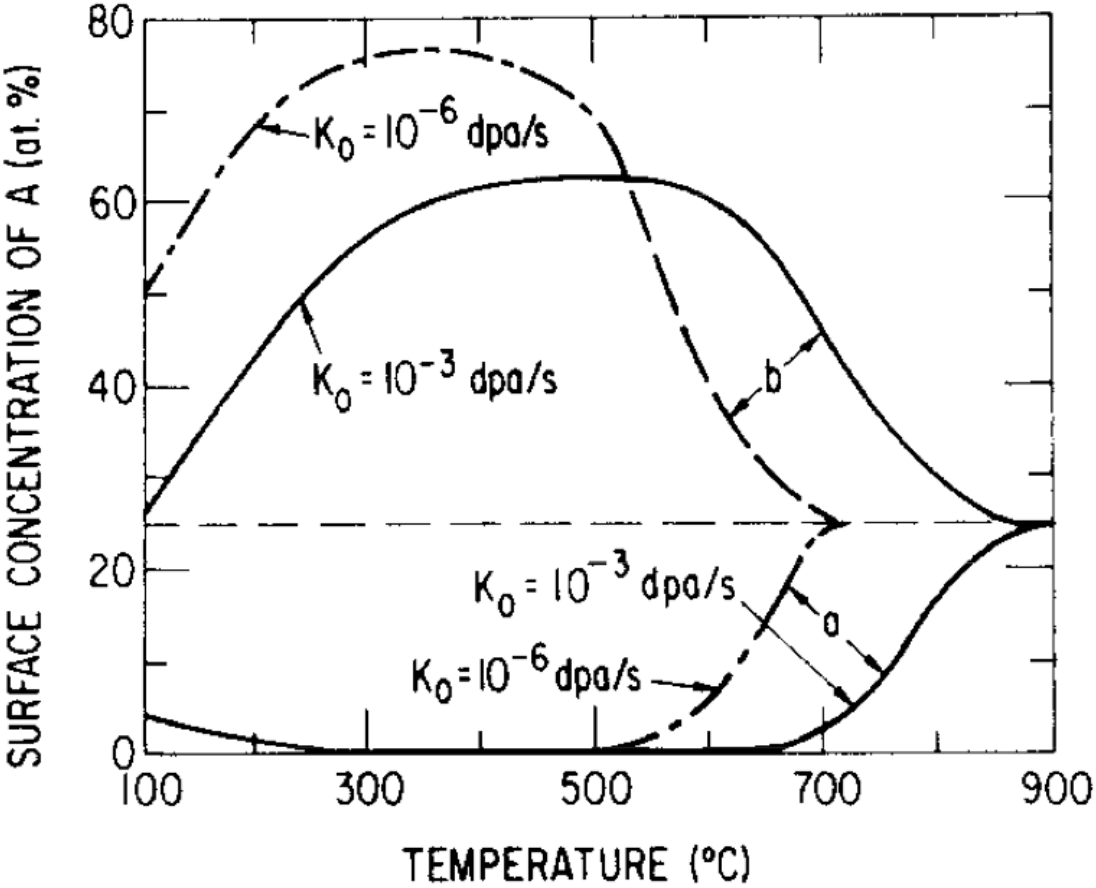

Figure 2.6. Steady-state surface concentration of A in a binary B-25%A alloy, as a function of irradiation temperature for two different irradiation dose rates. Top pair of curves shows preferential transport of A via interstitials, leading to A enrichment. Bottom pair of curves shows preferential transport of A via vacancies, leading to A depletion. From [35].

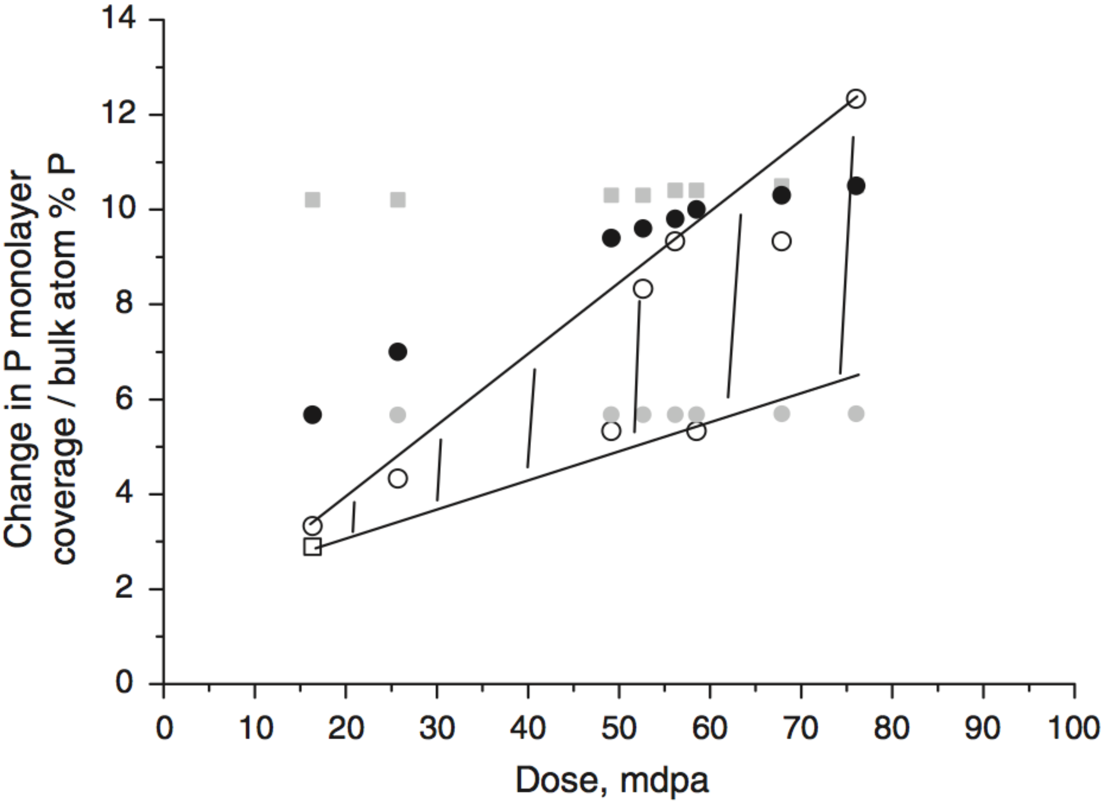

Figure 2.7. Faulkner's solute drag mechanism model prediction of phosphorus RIS (grey squares) for VVER steel, compared to experimental results (open circles) obtained following 300°C neutron irradiation at dose rates ~10^{-8}-10^{-10} dpa/sec. Solid circles represent predicted P RIS assuming free carbon content is changing due to vanadium carbide particle coarsening under irradiation. From [47].

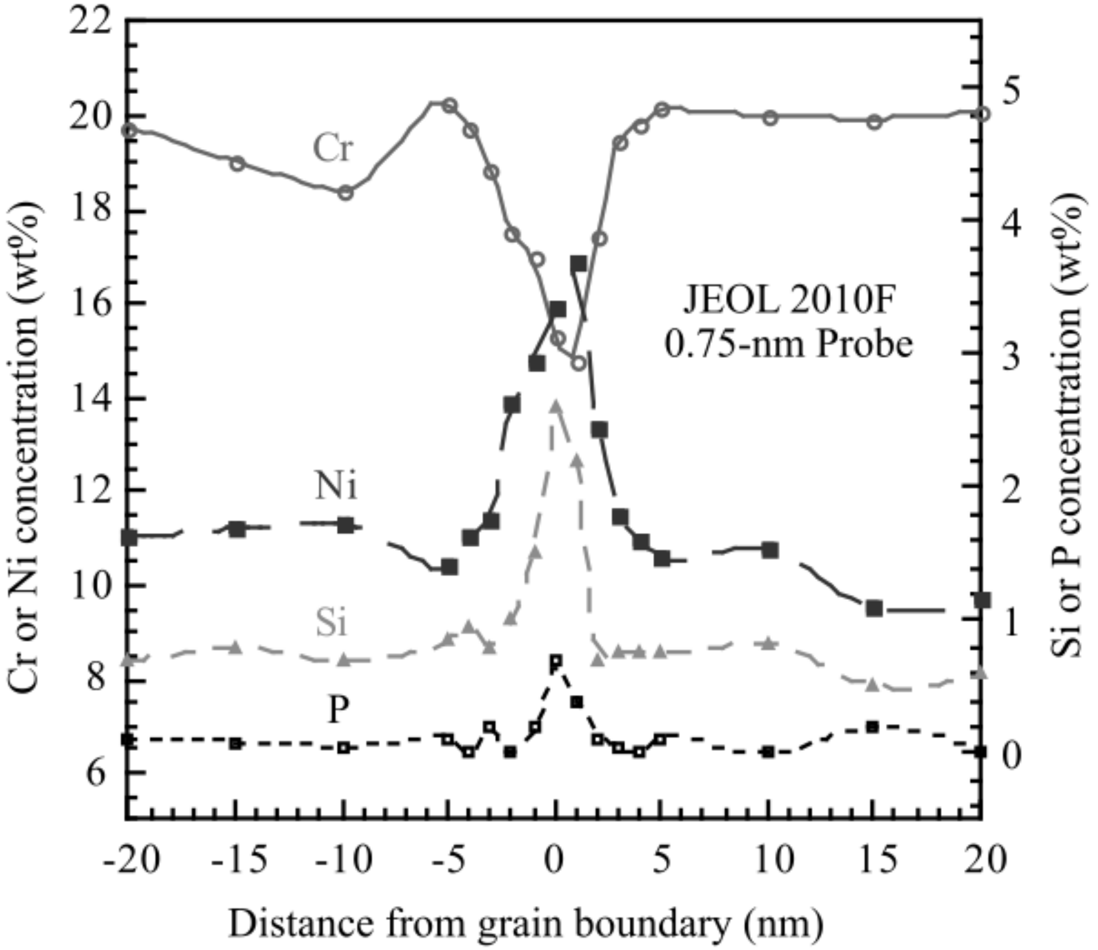

Figure 2.8. RIS profiles of Cr, Ni, Si, and P, at a grain boundary in a 300-series stainless steel neutron-irradiated to several dpa at ~300°C in a light water reactor. These profiles are typical of austenitic steels. From [19].

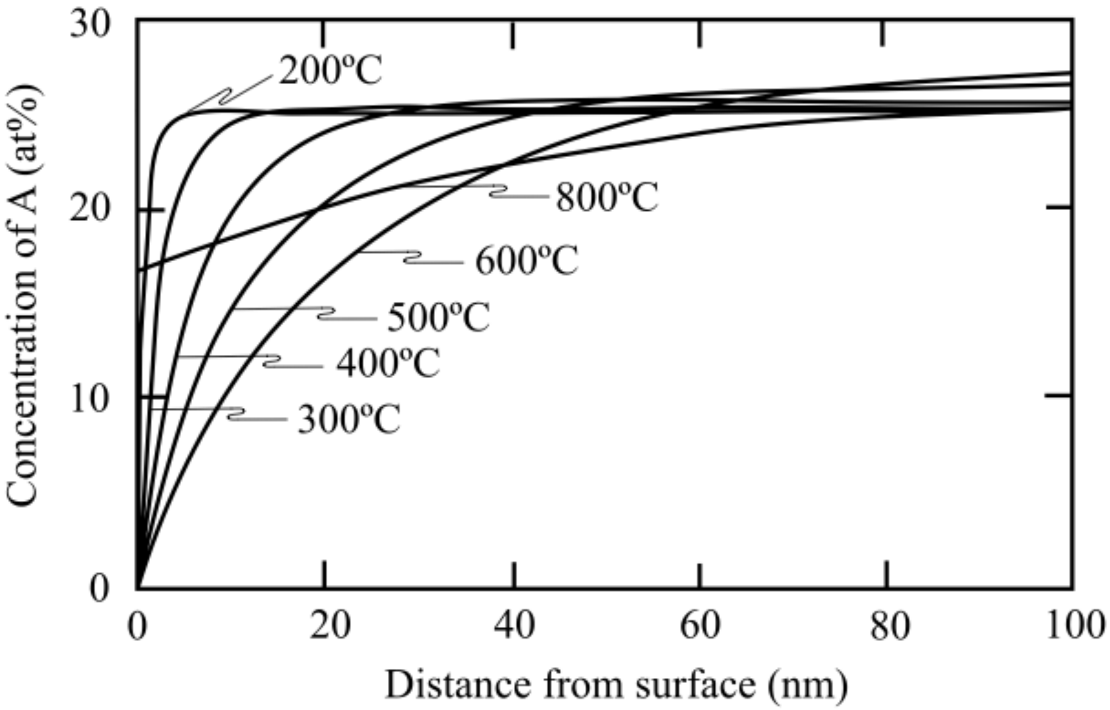

Figure 2.9. Typical temperature dependence of RIS concentration profiles in austenitic stainless steel. These profiles are based upon an inverse Kirkendall simulation at a dose rate of 10^{-3} dpa/sec. From [19].

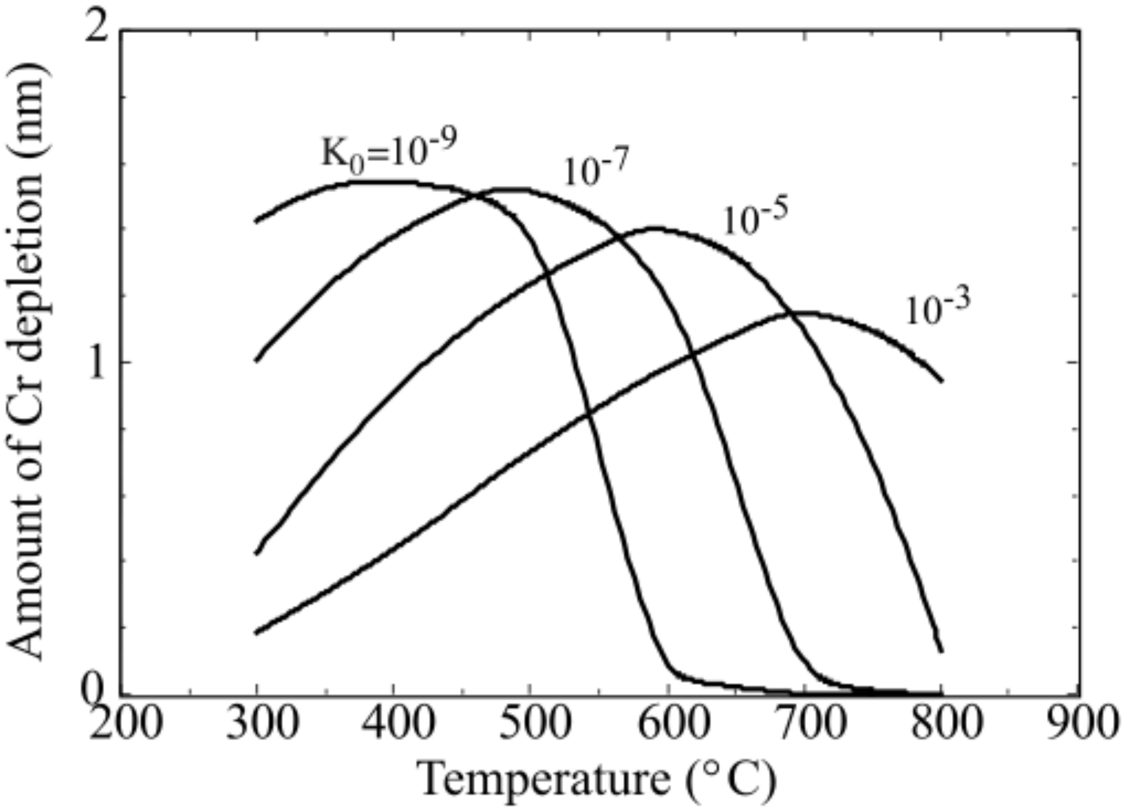

Figure 2.10. Dose rate dependence of grain boundary Cr depletion in typical austenitic stainless steels, as calculated by Allen's modified inverse Kirkendall model [18]. Plot taken from [19].

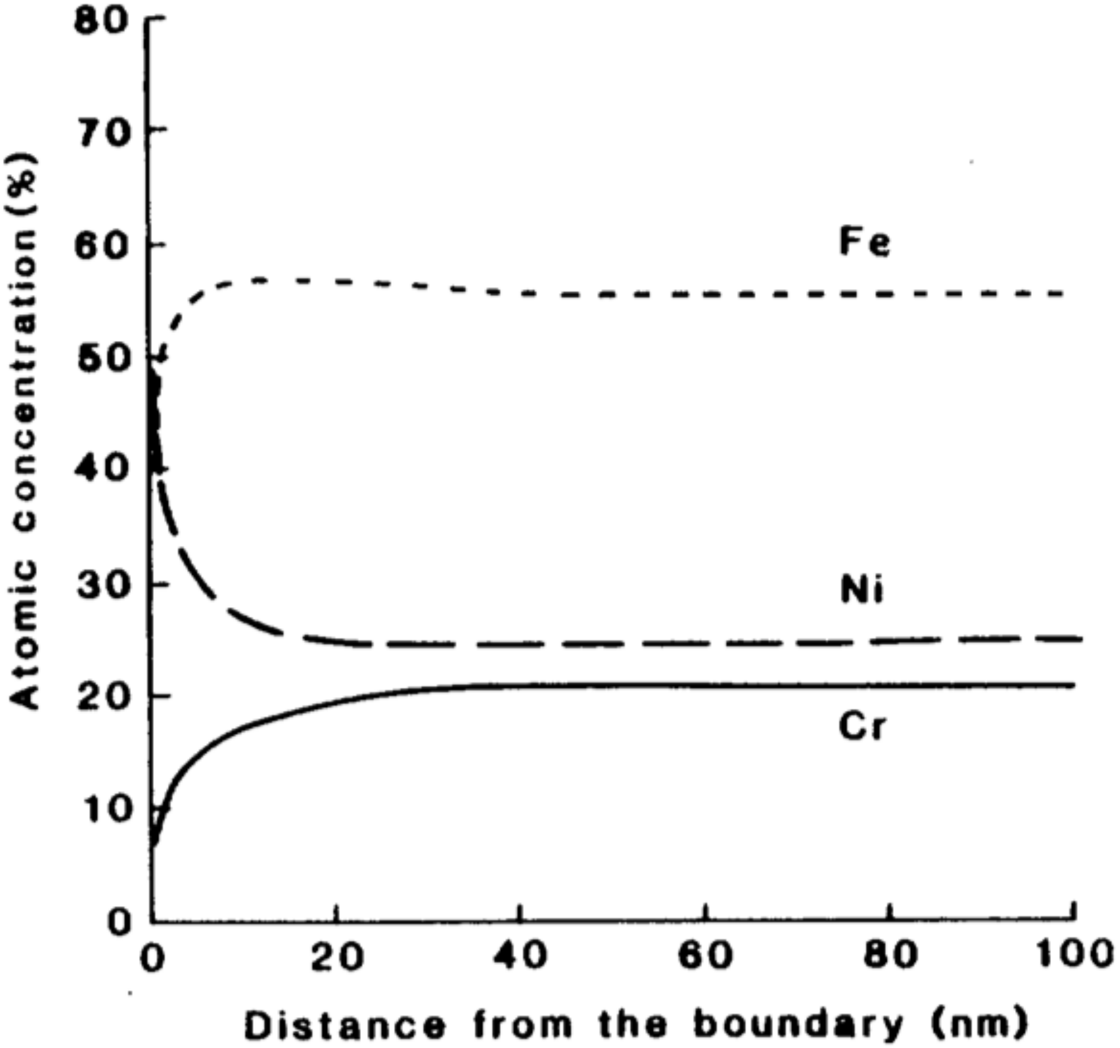

Figure 2.11. Perks model-predicted RIS in Fe-20Cr-25Ni following 450°C irradiation to 1 dpa at a dose rate of 2 x 10^{-8} dpa/sec, from [17].

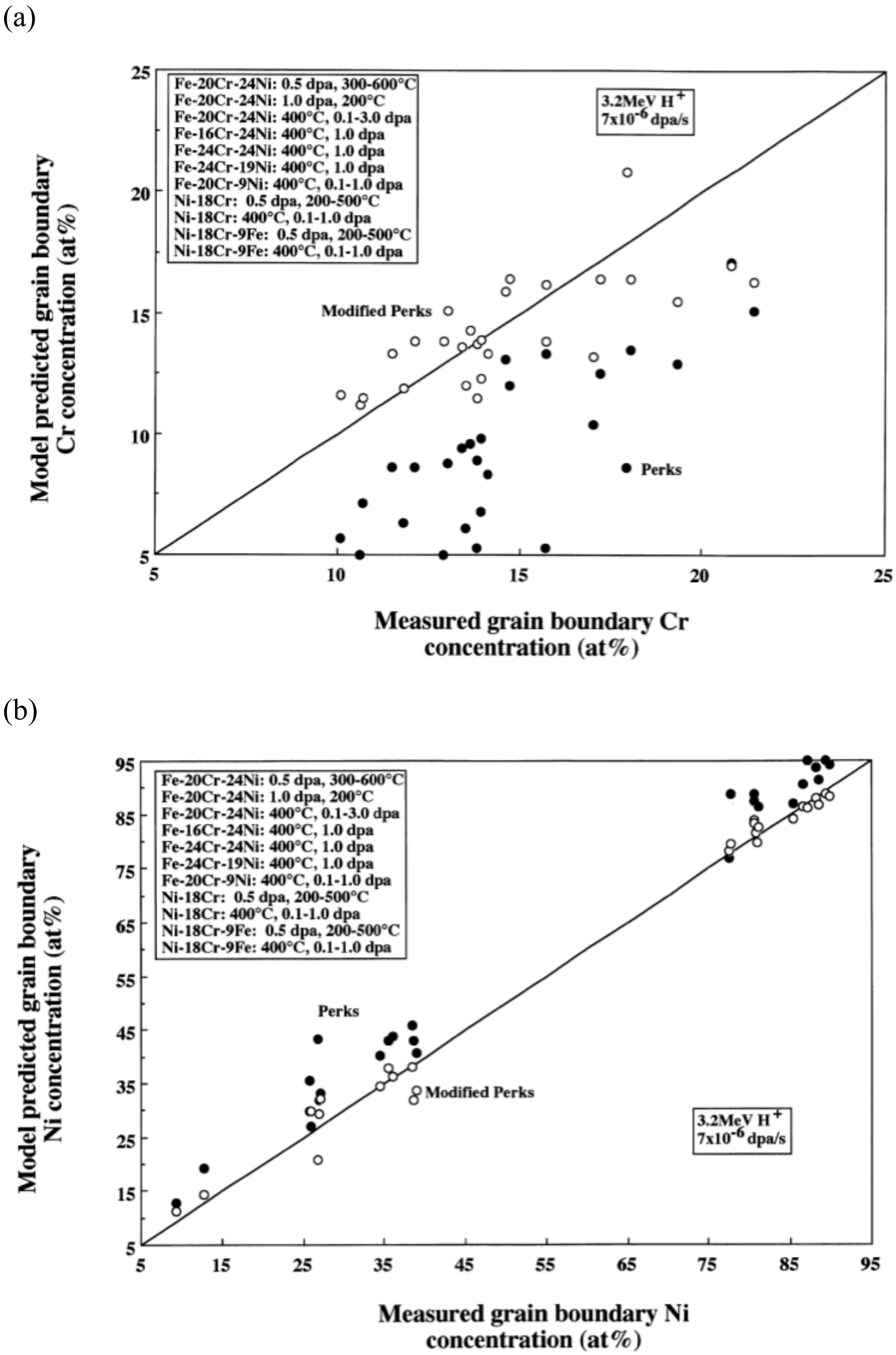

Figure 2.12. Relationship between model predicted and measured grain boundary (a) Cr and (b) Ni concentration for a range of austenitic alloys proton-irradiated over a range of temperatures and doses, showing that the MIK model is a better predictive tool than the Perks model, from [18].

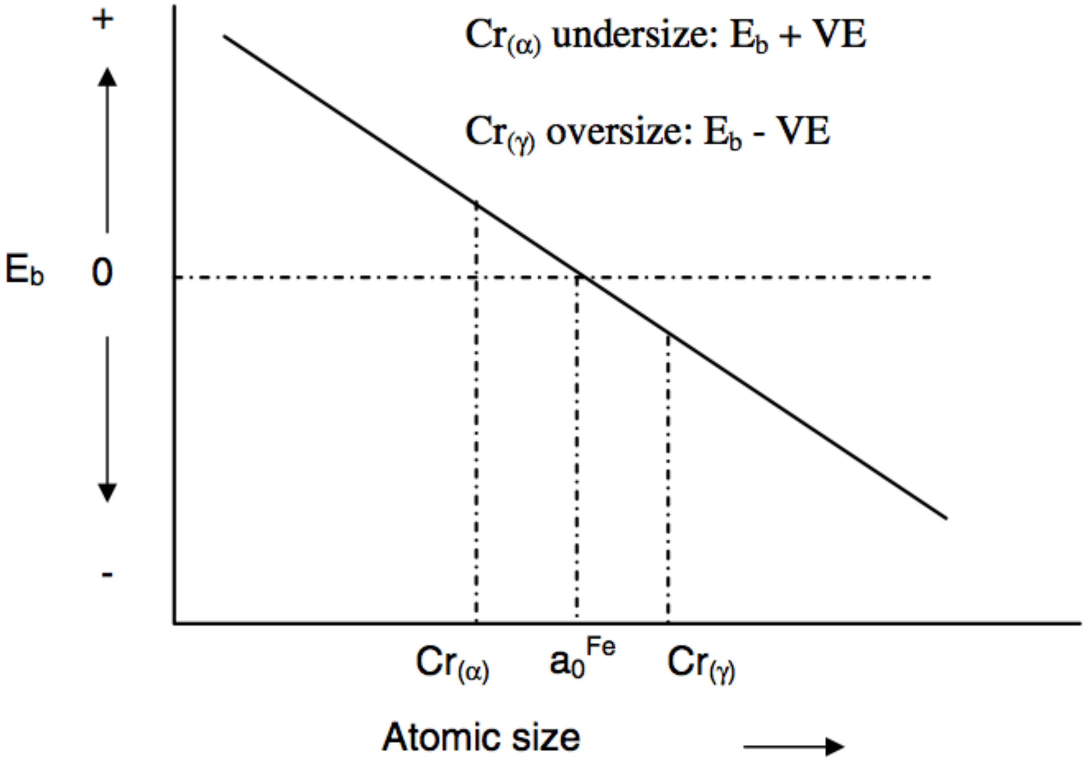

Figure 2.13. Qualitative illustration of relative atomic size of Cr (Cr_{γ}), b.c.c. Fe (a_0^{Fe}), and Cr (Cr_{α}) in a b.c.c. Fe-Cr alloy containing significant quantities of oversized alloying components such as W and Nb. The illustration suggests that the more undersized an atom, the more likely it is to have positive solute-interstitial binding. From [80].

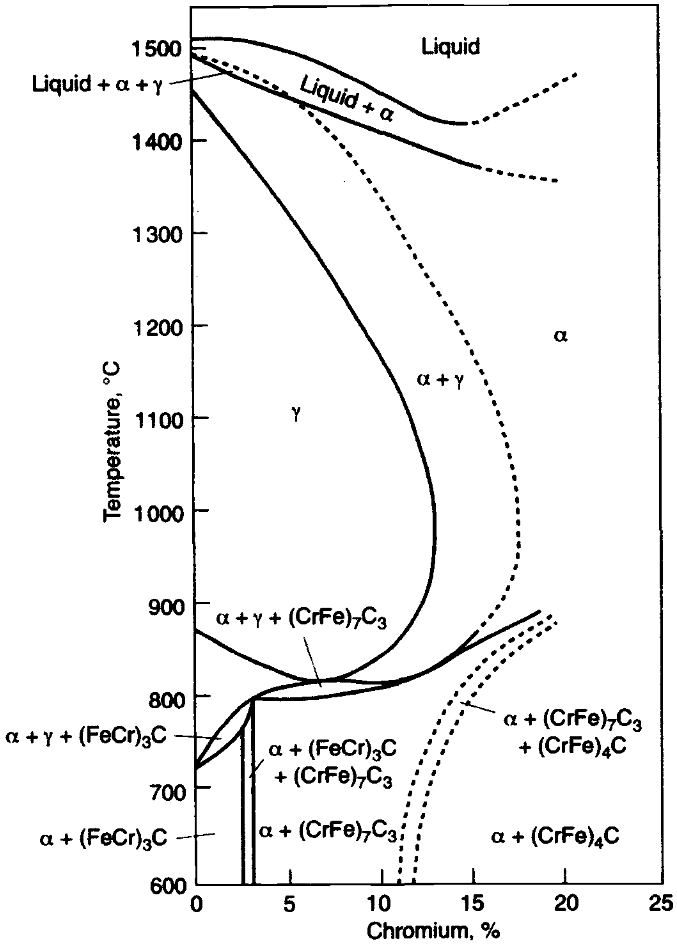

Figure 2.14. Effect of Cr on the phase constitution of Fe-Cr alloys containing 0.1 wt% C, from [1].

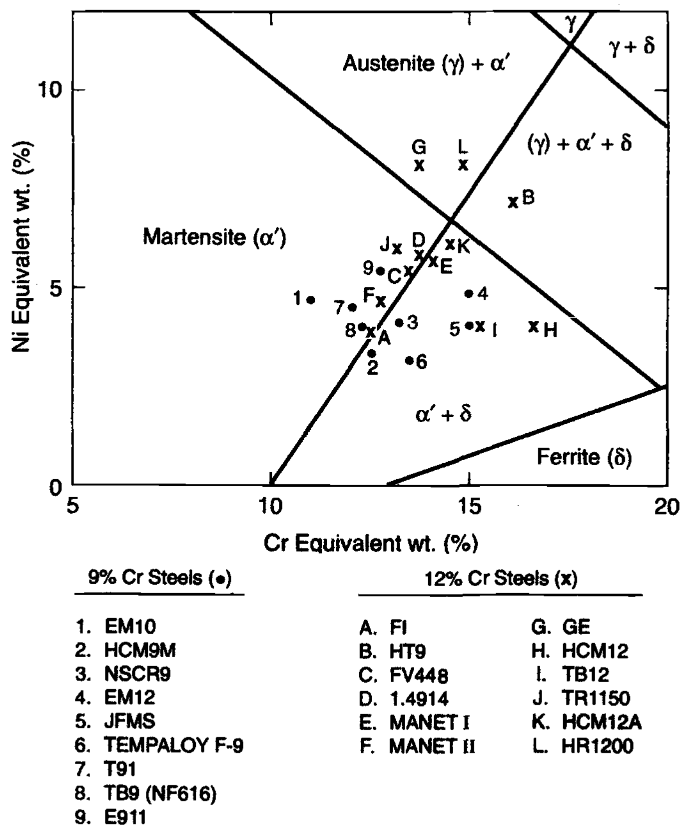

Figure 2.15. Schaeffler-Schneider diagram for predicting phases present in steels, from [1].

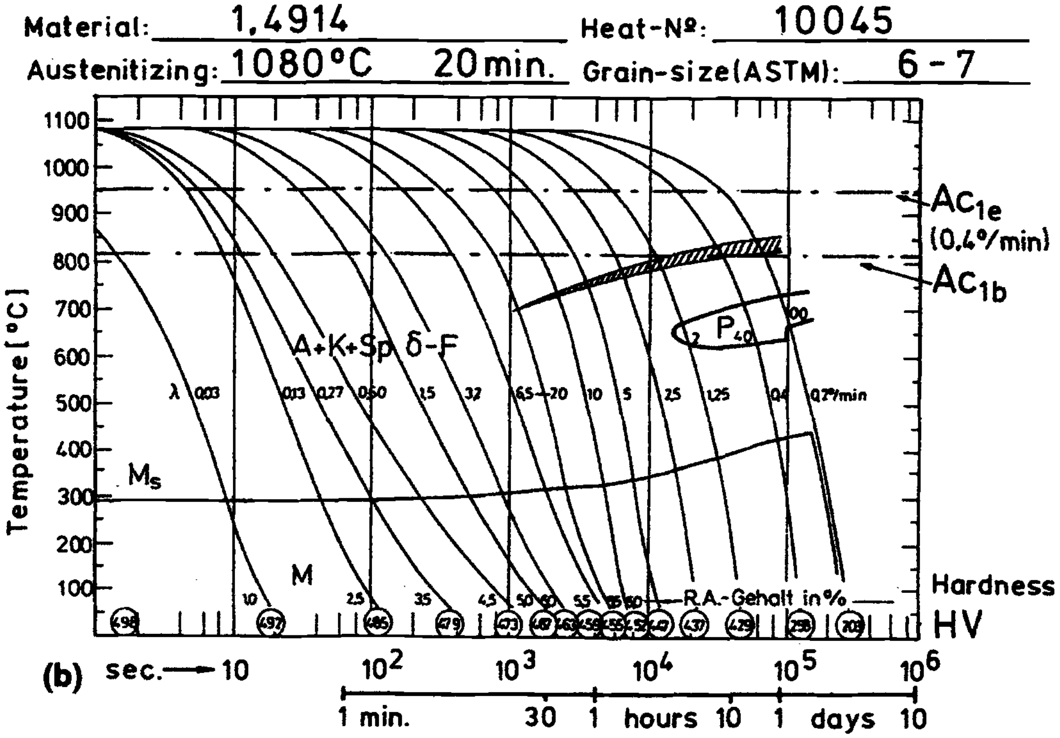

Figure 2.16. CCT diagram for a 12Cr-MoVNb martensitic steel, where A = austenite, K = carbide, Sp δ-F = trace of ferrite, M = martensite, P = pearlite, Ac_{1b} = start of austenite formation on heating, Ac_{1e} = completion of austenite formation on heating, and λ = cooling rate (°C/min) from 800-500°C, from [1].

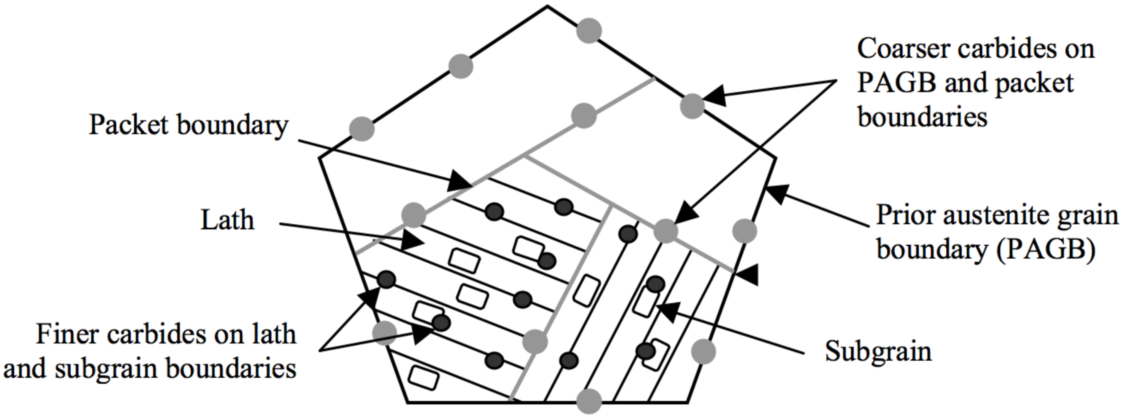

Figure 2.17. Typical F-M microstructure following tempering.

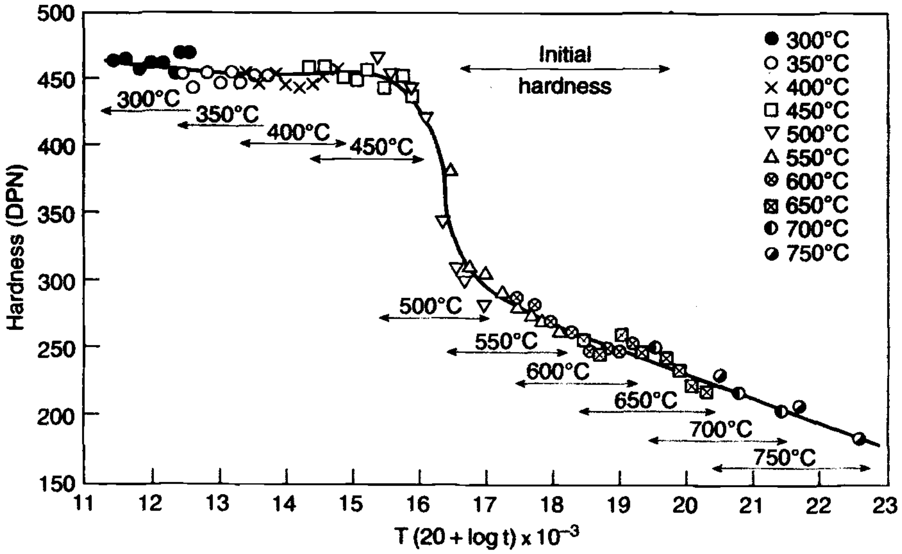

Figure 2.18. Hardness behavior of a 12Cr-0.14C steel during tempering, from [1].

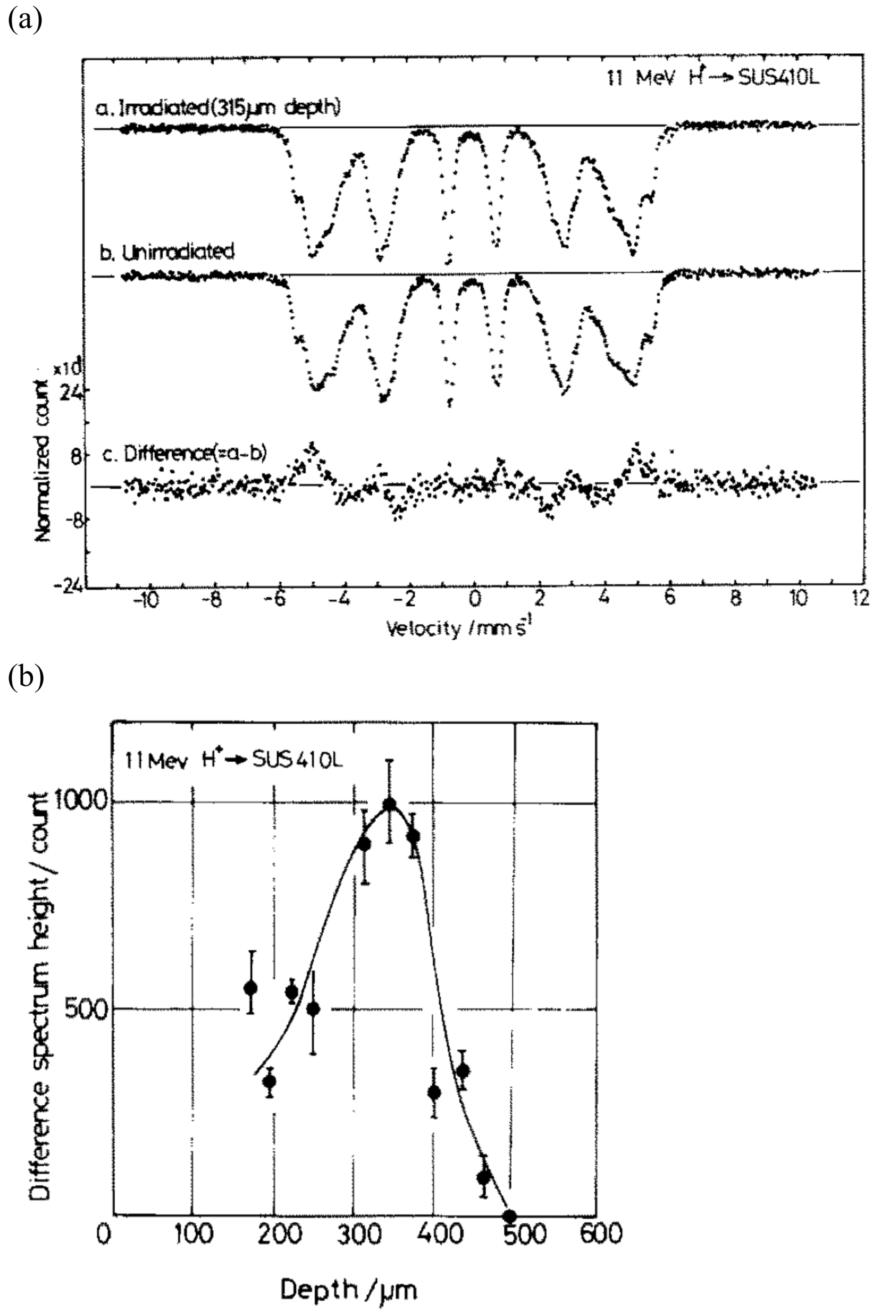

Figure 2.19. (a) Mössbauer spectrum of 11 MeV proton-irradiated SUS410L ferritic steel at a depth of 315 μm (top), compared to the unirradiated SUS410L spectrum (middle), and their difference spectrum (bottom), showing peaks at ±5 mm/s. (b) Amplitude of peaks at ±5 mm/s in the difference spectra of 11 MeV proton-irradiated SUS410L, as a function of depth into the damage peak. From [80].

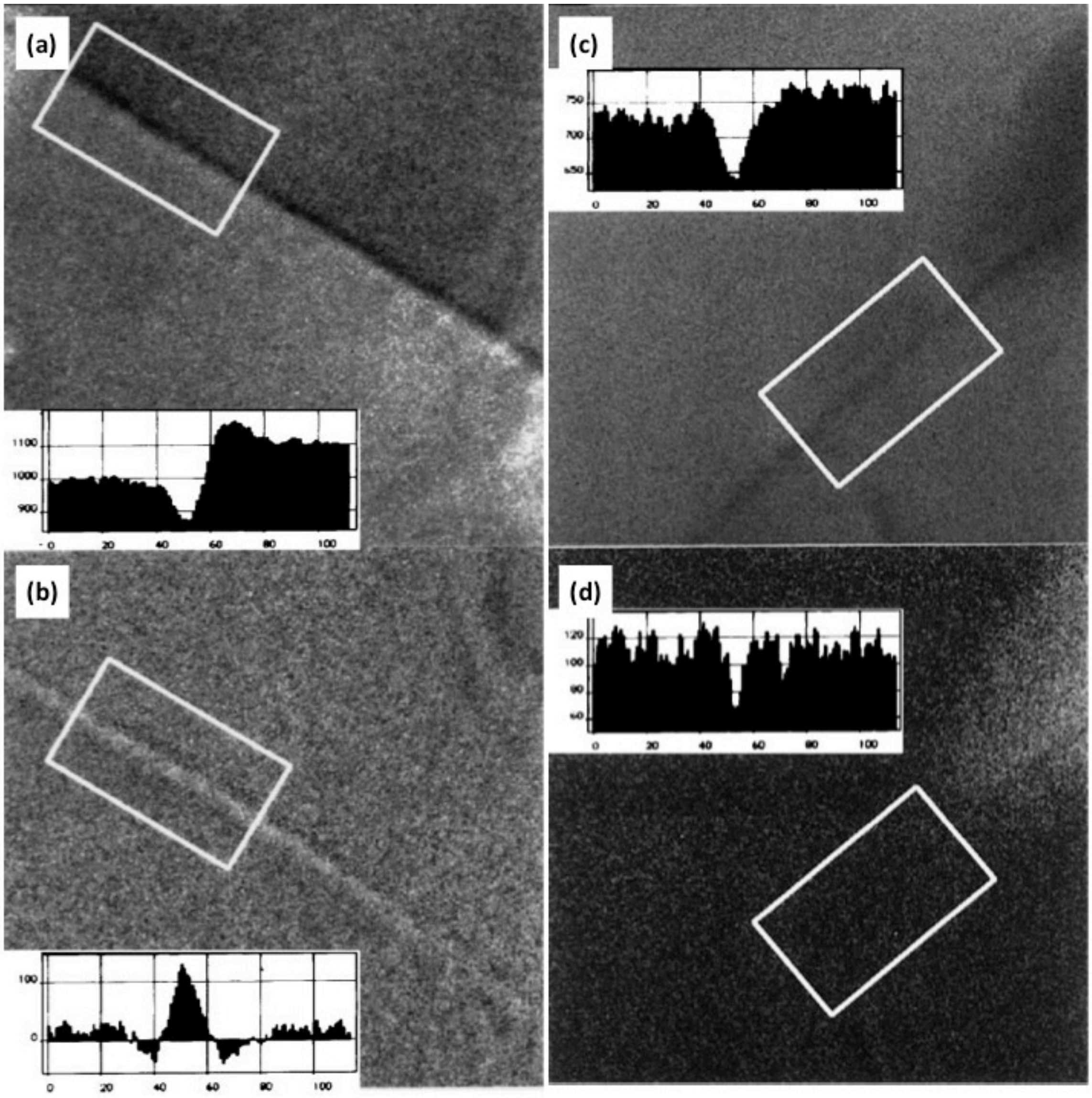

Figure 2.20. EFTEM element maps of: (a) Fe and (b) Cr in as-received F82H showing Fe depletion and Cr enrichment, and (c) Fe and (d) Cr in proton-irradiated F82H to 0.5 dpa at 250°C, showing depletion of both Fe and Cr, from [10].

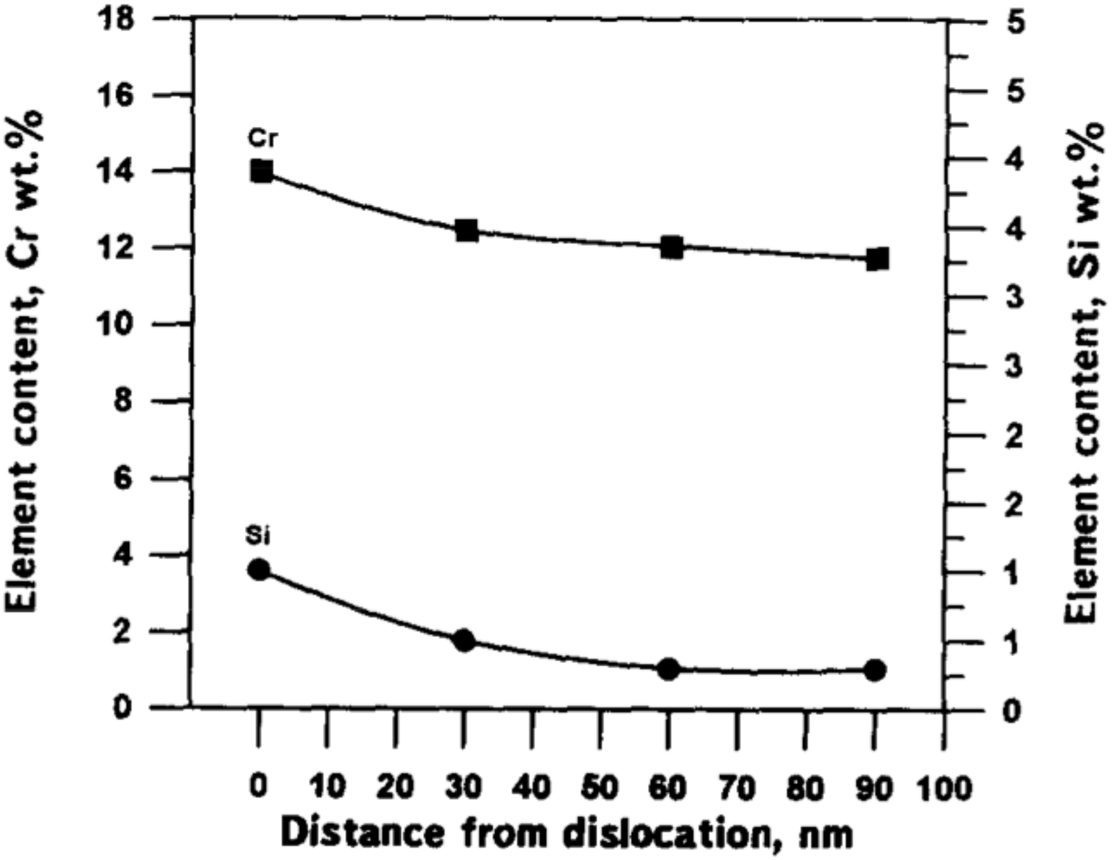

Figure 2.21. Concentration profile at a <100> dislocation loop in 13Cr-2Mo-NbVB irradiated with 1 MeV Cr^{3+} ions at 575°C to 48 dpa, from [10].

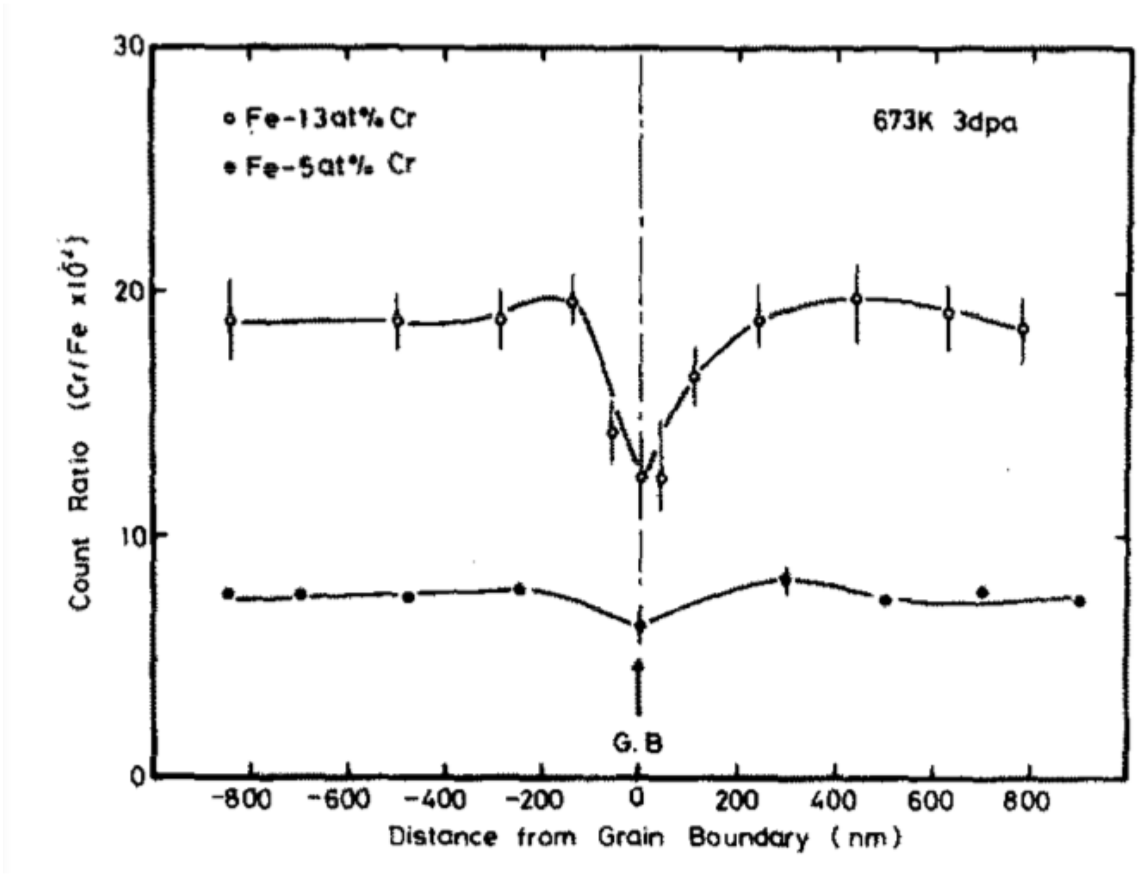

Figure 2.22. Concentration profiles of Cr, showing Cr depletion at the grain boundary, in Fe-13Cr (top) and Fe-5Cr (bottom) irradiated to 3 dpa at 400°C with 650 kV electrons.

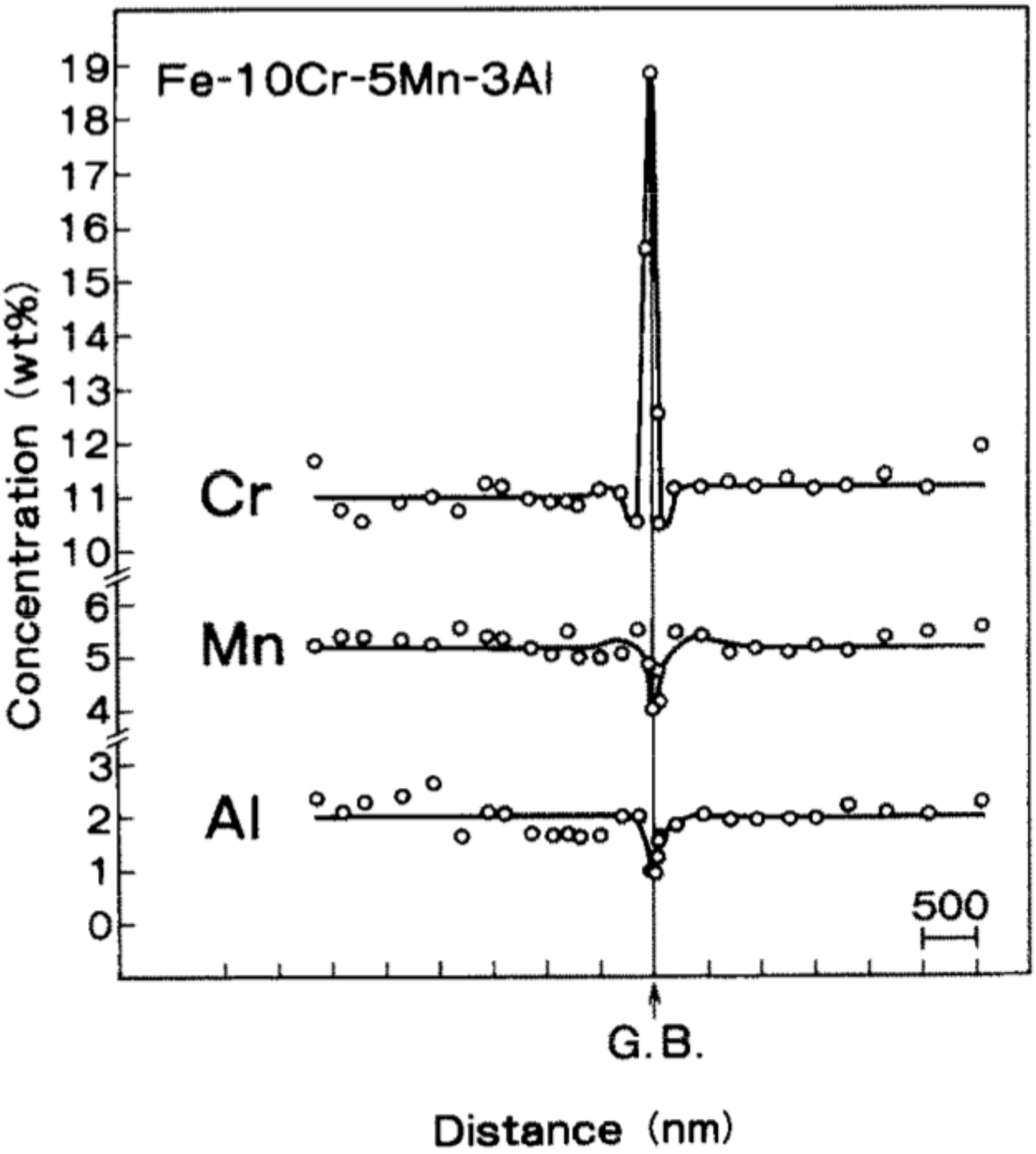

Figure 2.23. Concentration profiles showing Cr enrichment and Al and Mn depletion across a grain boundary in ferritic Fe-10Cr-5Mn-3Al irradiated with 1 MV electrons to 10 dpa at 450°C, from [4].

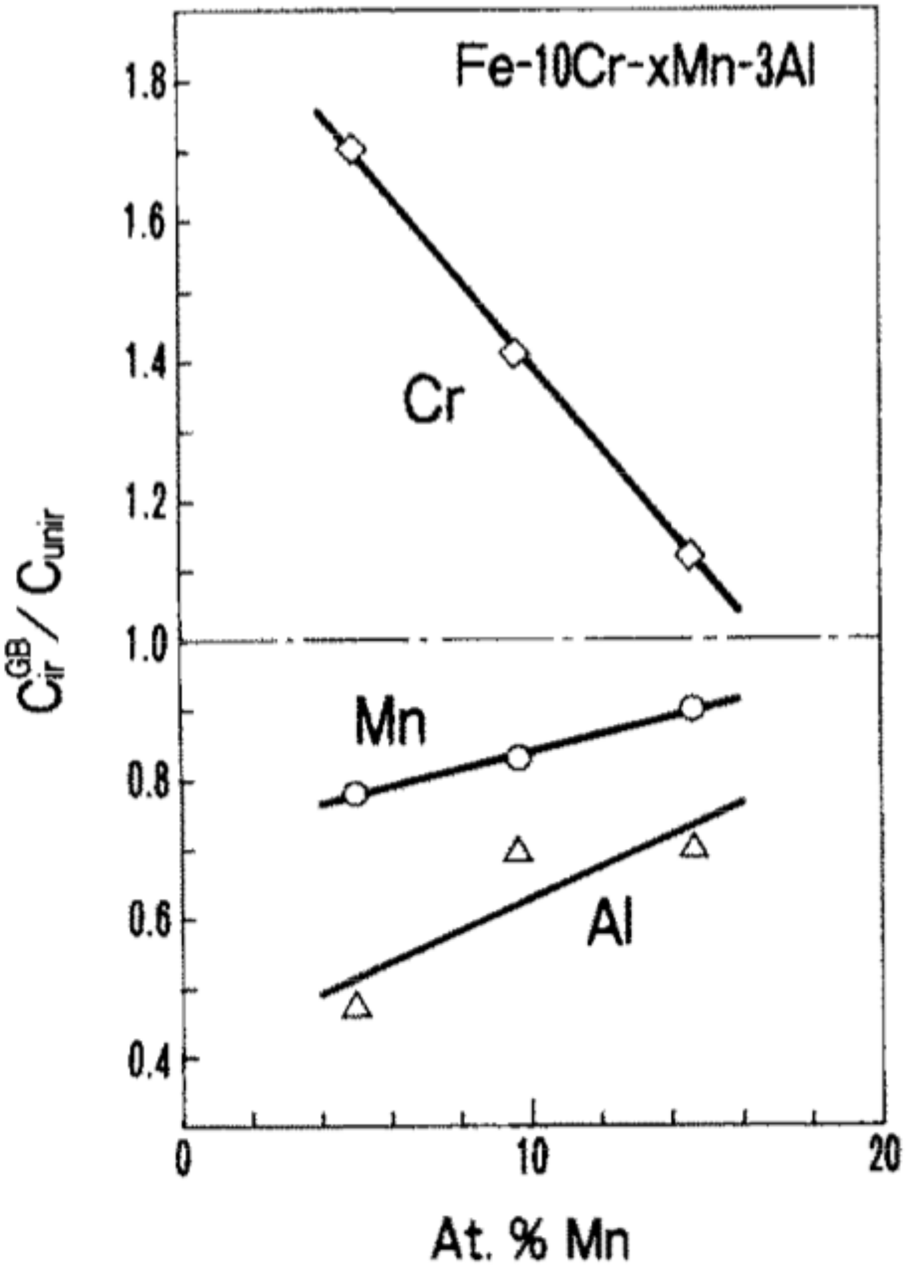

Figure 2.24. Grain boundary RIS of Cr, Mn, and Al (in units of irradiated grain boundary concentration divided by unirradiated bulk concentration), as a function of bulk Mn concentration, in ferritic Fe-10Cr-*x*Mn-3Al irradiated with 1 MV electrons to 10 dpa at 450°C, from [4].

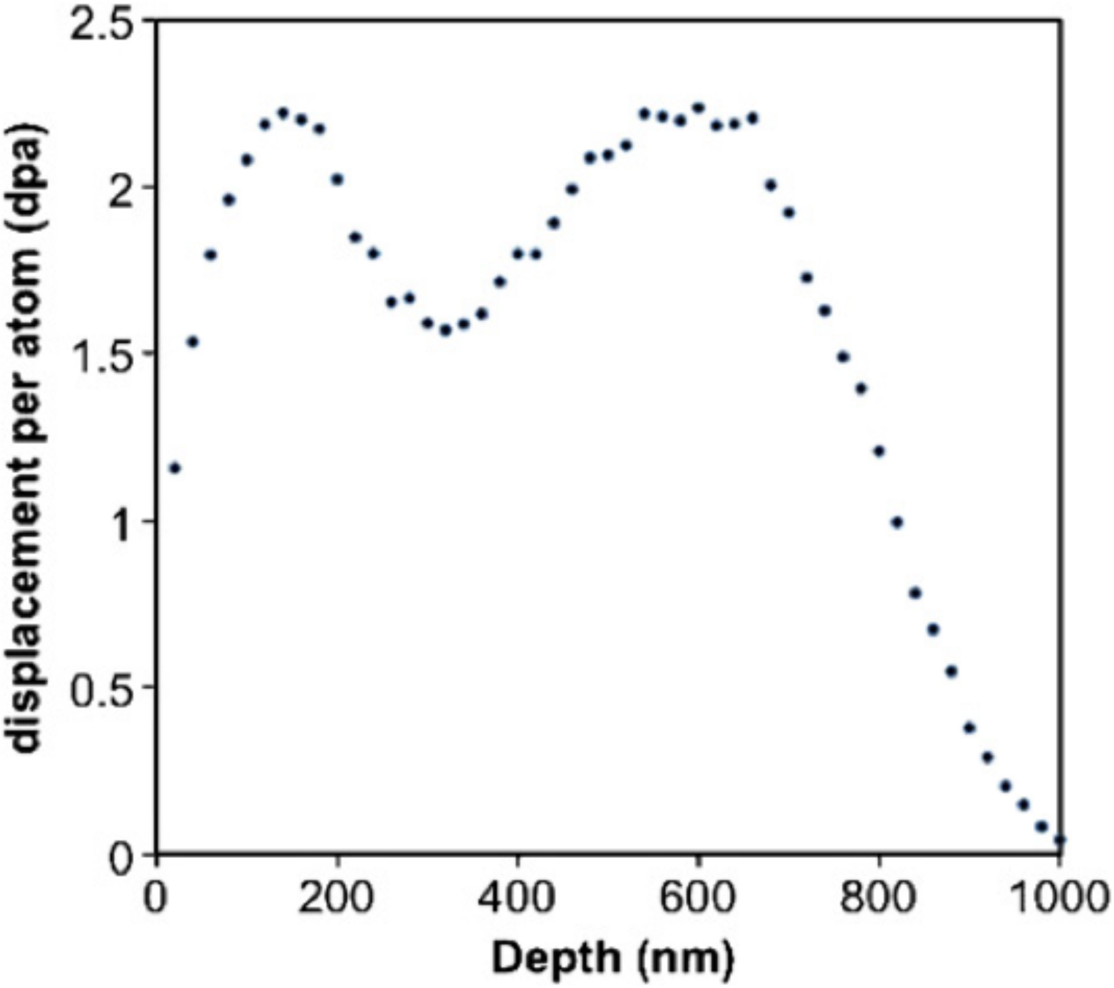

Figure 2.25. Damage profile generated in Fe-14.25 wt% Cr model F-M alloy, by fluxes of 0.5 MeV and 2 MeV Fe^+ ions, from [14].

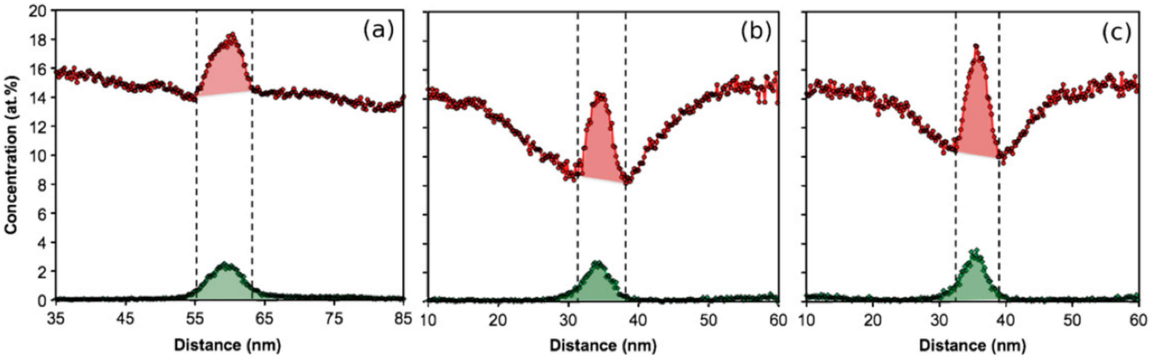

Figure 2.26. Concentration profiles of Cr (red, top) and C (green, bottom) across a grain boundary in Fe-14.25 wt% Cr irradiated with 0.5 MeV and 2 MeV Fe+ ions at 350°C, measured by APT at depths of (a) 2 µm, corresponding to 0 dpa, (b) 300 nm, corresponding to ~2 dpa, and (c) 800 nm, corresponding to ~0.5 dpa, from [14].

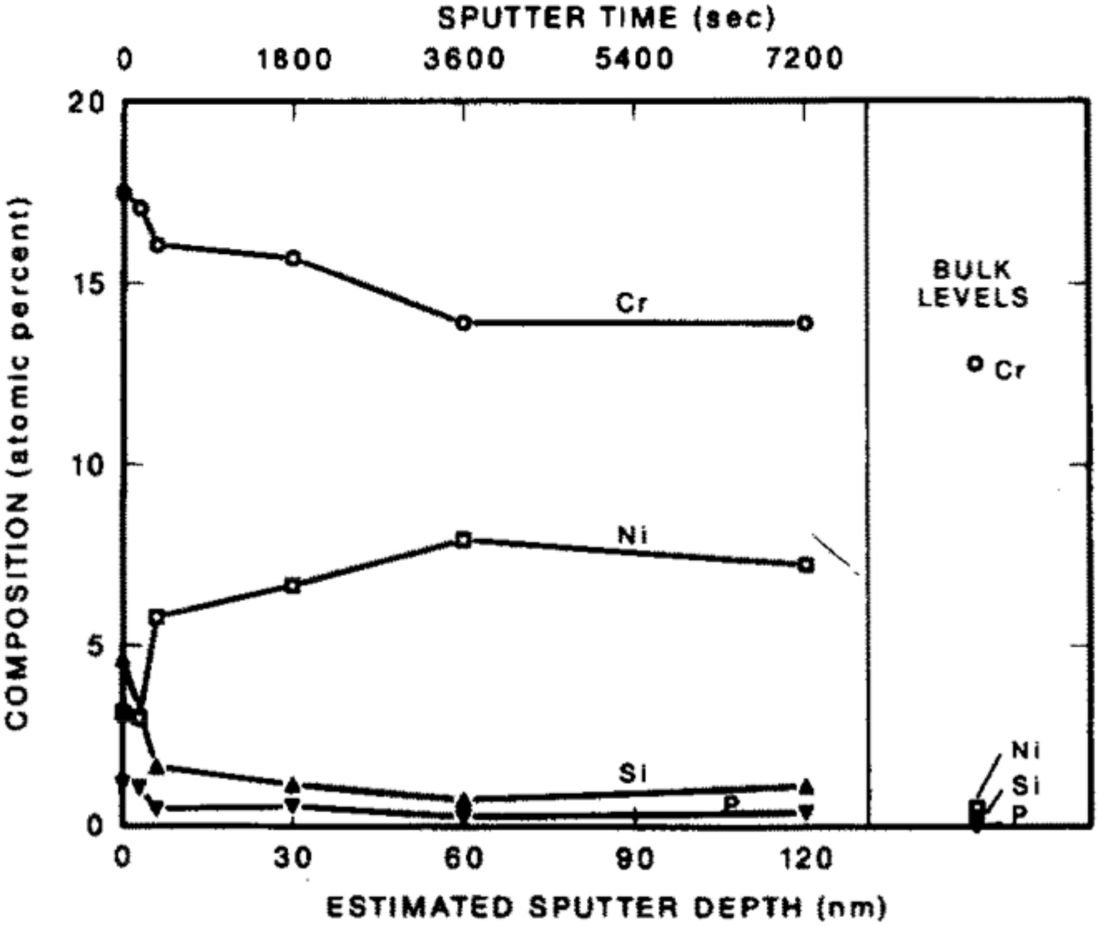

Figure 2.27. Concentration of Cr, Ni, Si, and P, as a function of depth into the surface of fracture macro-facets on HT9 irradiated with fast neutrons to 13 dpa at 410°C. As compared to bulk levels, all elements are shown to enrich at the macro-facet, which is theorized to be a PAGB. From [8].

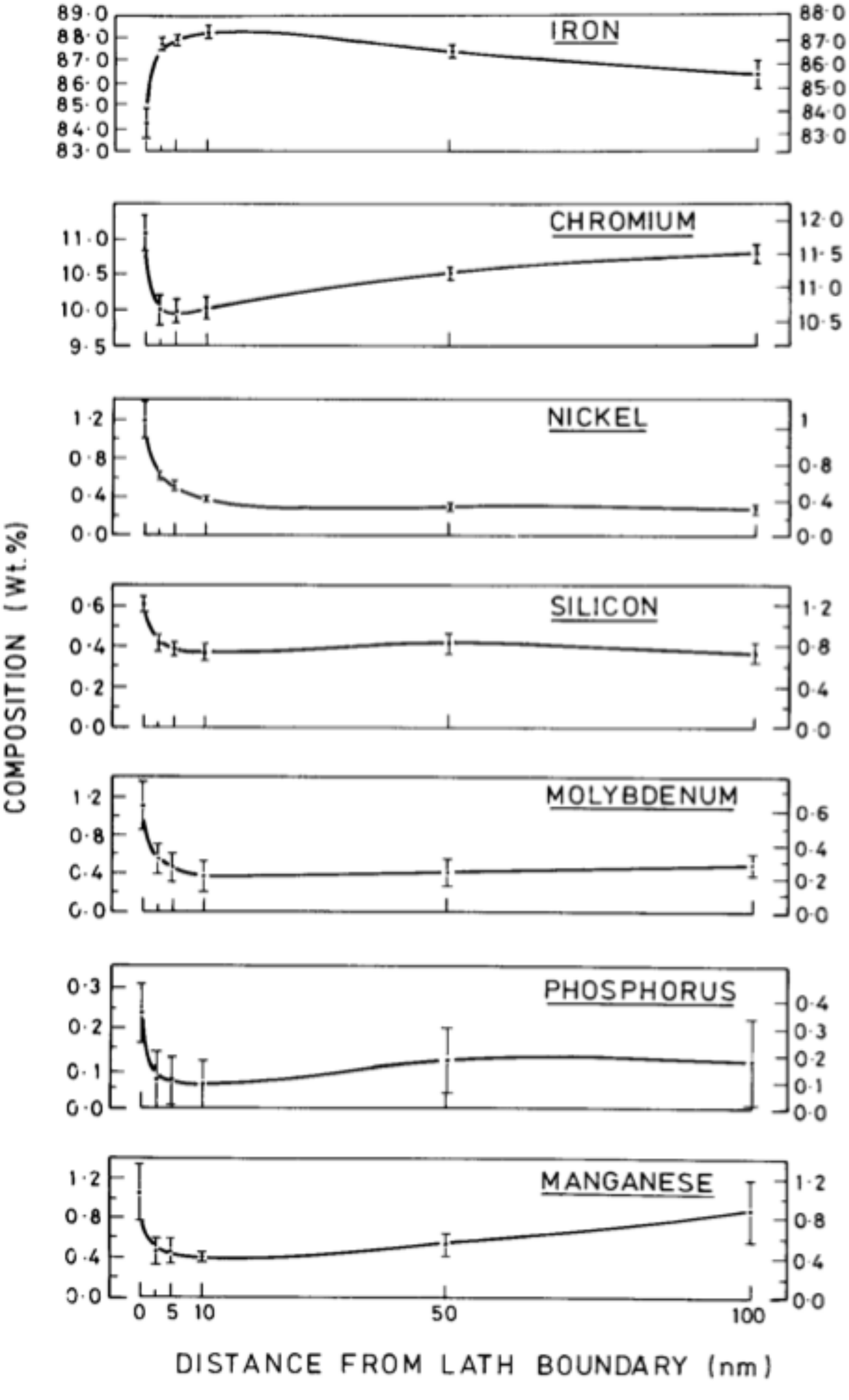

Figure 2.28. RIS profiles of Fe, Cr, Ni, Si, Mo, P, and Mn, averaged over several lath boundaries, in Fe-12CrMoVNb irradiated to 46 dpa at 465°C in a fast reactor, from [7].

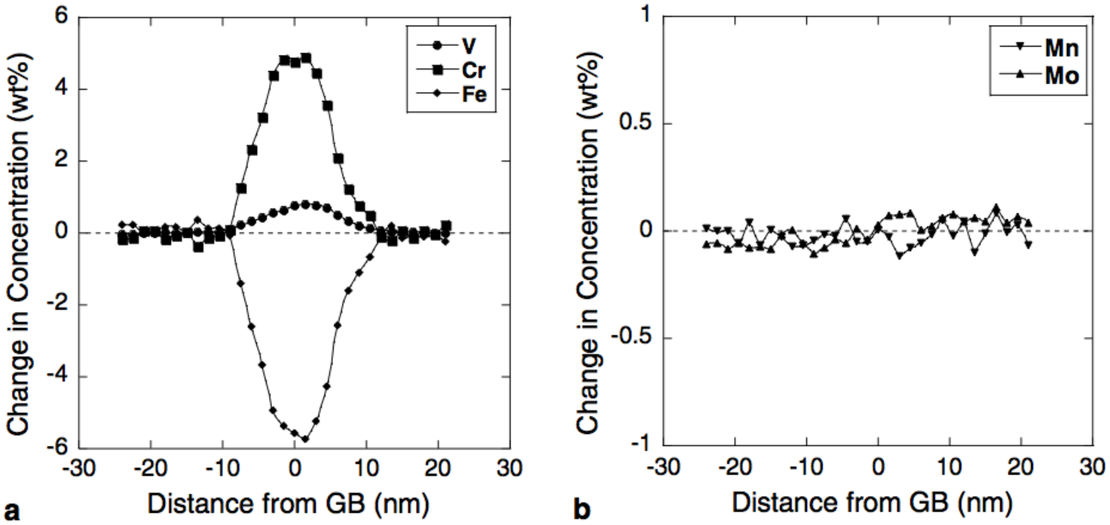

Figure 2.29. RIS profiles showing Cr and V enrichment, Fe depletion, and no variation in Mn and Mo concentrations, in T91 irradiated with 2.0 MeV protons to 10 dpa at 450°C, from [11].

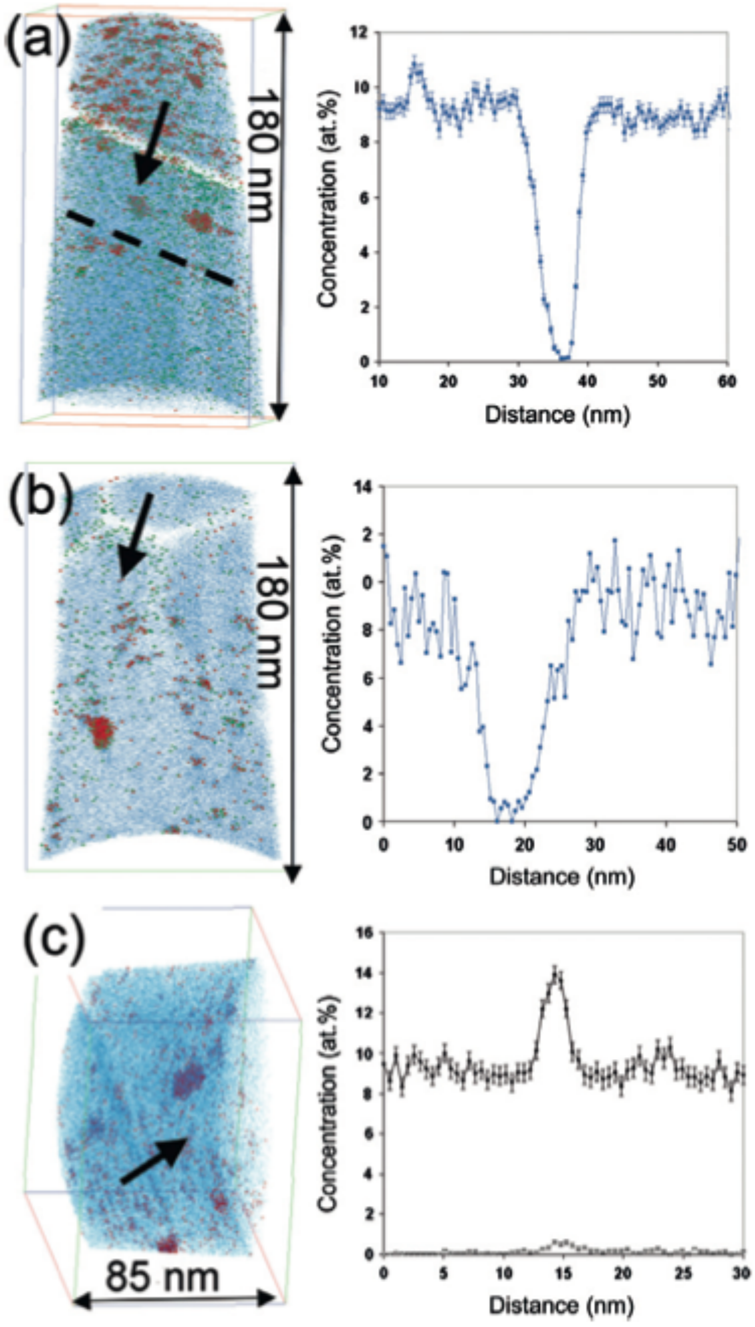

Figure 2.30. Three-dimensional reconstructions of APT specimens of model Fe-12Cr ODS steel, accompanied by one-dimensional concentration profiles traversing the grain boundary. Specimens have been irradiated with Fe^+ ions at 500°C, and exhibit both Cr depletion (a) and (b), and Cr enrichment (c). From [13].

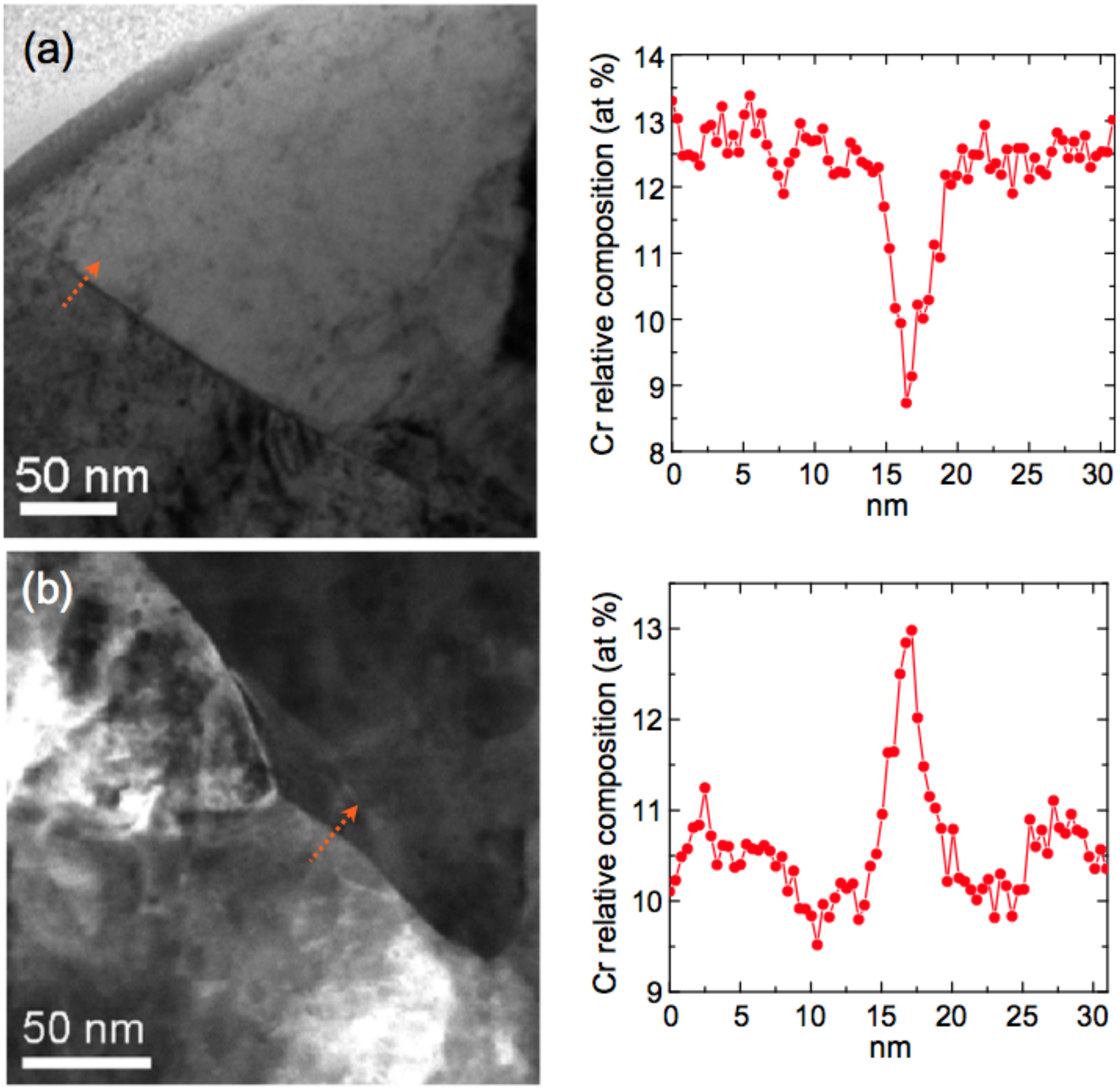

Figure 2.31. Planar specimen of a model Fe-12Cr ODS irradiated with Fe^+ ions at 500°C, exhibiting (a) Cr depletion at 60 nm depth, as measured by EELS concentration profile (right) traversing the grain boundary indicated in the bright field TEM image (left), and (b) Cr enrichment at 600 nm depth, as measured by EELS concentration profile (right) traversing the grain boundary indicated in the HAADF-STEM image (left), from [13].

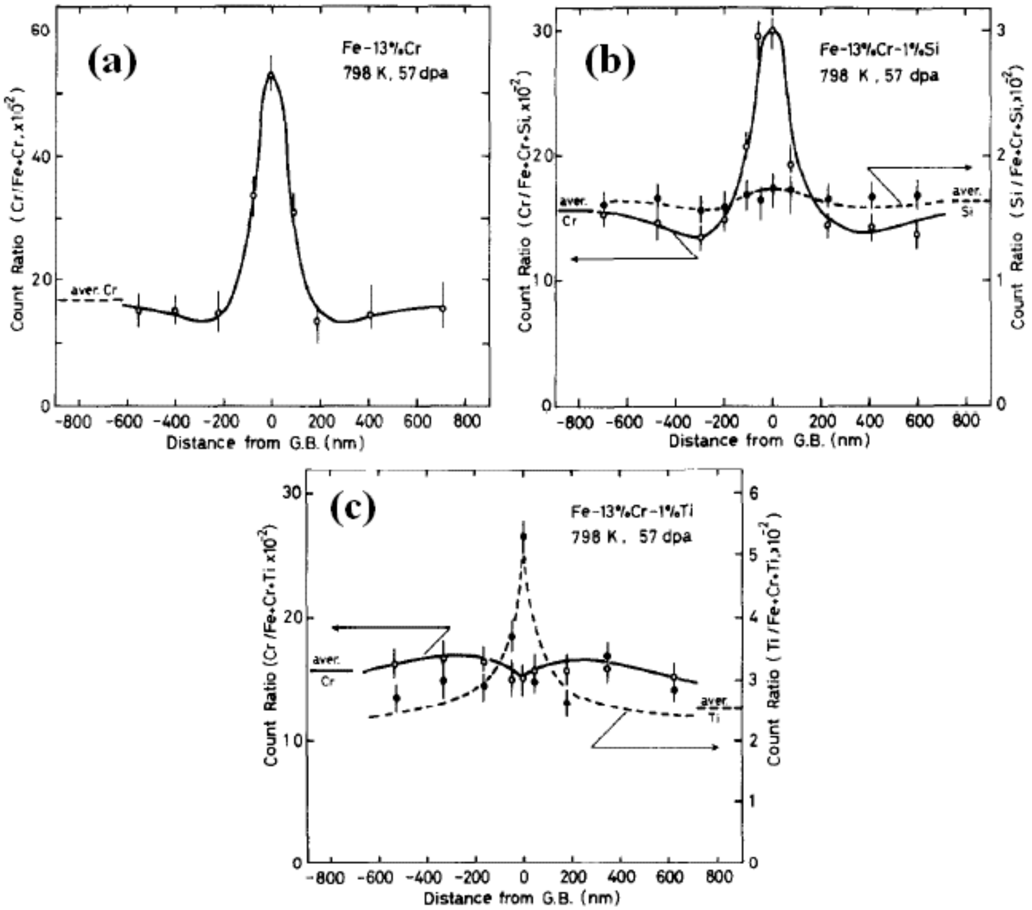

Figure 2.32. Concentration profiles across grain boundaries following 57 dpa, 525°C irradiation with 200 keV C^+ ions, showing (a) Cr enrichment in Fe-13Cr, (b) Cr and Si enrichment in Fe-13Cr-1Si, and (c) Cr depletion and Ti enrichment in Fe-13Cr-1Ti, from [5].

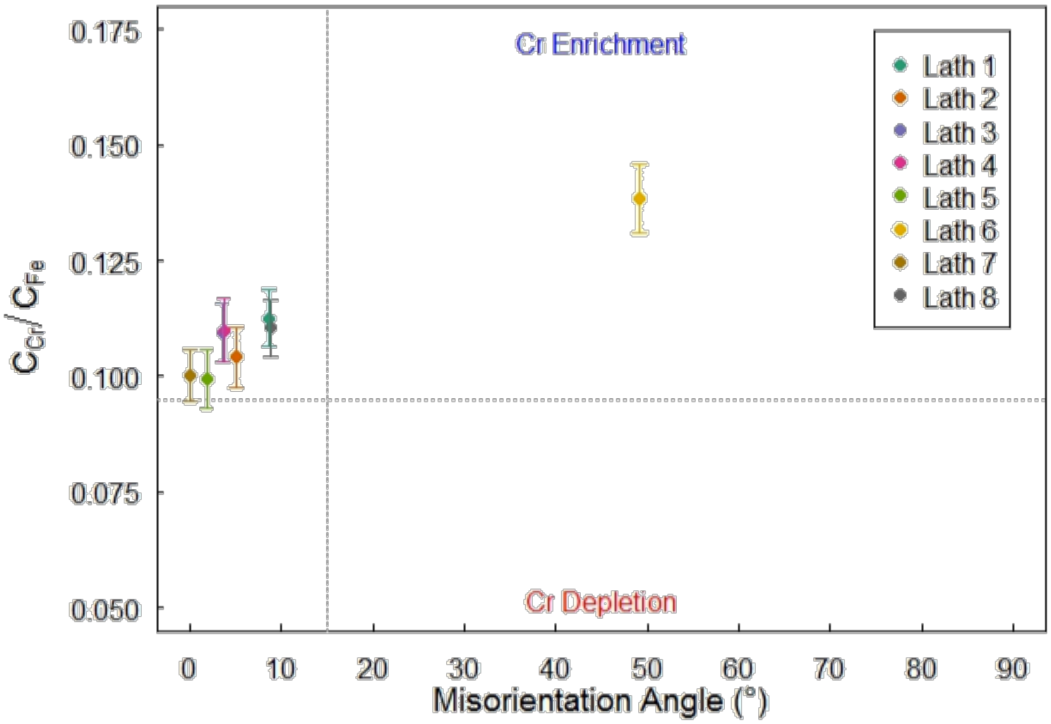

Figure 2.33. Dependence of RIS on boundary misorientation angle, shown in terms of Cr:Fe concentration ratios at the grain boundary, in F-M model alloy Fe-9Cr proton-irradiated to 2 dpa at 400°C, from [64].

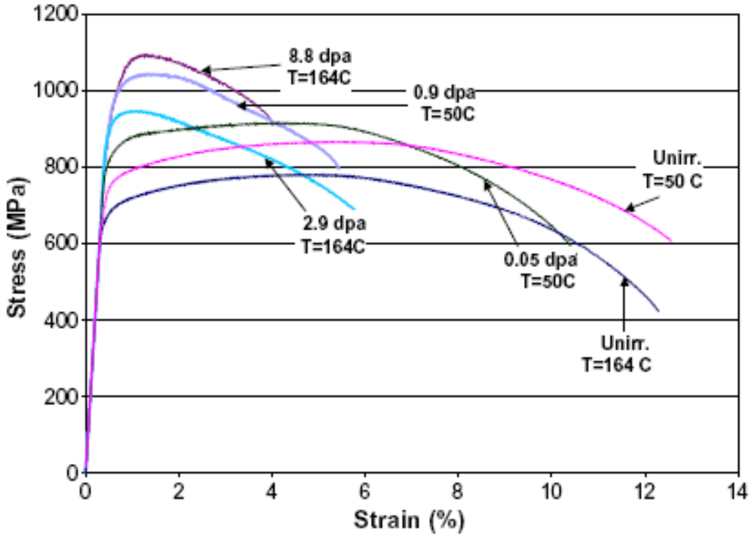

Figure 2.34. Stress-strain curves of unirradiated and irradiated (up to ~9 dpa) T91 at 50°C and 164°C, showing an increase in hardening, yield stress, and ultimate tensile stress, as a function of increasing irradiation dose, from [1].

CHAPTER 3 OBJECTIVE

The objective of this thesis is to determine the mechanism of radiation-induced segregation in ferritic-martensitic alloys. This objective will be accomplished with a combined experimental and modeling approach, in which experimental measurements of RIS in F-M alloys will be determined to be either consistent or inconsistent with a modeled RIS mechanism. Consistency between experiments and models will be assessed with respect to experimentally-alterable parameters: temperature, bulk Cr composition, dose, and dose rate.

Extensive work in the peer-reviewed literature has shown that RIS in austenitic steels is consistent with an inverse Kirkendall mechanism. It is therefore hypothesized that the mechanism of RIS in F-M alloys can likewise be described by an inverse Kirkendall mechanism. In this mechanism, point defect fluxes generate an atomic concentration gradient at grain boundaries, due to differences in the atom-defect exchange rates of constituent atoms.

As a means toward accomplishing the overall objective of this thesis, the first sub-objective is to model the inverse Kirkendall mechanism. A computational model of this mechanism will establish the hypothesized behaviors of RIS in F-M alloys. The IK model which will be used in this work is based on the well-established Perks model [17], [37], which was originally developed for ternary austenitic alloys. In this work, the model is adapted for a binary Fe-Cr F-M alloy system. Amongst the many input parameters to the IK model are parameters which describe the experimental conditions being simulated: temperature, bulk Cr composition, dose, and dose rate. A number of IK model cases are run to determine the dependence of the calculated Cr RIS on each of the aforementioned experimental parameters. The model cases are as follows:

- *Temperature dependence*: 17 cases between 100°C and 900°C at 50°C intervals, with fixed concentration (Fe-9Cr), dose (steady-state 15 dpa) and dose rate (10^{-5} dpa/sec)
- *Composition dependence*: 9 cases between Fe-7Cr and Fe-15Cr and 1Cr intervals, with fixed temperature (400°C), dose (steady-state 15 dpa) and dose rate (10^{-5} dpa/sec)
- *Dose dependence*: 13 cases between 0.00001 dpa and 100 dpa at intervals of approximately a decade, with fixed temperature (400°C), composition (Fe-9Cr), and dose rate (10^{-5} dpa/sec)
- *Dose rate dependence*: 9 cases between 10^{-9} dpa/sec and 0.1 dpa/sec at intervals of a decade, with fixed temperature (400°C), composition (Fe-9Cr) and dose (steady-state)

The second sub-objective of this thesis is to measure RIS in F-M alloys and compare these measurements to the model calculations. Specimens of F-M alloys will be irradiated with 2.0 MeV protons over a range of experimental conditions. The experimental conditions are selected so as to test the parametric dependencies determined using the IK model:

- *Temperature dependence*: 6 experiments at 300°C, 400°C, 450°C, 500°C, 600°C, and 700°C, with fixed alloy (T91), dose (3 dpa) and dose rate (~10^{-5} dpa/sec)
- *Composition dependence*: 4 experiments on T91, an Fe-9Cr model alloy, HCM12A, and HT9, at fixed temperature (400°C), dose (3 dpa) and dose rate (~10^{-5} dpa/sec)
- *Dose dependence*: 4 experiments each on T91 and an Fe-9Cr model alloy to 1, 3, 7, and 10 dpa, at fixed temperature (400°C) and dose rate (10^{-5} dpa/sec)

The comparison of experimental to modeled RIS results will focus on both the general trends or behaviors, as well as the amount or magnitude of RIS. This critical comparison of experiment to model will aid in determining whether RIS in F-M alloys is driven by the inverse Kirkendall mechanism.

Since the overall objective of this thesis is to determine the mechanism of RIS, demonstrating consistency between measured RIS and a mechanism does not alone meet this objective. Measured RIS must also be shown to be *inconsistent* with other mechanisms. Thus, the final sub-objective of this thesis is to investigate the alternative RIS mechanism of solute drag, then compare this mechanism to the experimental results.

CHAPTER 4 EXPERIMENTAL

This chapter will describe the experimental techniques and measurements utilized in this thesis. The chapter is organized into sections for each step in the experimental procedures: (1) alloys and sample preparation, (2) proton irradiations, (3) post-irradiation examination and specimen preparation, (4) RIS measurements, and (5) microstructure studies.

4.1 Alloys and Sample Preparation

This thesis focuses on the behavior of RIS in four different F-M alloys. Three of the alloys are commercial F-M steels (HT9, T91, HCM12A), the study of which may offer insight into the dependence of RIS on bulk chromium concentration and the effects of minor element and impurity concentrations. A fourth alloy, a laboratory-purity model alloy of composition Fe-9Cr, is also studied to aid in understanding the effects of carbides, precipitates, and minor and impurity elements on RIS. These four alloys and their processing will be described in this section, along with the method of preparing the alloys for irradiation.

4.1.1 Alloys and Processing

The three commercial F-M alloys selected for this study are T91, HCM12A, and HT9. The standard designations of these steels are 9Cr-MoVNb, 12Cr-MoVNbWCu, and 12Cr-MoVW, for T91, HCM12A, and HT9, respectively. A laboratory-purity 9Cr model alloy is also included in this work. The compositions of the heats of these alloys used in this thesis are provided in Table 4.1.

The alloys have all been heat treated with both austenitization and tempering steps, which allowed for the development of the desired microstructures. The heat treatment processes for each alloy are shown in Table 4.2. T91 is fully martensitic, with an average PAGB diameter of 11 μm and martensite laths 0.4 μm in width by 5.4 μm in length. HCM12A exhibits a two-phase coexistence of martensite laths with δ-ferrite needles, both on the order of 0.9 μm wide and 6.1 μm long, present in PAGBs of average diameter 16.8 μm. Lastly, HT9 exhibits a three-phase coexistence comprised largely of martensite, with small amounts of retained austenite islands and δ-ferrite grains. In HT9, the martensite laths are 0.4 μm wide and 14.6 μm long, while the PAGBs are 47.3 μm in diameter, on average. These observations are consistent with the phases predicted by the Schaeffler-Schneider diagram. Bright field TEM images of the as-received microstructures are provided in Figure 4.1 for all four alloys.

Following heat treatment, the alloys are cut into 1.5 x 1.5 x 20 mm TEM bar specimens by electrical discharge machining (EDM). In EDM, high frequency sparks are applied across a 10-100 μm gap between a copper wire and the desired cut area on the material. The sparks cause material removal without cold working, which is a concern in conventional machining. The typical sample geometry, following EDM, is shown in Figure 4.2.

4.1.2 Sample Preparation

Following EDM, the samples are prepared for irradiation experiments. The method of preparation involves a series of polishing steps, beginning with mechanical polishing and ending with electropolishing.

Samples are prepared for mechanical polishing by mounting them onto a flat, aluminum polishing block. The block is warmed on a hot plate to just high enough of a temperature to melt Crystalbond™ 509 resin wax, which bonds the samples to the block. The samples are mounted onto the block in the order in which they will be arranged on the irradiation stage; this ensures that the samples on the irradiation stage will have a flat, planar surface. The samples are then wet polished on Struers® SiC paper, beginning with grit 320, and working up the grits to 4000.

Only two surfaces of the samples are polished. First, the surface that will be placed face-down onto the irradiation stage (i.e. opposite the irradiated face) is polished. Afterward, the samples and polishing block are re-heated on the hot plate to melt the resin wax and free the samples. The samples are ultrasonically cleaned in acetone, then mounted back onto the polishing block with the irradiated surface facing up, to be polished. Once the irradiated faces are polished, the samples are again removed from the polishing block and cleaned in acetone, using the same procedures as already described.

Mechanical polishing will always introduce a layer of plastic deformation on the samples, even at grits as high as 4000. This plastically-deformed layer is removed by electropolishing. Conditions for electropolishing are selected such that they yield a mirror finish surface, absent of pitting or etching.

During the electropolish, samples are immersed, one at a time, in 500 mL of a 90% methanol and 10% perchloric acid solution. The solution is contained in a beaker of inner diameter ~6 inches, which itself is immersed in a bath of methanol and dry ice, so as to maintain the solution at temperatures between -40°C and -50°C. A cylindrical platinum mesh cathode approximately 40 mm long with diameter slightly less than 6 inches is placed at the bottom of the solution-containing beaker. During electropolishing, individual samples are held upright, with their 20 mm length centered vertically in the 40 mm cathode; the specimen is also centered radially in the middle of the beaker. Samples are electropolished for 20 seconds with an applied potential of 35 V between the sample and a cylindrical platinum mesh cathode, as verified by a digital multi-meter. A magnetic stirring bead with a frequency of ~650 rpm creates a circular flow in the polishing solution with a vortex of approximately 0.75 inch. Samples are immersed in the vortex during polishing, such that the flow impacts the to-be-irradiated surface head-on; this level of agitation in the flow removes oxygen bubbles from the sample surface, which would otherwise cause pitting. Reducing the stirring bead frequency to eliminate the vortex results in insufficient removal of oxygen bubbles from the sample surface, thus producing a highly pitted, cloudy surface finish. A schematic of the electropolishing assembly is shown in Figure 4.3. Following electropolishing, samples are immediately submerged in acetone, then methanol, to remove residual acid. Finally, the samples are cleaned ultrasonically in pure ethyl alcohol, then stored in plastic vials, until the time of irradiation.

4.2 Proton Irradiations

This section covers the experimental setup and techniques utilized in the proton irradiations. Alloy samples have been irradiated with 2.0 MeV protons at the Michigan Ion Beam Laboratory using a General Ionex Tandetron accelerator. Numerous aspects contribute to a successful proton irradiation, including a specialized irradiation setup and stage design, calculation of displacement damage, aperture systems, beam scanning systems, temperature measurement, experiment monitoring, and subsequent activity measurements to ensure irradiation uniformity. Each of these aspects shall be discussed in this section. There are, however, a few deviations from the procedures described in Sections 4.2.1-4.2.6 for the 700°C irradiation. Irradiating a metallic specimen at such a high temperature presents unique challenges, and requires a slightly different experimental setup than for the irradiations performed at ≤600°C. Therefore, the final subsection here, Section 4.2.7, will describe the differing methodology for the 700°C irradiation.

4.2.1 Irradiation Setup

Irradiations are performed under high vacuum conditions. The entire accelerator beam line is maintained at pressures less than 10^{-7} torr. Because the irradiations are performed at elevated temperatures between 300°C and 700°C, a slow heat-up to the irradiation temperature is conducted, so as to maintain high vacuum pressures throughout the outgassing process.

Samples are mounted onto an irradiation stage, which is attached to, but electrically isolated from, the accelerator beam line. Two stages, both of the same design, are used in the proton irradiation experiments. One stage, made of copper, is used for irradiations up to 500°C; it is not operated at higher temperatures because the brazing used in manufacturing the stage has a melting temperature near 650°C. A second stage, then, made of nickel, is used for irradiations at temperatures above 500°C. The temperatures of the stage and samples are monitored with a 2D infrared thermal pyrometer and maintained with a combination of an electrical resistance heater and air cooling loop, as shown schematically in Figure 4.4, which is a view from above the chamber and beam line, showing the irradiation stage, heater in back, and relative position of the pyrometer. The details of the irradiation stage, temperature control, and pyrometer components, shall be discussed in the following paragraphs.

Assembling the irradiation stage consists of several steps. First, a stainless steel shim is placed on top of the copper or nickel stage. Centered on the shim is an opening, either 10 or 18 mm wide, and 10 mm tall, within which indium is filled. The shim is 0.65 mm thick, but since indium expands upon melting, a 0.60 mm thick layer of indium placed in the shim sufficiently fills the entire shim upon melting. The shim is manufactured specifically to fit tightly atop the stage, to prevent leakage of indium, once it is melted at the irradiation temperature. Samples are then placed on top of the shim and centered over the indium. The two different sizes of shim openings allow for different irradiation areas. Indium, once melted, provides excellent thermal conductivity between the Cu/Ni stage and samples, and thus the sample area being irradiated should correspond with the size of the shim opening. If only a few samples are to be irradiated, the 10 mm x 10 mm shim can be used, whereas the 18 mm x 10 mm shim can accommodate twelve 1.5 mm wide samples. The typical sample arrangement consists of TEM bar samples side-by-side, bookended by two guide bars. The proton beam will overlap onto the guide bars, which will ensure a full, uniform irradiation dose across all of the TEM bars.

The samples and guide bars are held in place with hold-down bars, which are shown schematically in Figure 4.5. As seen in Figure 4.5 (a), the hold-down bars have a triangular cross-section, and are so designed to minimize the amount of thermal reflection onto the samples during irradiation. The hold-down bars fit tightly over the samples, shim, and stage, and are secured to the stage with four set screws, seen in Figure 4.5(b). This setup ensures good thermal contact between the samples, indium, and stage. Next, thermocouples are spot-welded onto certain samples to aid in proper temperature measurement; the thermocouples will be described in greater detail in Section 4.2.5. Lastly, a tantalum aperture assembly is mounted above the stage using isolating ceramic standoffs adjacent to the stage; this system will be further discussed in Section 4.2.4. A detailed schematic of the irradiation stage assembly, as described in the preceding two paragraphs, is shown in Figure 4.6. A photo of a loaded stage is shown in Figure 4.7.

Temperature control of the irradiation stage is achieved by a combination of approaches. A Watlow FIREROD® resistance heater cartridge is inserted into the back of the copper or nickel block, which forms the base of the stage. This heater cartridge is 1 cm in diameter, 4 cm long, and has a maximum operating temperature of 760°C. With a maximum wattage of 300 W, this heater can alone provide up to ~600°C on the samples. Cooling lines run through the copper and nickel blocks, and serve to remove heat from the stage during irradiation. Because of the excellent thermal contact between the stage and samples, due to the liquid indium interface, the thermal control and temperature stability during the irradiation are maximized. Indium melts at 156°C, and is thus in its liquid state throughout the duration of the irradiations. Following the irradiation, the solidified indium is removed from the copper or nickel stage, in preparation for the next experiment that will utilize the stage.

4.2.2 Displacement Damage

Displacement damage of the incident 2.0 MeV protons is calculated with the Stopping and Range of Ions in Matter (SRIM) 2006™ program [81]. The SRIM result is given as the number of displacements produced per unit length per ion (displacements/Å-ion), and is calculated as a function of depth into the irradiated material. For this thesis, the SRIM calculations were selected to be detailed calculations (as opposed to the "quick" mode, which simply uses the Kinchin-Pease approximation) with full damage cascades using a total of 1,000,000 incident ions. A large number of incident ions is chosen to improve counting statistics, providing a more accurate and smooth damage profile.

The SRIM code requires definition of the displacement energy of each specie of atom present in the material. As recommended by ASTM E 521-89 [82], for metals and alloys, a displacement energy of 15 eV was used for Si, 60 eV for Mo, and 40 eV for all other species present in the alloys (e.g. Fe, Cr, Ni, W, V, Mn). SRIM calculates, for 2.0 MeV protons perpendicularly incident on HT9, a fairly uniform damage profile between 5 μm and 15 μm into the specimen, with peak damage occurring at a depth of 19 μm. This result is shown in Figure 4.8.

Because the damage profile generated by energetic protons is not entirely uniform, however, it is critical that one defines a specific depth at which all dose measurements and analyses will be performed. This depth is chosen to be at a distance of 50% of the depth of the damage peak, or 9.5 μm from the irradiated surface. This depth is selected because it is sufficiently removed from both surface effects and damage peak effects. Furthermore, its location on a relative flat portion of the damage profile is conducive to post-irradiation TEM sample preparation. At 9.5 μm from the surface, the damage rate calculated by SRIM is 7.58 x 10^{-5} displacements/Å-ion.

4.2.3 Irradiation Dose Calculation

The irradiation dose is directly related to the current of the proton beam incident on the irradiation stage. Thus, the beam current must be monitored closely throughout the irradiation to ensure an appropriate dose is delivered to the samples. Beam current is measured by collecting the total charge incident upon the stage, using a wire connected from the exterior of the stage chamber to a monitoring computer. This technique for measuring beam current is made possible because the stage and stage chamber are electrically connected to one another, but electrically isolated from the rest of the beam line by a ceramic isolator (see Figure 4.4). The aperture is also electrically isolated from the stage by its ceramic standoffs (see Figure 4.6(a)), so proton beam current incident upon the aperture passes to a feed-through connector before being passed to the monitoring computer.

The monitoring computer integrates the current and arbitrarily assigns one "count" for every μC of charge collected, or 10^6 counts/C. The number of counts recorded, then, is used to determine the irradiation dose, according to the following equation:

$$\frac{counts}{dpa} = \frac{N\left(\frac{at}{cm^3}\right)\cdot q\left(\frac{C}{ion}\right)\cdot Area\left(cm^2\right)\cdot\left(\frac{counts}{C}\right)}{R_D\left(\frac{displacements}{angstrom\cdot ion}\right)}, \qquad (4.1)$$

where N is the atomic density, q is the charge per incident ion, R_D is the displacement rate from SRIM, and the *Area* is the irradiation area, which is conveniently equivalent to the area inside the aperture. In the experiments presented here, the irradiation area is either 1.0 cm^2 or 1.8 cm^2, as defined by the aperture used, and corresponding with the area of the shim opening used, as discussed previously in Section 4.2.1. The atomic density is assumed constant for all alloys, 8.34 x 10^{22} atoms/cm^3. Because a proton carries a single unit charge, the value of q is 1.6 x 10^{-19} C/p^+. And as discussed in the previous section, the displacement rate from SRIM, R_D, is 7.58 x 10^{-5} displacements/Å-ion. Working through Equation 4.1, for 2.0 MeV protons the required number of counts/dpa is 3.31 million for a 1.8 cm^2 irradiation area, or 1.84 million for a 1.0 cm^2 irradiation area.

4.2.4 Apertures and Beam Scanning

An aperture system, attached but electrically isolated from the irradiation stage, ensures proper beam alignment on the samples. The aperture is comprised of four tantalum plates, each one electrically isolated from the others, and the entire assembly electrically isolated from the stage with ceramic standoffs. This arrangement is shown schematically in Figure 4.9. A rectangular hole between the tantalum plates allows for the proton beam to pass through onto the samples. The distance between the tantalum plates is 10 mm vertically and either 10 mm or 18 mm horizontally. The two different horizontal spans correspond with the two different shims used, discussed in Section 4.2.1, allowing for a larger or smaller irradiation area, depending on the number of samples one wishes to irradiate. Each tantalum piece is individually connected with a wire to a feed-through, which passes charge collected on each aperture piece to a monitoring computer. Just as the monitoring computer calculates the proton beam current on the stage by equating one count to one μC of charge collected, so is the beam current incident on each aperture piece determined.

Prior to irradiation, the aperture must be aligned to the samples, to prevent the aperture from shadowing portions of the samples. The alignment is performed on the laboratory benchtop, with the irradiation stage set on its side, just as it will be oriented on the accelerator beam line. A laser pen is positioned approximately 20 feet away from, and oriented perpendicular to, the irradiation stage. This setup is shown in Figure 4.10. The focused laser is first centered in the hole in the center of the aperture, using purely horizontal and vertical translations to the jig on which the laser is mounted. The laser beam is then is diffused using a thin sheet of plastic to mimic the scanned proton beam. The aperture is then adjusted until the diffuse laser beam is centered horizontally and vertically on all of the samples, with some overlap onto the guide bars to ensure the samples receive a uniform irradiation; this beam alignment is shown schematically in Figure 4.11.

When beginning an irradiation, the focused proton beam is measured for size in a beam profile monitor. The focused proton beam has a FWHM of at most 3 mm. During irradiation, the focused proton beam is raster-scanned across the samples at a frequency of 2061 Hz in the vertical direction and 255 Hz in the horizontal direction. The duration of one scanning cycle in the vertical direction is 0.48 ms, and 3.92 ms in the horizontal direction. The ratio of these two scanning cycles is a non-integer number, which guarantees that the beam path is offset from the previous scan cycle, thus ensuring good spatial uniformity of the scanned beam area. Figure 4.12 illustrates this scanning pattern, overlaid onto the apertures. The raster-scanning allows for a small, circular focused proton beam to irradiate a larger rectangular area quite uniformly.

The raster-scanned proton beam must overlap onto all of the aperture pieces, to ensure a full, uniform irradiation is delivered to the samples, as set during the alignment step with the diffuse laser. One full beam diameter, or 3 mm, must overlap onto each aperture piece during raster-scanning. So although the irradiated area of the samples is only 10 mm x 10 mm or 18 mm x 10 mm, the scanned beam will have a total area of either 16 mm x 16 mm or 24 mm x 16 mm, respectively. A schematic of this beam overlap onto the apertures is shown in Figure 4.13. Since current is directly proportional to area, the stage:aperture current ratios, based on geometry are approximately 1:1.5 and 1:1 for the 10 mm x 10 mm and 18 mm x 10 mm apertures, respectively.

4.2.5 Thermocouples

Four of J-type thermocouples, spot-welded to different positions on the irradiation stage, are used upon initial irradiation start-up to calibrate the 2D infrared thermal pyrometer, which is then used for temperature monitoring through the duration of the irradiation. The pyrometer will be discussed in the next section, but the thermocouples will be described here.

The J-type thermocouples operate at temperatures up to 750°C, and are made of 0.005" iron and constantan wires. The two wires are insulated with ceramic beads to prevent them from shorting with one another, with other thermocouples, or with any other component of the irradiation stage. Four thermocouples provide redundancy. They are arranged onto different alloys and on different regions of the samples, to check for temperature uniformity across the stage and possible heat conduction differences between the different alloys being irradiated. The thermocouples are attached outside of the irradiated area, with the insulating ceramic beads as far outside the stage area as possible, to prevent thermal reflections. The welded thermocouples are shown in the photograph of the stage in Figure 4.7.

Thermocouples are attached to samples by a spot-weld. The iron and constantan wires are crossed at their contact with the sample; this is the point at which they are attached to the samples. A new set of thermocouples is made for each irradiation, as the irradiation can embrittle the wires and cause ultimate failure of thermocouple functionality.

Lastly, a coated probe J-type thermocouple from Omega® is inserted into a port on the back of the copper or nickel stage. This thermocouple monitors the temperature of the irradiation stage throughout the irradiation. It is useful in ensuring that the stage temperature is not becoming too low so as to freeze the liquid indium.

4.2.6 Irradiation Startup and Monitoring

Beginning the irradiation involves both thermocouple calibration and balancing of the proton beam on the apertures. During the irradiation, close monitoring of the experiment ensures well-controlled temperature and beam current. These processes will be described in this section.

Prior to sending the irradiating proton beam onto the samples, the samples are heated to the irradiation temperature using only the resistance heater. The samples are stabilized at the irradiation temperature, based on the four thermocouples. It is at this point, then, that the 2D infrared thermal pyrometer is calibrated to the thermocouple readings. An IRCON™ Stinger thermal imaging system is positioned outside of the beam line at an angle as shown in Figure 4.4. Areas of interest (AOI) are set up on the thermal image through the Stinger software. Three AOIs are created on each TEM bar sample; the AOIs are typically round, with a diameter of approximately 2-3 mm, or up to five or six pixels. As an example, a Stinger image from a 500°C, 7 dpa irradiation is shown in Figure 4.14, with eight TEM bars being irradiated and three AOIs on each sample. Each AOI has a user-assigned emissivity, which correlates to the temperature reading of that AOI. Once the samples are stabilized at the irradiation temperature, the AOI emissivities are adjusted such that the AOI temperatures match the thermocouple readings.

Because the proton beam adds 100-150°C of heat to the samples, the samples are cooled following AOI emissivity calibration but preceding beam-on. Once the beam is sent to the samples, the temperature is maintained at the target irradiation temperature ±10°C, by making adjustments to the resistance heater and air cooling. The current is also balanced on each of the four aperture pieces, such that the two horizontal aperture pieces receive approximately the same current and the two vertical aperture pieces receive approximately the same current. The current is balanced using a beam steerer, which controls the horizontal and vertical position of the beam. The scanned area of the beam is also set to ensure that the ratio of the stage:aperture current ratio is consistent with the values calculated in Section 4.2.4. The scanned area is set with the beam scanner, which can increase or decrease the horizontal and vertical amplitudes of the scanned area.

Both temperature and current are monitored through the duration of the irradiation. The monitoring computers record each AOI temperature once every 20 seconds, during which time 60 measurements are collected on each AOI, then averaged to determine the recorded value for that particular AOI. Stage and aperture currents, and back and spot-welded thermocouple temperatures are recorded every minute. Data acquisition is performed using the Labview™ program.

The high-frequency data acquisition ensures good temperature control and current uniformity throughout the irradiation. If any of the AOI temperatures drift outside of the acceptable ±10°C range about the target temperature, audible alarms sound. The heater voltage and air cooling loop pressure are then adjusted to bring the AOIs back into the acceptable temperature range. The heater provides fine adjustments to the AOI temperatures, which take several minutes to set in, while the air cooling loop pressure provide a coarse, rapid response. Similarly, an alarm sounds if the proton beam shifts such that the apertures begin to receive unbalanced amounts of current. The beam is returned to its proper dimensions and balanced on all of the aperture pieces by making adjustments with the steerer and scanner system.

4.2.7 700°C Irradiation

The 700°C irradiation for this thesis represents the first >600°C proton irradiation of metallic specimens ever performed at the Michigan Ion Beam Laboratory. Being the first of its kind, it poses some unique challenges, which require deviation from the typical proton irradiation methodology presented in Section 4.2.1-4.2.6. In particular, issues unique to the 700°C irradiation are: (1) inability to use liquid indium as thermal contact medium between samples and stage, and (2) difficulty heating samples to 700°C for emissivity calibration. Each of these issues will be addressed in this section.

Indium is typically used to provide efficient and even heat transfer between the irradiated sample and the stage. The effectiveness of liquid indium is manifest in the excellent temperature control (±10°C) normally observed in the proton irradiations.

However, at temperatures as high as 700°C, the vapor pressure of indium [83] inhibits its use as a heat transfer medium. An alternative method, which utilizes pyrolitic graphite for heat transfer, is investigated.

The new irradiation stage configuration will be described here, and is illustrated in Figure 4.15. The Ni stage is mechanically polished with SiC paper, working through the grits from 320 to 4000, to achieve a very smooth surface. A single layer of 0.1 mm high thermal conductivity pyrolitic graphite sheet (PGS), is cut to dimensions of 18 mm x 20 mm, and placed directly atop the polished Ni stage. A single plate specimen of T91, with dimensions 15 mm x 20 mm x 2 mm, is then placed atop the PGS. The standard hold-down bars are secured on top of the T91 specimen, applying compression to the PGS. The PGS is a highly oriented graphite polymer film and is very flexible, which allows it to form or pack into the surface roughness of the specimen surface and stage surface, mimicking the “wetting” effect of liquid indium.

Prior to irradiating, however, the evenness of the heat transfer of the PGS is tested. The irradiation area will be 10 mm x 10 mm, centered on the specimen, as shaded in Figure 4.15. It is critical that the PGS provide even heat transfer at least in the 10 mm x 10 mm irradiation region. Eight thermocouples are spot-welded onto the 10 mm x 10 mm region in the arrangement shown in Figure 4.16. The stage is then placed under vacuum and heated to 690°C (more on this temperature later), where seven of the eight thermocouples read within a 5°C spread, as shown in Figure 4.17. This result suggests that the PGS can provide even heat transfer across the 10 mm x 10 mm irradiation region. Note that the spot weld of the thermocouples, number 4 from Figure 4.16, came undone during the heat-up process, and thus its reading is not shown in Figure 4.17.

For the actual irradiation, a new sample, without the weld spots from the eight thermocouples, is used. On this new sample, four thermocouples are welded, as in the standard irradiations (see Section 4.2.5). However, these four thermocouples are welded at the four corners of the 10 mm x 10 mm irradiation area centered on the sample. This is done because the testing (as described in the preceding paragraph) confirmed evenness of heat transfer only in the 10 mm x 10 mm irradiation region.

The second challenge for the 700°C irradiation is heating the sample to the irradiation temperature for pre-irradiation calibration of emissivities (the purpose and procedure for which is described in Section 4.2.6). The heater used for the lower-temperature irradiations is capable of heating the sample to only ~600°C. A more powerful heater, a Watlow FIREROD® cartridge heater 1 cm in diameter and 3.5 cm long, with a maximum power output of 400 W, is used. This heater, however, has a maximum operating temperature of 760°C, which is exceeded as the sample reaches ~690°C. Without a more powerful heater to use, the emissivities of the 700°C experiment must be calibrated at 690°C.

Emissivities are calibrated throughout the duration of the heatup, to determine the temperature dependence of the emissivity. Emissivity is temperature-dependent because the 2D infrared thermal pyrometer image can be distorted by reflections of warmer regions onto colder regions, especially as the overall temperature of the system increases. During heatup, the emissivity is calibrated approximately every 50°C, and a linear temperature dependence is observed above ~400°C, as shown in Figure 4.18. Nine AOIs, each circular in shape with diameter 2-3 mm, are arranged onto the T91 plate, all within the 10 mm x 10 mm irradiation region. The spread in the emissivity values amongst the nine AOIs is typical, and is largely attributed to the angle between the thermal pyrometer and the plane of the sample (this can be seen in Figure 4.4). It is clear from Figure 4.18, however, that small changes in emissivity can lead to relatively large changes in the temperature reading. To obtain the most accurate emissivity values for 700°C, it is assumed that the linear trend illustrated in Figure 4.18 persists above 690°C, and this linear trend is then extrapolated to 700°C. The measured and extrapolated emissivities are given in Table 4.6.

Aside from the issues discussed in this section, the 700°C irradiation proceeds much like the lower-temperature irradiations. It will be shown in the results in Chapter 5 that the temperature control and dose rate of the 700°C irradiation is comparable to those of lower-temperature irradiations.

4.3 Post-Irradiation Examination and Specimen Preparation

Following proton irradiation, a radioactivity measurement is performed to ensure safe handling of the samples and to confirm a uniform irradiation across all samples. The irradiated TEM bars are then cut into TEM samples. The procedures for both of these techniques will be discussed in this section.

4.3.1 Radioactivity and Beta Counting

Proton irradiation induces small amounts of radioactivity in metallic samples as the incident protons undergo (p^+, n) nuclear reactions with elements in the samples. Since the incident protons have energies of 2.0 MeV, the nuclear reactions must all have threshold energies below 2.0 MeV. A large number of isotopes are produced. Although many of the isotopes are non-radioactive or are not of radiological concern because of their extremely short or extremely long half-lives, an assessment of the residual activity must nevertheless be performed. Coincidentally, these activity measurements can also be used to assess whether all samples receive a uniform irradiation.

Three reactions are of importance when irradiation with 2.0 MeV protons. These reactions begin with parent isotopes of Cr-53, Mn-55, and Fe-57, and all yield daughter isotopes which release radioactivity by beta decay [84]. Table 4.3 lists these three isotopes, their reaction energy thresholds and cross sections, their daughter nuclei, and the half-lives.

Within a few days of completing the irradiation, beta activity is counted in a simple 2π scintillation detector. One at a time, each irradiated sample is placed irradiated face-up in the sample tray, and its activity counted for 15 minutes. The resulting beta counts are normalized to irradiated area and to Fe content. For obvious reasons, a sample with a larger irradiation area will produce a greater number of beta counts than a sample with a smaller irradiation area. With regard to Fe content, recall from Table 4.3 that Fe is one of the isotopes of greatest radiological concern. Since Fe is present in such high concentrations in F-M alloys (~90 at% for all alloys being studied in this thesis), the contribution of Fe to the activity measurements will be quite significant. Since the alloys studied are all of the F-M type, with relatively similar concentrations of all other elements, their beta counts can reasonably be normalized by Fe concentration to allow for cross-alloy comparisons of activity. Ultimately, the normalized beta activity measurements can be compared across all of the samples on a single irradiation stage, to ensure a uniform irradiation dose has been delivered to all samples.

4.3.2 TEM Sample Preparation

The magnetic properties of the F-M alloys involved in this study pose a unique challenge for TEM investigation. Magnetic materials easily distort the TEM electron beam, making it difficult to align the microscope, obtain a focused image free of drift, and most importantly, to perform STEM line scans to measure RIS. A practical solution to the magnetism problem is to minimize the volume of the magnetic material. So instead of traditional 3 mm diameter TEM discs, the F-M alloys are cut into 1.5 mm x 1.5 mm squares, then mounted onto a 3 mm outer diameter gold ring, so that they will fit into a TEM sample holder.

The irradiated TEM bars are first mechanically thinned from the back (unirradiated) surface, to 200-400 μm using Struers® SiC paper. Next, a diamond wafering blade is used to cut the irradiated area of the bar into 1.5 mm x 1.5 mm squares. The entire front surface area of the resultant 200-400 μm-thick square foils is the irradiated surface of the sample, as shown in Figure 4.19. These square-shaped foils are then mechanically thinned from their unirradiated side to ~80-100 μm, using 2400 grit and 4000 grit Struers® SiC paper. The thin square foils are mounted with M-Bond onto a 100 μm thick gold ring, with an outer diameter of 3 mm and an inner diameter of 0.8 mm. The irradiated face of the square foil faces up, while the unirradiated face is bonded to the ring. The M-Bond is cured overnight at ~80°C to avoid annealing out any irradiation-induced damage. Finally, the sample is jet electropolished to perforation. This TEM disc arrangement is shown schematically in Figure 4.20.

Jet electropolishing of the TEM discs is performed at temperatures below -40°C in a solution of 5% perchloric acid, 15% 2-butoxyethanol (also known as ethylene glycol monobutyl ether), and 80% methanol, using a South Bay Technologies single-sided jet electropolisher. First, the discs are thinned from the irradiated face for approximately 10 seconds. Then, the discs are thinned to perforation from the unirradiated face. Jet electropolishing on the irradiated surface is intended to remove 9.5 μm to reach the analysis depth as discussed previously in Section 4.2.2.

4.4 Radiation-Induced Segregation Measurements

The objective of this thesis concerns the behavior of RIS in F-M alloys. Measuring RIS is a difficult task, and historically, numerous techniques have been utilized, including Mössbauer spectroscopy, atomic emission spectroscopy, TEM-EDX, and STEM-EDX. More recently, APT has been utilized for RIS measurements. However, for this thesis, RIS measurements are performed with STEM-EDX. This is a common, well-understood, high-resolution technique for composition measurement, particularly for spatially-dependent composition measurement, such as across a grain boundary. A number of analytical methods contribute to a sound RIS measurement. Error analysis, for example, is critical to ensuring a statistically-significant measurement is collected. Understanding the minimum detectable concentration of each element in the STEM-EDX instrumentation, is also important to this study. In this section, the experimental instrumentation, techniques, and analysis methods of STEM-EDX RIS measurements will be described in detail.

4.4.1 STEM Instrumentation

Grain boundary RIS measurements are performed on a Philips CM200 field emission gun (FEG) TEM/STEM, equipped with an EDX detector, at Oak Ridge National Laboratory. The microscope can be focused to optimize the electron probe at a diameter ≤1.4 nm, full width at one-tenth maximum, using an accelerating voltage of 200 kV and beam current on the order of 1 nA. A Philips Compustage double-tilt specimen holder is used at room temperature, which minimizes specimen drift during analysis.

This specimen holder has a tilt range of ±30° in each of two perpendicular directions, which provides sufficient range to bring grain boundaries into edge-on alignment with the electron probe. Prior to insertion into the microscope, both the specimen and the Compustage are plasma-cleaned in a South Bay Technologies PC150 unit. This 10 minute cleaning in an argon plasma removes hydrocarbons from the TEM specimen surface, which minimizes the amount of contamination that the focused electron probe will introduce onto the sample during the extended dwell times required for RIS measurements.

The Digital Micrograph software package is used for STEM image acquisition and EDX microchemistry data collection and analysis. The user may acquire a STEM image of the aligned grain boundary, on which can be designated the line on which RIS measurements shall be collected, a sub-region of the image to be used in drift correction, and the dwell position for the electron probe once the RIS line scan has completed. An example STEM image from Digital Micrograph, with all of these designations, is shown in Figure 4.21. The Digital Micrograph software allows for seamless interface between image acquisition and the setup of microchemical analysis.

4.4.2 STEM-EDX RIS Measurements

Selecting a grain boundary for RIS measurement can be a complicated process. While it is desired that only PAGBs be studied for RIS, since they tend to be higher-angle boundaries, they are often covered with large carbides, which make it difficult to locate a clear PAGB segment free of carbides. RIS measurements are never performed within 20 nm of a carbide, as the carbide tends to influence measurements out to such a distance. When selecting a PAGB to study, one must also consider the contrast of the grains adjacent to the boundary. It is desirable to choose a boundary having low-contrasting grains on both sides, which suggest that the grains are not strongly diffracting. A strongly diffracting grain increases beam broadening effects through the thickness of the specimen, which greatly reduces the resolution of the RIS profile. Selecting a boundary located in a thin region of the specimen also minimizes beam broadening effects

Once an ideal PAGB segment is located, the segment is aligned edge-on to the incident electron probe. Edge-on alignment optimizes the measurement, such that the result is most accurate and maximally exposes the boundary to the electron beam. An edge-on boundary minimizes the amount of matrix being sampled in the excitation volume of a given point along the line scan, thus minimizing the magnitude to which the matrix is diluting the grain boundary concentrations; this effect is shown schematically in Figure 4.22. Because of the magnetic nature of the F-M specimens, the maximum magnification at which RIS measurements can be performed is typically 200,000x.

RIS is measured by taking an EDX scan along a line perpendicularly traversing a grain boundary. In these scans, the electron probe dwells on a point for a user-specified time; an EDX spectrum is acquired from that point. The electron then moves to the next point along the line, typically 1.5 nm from the previous point, and an EDX spectrum is obtained there. This process is repeated over the entire length of the user-specified line. Multiple line scans are collected at each irradiation condition. Each line scan is typically comprised of 41 points spaced 1.5 nm apart, totaling a 60 nm scan length across a PAGB. In addition, two line scans are collected in the matrix for each specimen, the results of which are used in determining *k*-factors, which shall be discussed in the next section. These matrix line scans are each comprised of 61 points, 3 nm apart, for a total length of 180 nm; such a large number of measurements minimizes the effect of local composition variations. All measurements are performed with drift correction.

4.4.3 Amount of Data Needed

It is necessary to establish the amount of data that need be collected. There are several components to collecting RIS data. First, the number of counts to be collected at a single point in a single line scan must be established; this value will correspond with the inherent counting error of the measurement. Second, the number of line scans that will be collected on a given alloy, at a given irradiation condition, must also be determined. These ideas are the topic of this section.

Each line scan is an independent measurement, as opposed to one of a repeated number of measurements in a sample size. Therefore, the only way to reduce the noise and uncertainty of a measurement is to increase the number of counts collected. Noisiness and uncertainty are directly related to the count time and the number of counts collected. Since Cr is the primary element of interest, the number of counts in the Cr peak in the EDS spectrum is considered of greatest importance. A confidence interval of 95% can be achieved on each point along the line scan with a 2% counting error (counting error being the square root of the number of counts) by collecting 10,000 counts in the Cr peak; the counting error can be reduced to 1% when collecting 35,000 counts in the Cr peak.

All line scans collected for this thesis aim for a minimum of 20,000 counts in the Cr peak. This goal number of counts is selected as a result of two competing concerns: that of minimizing the error, and that of collecting data within a safe and reasonable amount of time. The counting error from 20,000 counts is only 1.4%, and this number of counts can typically be achieved with a dwell time of 2.5-3.5 minutes on each point along the scan. Although 35,000 counts would slightly improve the counting error, it would typically require close to 5 minutes of dwell time on each point, which is long enough that one risks burning a hole through the TEM foil with the electron beam. Therefore, targeting 20,000 counts in the Cr peak offers sufficient error reduction without risking damage to the TEM foil. Dwell time is dependent upon specimen tilt, specimen thickness, and lattice orientation relative to the electron beam. Prior to beginning a line scan, a count rate can be obtained from a spot in the matrix (i.e. away from the grain boundary), from which the required dwell time on each point can then be calculated. Note that the dwell time may differ for each boundary studied, even for boundaries on the same TEM specimen.

The error reduction approach for the line scans relies only on the number of counts in the Cr peak. Indeed, this thesis is concerned with RIS of other elements, such as Si, Ni, Cu, and Fe. Because the bulk Fe concentration is much greater than the bulk Cr concentration, the line scans will always collect far more Fe counts than Cr counts, and thus the Fe counting error will be smaller than that of Cr. On the other hand, the bulk Si, Ni, and Cu concentrations are so low that collecting even 10,000 counts in these peaks would take an unreasonable amount of time and would surely damage the TEM foil.

At a given irradiation condition, RIS is measured across at least two PAGBs, to ensure consistency from boundary to boundary. On each PAGB, at least two line scans should be collected, to ensure consistency along a given boundary. In total, at least five line scans should be collected for a given condition. These line scans provide insight into the grain boundary concentrations of elements, as well as the shape of the RIS profiles. However, since the typical 41-point line scans can take a very long time to acquire, one can take short scans of only say 5 points, at the PAGB. These short scans can be collected quite rapidly, and will provide a larger volume of PAGB concentration data.

4.4.4 Composition Determination

Microchemical data collected by EDX and Digital Micrograph are given in units of counts under an x-ray emission peak at a given energy. These counts must be converted to wt% to facilitate the determination of RIS magnitudes. The elements analyzed for RIS are: Si, V, Cr, Fe, Ni, Cu, and W. The x-ray energies of each of these elements, which are selected for use in this study, are shown in Table 4.4. The chosen x-ray energies are selected primarily for their high intensities; in some cases, two energy peaks are so close to one another (e.g. Si $K_{\alpha 1}$ at 1.740 keV and Si $K_{\alpha 2}$ at 1.739 keV), that they are inseparable, and must both be integrated. Also shown in Table 4.4 are the energy windows bounding each of the x-ray energies studied; these windows are the range of energies over which the number of counts under the x-ray peak is integrated. The energy windows are utilized extremely consistently for each alloy and each irradiation condition analyzed in this study. Following peak integration, the background is subtracted, resulting in the total number of counts of that specific element. Background subtraction is performed within Digital Micrograph, and is accomplished by combining the measured continuum energy-distribution function with the detector response function to calculate a background spectrum, which is subtracted from the observed spectral distribution.

Converting counts to concentration begins with the Cliff-Lorimer equation [85], which states that the ratio of the concentrations of atom A to atom B, in the material studied, is proportional to the ratio of their measured intensities:

$$\frac{C_A}{C_B} = k_{AB} \frac{I_A}{I_B} \text{ ,} \tag{4.2}$$

where C represents the concentrations, I represents the intensities measured, and k_{AB} is the Cliff-Lorimer factor or *k*-factor for short. The k-factor is not a physical constant, but rather varies based on the microscope, STEM-EDX systems, and electron probe energy. The Cliff-Lorimer analysis can be extended for any number of alloying elements, and is extended here for an example A-B-C ternary alloy:

$$\frac{C_A}{C_C} = k_{AC} \frac{I_A}{I_C} \text{ ,} \tag{4.3}$$

$$\frac{C_B}{C_C} = k_{BC} \frac{I_B}{I_C} \text{ ,} \tag{4.4}$$

Then, assuming no other elements are present in the material:

$$C_A + C_B + C_C = 1 \text{ .} \tag{4.5}$$

The series of Equations 4.2-4.4 can be solved simultaneously. If the *k*-factors are known relative to one constituent element, then the concentrations of all elements can be calculated with ease. In this study, the *k*-factors are all calculated relative to Cr (e.g. k_{CrFe}, k_{CrNi}). The *k*-factors are determined by comparing matrix STEM-EDX measurements against the known alloy concentrations, which are listed in Table 4.1. For each matrix measurement (i.e. each point on the matrix line scan discussed in Section 4.4.2), a set of *k*-factors is generated for all constituent elements; these sets of *k*-factors are then averaged to determine the overall *k*-factors that will be applied to the Cliff-Lorimer analysis for the given alloy and irradiation condition.

4.4.5 Error Propagation

At each point along a line scan, the measured number of counts for each element has an associated error, which provides an interval of confidence in the value and suggests a range over which one might expect to find a value from a measurement conduced under identical conditions. At point *i* on the line scan, this "counting error" of element *j* is simply the square root of the number of counts, *N*, acquired under the x-ray peak of element *j*, and can be expressed as:

$$\sigma_{i,j} = \sqrt{N_{i,j}} \ . \qquad (4.6)$$

This counting error propagates through the Cliff-Lorimer equations, as the number of counts is converted into a concentration. When operations are performed on a value having an associated error, that error is propagated through the operation following the addition/subtraction rule, product and quotient rule, power rule, exponential rule, and logarithmic rule of error propagation.

4.4.6 Detectability Limits

The alloys irradiated in this work contain very small concentrations (<<0.1 wt%) of a number of minor alloying elements and impurities. While the RIS behavior of these elements may provide insight into the bulk RIS behavior of, say, Cr, it may not be feasible to measure RIS of all of these elements. Every STEM-EDX system has a detectability limit for each element, that is, a minimum concentration of that particular element that must be present in order for it to be detectable by the STEM-EDX system. Detectability is dependent on a number of factors, including the configuration of the EDX relative to the microscope, the STEM probe current, and the resolution of the EDX. The detectability limits for the CM200 STEM-EDX system used in this work will be determined in this section.

Ideally, detectability limits for an instrument are calculated with the use of standards for each element of interest, along with another measureable element in the alloy (such as Fe, say), to determine the ratio of their intensities on the instrument. From the intensity ratio, the minimum signal required for detection of the element can be calculated. Unfortunately, standards to make these measurements are unavailable, so an alternative approach must be used.

Here, detectability limits will be determined with respect to the known concentration of Fe, since, considering the prevalence Fe in all of the alloys, it is surely a detectable element. As an example, the detectability of Ni in an Fe matrix will be computed, but the same procedure can be applied to all elements for which detectability limits are desired.

First, it is assumed that a Ni x-ray signal measuring twice the background signal is required for detection above the background noise. The Ni x-ray peak is compared to a nearby Fe x-ray peak to minimize the effect of changes in detector efficiency as a function of energy. The Ni peaks used in EDX analysis are $K_{\alpha 1}$ at 7.478 keV and $K_{\alpha 2}$ at 7.461 keV, which appear as a single peak because they are so close in energy that they cannot be separated from one another. The intensities of these two peaks are $I_{\alpha 1} = 24.0$ and $I_{\alpha 2} = 12.2$. Similarly, the Fe peaks used in the analysis are $K_{\alpha 1}$ at 6.404 keV and $K_{\alpha 2}$ at 6.391 keV (again appearing as a single peak since they are so close in energy), with intensities $I_{\alpha 1} = 20.2$ and $I_{\alpha 2} = 10.2$, respectively.

The fluorescence yield for x-rays from electron interactions is approximated by the following equation [86]:

$$\omega = \frac{Z^4}{a + Z^4} \ , \qquad (4.7)$$

where ω is the fluorescence yield, Z the atomic number, and a is a constant with the value of approximately 10^6 for K-shell electrons. From the Table of Isotopes [87], fluorescence yields for the K-shell electrons of Ni and Fe are $\omega_K^{Ni} = 0.421$ and $\omega_K^{Fe} = 0.355$, respectively.

The minimum detectable Ni concentration is that which produces the same normalized signal as Fe. The product of the element concentration, the intensity of the x-rays, and the x-ray fluorescence provides the total signal obtained by EDX analysis. This total signal must then be normalized by the K-shell x-ray intensity (which is the basis of the fluorescence yield) and the number of counts under the peak. This is expressed in the following equation:

$$\frac{\omega_K^{Ni}}{C_{used}^{Ni}} \cdot \frac{I_{used}^{Ni}}{I_{K_\alpha}^{Ni}} \cdot X_{wt\%}^{Ni} = \frac{\omega_K^{Fe}}{C_{used}^{Fe}} \cdot \frac{I_{used}^{Fe}}{I_{K_\alpha}^{Fe}} \cdot X_{wt\%}^{Fe} \ , \qquad (4.8)$$

where $\omega_K^{Ni,Fe}$ is the fluorescence yield of Ni or Fe K-shell electrons, $C_{used}^{Ni,Fe}$ is the number of counts in Ni or Fe peaks selected for use in EDX analysis, $I_{used}^{Ni,Fe}$ is the intensity of Ni or Fe peaks selected for use in EDX analysis, $I_{K_\alpha}^{Ni,Fe}$ is the intensity of the Ni or Fe K_α

peak, $X_{wt\%}^{Ni}$ is the minimum detectable Ni concentration, and $X_{wt\%}^{Fe}$ is the known Fe concentration. Rearranging, the minimum detectability is given by:

$$X_{wt\%}^{Ni} = \frac{C_{K_{\alpha 1}+K_{\alpha 1}}^{Ni}}{C_{K_{\alpha 1}+K_{\alpha 1}}^{Fe}} \cdot \frac{I_{K_\alpha}^{Ni}}{I_{used}^{Ni}} \cdot \frac{I_{used}^{Fe}}{I_{K_\alpha}^{Fe}} \cdot \frac{\omega_K^{Fe}}{\omega_K^{Ni}} \cdot X_{wt\%}^{Fe} \ . \qquad (4.9)$$

The minimum detectable concentration for every element in all alloys can be computed with just a few input variables. First, the bulk Fe concentration in each alloy is used for $X_{wt\%}^{Fe}$. The x-ray fluorescence yields and intensities are found from the Table of Isotopes [87]. A typical EDX line scan in the matrix of each alloy is used to determine the typical Fe intensity (i.e. number of counts in Fe peak) and the background counts (twice which is the minimum intensity necessary to detect other elements). The absolute values of the typical EDX Fe intensity and background counts are unimportant; rather, their relative values are important, as indicated by Equation 4.8.

Input values to Equation 4.8, along with the resulting minimum detectable concentrations of all elements in each alloy, are shown in Table 4.5; detectable elements are highlighted in yellow. When the minimum detectable concentration exceeds the bulk concentration, that element is considered detectable in the alloy. There are a few notable exceptions. Silicon, for one, has a minimum detectable concentration greater than its bulk concentration. However, the x-ray energy of Si (~1.74 keV) is very different than that of Fe (~6.4 keV); the energies should be as close as possible for accurate detectability calculations. Furthermore, RIS line scans have shown that it is possible to obtain a clear Si signal, so Si is considered to be detectable despite the predictions of Equation 4.8. On the other hand, Mo has a calculated minimum detectable concentration less than its bulk concentration, but the detectability predictions are not applicable given such dramatic x-ray energy differences between Mo (~17.4 keV) and Fe. In addition, the Mo concentration measured by EDX tends to be very noisy and difficult to distinguish above background; it is assumed that the detectability predictions are inaccurate for Mo, and thus Mo is considered undetectable in this study. The Mn x-ray energy is almost identical to the Cr L_α x-ray energies, and since the bulk Cr concentration far exceeds that of Mn, the Mn signal is almost impossible to distinguish from Cr. Thus, despite the predictions of Equation 4.8, Mn is also considered undetectable in this study.

Both Cr and Fe are detectable in all alloys; Si and Ni are detectable in all commercial alloys. Vanadium is detectable in HT9 and T91; Cu in T91 and HCM12A; and W is detectable in HCM12A only.

4.4.7 Confidence in RIS Measurements

It has been suggested that the segregated amount of the element Si may actually be several times greater than is measured by STEM/EDX techniques. An effect of this may be that the measured direction of Cr RIS is opposite the actual direction of Cr RIS, since the Cliff-Lorimer calculation forces the total concentration to sum to 100% (Equation 4.5). It is suggested that if significantly more Si is enriched at the boundary than is measured there, Cr could deplete to make way for the Si enrichment, but the Cliff-Lorimer calculation may be forcing Cr to enrich since only limited amounts of Si are detected. In this section, the measured direction of RIS will be confirmed.

This analysis will focus on the raw number of EDX counts, rather than the concentrations that have been calculated through the Cliff-Lorimer equations. The line scan T91_10dpa_400C_01-08_M_1-1-F will be used as an example throughout this analysis. At each point along this scan, the following are calculated: ratio of Cr counts to total counts, ratio of Si counts to total counts, and ratio of Fe counts to total counts. These ratios are plotted in Figure 4.23, which shows that more Si and Cr counts are collected at the grain boundary than in the matrix, and fewer Fe counts are collected at the boundary than in the matrix. These count ratios confirm that Si and Cr are enriched at the boundary, while Fe is depleted. If Cr is actually depleted at the boundary, the Cr/Total count ratio would exhibit a valley-type shape rather than a peak-type shape, because the contribution of Cr to the total number of counts collected would be smaller than it is in the matrix. Clearly, the contribution of Cr to the total number of counts collected is greater near the boundary than in the matrix, which demonstrates that Cr is indeed enriched at the grain boundary. This holds even if there are thickness variations along the line scan.

4.5 Microstructure Studies

Understanding the microstructure of the alloys of interest, and their microstructural evolution under irradiation, can aid in understanding RIS. In the forthcoming chapters of this thesis, the sink strengths based on TEM images of the microstructure, will be used to assist in modeling and analyzing RIS behaviors. Three major groups of sinks are identified in the F-M alloys: grain boundaries, precipitates, and dislocations. In this section, the sink strength calculations for each of these three major sink groups will be described, the microstructure measurements required for the sink strength calculations will be outlined, and the approach for collecting these measurements will be explained.

Grain boundaries can be classified as PAGBs, packet boundaries, or lath boundaries, all of which have the same sink strength formulation:

$$k_{gb}^{2} = \begin{cases} 6k/d, d > 10^{-3} cm \\ 24k/d, d < 10^{-3} cm \end{cases}, \qquad (4.10)$$

where d is the diameter of the grain and k is a constant that can be approximated as $k^2 \approx 10^{11}$ cm^{-2} [19]. For this thesis, all grain boundaries (i.e. PAGBs, packet boundaries, and lath boundaries) will be represented with a single sink strength. But because some lath boundaries are also packet boundaries or PAGBs, and some packet boundaries are also PAGBs, simply summing the individual sink strengths of PAGBs, packet boundaries, and lath boundaries will over-estimate the total grain boundary sink strength. Thus, the smallest grain unit, the lath, will be used to calculate the grain boundary sink strength. Determining a single value of d for a lath, however, involves an approximation, since laths tend to be elongated in shape (width << length). The mean of the average lath width and the average lath length is estimated for the value of d. A minimum of 100 laths are measured using basic bright-field TEM imaging at a magnification of 2,000x.

Precipitates studied for the sink strength analysis include only those visible in a bright-field TEM image collected at magnifications of up to 50,000x. The precipitates observed at these magnifications are largely incoherent carbides located on grain boundaries, although a few are observed within the matrix as well. Their sink strength is:

$$k_{ppt}^{2} = 4\pi r_{ppt} C_{ppt} , \qquad (4.11)$$

where r_{ppt} is the precipitate radius, and C_{ppt} is the number density [88]. A minimum of 400 precipitates (standard deviation of 5%) are measured using bright-field TEM imaging at 50,000x, in order to determine values of r_{ppt}. The number density is calculated by dividing the measured loop population by the TEM foil thickness, which is measured via electron energy loss spectroscopy (EELS).

Dislocations include both dislocation loops and dislocation lines. The sink strengths of these two features are:

$$k_{line}^2 = 2 l_{line} C_{line} \text{ , and} \tag{4.12}$$

$$k_{loop}^2 = 4 \pi r_{loop} C_{loop} \text{ ,} \tag{4.13}$$

where l_{line} is the length of a dislocation line, C_{line} is the dislocation line number density, r_{loop} is the radius of a dislocation loop, and C_{loop} is the loop number density [89]. Dislocation lines can be measured and counted using bright-field TEM imaging at a magnification of 50,000x, and the sample thickness can be measured with EELS. A minimum of 400 lines are measured, the average length of which is used for l_{line}. The line population is divided by the sample thickness to determine C_{line}.

Dislocation loops are slightly more complicated to image. Two loop types can exist in F-M alloys: cube-edge loops with <100> Burgers vector on [100] planes, and glissile edge loops with ½<111> Burgers vector on [111] planes [1]. Because the relative frequency with which the two types of loops occur is unknown, all loops must be imaged to determine an accurate value for the loop density. One of the simplest ways of viewing all loops is by looking along the <001> direction, in which the <001> loops will appear circular, the <100> and <010> loops will appear as ovals oriented perpendicular to one another, and the ½<111> loops will appear as ovals oriented at a 45° angle to the <100> and <010> loops. This configuration is illustrated in Figure 4.24. A minimum of 400 loops are imaged at a magnification of 50,000x. Their average radius is used for r_{loop}, and their population is divided by the sample thickness to determine C_{loop}.

The total sink strength of the specimen studied is the sum of all sink strengths of each sink type:

$$k_{total}^2 = k_{gb}^2 + k_{ppt}^2 + k_{line}^2 + k_{loop}^2 \text{ .} \tag{4.14}$$

Table 4.1. Chemical compositions (wt%) of the heats of alloys used in this thesis (the symbol '--' indicates the element is not present in the alloy).

Alloy / Element	**T91** [90]	**HCM12A** [91]	**HT9** [92]	**9Cr Model** [93]
Fe	89.15	84.22	84.92	90.9
Cr	8.37	10.83	11.63	9.0
Mo	0.9	0.3	1	--
Mn	0.45	0.64	0.52	--
Ni	0.21	0.39	0.5	--
V	0.216	0.19	0.3	--
Cu	0.17	1.02	0.04	--
W	--	1.89	0.52	--
Si	0.28	0.27	0.22	--
Nb	0.076	0.054	--	--
C	0.1	0.11	0.2	0.1
N	0.048	0.063	0.047	--
Al	0.022	0.001	<0.01	--
P	0.009	0.016	0.02	--
S	0.003	0.002	0.006	--

Table 4.2. Heat treatments of the heats of alloys used in this thesis.

	Austenitizing			Tempering		
Alloy	Temp. (°C)	Time (min)	Cooling	Temp. (°C)	Time (min)	Cooling
T91 [90]	1066	46	air	790	42	air
HCM12A [91]	1050	60	air	770	45	air
HT9 [92]	1040	30	air	760	60	air
9Cr Model [93]	950	60	air	750	60	air

Table 4.3. Relevant isotopes to the (p^+, n) reactions occurring in F-M alloys subject to 2.0 MeV proton irradiation, from [84].

Parent Isotope	(p^+, n) Reaction Energy Threshold (MeV)	Daughter Isotope	Half-Life	Cross Section for 2.0 MeV Protons (mbarns)
Cr-53	1.39	Mn-53	3.7×10^6 years	5
Mn-55	1.03	Fe-55	2.73 years	4.5
Fe-57	1.65	Co-57	271.8 days	0.9

Table 4.4. The x-ray emission energies used for chemical analysis of each element, along with the bounding energy window across which the number of counts in the peak was integrated.

Element	X-ray Energy (keV)	Energy Window Used
Si	$K_{\alpha 1}$ = 1.740 $K_{\alpha 2}$ = 1.739	1.675 – 1.825
V	$K_{\alpha 1}$ = 4.952 $K_{\alpha 2}$ = 4.945	4.732 – 5.172
Cr	$K_{\alpha 1}$ = 5.415 $K_{\alpha 2}$ = 5.405	5.290 – 5.546
Fe	$K_{\alpha 1}$ = 6.404 $K_{\alpha 2}$ = 6.391	6.258 – 6.549
Ni	$K_{\alpha 1}$ = 7.478 $K_{\alpha 2}$ = 7.461	7.348 – 7.608
Cu	$K_{\alpha 1}$ = 8.048 $K_{\alpha 2}$ = 8.028	7.918 – 8.178
W	$L_{\alpha 1}$ = 8.398	8.268 – 8.528

Table 4.5. Caclulation of minimum detectable concentrations (wt%) of elements in each alloy studied. X-ray fluorescences, energies, and intensities are taken from the Table of Isotopes [87]. Cells highlighted in yellow represent the detectable elements.

	Fluor.	X-rays Used & Energy (keV)	Inten-sity	HT9		T91		HCM12A		9Cr Model	
				Min. Det. (wt%)	Bulk Conc. (wt%)	Min. Det. (wt%)	Bulk Conc. (wt%)	Min. Det. (wt%)	Bulk Conc. (wt%)	Min. Det. (wt%)	Bulk Conc. (wt%)
C	0.0026	$K_{\alpha1}$=0.277	0.19	20.3	0.200	20.7	0.100	19.9	0.11	25.4	0.1
		$K_{\alpha2}$=0.277	0.09								
Si	0.050	$K_{\alpha1}$=1.740	3.300	1.0	0.22	1.0	0.28	1.0	0.27	--	
		$K_{\alpha2}$=1.739	1.64								
P	0.064	$K_{\alpha1}$=2.010	4.100	0.8	0.02	0.8	0.01	0.8	0.016	--	
		$K_{\alpha2}$=2.009	2.04								
S	0.080	$K_{\alpha1}$=2.308	5	0.6	0.01	0.7	0.00	0.6	0.002	--	
		$K_{\alpha2}$=2.307	2.49								
V	0.256	$K_{\alpha1}$=4.952	14.5	0.2	0.300	0.2	0.216	0.2	0.19	--	
		$K_{\alpha2}$=4.945	7.3								
Cr	0.288	$K_{\alpha1}$=5.415	16.4	0.2	11.63	0.2	8.37	0.2	10.83	0.2	9.0
		$K_{\alpha2}$=5.405	8.3								
Mn	0.321	$K_{\alpha1}$=5.899	18.3	0.2	0.52	0.2	0.45	0.2	0.64	--	
		$K_{\alpha2}$=5.888	9.3								
Fe	0.355	$K_{\alpha1}$=6.404	20.2	0.1	84.92	0.1	89.15	0.1	84.22	0.2	90.9
		$K_{\alpha2}$=6.391	10.2								
Ni	0.421	$K_{\alpha1}$=7.478	24	0.1	0.500	0.1	0.210	0.1	0.39	--	
		$K_{\alpha2}$=7.461	12.2								
Cu	0.454	$K_{\alpha1}$=8.048	26	0.1	0.040	0.1	0.170	0.1	1.02	--	
		$K_{\alpha2}$=8.028	13.3								
Nb	0.751	$L_{\alpha1}$=2.166	1.8	--	--	2.2	0.076	--	--	--	
		$L_{\alpha2}$=2.163	0.2								
Mo	0.767	$K_{\alpha1}$=17.479	42.6	0.1	1.000	0.1	0.900	0.1	0.3	--	
		$K_{\alpha2}$=17.374	22.4								
W	0.954	$L_{\alpha1}$=8.398	5.5	0.7	0.520	--	--	0.7	1.89	--	

Table 4.6. Measured and extrapolated emissivity values for 9 areas of interest in 700°C irradiation.

Calibration temperature (°C)	**Emissivity for AOI number**								
	1	**2**	**3**	**4**	**5**	**6**	**7**	**8**	**9**
370	0.138	0.131	0.153	0.138	0.139	0.152	0.136	0.134	0.134
424	0.14	0.132	0.154	0.141	0.141	0.152	0.139	0.136	0.136
490	0.145	0.137	0.159	0.148	0.148	0.158	0.144	0.142	0.142
535	0.150	0.142	0.164	0.154	0.154	0.163	0.146	0.148	0.148
570	0.154	0.146	0.168	0.158	0.158	0.168	0.150	0.152	0.152
585	0.155	0.147	0.169	0.160	0.160	0.170	0.152	0.154	0.153
620	0.158	0.150	0.172	0.164	0.164	0.173	0.154	0.158	0.157
656	0.162	0.154	0.176	0.168	0.168	0.177	0.157	0.162	0.161
677	0.164	0.156	0.178	0.171	0.171	0.180	0.158	0.164	0.163
690	0.165	0.157	0.179	0.172	0.172	0.181	0.159	0.166	0.165
700*	0.166	0.158	0.180	0.173	0.173	0.182	0.160	0.167	0.166

* = extrapolated, not measured

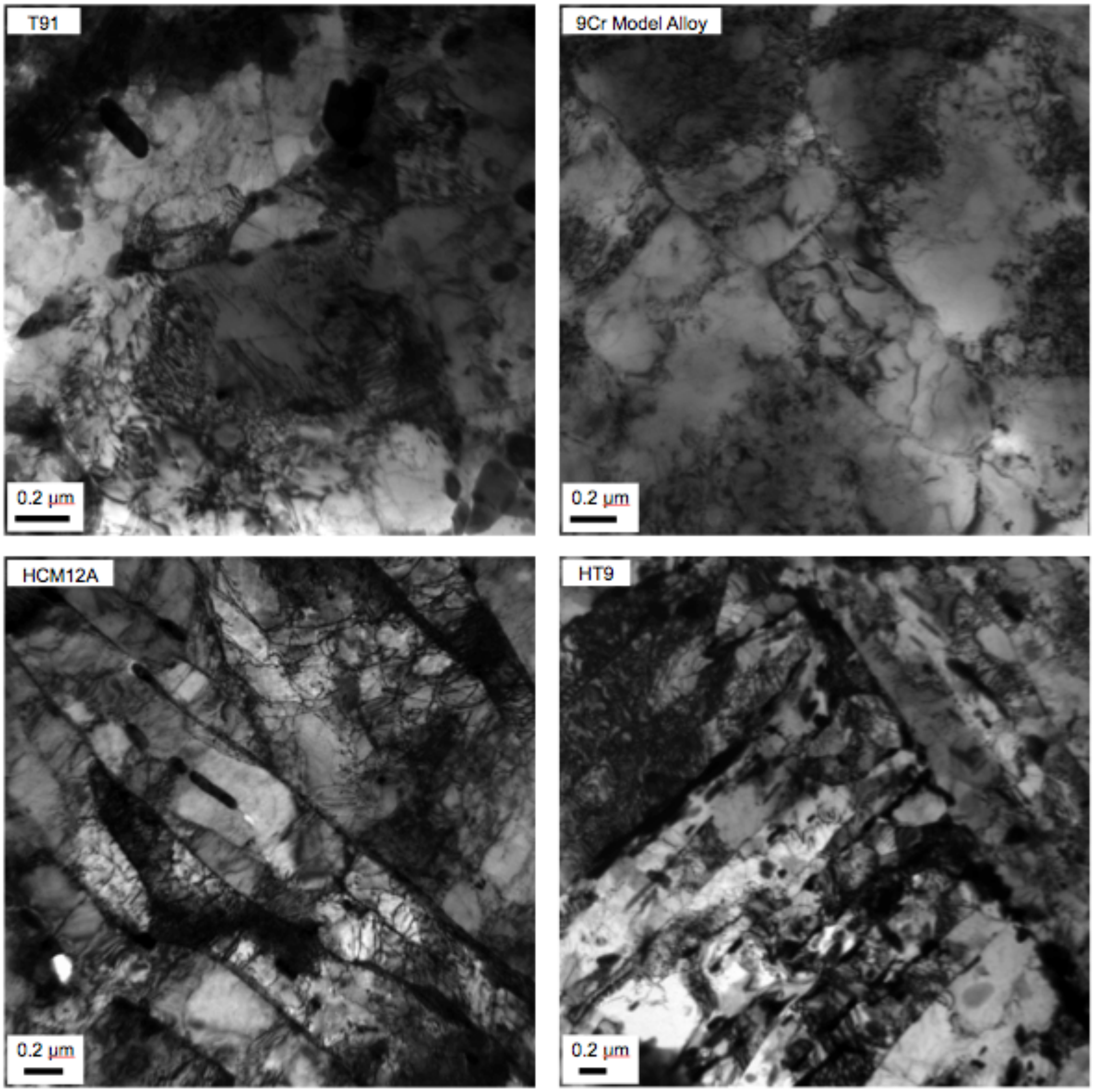

Figure 4.1. Bright field TEM images of the four alloys in this study, in their as-received conditions, showing the general microstructure, including the lath and subgrain structures, carbides, and network dislocations.

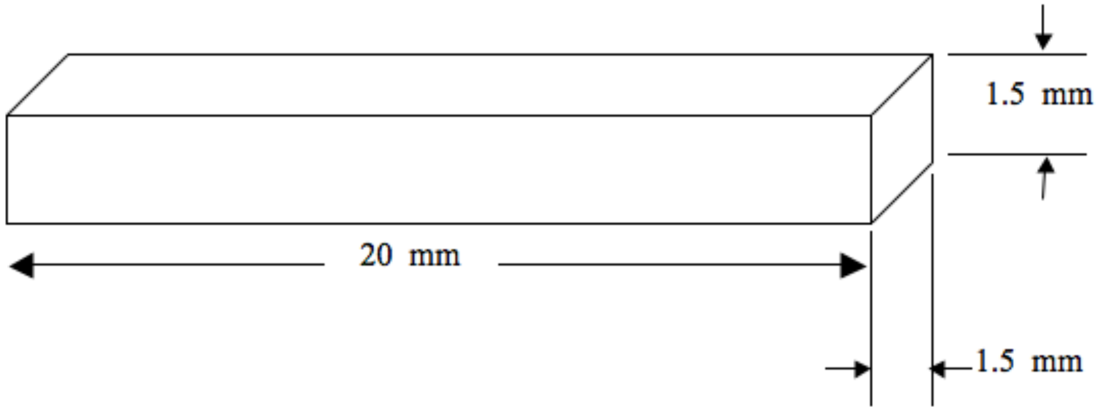

Figure 4.2. Schematic of the sample geometry following EDM. One of the 1.5 x 20 mm surfaces will be irradiated.

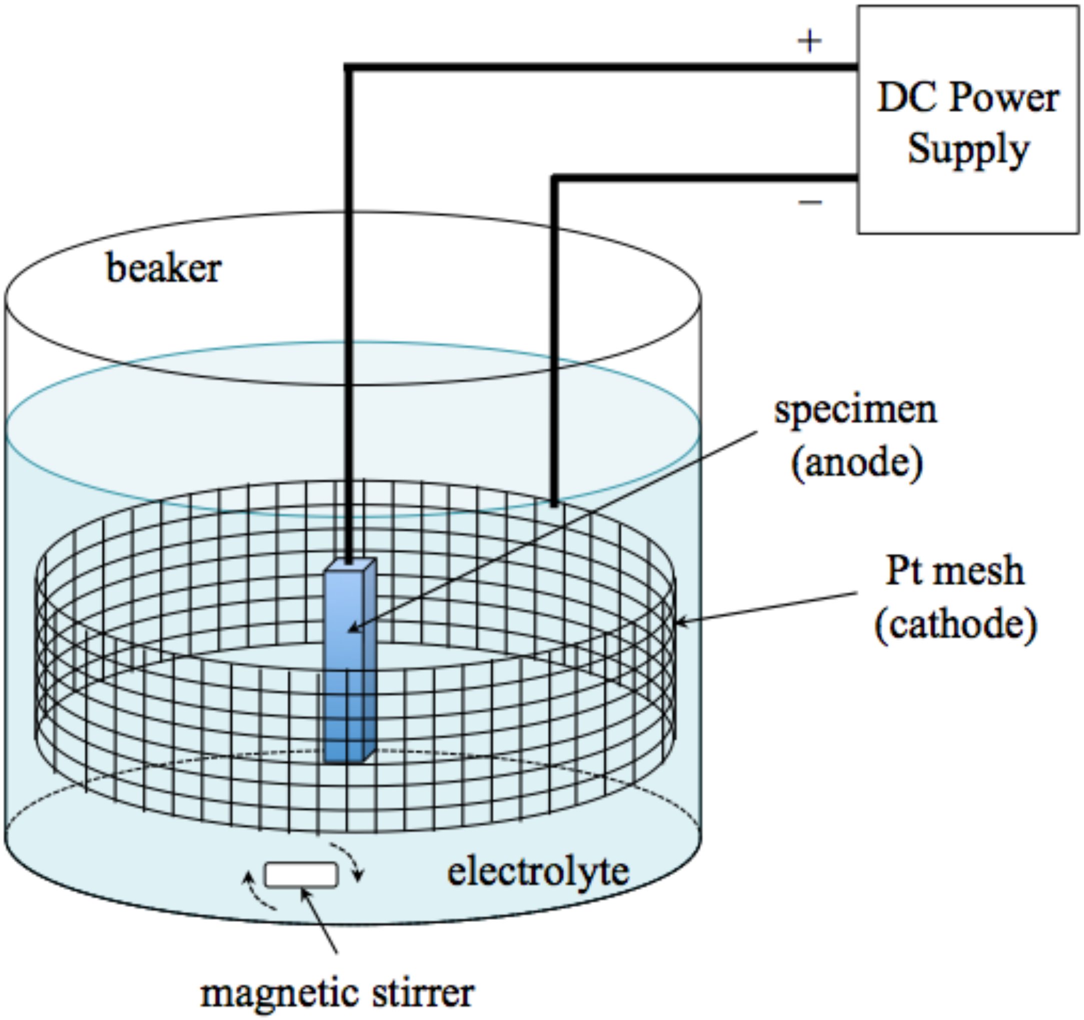

Figure 4.3. Schematic of electropolishing arrangement.

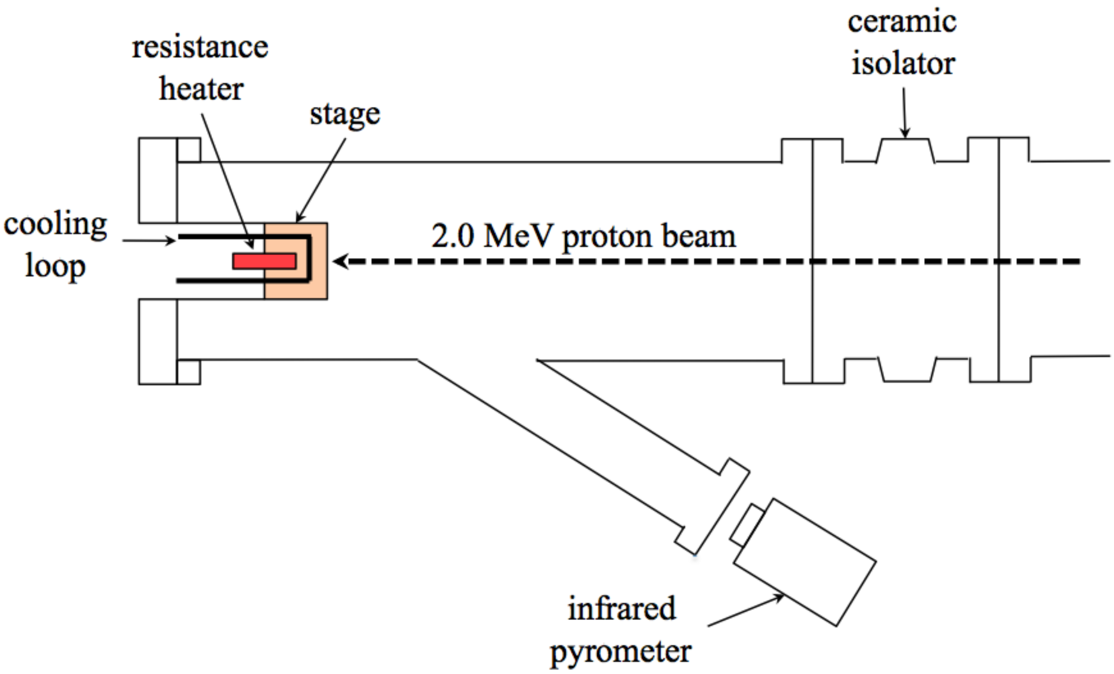

Figure 4.4. Schematic of irradiation stage and relative position of thermal pyrometer on beam line.

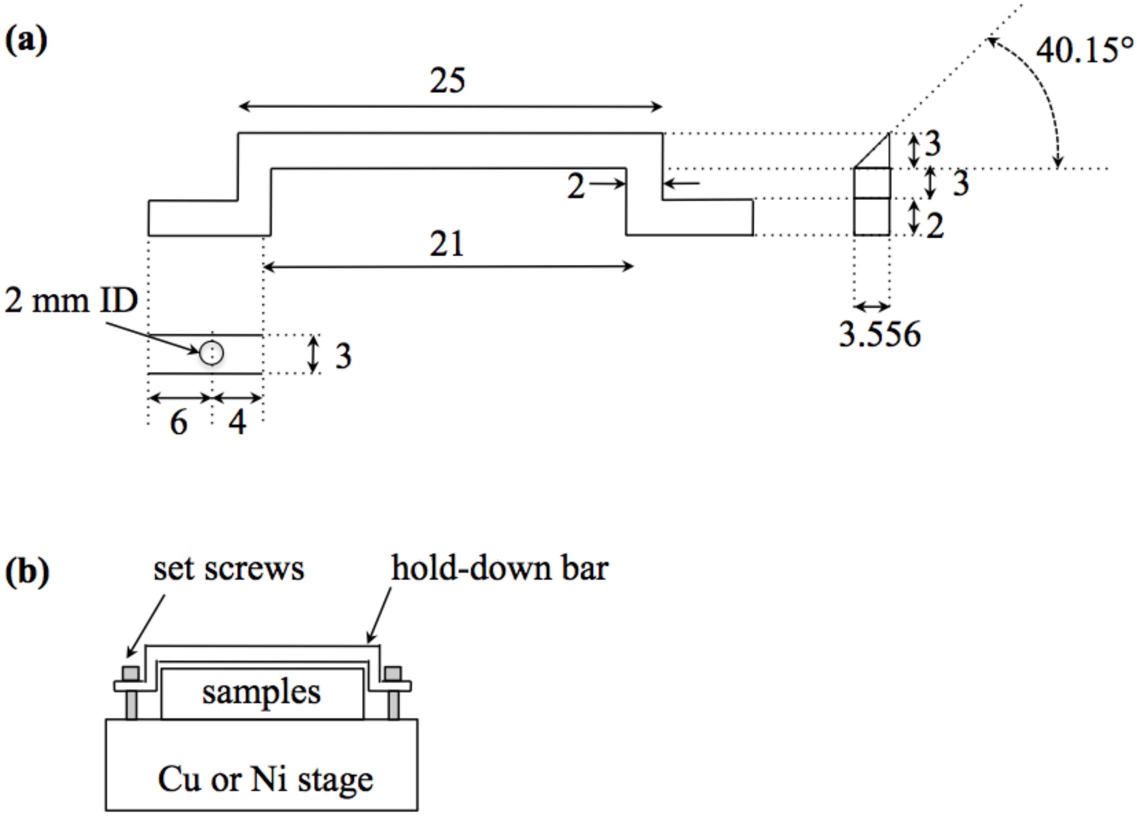

Figure 4.5. Schematic of hold-down bar (a) shape and dimensions and (b) attachment to and position on irradiation stage.

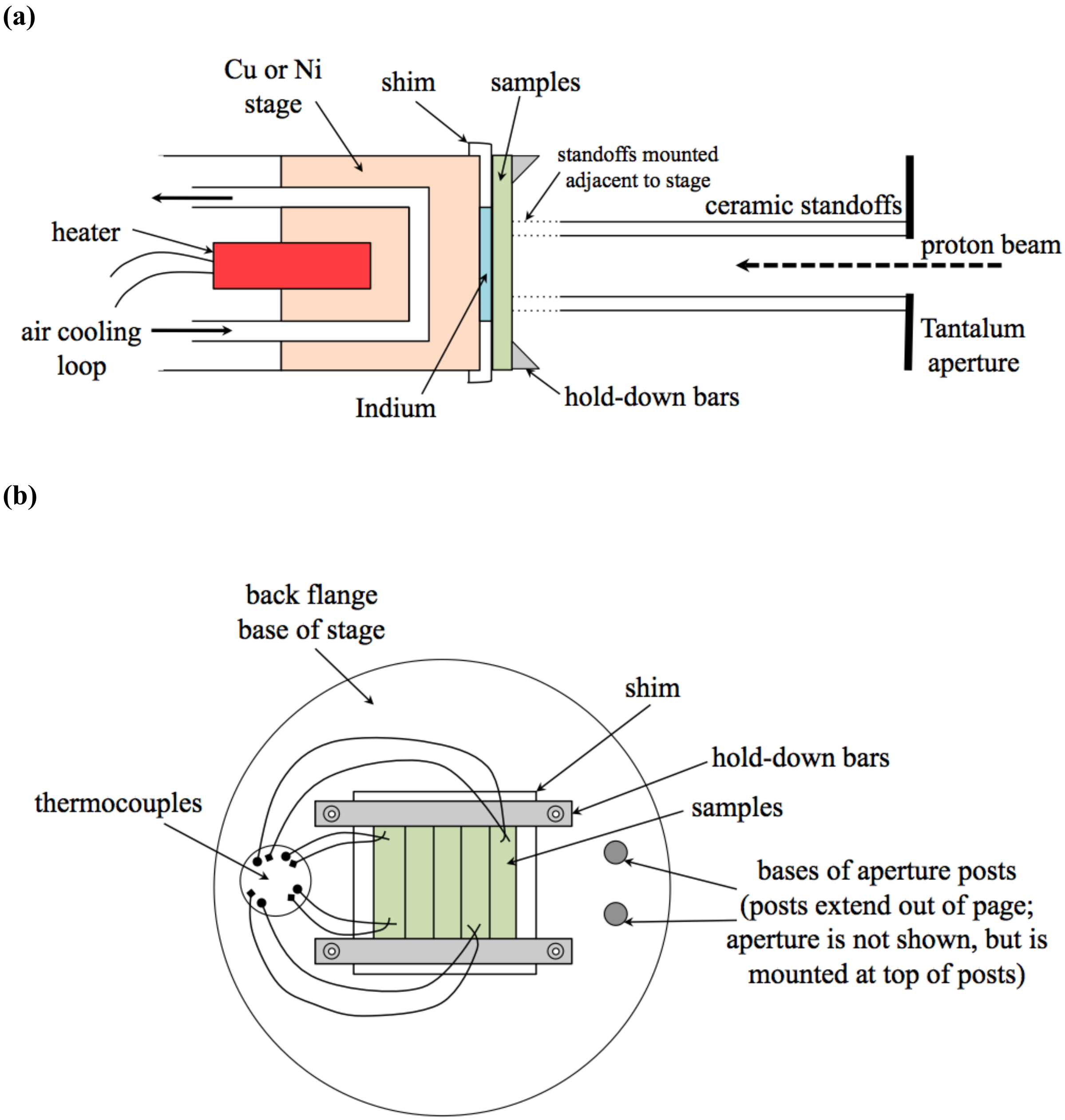

Figure 4.6. Schematic of (a) cross-section and (b) top view of assembled irradiation stage, showing heater, cooling loops, shim filled with indium, samples, hold-down bars, and aperture assembly.

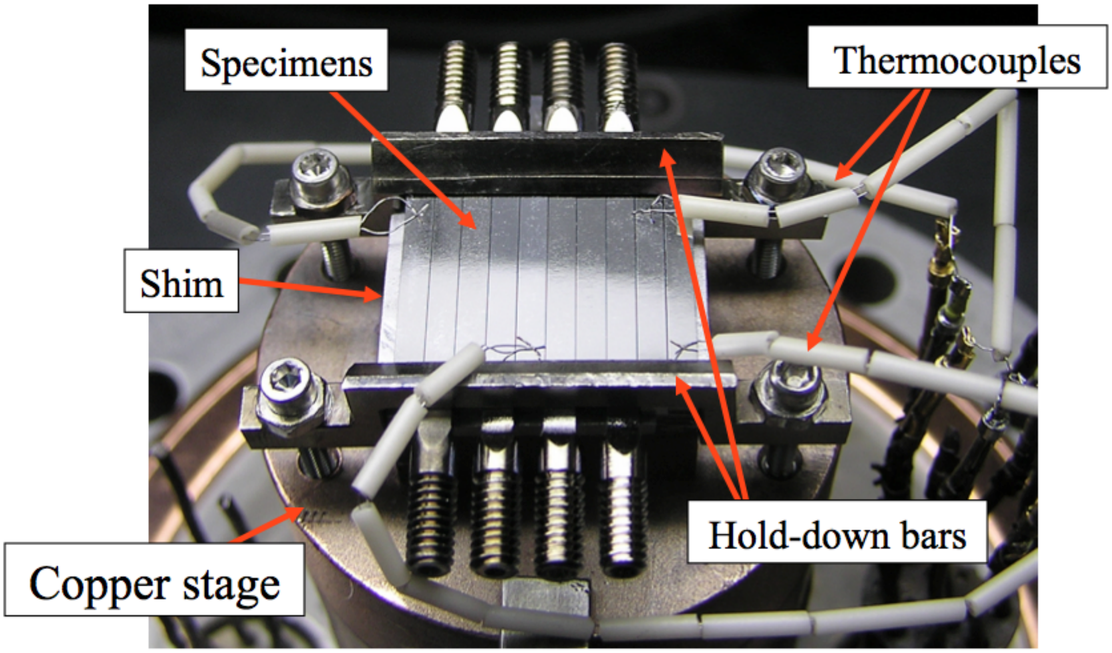

Figure 4.7. Photo of loaded stage, indicating specimens, hold-down bars, shim under specimens, and thermocouples.

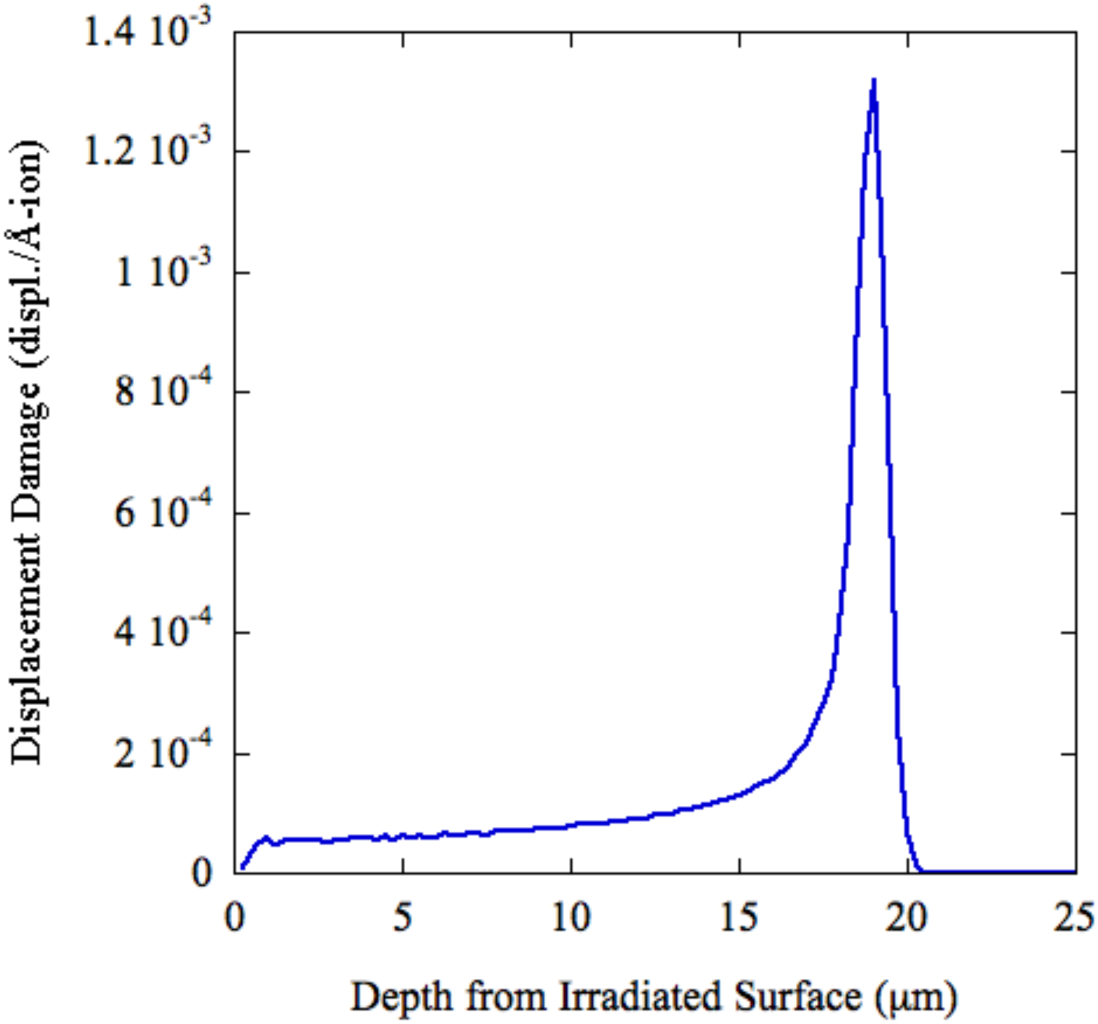

Figure 4.8. Displacement damage as a function of depth into the specimen, calculated by SRIM 2006 [81] for 2.0 MeV protons in HT9. A relatively uniform damage region is created in the range 5-15 μm, with maximum damage occurring 19 μm from the irradiated surface.

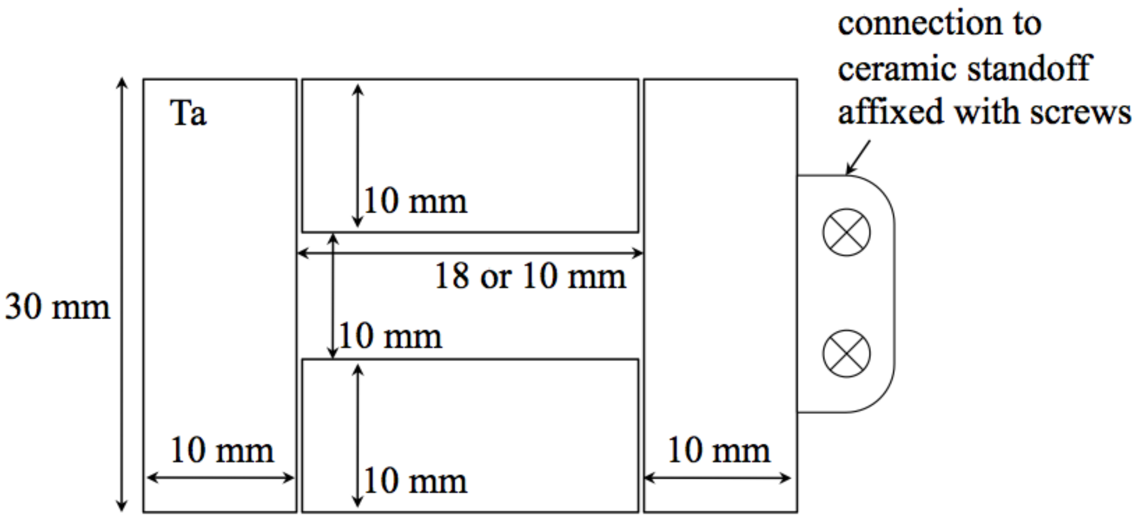

Figure 4.9. Schematic of tantalum aperture system.

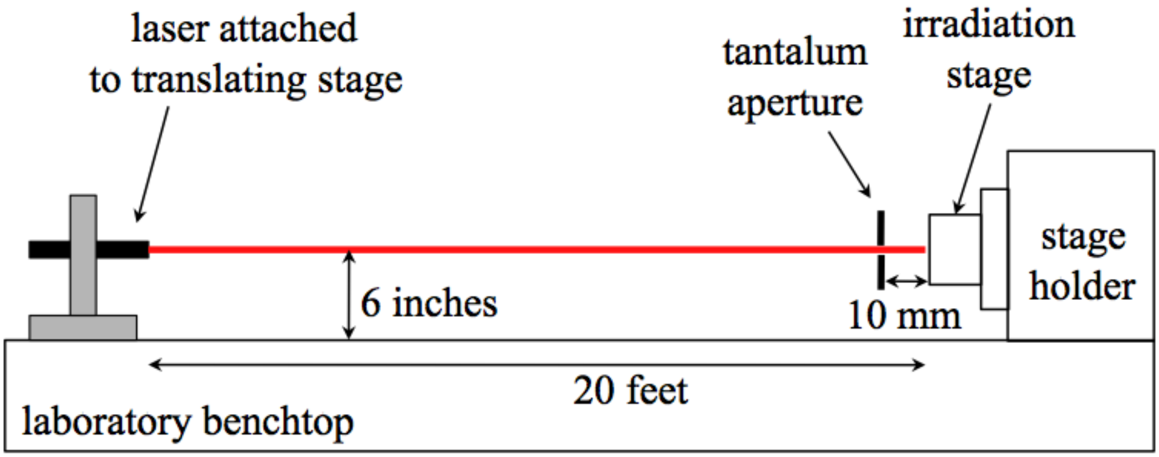

Figure 4.10. Schematic of aperture alignment step on the laboratory benchtop.

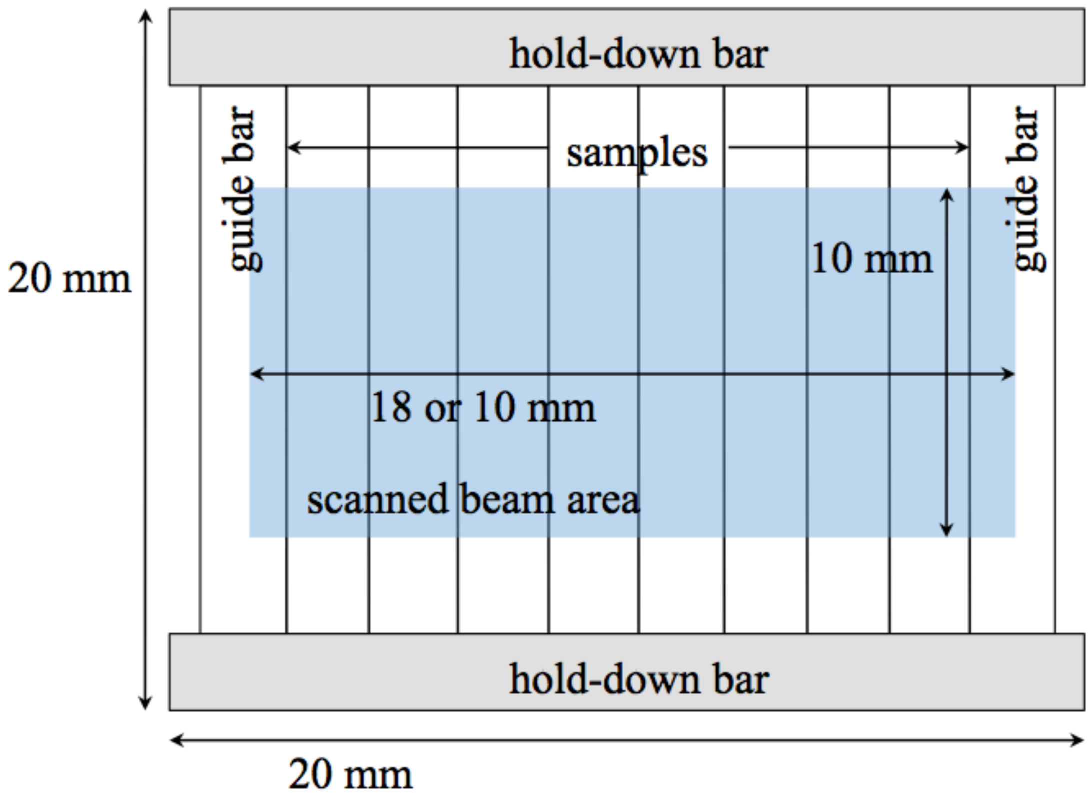

Figure 4.11. Schematic of scanned beam centered on the samples, horizontally and vertically, with some overlap onto the guide bars to ensure samples receive full irradiation.

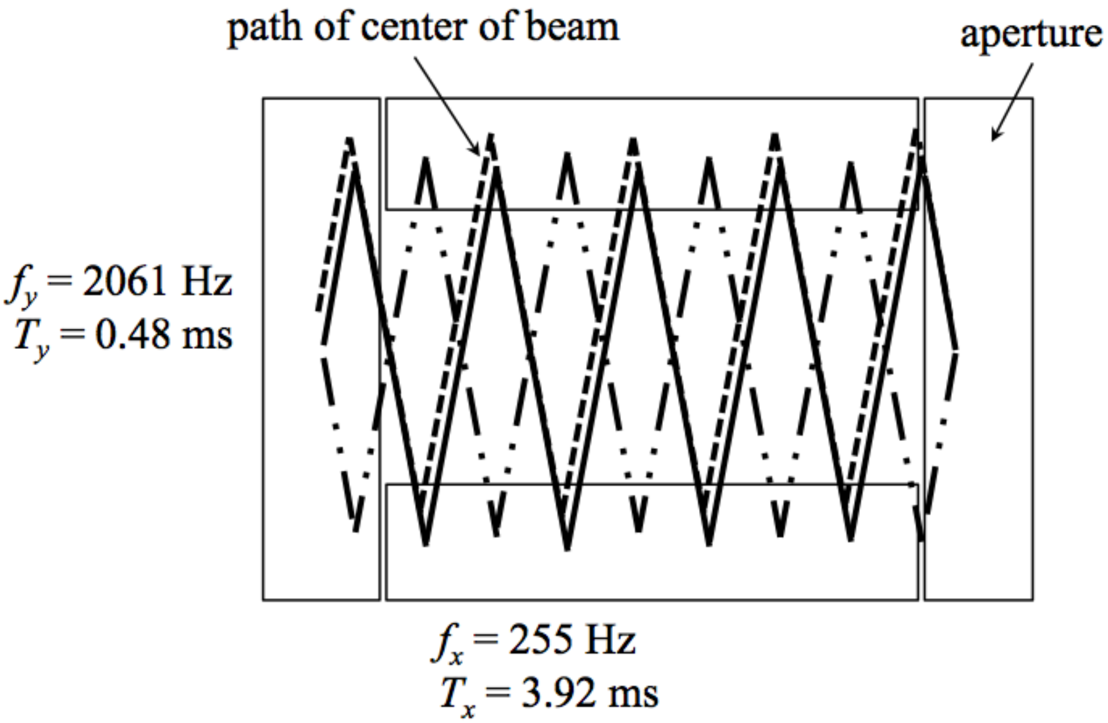

Figure 4.12. Pattern of raster-scanned proton beam during irradiations.

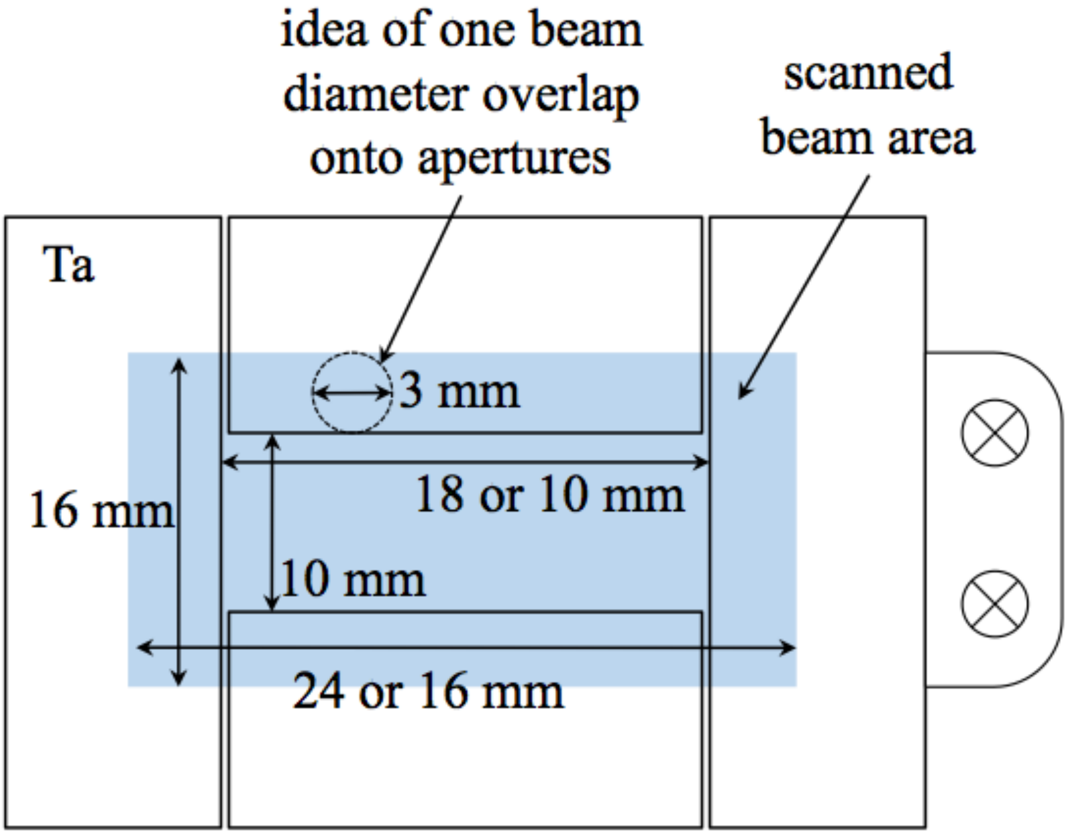

Figure 4.13. Schematic of overlap of scanned proton beam onto apertures, showing full overlap of 3 mm diameter beam onto each aperture piece.

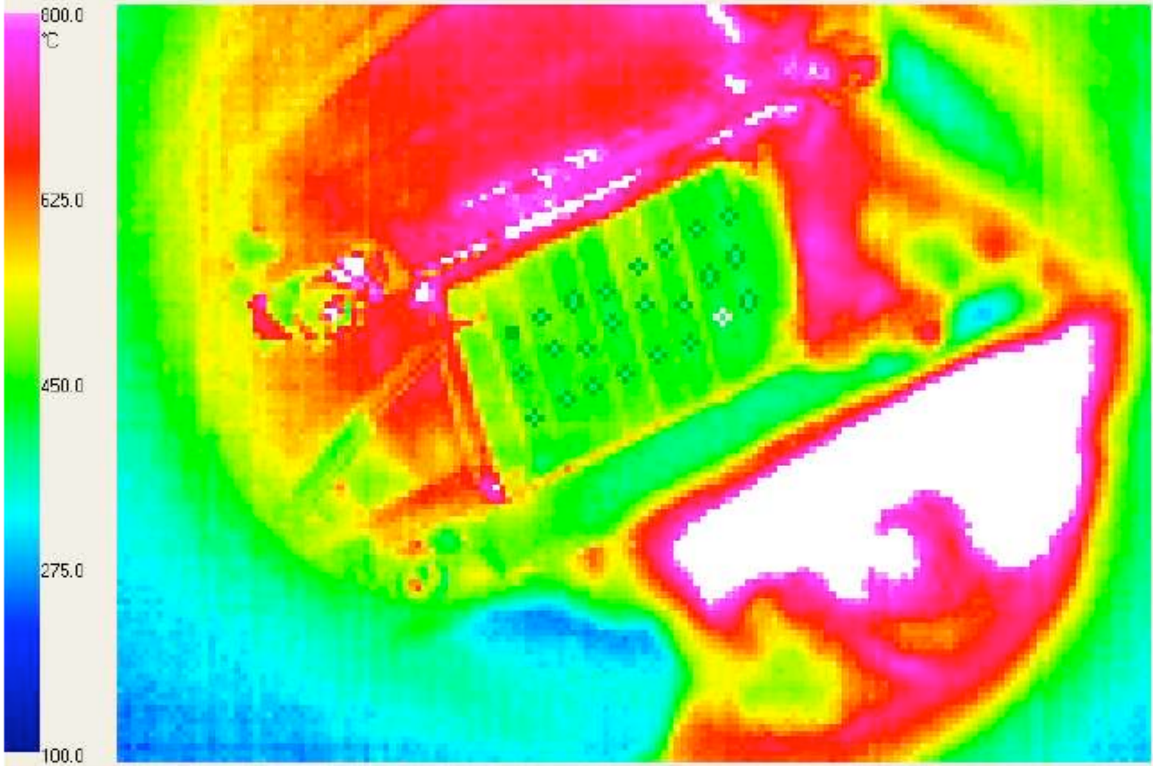

Figure 4.14. Example of 2D thermal infrared pyrometer image from a 500°C, 7 dpa proton irradiation. Eight TEM bars and two guide bars are being irradiated. Three AOIs are designated on each sample.

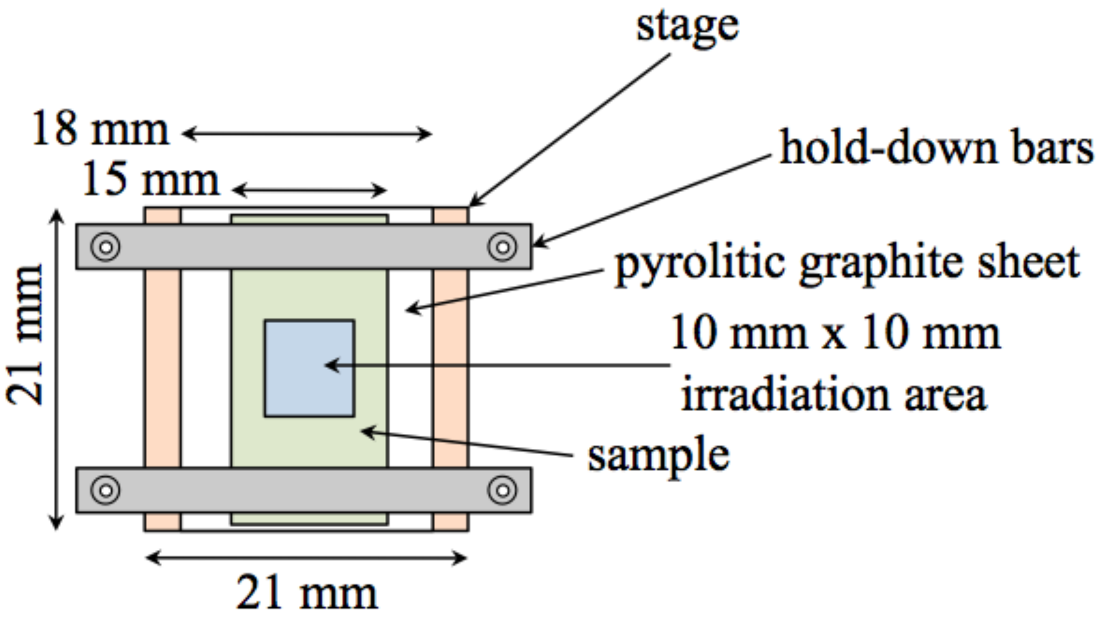

Figure 4.15. Schematic of 700°C proton irradiation stage build.

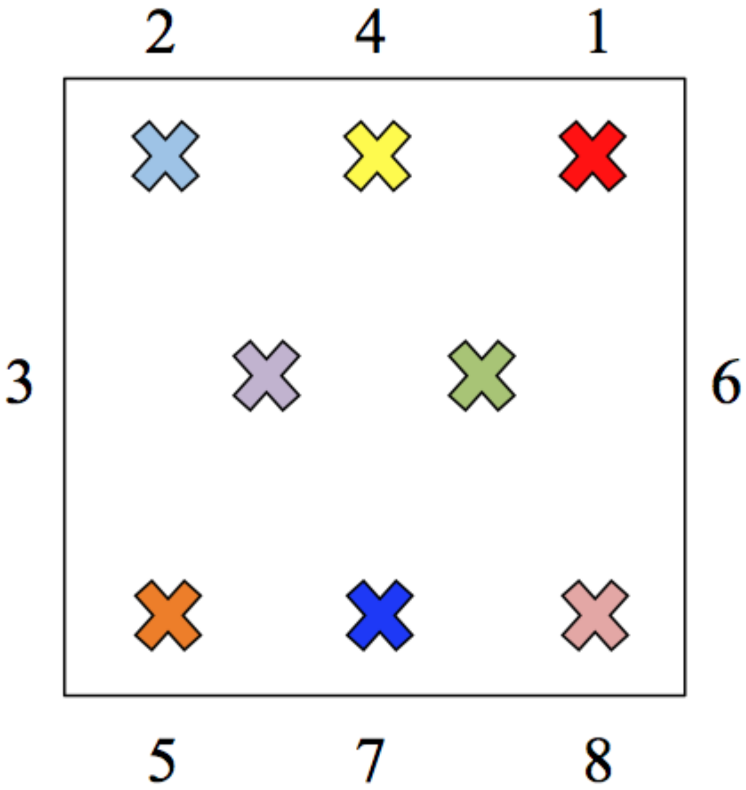

Figure 4.16. Arrangement of eight thermocouples within 10 mm x 10 mm irradiation area for 700°C irradiation testing.

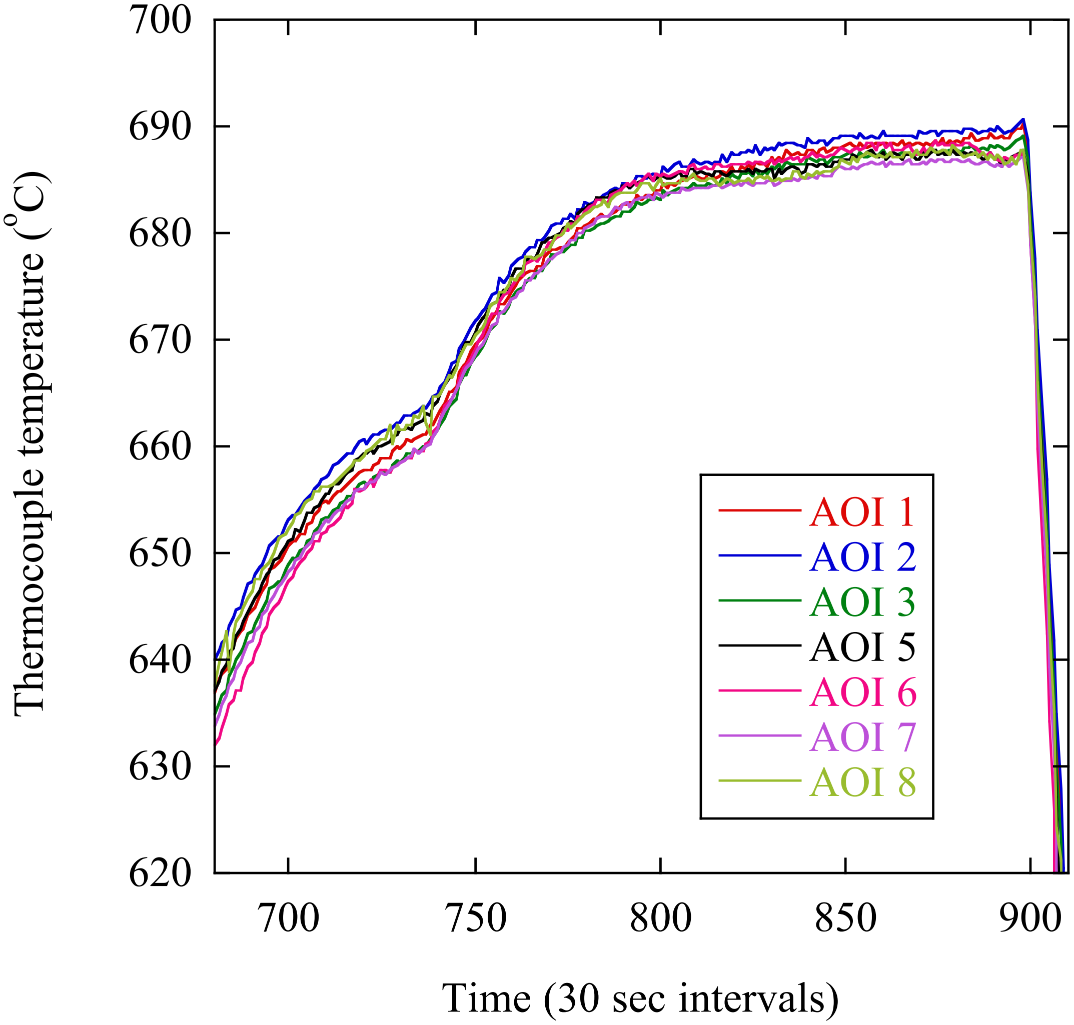

Figure 4.17. Thermocouples tracking within 5°C spread in 10 mm x 10 mm irradiation area for 700°C irradiation testing.

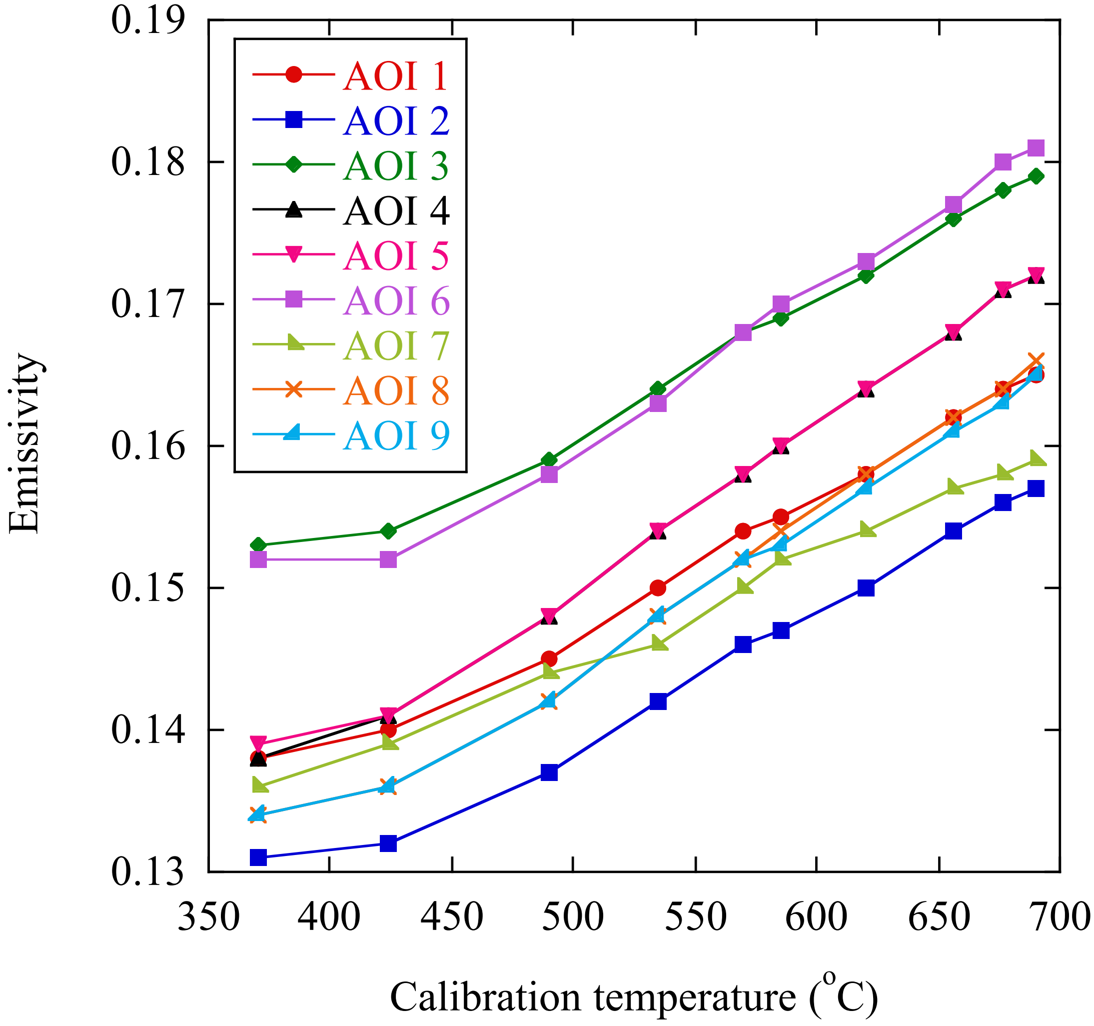

Figure 4.18. Temperature dependence of emissivity.

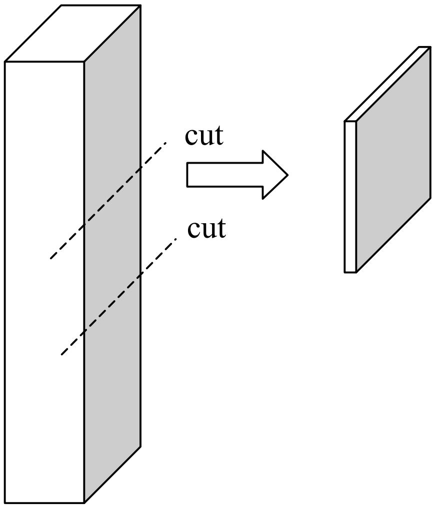

Figure 4.19. Cuts on the irradiated surface of the TEM bar create a square foil sample approximately 1.5 mm x 1.5 mm, with one surface of the foil being the irradiated face.

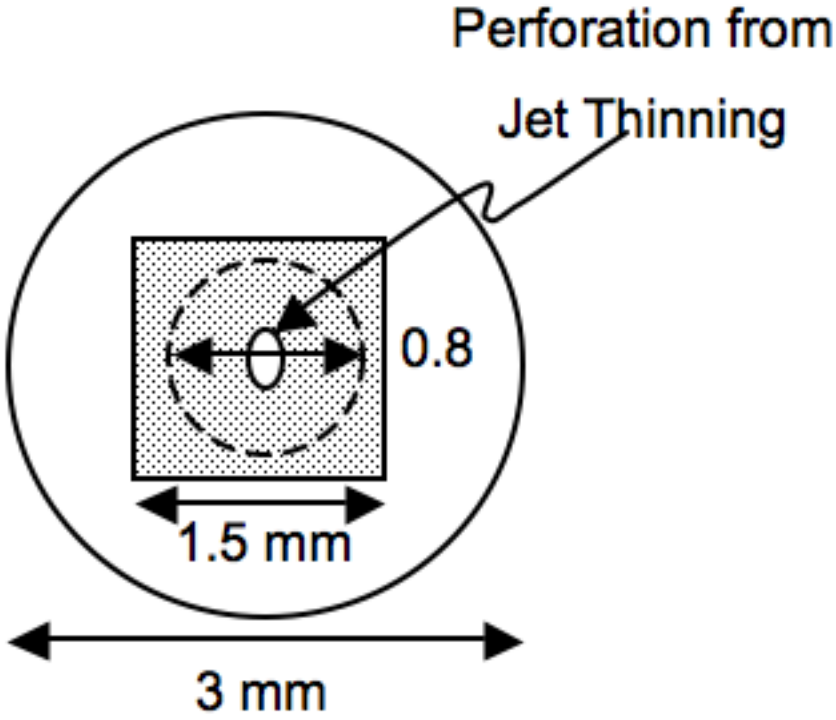

Figure 4.20. Schematic illustrating the irradiated F-M alloy TEM sample, with an irradiated specimen as the 1.5 mm square foil mounted onto a 3 mm gold ring.

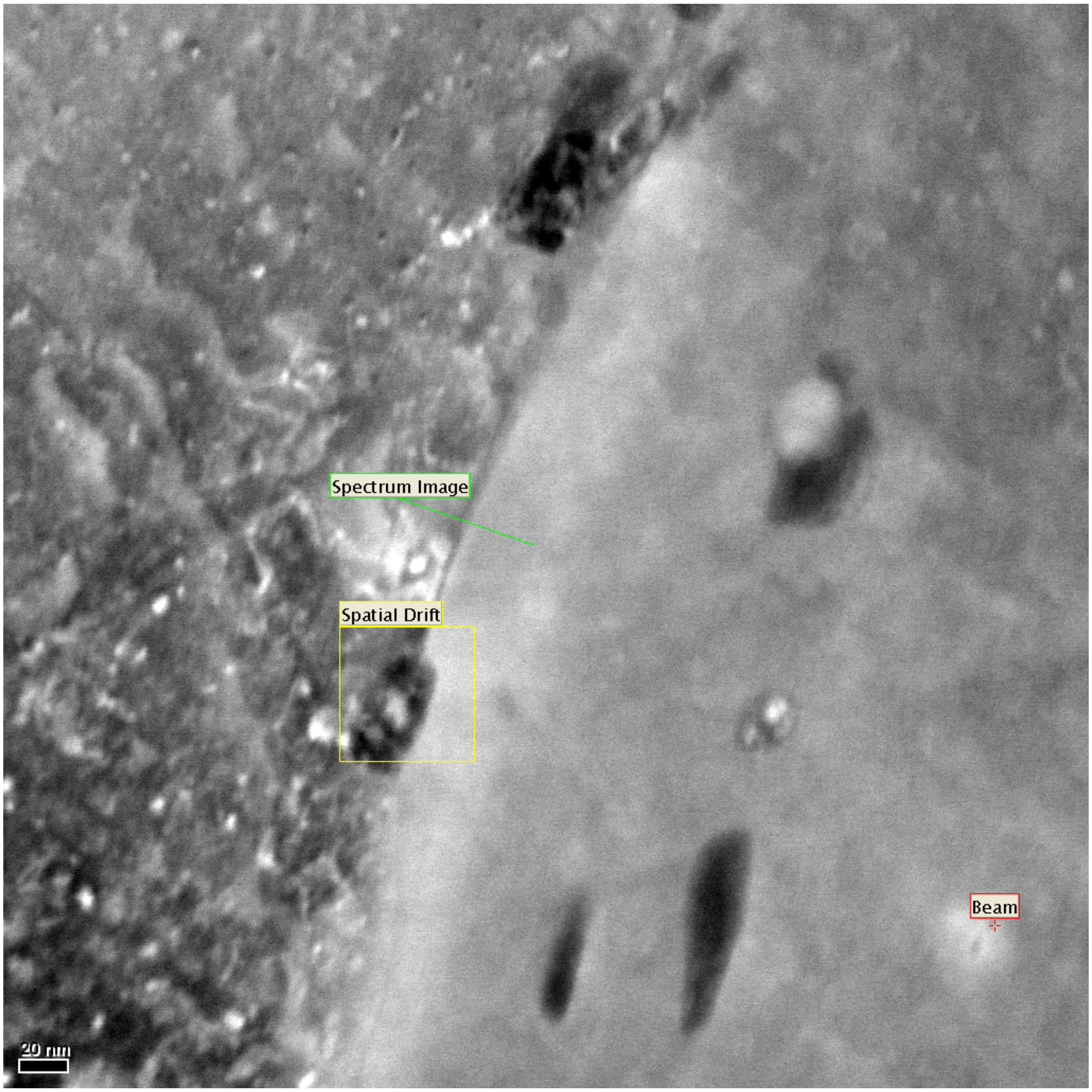

Figure 4.21. Example STEM image (200kx magnification) acquired in Digital Micrograph, with a RIS line scan (green line, "Spectrum Image") traversing the grain boundary, and a portion of the image designated for drift correction (yellow box, "Spatial Drift"). The beam is set to dwell (red crosshairs in bottom right corner) far from the boundary of interest once the scan has completed, to minimize contamination to the boundary.

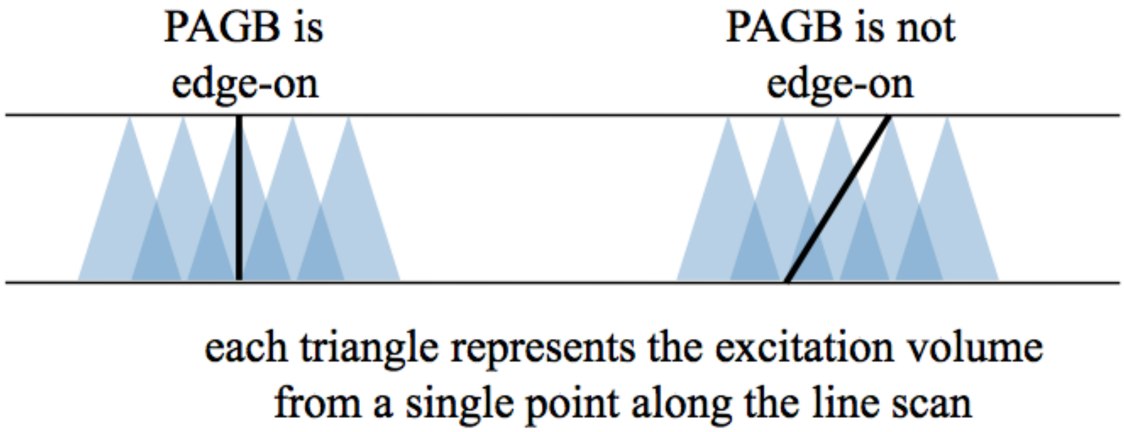

Figure 4.22. Effect of edge-on grain boundary alignment versus not edge-on alignment. When the boundary is aligned edge-on, a smaller amount of the matrix is sampled along with the boundary concentration, and the boundary receives maximum electron beam exposure.

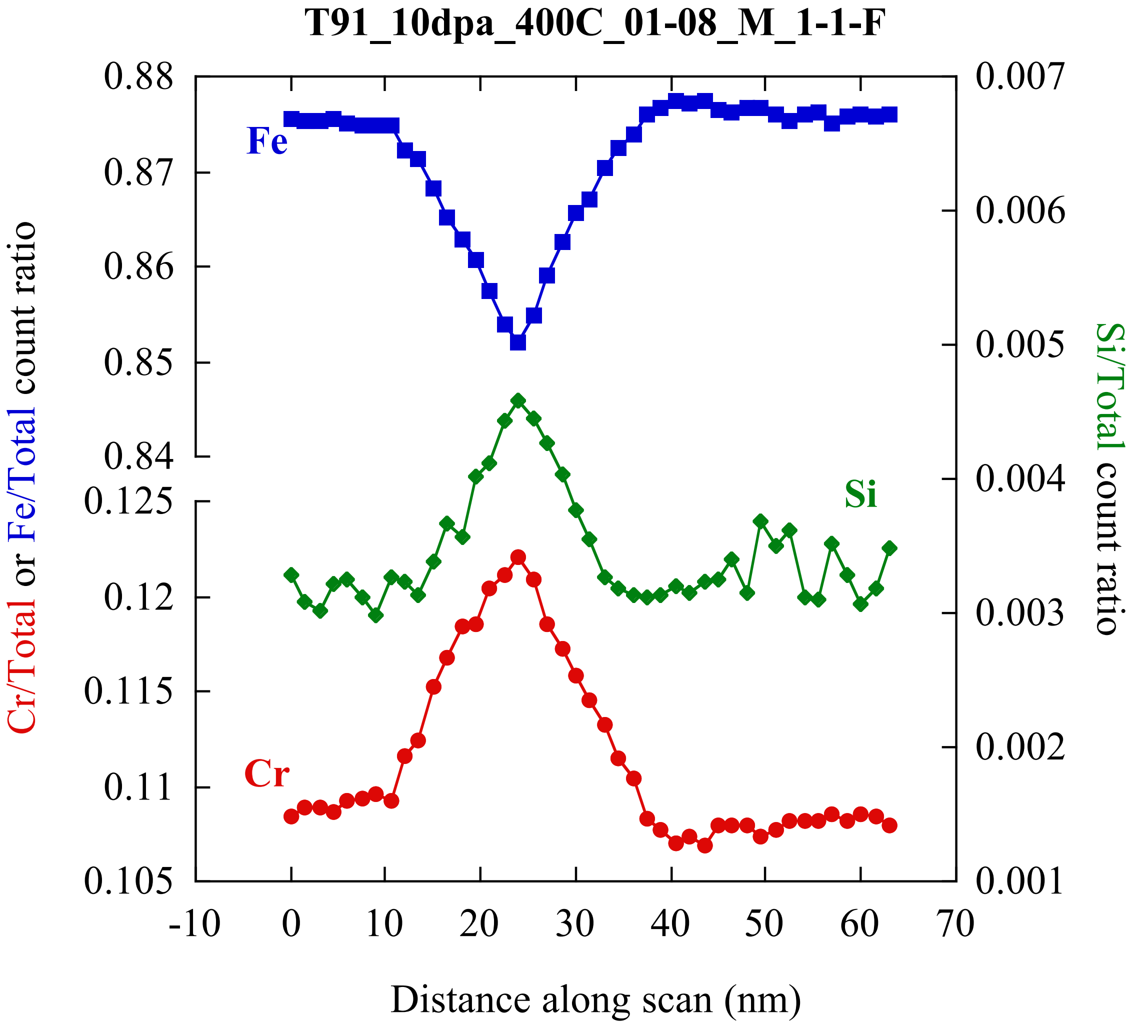

Figure 4.23. Ratio of Cr, Fe, or Si EDX counts to the total number of counts in the EDX spectrum, from scan T91_10dpa_400C_01-08_M_1-1-F, demonstrating Cr and Si enrichment and Fe depletion.

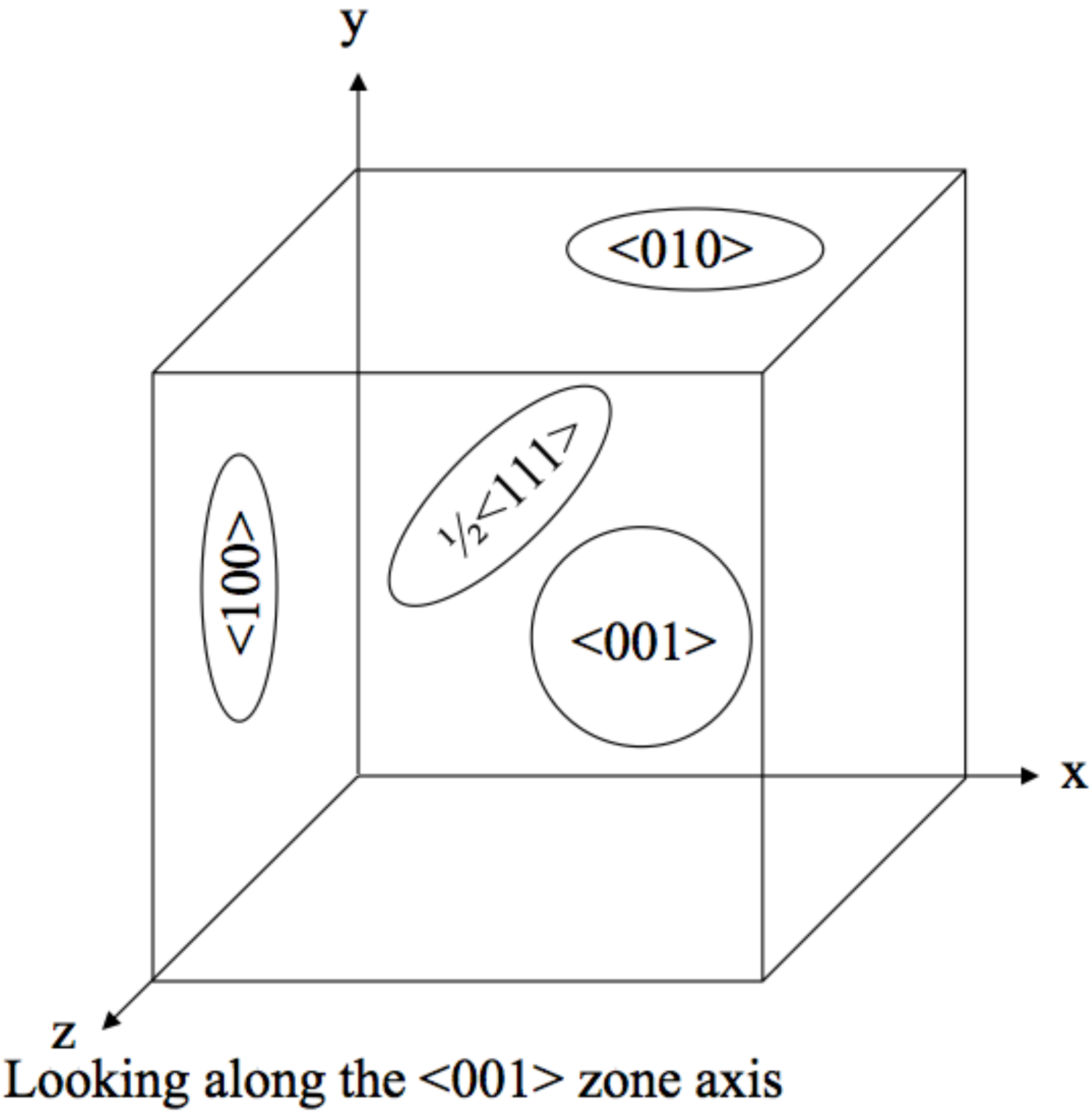

Figure 4.24. Orientation and relative shapes of dislocation loops in F-M alloys as seen along <001> axis.

CHAPTER 5 RESULTS

The experimental work contained within this thesis, as set forth in Chapter 4, is performed toward the objective of measuring radiation-induced segregation in F-M alloys irradiated under a number of conditions. As such, the experimental results fall into two general categories, according to which this chapter will be organized: (1) proton irradiations, and (2) radiation-induced segregation measurements. The first part of this chapter will affirm that the specimens were irradiated under the desired conditions, in a consistent manner. The second part of this chapter will present all RIS measurements collected for this thesis.

Each bar specimen irradiated in this thesis is assigned a four-part sample designation, which allows for easy identification of the alloy and its irradiation temperature, dose, and date. This sample designation will be carried throughout this thesis. The convention used is: alloy_dose_temperature_date, such that T91_3dpa_300C_01-12 indicates alloy T91 irradiated to 3 dpa at 300°C during the month of January 2012. As-received, unirradiated alloys are also studied, for which the sample designation convention is: alloy_UI, or T91_UI indicating unirradiated T91, for example. A list of specimens used in this thesis, along with their sample designations, is provided in Table 5.1.

Ten irradiations, in total, are performed for this thesis, and each is assigned an integer number for ease of identification through Tables 5.1-5.4. It is important to note that 10 dpa specimens (i.e. T91_10dpa_400C_01-08 and 9Cr_10dpa_400C_01-12) are irradiated in two parts: first to 3 dpa, then to 7 dpa. In addition, two different T91 specimens are irradiated to 7 dpa at 400°C, so as to confirm repeatability of both the irradiations and the RIS measurements.

5.1 Proton Irradiation Results

This section will demonstrate that the irradiations were set up and conducted properly, and that the results of the irradiation are both self-consistent and consistent with results published in the open literature. The setup, monitoring, and conduct of the irradiations will be discussed first. Then, results of the irradiations, including irradiation hardening and residual beta activity, will be covered.

Critical experimentally-adjustable parameters are the irradiation dose, dose rate, and temperature. Table 5.2 provides these parameters for all irradiations conducted in this thesis. All of the irradiations delivered a dose to the specimens within ±0.08 dpa of the target dose. The dose rate, on average, is 1.44×10^{-5} dpa/sec, and all irradiations fall within ±20% of that average dose rate. As was calculated in Chapter 4, approximately 3.3 million counts/dpa must be recorded for a 1.8 cm^2 irradiation area, or 1.8 million counts/dpa for a 1.0 cm^2 irradiation area. These values are consistent with the total number of counts recorded for each irradiation, as shown in Table 5.2. The average stage:aperture current ratios are also consistent with those values suggested in Chapter 4 – approximately 2:1 for a 1.8 cm^2 irradiation area, or approximately 1.5:1 for a 1.0 cm^2 irradiation area. The irradiation temperature is calibrated with thermocouples, and the thermocouple readings at calibration time are also shown in Table 5.2. In each irradiation, a minimum of three thermocouples are shown to be functional, and read temperatures within 5°C of each other, and within ±5°C of the target temperature. All irradiations are conducted in high vacuum of better than 9.9×10^{-8} torr at startup.

The actual irradiation temperature of each specimen is shown in Table 5.3. All samples are shown to have been irradiated at an average temperature within ±1.3°C of the intended temperature. Because the temperatures are recorded throughout the duration of every irradiation, a temperature histogram can be constructed for each specimen. The temperature histograms have a normal distribution, with $2\sigma < 10°C$. Temperature histograms for all specimens are shown in Appendix A, but an example is provided in Figure 5.1, which shows a normal temperature distribution for the top, middle, and bottom areas of interest on the specimen T91_3dpa_400C_12-07.

5.1.1 Irradiation Hardening

Irradiation hardening results are provided in Table 5.3. Pre-irradiation hardness values, post-irradiation hardness values, and the irradiation-induced hardening are shown, along with standard deviations, for all specimens studied. In general, alloy HCM12A exhibits the greatest amount of irradiation-induced hardening, with the 9Cr model alloy exhibiting the lowest amount of irradiation-induced hardening. HCM12A has been shown to nucleate a higher density of nm-scale Cu-rich and Ni-Si-Mn-rich precipitates [94], [95], than T91 and HT9, which likely contributes to the larger amount of hardening. Conversely, the carbide- and impurity-free 9Cr model alloy cannot form such precipitates, thus explaining its lower magnitude of irradiation-induced hardening.

The specimen and condition exhibiting the greatest amount of hardening is T91 irradiated to 10 dpa at 400°C, which hardens by 442.4 MPa. The two specimens of T91 irradiated to 7 dpa at 400°C, however, harden by 433.2 MPa and 423.5 MPa, suggesting that hardening begins to reach saturation between 7 and 10 dpa. A similar saturation behavior is observed in the 9Cr model alloy specimens irradiated to 7 and 10 dpa at 400°C, which exhibit hardening of 189.8 MPa and 198.6 MPa, respectively.

Hardening of T91, HT9, HCM12A, and 9Cr model alloy, irradiated at 400°C, is shown as a function of dose in Figure 5.2. The figure compares results from this work (closed symbols) with ~400°C irradiation hardening results reported in literature (open symbols). The saturation behavior of T91 and 9Cr model alloy is shown. The magnitude of hardening of T91 is in good agreement with that measured by Gupta, *et al.* [11] using 2.0 MeV protons at 400°C. The Gupta study, however, includes an additional data point at 5 dpa, which suggests the onset of saturation by as early as 5 dpa. T91 hardening measured in this study and the Gupta study is much greater than hardening of similar alloy 9Cr-1MoVNb irradiated with fast neutrons to 12 dpa and 15 dpa at 400°C and 393°C, respectively [57], [96]. Some fast neutron irradiation hardening data is available for HT9 [57], [96–98], but it is very difficult to compare with the data point from this study, as none of the literature data are taken at the same dose, nor the same temperature as this study.

The temperature dependence of hardening in T91 irradiated to 3 dpa is shown in Figure 5.3. Hardening decreases with increasing irradiation temperature, then a small amount of softening is actually observed at 600°C and 700°C.

5.1.2 Beta Activity

Beta activity is measured for every specimen following irradiation, the results of which are shown in Table 5.4. Beta activity is measured as a count rate in counts/minute (cpm). However, as was shown in Chapter 4, beta activation is linearly dependent upon the Fe composition of the alloy, the area irradiated, and the final dose to which the specimen has been irradiated. Thus, all of these factors can be removed from the beta count rate to obtain a "normalized" count rate. The dose normalization is accomplished by simply dividing the beta count rate by the dose. However, for Fe content, factors are calculated by dividing the Fe content of each condition by the minimum Fe content, such that the condition having the minimum Fe content will have a factor of 1.00. The same factor-type calculation is done for the irradiation area. The beta count rate is normalized for Fe content and irradiation area, then, by dividing by these factors. Ultimately, the beta count rate, normalized by the irradiation area factor, Fe content factor, and dose, is given in cpm/dpa, and shown in the second-from-right column in Table 5.4.

Even by normalizing the beta count rate, however, it is still not possible to directly compare beta activity measurements from irradiation to irradiation, because of the exponential rate of radioactive decay. Unless the specimens are all measured at the exact same interval of time following irradiation, radioactive decay will have removed different fractions of the total initial beta activity. Thus, it is instructive to plot the normalized beta count rate as a function of elapsed time between irradiation and counting, as shown in Figure 5.4. Clearly, the data follow an exponential behavior, to which a functional form can be fit:

$$cpm / dpa = 3569 e^{-0.005t} + 308230 e^{-0.16t}, \tag{5.1}$$

where t is the time elapsed, in hours, between the conclusion of the irradiation and the beta counting. This function, or model, can be applied to all F-M alloy proton irradiations, and shows that all irradiations conducted for this thesis have been performed in a consistent manner.

5.2 Radiation-Induced Segregation Results

There are nineteen conditions (including as-received) studied in this thesis. To ensure accurate concentrations are measured, a minimum of five concentration profiles (or line scans) are collected across a minimum of two grain boundaries for each condition. The conditions studied are listed in Table 5.5 along with the number of grain boundaries studied for each condition, and the number of line scans collected on each of those grain boundaries.

Every concentration profile is assigned a unique scan ID name. The scan IDs follow the convention: SD_AOI_Boundary-Scan-Length, where SD is the sample designation of the specimen being studied, AOI is the region ((‘T’)op, (‘M’)iddle, or (‘B’)ottom) on the irradiated bar from which the TEM foil was created, Boundary indicates the number of the boundary being studied, Scan indicates the number of the scan on that particular boundary, and Length indicates whether the scan is a full 60 nm (‘F’) or short 8-12 nm (‘S’). For example, then, T91_3dpa_400C_12-07_M_3-2-F is the second concentration profile taken across the third boundary studied in T91 irradiated to 3 dpa at 400°C in December 2007; the TEM foil is taken from the middle region of the irradiated specimen, and the concentration profile is 60 nm long.

One concentration profile is shown in tabular form in Table 5.6 for specimen T91_7dpa_400C_01-08_B_1-1-F. Here, the concentrations of Si, Cr, Fe, Ni, and Cu are measured every 1.5 nm along a 60 nm line scan traversing a grain boundary. As discussed in Chapter 4, these five elements (Si, Cr, Fe, Ni, and Cu) are deemed to be detectable in alloy T91. The table also associates an error with every concentration at every point; this error is calculated by propagating the measured counting error through the Cliff-Lorimer equations. Similar tables for all other concentration profiles are provided in Appendix B.

Throughout this chapter, only representative concentration profiles from each condition will be presented. A full presentation of all concentration profiles is reserved for Appendix C. Within this chapter, the average matrix concentrations, grain boundary concentrations, and delta (grain boundary minus matrix) concentrations are presented, in tabular form, for all line scans collected. Then, boundary- and condition-averaged delta concentrations with their standard deviations of the mean, are presented for each condition studied. This approach of presenting RIS and concentration profile results is based upon there being little variation in line scan results from boundary to boundary, a fact which shall be presented in the first sub-section of this chapter.

5.2.1 Boundary-to-Boundary Variation

This sub-section will demonstrate the consistency between boundaries, by using specimen T91_7dpa_400C_01-12 as an example. This sub-section will show that a representative concentration profile can sufficiently illustrate the features of all concentration profiles collected for a given condition, thereby providing a basis for the approach of presenting RIS and concentration profile results that shall be carried through the remainder of this chapter.

As shown in Table 5.5, three grain boundaries are examined in specimen T91_7dpa_400C_01-12. Six scans are collected on the first boundary, three on the second boundary, and three on the third boundary, for a total of 12 line scans at the given condition. All Cr and Si concentration profiles from each of those 12 line scans are shown in Figures 5.5 and 5.6, respectively. Clearly, major features of the concentration profiles are consistent amongst all scans, across all boundaries. All of the Cr concentration profiles shown in Figure 5.5 show consistent matrix concentrations, similar grain boundary concentrations, and a consistent shape and size of the Cr concentration gradient. Likewise, the same can be said of all of the Si concentration profiles shown in Figure 5.6. Clearly, the three boundaries studied exhibit very similar RIS behaviors.

The lack of boundary-to-boundary variation is true for all conditions studied. Thus, it is appropriate to select one line scan as being “representative” of the shape and size of all line scans collected at the given condition. These representative profiles shall be presented in the remainder of this chapter, along with the matrix, grain boundary, and delta concentrations for all line scans collected.

5.2.2 As-Received Alloys

Before any conclusions can be drawn about RIS at a grain boundary, it is essential to characterize the initial condition of that grain boundary. Post-irradiation Cr enrichment, for example, can have very different implications depending whether the grain boundary was enriched in Cr, depleted in Cr, or exhibited no Cr segregation, prior to the irradiation. Thus, the four alloys studied in this thesis—T91, HT9, HCM12A, and 9Cr model alloy—are first examined in their as-received, unirradiated state.

T91_UI: Four boundaries are studied in as-received T91, across which three, three, three, and four line scans are collected. The matrix, grain boundary, and delta concentrations of Si, Cr, Fe, Ni, and Cu, from each of these 13 line scans, are given in Table 5.7. Over all scans, the matrix and grain boundary concentrations are very consistent with one another. The delta concentrations indicate no greater than 0.06 wt% difference between the grain boundary and matrix concentrations, but as shown in the representative line scan in Figure 5.7, the delta concentrations are all well within the counting error, and there is no evidence of segregation of any of the elements.

HT9_UI: Two boundaries are studied in as-received HT9, across which three and two line scans are collected. The matrix, grain boundary, and delta concentrations of Si, Cr, Fe, and Ni (note Cu is not detectable in HT9), from each of these 5 line scans, are given in Table 5.8. As with as-received T91, the matrix and grain boundary concentrations are consistent with one another, and the delta concentrations indicate no segregation. Similarly, the representative line scan in Figure 5.8 provides no evidence of segregation of any of the elements.

HCM12A_UI: Three boundaries are studied in as-received HCM12A, across which three, three, and three line scans are collected. The matrix, grain boundary, and delta concentrations of Si, Cr, Fe, Ni, W, and Cu, from each of these 9 line scans, are given in Table 5.9. The matrix and grain boundary concentrations are consistent with one another, and the delta concentrations are within the counting errors. The representative line scan in Figure 5.9 also provides no evidence of segregation of any of the elements.

9Cr_UI: Finally, two boundaries are studied in as-received 9Cr model alloy, across which three and three line scans are collected. The matrix, grain boundary, and delta concentrations of Cr and Fe, from each of these 6 line scans, are given in Table 5.10. Matrix and grain boundary concentrations are very consistent with one another, and the delta concentrations indicate no segregation. The representative line scan in Figure 5.10 shows no evidence of segregation of either Cr or Fe.

Thus, it has been shown that there is no evidence of pre-existing segregation of any detectable element in the as-received state of T91, HT9, HCM12A, or 9Cr model alloy. Any segregation behavior observed in the irradiated specimens can thus be concluded to be entirely irradiation-induced.

5.2.3 RIS Results in T91

Alloy T91 has been irradiated over a range of temperatures, 300-600°C, and doses, 1-10 dpa. The RIS results from each of these conditions will be presented here. The results will begin with the lowest temperature and dose, then progress to higher temperatures and doses.

T91_3dpa_300C_01-12: Two boundaries are studied in T91 irradiated to 3 dpa at 300°C. Two full scans and two short scans are taken across the first boundary, while three full scans and two short scans are taken across the second boundary. Matrix, grain boundary, and delta concentrations of Si, Cr, Fe, Ni, and Cu, from all of these scans, are given in Table 5.11. The full scans reveal consistent matrix concentrations of all elements, while all scans reveal consistent grain boundary concentrations. The delta concentrations indicate no discernible segregation of Si, Ni, or Cu, but small amounts of Cr and Fe segregation. Cr is observed to enrich by 0.39-0.83 wt%, while Fe is observed to deplete by 0.46-0.88 wt%. A representative line scan is shown in Figure 5.11, which shows the ~0.5 wt% Cr enrichment and Fe depletion, with no evidence of RIS of Ni, Si, or Cu.

T91_1dpa_400C_04-09: Two boundaries are studied in T91 irradiated to 1 dpa at 400°C. Three full scans and five short scans are taken across the first boundary, while two full scans and four short scans are taken across the second boundary. Matrix, grain boundary, and delta concentrations from all scans are given in Table 5.12. The full scans show consistent matrix concentrations of all elements, and all scans show similar grain boundary concentrations. The delta concentrations indicate enrichment of Cr by 0.50-0.92 wt%, enrichment of Si, Ni, and Cu in the range 0.15-0.26 wt%, and depletion of Fe by 1.09-1.50 wt%. A representative line scan is shown in Figure 5.12.

T91_3dpa_400C_12-07: Three boundaries are studied in T91 irradiated to 3 dpa at 400°C. Only full scans are taken; two, three, and two scans are collected on each of the three boundaries, respectively. Matrix, grain boundary, and delta concentrations from all scans are given in Table 5.13. The scans show consistent matrix and grain boundary concentrations. The delta concentrations indicate more segregation than observed at 1 dpa, 400°C. Cr enrichment falls in the range of 1.27-1.71 wt%, enrichment of Si, Ni, and Cu is in the range of 0.07-0.52 wt%, and Fe depletion is in the range of 1.88-2.67 wt%. A representative line scan is shown in Figure 5.13.

T91_7dpa_400C_01-08, T91_7dpa_400C_01-12: In order to demonstrate repeatability of irradiations, two specimens of T91 are irradiated to the same conditions, 7 dpa at 400°C, four years apart. On the specimen from the earlier January 2008 irradiation, two full scans are collected from each of three boundaries. On the specimen from the later January 2012 irradiation, three boundaries are studied, on which six, three, and three scans are collected, respectively. All of the scans, from both specimens, show consistent matrix and grain boundary concentrations, as shown in Table 5.14. Cr enrichment is of approximately the same magnitude, or slightly greater, than that observed in T91 irradiated to 3 dpa at 400°C. The specimen from the January 2008 irradiation exhibits approximately the same amount of Cr enrichment (1.23-1.85 wt%) as does the specimen from the January 2012 irradiation (1.09-2.20 wt%). Similarly, Si, Ni, and Cu enrichment, and Fe depletion, are on the same order, from both the 2008 and 2012 irradiations. A representative line scan from each of the two irradiations is shown in Figure 5.14, in which the 2008 irradiation is represented by closed symbols and the

2012 irradiation by open symbols. The concentration profiles from both irradiation dates are very similar in size and shape for all elements studied.

T91_10dpa_400C_01-08: Five boundaries are studied in T91 irradiated to 10 dpa at 400°C. Three full scans are collected on each boundary, for a total of 15 scans at this condition. Matrix, grain boundary, and delta concentrations from all scans are given in Table 5.15, and are consistent across all scans. Cr enriches by 0.59-1.36 wt%, which is, in general, of a lower magnitude than the amount of Cr enrichment observed in T91 irradiated to only 7 dpa at 400°C. Likewise, the amounts of minor element and Fe RIS are lower at 10 dpa than at 7 dpa, being in the range of 0.02-0.31 wt% and 0.57-1.43 wt%, respectively. A representative line scan is shown in Figure 5.15.

T91_3dpa_450C_10-11: Two boundaries are studied in T91 irradiated to 3 dpa at 450°C. Four full scans and five short scans are taken across the first boundary, while two full scans and four short scans are taken across the second boundary. Matrix, grain boundary, and delta concentrations from all scans are given in Table 5.16. The full scans show consistent matrix concentrations of all elements, and all scans show similar grain boundary concentrations. The delta concentrations indicate enrichment of Cr in the range of 1.68-1.79 wt%, which is slightly greater than that observed in T91 irradiated to 3 dpa at 400°C. Si, Ni, and Cu enrich in the range 0.18-0.32 wt%, which is approximately on the same order as observed in T91_3dpa_400C_12-07. Likewise, Fe depletion of 2.35-2.57 wt% is observed. A representative line scan is shown in Figure 5.16.

T91_3dpa_500C_07-08: Two boundaries are studied in T91 irradiated to 3 dpa at 500°C. Two full scans are taken across the first boundary, and four full scans across the second. Matrix, grain boundary, and delta concentrations are consistent across all scans, as shown in Table 5.17. The amount of RIS is slightly less than already reported in T91 irradiated to 3 dpa at 400°C and 450°C. Cr enriches by 1.18-1.46 wt%, the minor elements enrich by 0.01-0.30 wt%, and Fe depletes by 1.77-2.08 wt%. A representative line scan is shown in Figure 5.17.

T91_3dpa_600C_01-12: Two boundaries are studied in T91 irradiated to 3 dpa at 600°C. Three full scans are taken across the first boundary, while two full scans and two short scans are taken across the second boundary. Matrix, grain boundary, and delta concentrations from all scans are given in Table 5.18. As has already been reported in

T91 irradiated to 3 dpa at 300°C, there is no discernible RIS of minor elements Si, Ni, and Cu. Likewise, Cr enrichment and Fe depletion are observed, but in only small amounts, in the range of 0.44-0.91 wt% and 0.45-1.27 wt%, respectively. A representative line scan is shown in Figure 5.18.

T91_3dpa_700C_05-12: Three boundaries are studied in T91 irradiated to 3 dpa at 700°C. Two full scans and two short scans are taken across both the first and second boundaries, and two full scans are taken across the third boundary. Matrix, grain boundary, and delta concentrations from all scans are given in Table 5.19. Much like in the T91 irradiated to 3 dpa at 300°C and 600°C, there is no discernible RIS of minor elements Si, Ni, and Cu. However, this is the first observation of Cr depletion and Fe enrichment. The amount of Cr depletion ranges from -0.31 wt% to -0.59 wt%, with approximately equal magnitudes of Fe enrichment. A representative line scan is shown in Figure 5.19.

5.2.4 RIS Results in 9Cr Model Alloy

A 9Cr model alloy has been irradiated at 400°C to a range of doses from 1 dpa to 10 dpa. The RIS results from each of these conditions will be presented here. The results will begin with the lowest dose, then progress to higher doses.

9Cr_1dpa_400C_04-09: Three boundaries are studied in the 9Cr model alloy irradiated to 1 dpa at 400°C. Three full scans are taken across each of the three boundaries. Matrix, grain boundary, and delta concentrations from all scans are given in Table 5.20. Matrix and grain boundary concentrations are consistent amongst all of the scans. The delta concentrations indicate a relatively large variation in the amount of Cr enrichment, however, from 0.00 wt% up to 1.00 wt%, matched with equal amounts of Fe depletion. A representative line scan is shown in Figure 5.20.

9Cr_3dpa_400C_01-12: Two boundaries are studied in the 9Cr model alloy irradiated to 3 dpa at 400°C. Four full scans and five short scans are taken across the first boundary, while two full scans and four short scans are collected on the second boundary. All scans demonstrate consistent matrix, grain boundary, and delta concentrations, as shown in Table 5.21. The delta concentrations suggest Cr enrichment by 0.72-0.82 wt%, with matching amounts of Fe depletion. A representative line scan is shown in Figure 5.21.

9Cr_7dpa_400C_04-09: Three boundaries are studied in the 9Cr model alloy irradiated to 7 dpa at 400°C. Two full scans and three short scans are taken across the first boundary, two full and two short on the second boundary, and two full and four short on the third boundary. All scans demonstrate consistent matrix, grain boundary, and delta concentrations, as shown in Table 5.22. Chromium enriches by 1.25-1.61 wt%, while Fe depletes by an equivalent amount. A representative line scan is shown in Figure 5.22.

9Cr_10dpa_400C_01-12: Two boundaries are studied in the 9Cr model alloy irradiated to 10 dpa at 400°C. Four full scans and four short scans are collected on the first boundary, with two full scans and four short scans collected on the second boundary. All scans demonstrate consistent matrix, grain boundary, and delta concentrations, as shown in Table 5.23. The amount of Cr enrichment and Fe depletion is on the same order as observed in 9Cr_7dpa_400C_04-09, or 1.30-1.79 wt%. A representative line scan is shown in Figure 5.23.

5.2.5 RIS Results in HT9 and HCM12A

Both HT9 and HCM12A are irradiated to 3 dpa at 400°C. The RIS results from each of these conditions will be presented here. The HT9 results will be presented first, followed by the HCM12A results.

HT9_3dpa_400C_12-07: Four boundaries are studied in HT9 irradiated to 3 dpa at 400°C. Two full scans are taken across each of the four boundaries. Matrix, grain boundary, and delta concentrations from all scans are given in Table 5.24. The table demonstrates consistent matrix and grain boundary concentrations amongst all scans. The results indicate enrichment of Cr by 0.55-0.75 wt%, enrichment of Ni by 0.53-0.68 wt%, enrichment of Si by ~0.04 wt%, and depletion of Fe by 1.19-1.39 wt%. A representative line scan is shown in Figure 5.24.

HCM12A_3dpa_400C_12-07: Two boundaries are studied in HCM12A irradiated to 3 dpa at 400°C. Three full scans are taken across the first boundary, and four full scans across the second. Matrix, grain boundary, and delta concentrations from all scans are given in Table 5.25. The table demonstrates consistent matrix and grain boundary concentrations amongst all scans. The results indicate enrichment of Cr by 0.59-1.13 wt% and depletion of Fe by 0.95-2.45 wt%. Minor elements Si, Ni, Cu, and W have quite variable delta concentration values. A representative line scan is shown in Figure 5.25.

5.2.6 Summary of RIS Results

A few key behaviors can be identified from the RIS results presented in this chapter. First, the temperature dependence of RIS is identified. The dose evolution of RIS is also observed. And finally, the dependence of RIS on alloy is determined. Each of these behaviors will be described here.

In alloy T91 irradiated to 3 dpa, RIS is maximized between 400°C and 500°C, and more suppressed at temperatures above and below that range. This can be seen in Figure 5.26, which overlays the representative Cr RIS profiles at all temperatures onto the same plot. Clearly, small amounts of Cr RIS are observed at the more extreme temperatures—small amounts of Cr enrichment at 300°C and 600°C, with small amounts of Cr depletion at 700°C—while larger amounts of enrichment are found at 400-500°C. It can also be seen from Figure 5.26 that the RIS profiles broaden with increasing temperature.

The dose evolution of RIS is observed in both T91 and a 9Cr model alloy at 400°C. In T91, the amount of Cr enrichment increases from 1 dpa to 7 dpa, but decreases between 7 dpa and 10 dpa. This behavior can clearly be seen when the representative Cr RIS profiles from each of these irradiation conditions is overlaid on the same plot, as in Figure 5.27. One can also see that the T91 Cr RIS profiles broaden with increasing dose, beginning as narrow concentration gradients at 1 dpa and 3 dpa, then broadening from 3 to 7 dpa, and broadening even further from 7 to 10 dpa. A similar plot, overlaying all representative Cr RIS profiles, is given for the 9Cr model alloy irradiated at 400°C in Figure 5.28. In this plot, Cr enrichment continues to increase from 1 dpa through 10 dpa, unlike in T91, where a decrease in enrichment is observed between 7 and 10 dpa. But similar to the T91 behavior, the 9Cr model alloy concentration profiles broaden with increasing dose. Average values for the change in grain boundary Cr concentration are plotted as a function of dose for both T91 and 9Cr model alloy, irradiated at 400°C, in Figure 5.29. This figure clearly illustrates the decrease in Cr enrichment in T91 between 7 and 10 dpa, in great contrast to the dose evolution of the 9Cr model alloy, which may be approaching a steady-state behavior between 7 and 10 dpa.

Finally, the amount of Cr RIS generally decreases as a function of increasing bulk Cr concentration, in the commercial F-M alloys studied (T91, HCM12A, and HT9). This behavior can be seen in Figure 5.30, which overlays the representative Cr RIS profiles from each alloy, irradiated at 400°C to 3 dpa, onto the same plot. Clearly, as the bulk Cr concentration increases from ~8.5 wt% in T91 to ~11 wt% in HCM12A to ~12 wt% in HT9, the amount of Cr enrichment (i.e. the difference between the grain boundary value and the matrix value) decreases. Only the 9Cr model alloy does not appear to follow this behavior, and the potential reasons for this will be discussed in Chapter 7.

An average of the change in grain boundary concentrations, for each element studied, is taken across all line scans collected from a given boundary, then across all boundaries in a given condition. These average values also have an associated standard deviation of the mean. All of these average values and standard deviations are summarized in Table 5.26 for T91, Table 5.27 for 9Cr model alloy, Table 5.28 for HT9, and Table 5.29 for HCM12A.

Overall, RIS in the F-M alloys studied is of very low magnitude. Enrichment of Cr is observed in all irradiated conditions studied except for T91 irradiated to 3 dpa at 700°C, but never exceeds ~2 wt%. Likewise, Fe depletion is observed in all irradiated conditions except T91 at 700°C and 3 dpa, but it, too, never exceeds ~2.5 wt%. Minor element RIS primarily involves Si, Ni, and Cu whenever they are present. These minor elements are only observed to enrich, never to depelete, and they enrich by no more than ~1.5 wt%. Experiments and measurements are highly repeatable, as there is little variation amongst line scans collected on a specific boundary, and there is little variation amongst line scans collected from a specific condition.

5.3 Microstructure Results

Microstructure is studied in T91 and the 9Cr model alloy, in their as-received conditions as well as in the specimens of these alloys irradiated at 400°C to doses of 1, 3, 7, and 10 dpa. These conditions are selected because the microstructure results will primarily be used in the discussion of the dose dependence of RIS, to be presented in Chapter 7. Measurements of the grain sizes, precipitate size and density, dislocation line length and density, and dislocation loop size and density will be presented in this section. Then, the section will conclude with the sink strength calculation.

Lath dimensions, precipitate sizes and densities, and dislocation lines, can all be measured from bright field TEM images. Examples of these bright field images are shown for T91 at 1, 3, 7, and 10 dpa at 400°C in Figures 5.31 and for the 9Cr model alloy at the same conditions in Figure 5.32. The measurements are summarized in Table 5.30 for T91 and Table 5.31 for the 9Cr model alloy. Note that for alloy T91, the range of values found in literature for all measurements is given in the rightmost column of Table 5.30; the literature data are all very consistent with the measurements of this work.

Laths in alloy T91 have, on average, a length of 5.07 µm and a width of 0.44 µm. But because the sink strength calculation considers a single grain size parameter, *d*, the elongated rectangular shape of the lath can be mathematically equated to a more symmetric square shape. The effective *d* for T91 is calculated to be 1.49 µm, resulting in a sink strength of 10.76 µm^{-2} for boundaries. Irradiation does not change the grain size, and the same dimensions can be used at all doses. The 9Cr model alloy has lath dimensions similar to those of T91: 4.63 µm in length, 0.40 µm in width, for an effective *d* of 1.36 µm. In the 9Cr model alloy, the lath boundary sink strength is 12.96 µm^{-2}.

Carbides are found at an order-of-magnitude higher number density in T91 (1.13 x 10^{20} m^{-3} as-received) as they are in the 9Cr model alloy (1.21 x 10^{19} m^{-3} as-received). The carbide size in T91 (0.156 µm as-received) is also slightly greater than that in the 9Cr model alloy (0.126 µm as-received). In both alloys, very little growth is seen in the carbides under irradiation, although a small increase is measured in their number density. Carbide size and density measured in T91 is in agreement with those measurements found in literature. The dose evolution of the carbide size and number density is illustrated in Figure 5.33, which shows T91 as closed symbols and 9Cr model alloy as open symbols. The resulting sink strength of the precipitates is 220-250 μm^{-2} for T91, and only 19-20 μm^{-2} for the 9Cr model alloy.

The dislocation network is measured to be approximately four times denser in T91 (6.25 x 10^{14} m^{-2} as-received) than in the 9Cr model alloy (1.62 x 10^{14} m^{-2}). But the dislocation lines in both alloys are of approximately the same length, 0.52 μm in T91 and 0.47 μm in 9Cr model alloy. There is no change to the dislocation network as a function of irradiation dose. The dislocation line length and network density measured in T91 fall into the ranges measured in literature. The dislocation lines have a sink strength of 888 μm^{-2} in T91, and 217 μm^{-2} in the 9Cr model alloy.

Dislocation loops are the final contribution to the overall sink strength of the materials. Example TEM images of dislocation loops in T91 are shown in Figure 5.34 from specimens irradiated at 400°C to 1, 3, 7, and 10 dpa. Loop images from 9Cr model alloy, irradiated under the same conditions, are shown in Figure 5.35. The size and number density of the dislocation loop population increase with increasing irradiation dose in both T91 and the 9Cr model alloy, as summarized in Table 5.30 for T91 and Table 5.31 for the 9Cr model alloy. The dislocation loop number density in the 9Cr model alloy is about half that in T91, although the loop sizes are comparable in both alloys. In alloy T91, the measured loop size and density compare favorably to the size range and density range measured in literature. The sink strength of the dislocation loops continues to increase with irradiation dose, as the loop size and density increase, but for T91, the sink strength ranges from 673 μm^{-2} at 3 dpa to 8621 μm^{-2} at 10 dpa. The sink strength of loops in 9Cr model alloy are approximately half that in T91, because their density is approximately half that in T91. The behavior of dislocation loop size and density, as a function of irradiation dose, in both T91 and the 9Cr model alloy, is illustrated in Figure 5.36, and the loop size distribution is provided in Figure 5.37.

The total sink strength of the material is calculated by summing the sink strengths of the individual features: lath boundaries, precipitates, dislocation lines, and dislocation loops. In general, the sink strength increases rather linearly as a function of dose, largely due to the growth of the dislocation loop sink strength as a function of dose. The T91 sink strength is approximately double that of the 9Cr model alloy at each dose studied. The sink strengths of both alloys are plotted as a function of dose in Figure 5.38.

Table 5.1. List of samples used in this thesis, including irradiation date and number of RIS scans collected from each sample.

Sample Designation	Alloy	Intended Irradiation Temperature (°C)	Intended Irradiation Dose (dpa)	Date of Irradiation (Irradiation Number)
T91_3dpa_300C_01-12	T91	300	3	January 2012 (7)
T91_1dpa_400C_04-09	T91	400	1	April 2009 (4)
T91_3dpa_400C_12-07	T91	400	3	December 2007 (1)
T91_7dpa_400C_01-08	T91	400	7	January 2008 (2)
T91_7dpa_400C_01-12	T91	400	7	January 2012 (9)
T91_10dpa_400C_01-08	T91	400	10	January 2008 (1+2)
T91_3dpa_450C_10-11	T91	450	3	October 2011 (6)
T91_3dpa_500C_07-08	T91	500	3	July 2008 (3)
T91_3dpa_600C_01-12	T91	600	3	January 2012 (10)
T91_3dpa_700C_05-12	T91	700	3	May 2012 (11)
9Cr_1dpa_400C_04-09	9Cr model	400	1	April 2009 (4)
9Cr_3dpa_400C_01-12	9Cr model	400	3	January 2012 (8)
9Cr_7dpa_400C_04-09	9Cr model	400	7	April 2009 (5)
9Cr_10dpa_400C_01-12	9Cr model	400	10	January 2012 (8+9)
HCM12A_3dpa_400C_12-07	HCM12A	400	3	December 2007 (1)
HT9_3dpa_400C_12-07	HT9	400	3	December 2007 (1)
T91_UI	T91	n/a	0	n/a
9Cr_UI	9Cr model	n/a	0	n/a
HCM12A_UI	HCM12A	n/a	0	n/a
HT9_UI	HT9	n/a	0	n/a

Table 5.2. List of irradiations completed for this thesis, including important irradiation parameters.

Irrad. Number	Sample Designation	Actual Dose (dpa)	Dose Rate (10^{-5} dpa/s)	Irrad. Area (mm x mm)	Total Counts (10^6)	Irrad. Time (hours)	Currents		Thermocouples at Calibration					Beginning Pressure (10^{-8} torr)
							Average Stage Current (μA)	Average Aperture Current (μA)	TC1 (°C)	TC2 (°C)	TC3 (°C)	TC4 (°C)	Back (°C)	
1	T91_3dpa_400C_12-07 T91_10dpa_400C_01-08* HCM12A_3dpa_400C_12-07 HT9_3dpa_400C_12-07	3.001	1.26	10 x 18	9.5	38.7	37.4	18.2	396	397	399	400	415	9.90
2	T91_7dpa_400C_01-08 T91_10dpa_400C_01-08*	7.03	1.28	10 x 18	22.8	152.5	41.5	21.9	399	402	n.r.	404	416	9.90
3	T91_3dpa_500C_07-08	3.002	1.32	10 x 18	9.75	63	41.5	20.3	496	n.r.	498	498	512	9.90
4	T91_1dpa_400C_04-09 9Cr_1dpa_400C_04-09	1.01	1.35	10 x 18	3.26	21	40.9	20.0	399	398	401	n.r.	414	9.91
5	9Cr_7dpa_400C_04-09	6.98	1.23	10 x 18	23.74	158	40.0	22.0	398	n.r.	399	401	404	9.96
6	T91_3dpa_450C_10-11	3.01	1.53	10 x 10	5.73	54.5	29.1	19.9	n.r.	450	452	449	429	9.96
7	T91_3dpa_300C_01-12	3.002	1.71	10 x 10	5.53	48.7	31.5	20.8	n.r.	298	295	297	303	9.37
8	9Cr_3dpa_400C_01-12 9Cr_10dpa_400C_01-12*	3.00	1.53	10 x 10	5.55	54.5	29.1	19.3	398	396	n.r.	398	408	9.91
9	T91_7dpa_400C_01-12 9Cr_10dpa_400C_01-12*	7.003	1.61	10 x 10	12.9	121.0	29.7	20.8	n.r.	401	400	402	411	9.89
10	T91_3dpa_600C_01-12	3.08	1.57	10 x 10	5.78	54.5	31.0	21.9	599	n.r.	596	596	648	9.69
11	T91_3dpa_700C_05-12	3.002	1.74	10 x 10	5.53	48.0	32.1	21.3	n.r.	690	689	687	763	9.01

n.r. = not reading

* = same specimen irradiated twice, once to 3 dpa and once to 7 dpa for a total of 10 dpa

Table 5.3. Actual irradiation temperature and irradiation-induced hardening for each sample used in this thesis.

		Sample Temperature			Pre-Irradiation Hardness		Post-Irradiation Hardness		Irradiation Hardening	
Sample Designation	Irradiation Number	Average (°C)	2σ (°C)	AOI Emissivity Range	Hardness (HV)	Standard Deviation (HV)	Hardness (HV)	Standard Deviation (HV)	Hardening (ΔMPa)	Standard Deviation (ΔMPa)
T91_3dpa_300C_01-12	7	299.9	4.9	0.136-0.161	221.5	1.5	333.9	3.5	343.7	11.6
T91_1dpa_400C_04-09	4	400.6	6.6	0.119-0.131	213.9	1.5	258.1	2.6	135.3	9.3
T91_3dpa_400C_12-07	1	400.0	7.5	0.113-0.125	205.4	1.2	275.7	1.5	215.0	6.1
T91_7dpa_400C_01-08	2	400.0	6.8	0.108-0.110	206.3	1.5	347.9	2.5	433.2	9.1
T91_7dpa_400C_01-12	9	399.3	6.4	0.122-0.142	210.8	1.4	349.2	1.9	423.5	7.2
T91_10dpa_400C_01-08	1+2	400.6	8.2	0.110-0.125	201.9	1.1	346.5	2.2	442.4	8.3
T91_3dpa_450C_10-11	6	450.3	7.2s	0.106-0.117	231.8	1.6	302.2	4.0	215.2	13.3
T91_3dpa_500C_07-08	3	500.2	8.5	0.123-0.129	217.5	1.2	226.6	1.9	27.7	6.8
T91_3dpa_600C_01-12	10	599.4	7.3	0.113-0.135	214.7	1.5	207.8	2.5	-21.1	8.9
T91_3dpa_700C_05-12	11	700.8	7.4	0.160-0.182	240.2	1.2	208.4	1.7	-97.3	6.2
9Cr_1dpa_400C_04-09	4	400.6	7.1	0.110-0.125	163.3	1.8	188.9	3.7	78.3	12.7
9Cr_3dpa_400C_01-12	8	400.1	6.2	0.117-0.144	180.6	1.3	223.3	1.7	130.9	6.5
9Cr_7dpa_400C_04-09	5	398.7	7.4	0.100-0.110	166.9	1.3	228.9	1.3	189.8	5.8
9Cr_10dpa_400C_01-12	8+9	400.4	6.2	0.129-0.159	177.4	1.6	242.3	2.5	198.6	9.1
HCM12A_3dpa_400C_12-07	1	400.3	7.6	0.115-0.131	220.7	1.5	350.5	2.4	397.2	8.6
HT9_3dpa_400C_12-07	1	399.6	7.7	0.112-0.116	250.0	1.3	313.5	1.9	194.4	7.0

Table 5.4. Post-irradiation beta activity measurements for each sample used in this thesis.

Sample Designation	Irrad. No.	Time Elapsed (hours)	Beta Count Rate (cpm)	Counting Error	Dose (dpa)	Irrad. Area (mm^2)	Area Factor	Fe Content (wt%)	Fe Factor	Beta Count Rate Normalized by Area Factor, Fe Factor, & Dose (cpm/dpa)	Modeled Normalized Beta Count Rate (cpm/dpa)
T91_3dpa_300C_01-12	7	59	24423	107	3	50	3.33	88.65	1.067	2290	2616
T91_1dpa_400C_04-09	4	31	5563	161	1	15	1.00	88.65	1.067	5215	5255
T91_3dpa_400C_12-07	1	74.5	9952	108	3	20	1.33	88.65	1.067	2332	2382
T91_7dpa_400C_01-08	2	185	17557	94	7	20	1.33	88.65	1.067	1764	1305
T91_7dpa_400C_01-12	9	73	27833	118	7	20	1.33	88.65	1.067	2796	2402
T91_10dpa_400C_01-08	1	74.5	10177	109	3	20	1.33	88.65	1.067	2385	2382
T91_3dpa_450C_10-11	6	144	3960	79	3	15	1.00	88.65	1.067	1238	1631
T91_3dpa_500C_07-08	3	180	5543	81	3	20	1.33	88.65	1.067	1299	1341
T91_3dpa_600C_01-12	10	36	37844	133	3	50	3.33	88.65	1.067	3548	3946
T91_3dpa_700C_05-12	11	1.5	194674	213	3	100	6.67	88.65	1.067	9125	9189
9Cr_1dpa_400C_04-09	4	31	5898	164	1	15	1.00	91.00	1.095	5387	5255
9Cr_3dpa_400C_01-12	8	42	12313	137	3	15	1.00	91.00	1.095	3748	3230
9Cr_7dpa_400C_04-09	5	96	14771	98	7	15	1.00	91.00	1.095	1927	2117
9Cr_10dpa_400C_01-12	8	87	8673	115	3	15	1.00	91.00	1.095	2640	2224
HCM12A_3dpa_400C_12-07	1	74.5	9067	106	3	20	1.33	83.11	1.000	2267	2382
HT9_3dpa_400C_12-07	1	74.5	9471	108	3	20	1.33	84.45	1.016	2330	2382
T91_10dpa_400C_01-08	1+2	185	17120	93	7	20	1.33	88.65	1.067	1720	1305
9Cr_10dpa_400C_01-12	8+9	73	28393	114	10	15	1.00	91.00	1.095	2593	2402

Table 5.5. Number of composition profiles scans collected from each specimen.

Sample Designation	Number of Boundaries Studied for RIS	Number of Scans Collected on Each Boundary
T91_3dpa_300C_01-12	2	4 / 5
T91_1dpa_400C_04-09	2	8 / 6
T91_3dpa_400C_12-07	3	2 / 3 / 2
T91_7dpa_400C_01-08	3	2 / 2 / 2
T91_7dpa_400C_01-12	3	6 / 3 / 3
T91_10dpa_400C_01-08	5	3 / 3 / 3 / 3 / 3
T91_3dpa_450C_10-11	2	9 / 6
T91_3dpa_500C_07-08	2	2 / 4
T91_3dpa_600C_01-12	2	3 / 4
T91_3dpa_700C_05-12	3	4 / 4 / 2
9Cr_1dpa_400C_04-09	3	3 / 3 / 3
9Cr_3dpa_400C_01-12	2	9 / 6
9Cr_7dpa_400C_04-09	3	5 / 4 / 6
9Cr_10dpa_400C_01-12	2	8 / 6
HCM12A_3dpa_400C_12-07	2	3 / 4
HT9_3dpa_400C_12-07	4	2 / 2 / 2 / 2
T91_UI	4	3 / 3 / 3 / 4
9Cr_UI	2	3 / 3
HCM12A_UI	3	3 / 3 / 3
HT9_UI	2	3 / 2

Table 5.6. Example RIS line scan data, from T91_7dpa_400C_01-08_B_1-1-F.

Distance from PAGB (nm)	Measured Concentration (wt%)					Error on Concentration (wt%)				
	Si	Cr	Fe	Ni	Cu	Si	Cr	Fe	Ni	Cu
-28.5	0.27	8.50	90.61	0.21	0.18	0.22	0.77	0.82	0.17	0.14
-27.0	0.28	8.48	90.65	0.21	0.17	0.22	0.76	0.82	0.16	0.13
-25.5	0.29	8.47	90.64	0.20	0.18	0.23	0.76	0.82	0.16	0.14
-24.0	0.29	8.48	90.63	0.22	0.16	0.23	0.76	0.82	0.17	0.13
-22.5	0.29	8.51	90.60	0.22	0.16	0.23	0.77	0.82	0.18	0.13
-21.0	0.29	8.52	90.58	0.22	0.17	0.23	0.77	0.82	0.18	0.14
-19.5	0.28	8.46	90.67	0.21	0.16	0.22	0.76	0.82	0.17	0.13
-18.0	0.29	8.51	90.58	0.22	0.19	0.23	0.77	0.82	0.18	0.15
-16.5	0.29	8.49	90.59	0.22	0.18	0.23	0.76	0.82	0.18	0.14
-15.0	0.28	8.51	90.62	0.20	0.17	0.22	0.77	0.82	0.16	0.14
-13.5	0.28	8.51	90.59	0.22	0.18	0.23	0.77	0.82	0.17	0.14
-12.0	0.29	8.53	90.57	0.22	0.17	0.23	0.77	0.82	0.18	0.14
-10.5	0.29	8.54	90.57	0.22	0.17	0.23	0.77	0.82	0.17	0.14
-9.0	0.28	8.52	90.53	0.27	0.18	0.23	0.77	0.81	0.22	0.14
-7.5	0.31	8.71	90.29	0.32	0.17	0.25	0.78	0.81	0.25	0.13
-6.0	0.34	8.77	90.09	0.36	0.23	0.27	0.79	0.81	0.29	0.19
-4.5	0.37	9.09	89.66	0.39	0.29	0.30	0.82	0.81	0.31	0.23
-3.0	0.40	9.29	89.30	0.44	0.36	0.32	0.84	0.80	0.36	0.29
-1.5	0.43	9.51	88.97	0.47	0.42	0.34	0.86	0.80	0.37	0.34
0.0	0.47	9.91	88.38	0.52	0.48	0.37	0.89	0.80	0.42	0.39
1.5	0.44	9.61	88.83	0.50	0.42	0.35	0.87	0.80	0.40	0.33
3.0	0.41	9.32	89.28	0.46	0.33	0.32	0.84	0.80	0.37	0.26
4.5	0.38	9.06	89.65	0.42	0.29	0.30	0.82	0.81	0.34	0.23
6.0	0.34	8.88	89.97	0.39	0.21	0.27	0.80	0.81	0.31	0.17
7.5	0.33	8.65	90.28	0.36	0.18	0.26	0.78	0.81	0.29	0.14
9.0	0.29	8.51	90.48	0.32	0.18	0.23	0.77	0.81	0.26	0.14
10.5	0.28	8.46	90.60	0.26	0.17	0.23	0.76	0.82	0.21	0.14
12.0	0.28	8.51	90.59	0.22	0.18	0.23	0.77	0.82	0.18	0.14
13.5	0.28	8.47	90.64	0.21	0.18	0.22	0.76	0.82	0.17	0.14
15.0	0.28	8.51	90.59	0.22	0.18	0.23	0.77	0.82	0.17	0.14
16.5	0.29	8.55	90.55	0.21	0.18	0.23	0.77	0.81	0.16	0.14
18.0	0.28	8.52	90.62	0.21	0.17	0.22	0.77	0.82	0.17	0.13
19.5	0.28	8.48	90.63	0.22	0.17	0.23	0.76	0.82	0.17	0.14
21.0	0.29	8.50	90.60	0.21	0.18	0.23	0.77	0.82	0.17	0.14
22.5	0.28	8.53	90.60	0.20	0.18	0.22	0.77	0.82	0.16	0.14
24.0	0.29	8.52	90.59	0.21	0.16	0.23	0.77	0.82	0.17	0.13
25.5	0.29	8.50	90.60	0.20	0.19	0.23	0.77	0.82	0.16	0.15
27.0	0.29	8.49	90.60	0.22	0.18	0.23	0.76	0.82	0.18	0.14
28.5	0.28	8.50	90.62	0.20	0.16	0.23	0.77	0.82	0.16	0.13
30.0	0.28	8.52	90.60	0.22	0.17	0.23	0.77	0.82	0.18	0.13
31.5	0.28	8.52	90.58	0.21	0.19	0.23	0.77	0.82	0.17	0.15

Table 5.7. Measured matrix and grain boundary concentrations from each line scan collected in as-received T91.

	Matrix Concentration (wt%)					**Grain Boundary Concentration (wt%)**					**Δ Concentration (wt%)**				
Scan ID	**Si**	**Cr**	**Fe**	**Ni**	**Cu**	**Si**	**Cr**	**Fe**	**Ni**	**Cu**	**Si**	**Cr**	**Fe**	**Ni**	**Cu**
T91_UI_1-1-F	0.28	8.39	89.19	0.21	0.17	0.28	8.40	89.20	0.22	0.17	0.00	0.01	0.01	0.01	0.00
T91_UI_1-2-F	0.28	8.36	89.23	0.21	0.17	0.28	8.35	89.27	0.21	0.17	0.00	-0.01	0.04	0.00	0.00
T91_UI_1-3-F	0.28	8.35	89.24	0.21	0.17	0.28	8.41	89.19	0.21	0.17	0.00	0.06	-0.06	0.00	0.00
T91_UI_2-1-F	0.28	8.37	89.22	0.21	0.17	0.28	8.36	89.21	0.21	0.17	0.00	0.00	-0.01	0.00	0.00
T91_UI_2-2-F	0.28	8.36	89.22	0.21	0.17	0.29	8.34	89.21	0.21	0.16	0.01	-0.02	-0.01	0.00	-0.01
T91_UI_2-3-F	0.28	8.36	89.22	0.21	0.17	0.28	8.39	89.17	0.21	0.17	0.00	0.03	-0.05	0.00	0.00
T91_UI_3-1-F	0.28	8.35	89.22	0.21	0.17	0.28	8.32	89.27	0.21	0.17	0.00	-0.03	0.05	0.00	0.00
T91_UI_3-2-F	0.28	8.40	89.20	0.21	0.17	0.28	8.36	89.22	0.21	0.17	0.00	-0.03	0.02	0.00	0.00
T91_UI_3-3-F	0.28	8.41	89.19	0.21	0.17	0.28	8.37	89.20	0.21	0.17	0.00	-0.04	0.01	0.00	0.00
T91_UI_4-1-F	0.28	8.42	89.14	0.21	0.17	0.28	8.45	89.09	0.21	0.17	0.00	0.03	-0.05	0.00	0.00
T91_UI_4-2-F	0.28	8.37	89.23	0.21	0.17	0.28	8.39	89.18	0.21	0.17	0.00	0.02	-0.05	0.00	0.00
T91_UI_4-3-F	0.28	8.38	89.21	0.21	0.17	0.28	8.35	89.22	0.21	0.18	-0.01	-0.03	0.01	0.00	0.01
T91_UI_4-4-F	0.28	8.38	89.22	0.21	0.17	0.28	8.35	89.27	0.21	0.16	0.00	-0.03	0.05	0.00	0.00

Table 5.8. Measured matrix and grain boundary concentrations from each line scan collected in as-received HT9.

	Matrix Concentration (wt%)					**Grain Boundary Concentration (wt%)**					**Δ Concentration (wt%)**				
Scan ID	**Si**	**Cr**	**Fe**	**Ni**	**Cu**	**Si**	**Cr**	**Fe**	**Ni**	**Cu**	**Si**	**Cr**	**Fe**	**Ni**	**Cu**
HT9_UI_1-1-F	0.22	11.79	84.60	0.51	N.D.	0.25	11.83	84.57	0.50	N.D.	0.02	0.04	-0.03	-0.01	N.D.
HT9_UI_1-2-F	0.23	11.82	84.78	0.50	N.D.	0.22	11.78	84.82	0.47	N.D.	0.00	-0.04	0.04	-0.03	N.D.
HT9_UI_1-3-F	0.23	11.81	84.82	0.50	N.D.	0.23	11.83	84.80	0.43	N.D.	0.00	0.02	-0.02	-0.07	N.D.
HT9_UI_2-1-F	0.22	11.67	84.93	0.51	N.D.	0.22	11.72	84.94	0.50	N.D.	-0.01	0.05	0.01	0.00	N.D.
HT9_UI_2-2-F	0.23	11.63	85.07	0.51	N.D.	0.22	11.61	85.02	0.49	N.D.	0.00	-0.02	-0.05	-0.02	N.D.

N.D. = not detectable

Table 5.9. Measured matrix and grain boundary concentrations from each line scan collected in as-received HCM12A.

	Matrix Concentration (wt%)						**Grain Boundary Concentration (wt%)**						**Δ Concentration (wt%)**					
Scan ID	**Si**	**Cr**	**Fe**	**Ni**	**W**	**Cu**	**Si**	**Cr**	**Fe**	**Ni**	**W**	**Cu**	**Si**	**Cr**	**Fe**	**Ni**	**W**	**Cu**
HCM12A_UI_1-1-F	0.29	11.01	85.18	0.40	2.05	1.07	0.34	11.06	84.99	0.46	2.21	0.94	0.05	0.05	-0.19	0.06	0.16	-0.13
HCM12A_UI_1-2-F	0.29	11.03	85.15	0.40	2.05	1.08	0.30	11.16	84.98	0.44	1.98	1.14	0.01	0.13	-0.17	0.04	-0.07	0.06
HCM12A_UI_1-3-F	0.29	10.99	85.20	0.38	2.08	1.04	0.30	11.13	85.05	0.43	1.99	1.10	0.01	0.14	-0.15	0.05	-0.09	0.06
HCM12A_UI_2-1-F	0.29	11.03	85.17	0.38	2.10	1.04	0.25	11.00	85.16	0.40	2.03	1.16	-0.04	-0.03	-0.01	0.02	-0.07	0.12
HCM12A_UI_2-2-F	0.30	11.04	85.13	0.39	2.07	1.06	0.30	11.15	85.29	0.40	1.91	0.95	0.00	0.11	0.16	0.01	-0.16	-0.11
HCM12A_UI_2-3-F	0.30	10.99	85.20	0.40	2.09	1.03	0.28	11.01	85.09	0.40	2.06	1.16	-0.02	0.02	-0.11	0.00	-0.03	0.13
HCM12A_UI_3-1-F	0.30	11.02	85.09	0.39	2.10	1.10	0.27	11.10	85.07	0.39	1.98	1.19	-0.03	0.08	-0.02	0.00	-0.12	0.09
HCM12A_UI_3-2-F	0.29	10.99	85.24	0.37	2.05	1.05	0.26	11.08	84.98	0.47	2.07	1.14	-0.03	0.09	-0.26	0.10	0.02	0.09
HCM12A_UI_3-3-F	0.29	11.02	85.17	0.40	2.07	1.05	0.25	11.05	85.01	0.35	2.22	1.12	-0.04	0.03	-0.16	-0.05	0.15	0.07

Table 5.10. Measured matrix and grain boundary concentrations from each line scan collected in as-received 9Cr model alloy.

	Matrix Concentration (wt%)					**Grain Boundary Concentration (wt%)**					**Δ Concentration (wt%)**				
Scan ID	**Si**	**Cr**	**Fe**	**Ni**	**Cu**	**Si**	**Cr**	**Fe**	**Ni**	**Cu**	**Si**	**Cr**	**Fe**	**Ni**	**Cu**
9Cr_UI_1-1-F	N.D.	9.01	90.99	N.D.	N.D.	N.D.	8.97	91.03	N.D.	N.D.	N.D.	-0.04	0.04	N.D.	N.D.
9Cr_UI_1-2-F	N.D.	8.99	91.01	N.D.	N.D.	N.D.	9.03	90.97	N.D.	N.D.	N.D.	0.03	-0.03	N.D.	N.D.
9Cr_UI_1-3-F	N.D.	9.01	90.99	N.D.	N.D.	N.D.	9.00	91.00	N.D.	N.D.	N.D.	0.00	0.00	N.D.	N.D.
9Cr_UI_2-1-F	N.D.	8.99	91.01	N.D.	N.D.	N.D.	8.97	91.03	N.D.	N.D.	N.D.	-0.03	0.03	N.D.	N.D.
9Cr_UI_2-2-F	N.D.	9.00	91.00	N.D.	N.D.	N.D.	9.01	90.99	N.D.	N.D.	N.D.	0.01	-0.01	N.D.	N.D.
9Cr_UI_2-3-F	N.D.	9.00	91.00	N.D.	N.D.	N.D.	8.99	91.01	N.D.	N.D.	N.D.	-0.01	0.01	N.D.	N.D.

N.D. = not detectable

Table 5.11. Measured matrix and grain boundary concentrations from each line scan collected in T91 irradiated to 3 dpa at 300°C.

	Matrix Concentration (wt%)					**Grain Boundary Concentration (wt%)**					**Δ Concentration (wt%)**				
Scan ID	**Si**	**Cr**	**Fe**	**Ni**	**Cu**	**Si**	**Cr**	**Fe**	**Ni**	**Cu**	**Si**	**Cr**	**Fe**	**Ni**	**Cu**
T91_3dpa_300C_01-12_T_1-1-F	0.28	8.47	90.63	0.22	0.18	0.29	8.89	90.17	0.25	0.17	0.02	0.39	-0.46	0.04	0.00
T91_3dpa_300C_01-12_T_1-2-F	0.26	8.52	90.63	0.21	0.17	0.28	9.00	90.13	0.21	0.17	0.01	0.50	-0.50	-0.01	0.00
T91_3dpa_300C_01-12_T_1-3-S	n/a	n/a	n/a	n/a	n/a	0.28	8.94	90.16	0.24	0.17	0.01	0.45	-0.47	0.02	0.00
T91_3dpa_300C_01-12_T_1-4-S	n/a	n/a	n/a	n/a	n/a	0.29	9.08	90.02	0.24	0.15	0.02	0.59	-0.61	0.02	-0.02
T91_3dpa_300C_01-12_T_2-1-F	0.27	8.49	90.64	0.22	0.17	0.26	9.24	89.88	0.23	0.18	-0.02	0.75	-0.75	0.02	0.01
T91_3dpa_300C_01-12_T_2-2-F	0.28	8.49	90.63	0.21	0.17	0.27	9.14	89.95	0.24	0.17	-0.01	0.64	-0.68	0.03	0.00
T91_3dpa_300C_01-12_T_2-3-F	0.29	8.51	90.60	0.21	0.17	0.28	9.13	89.99	0.21	0.17	0.00	0.63	-0.63	0.00	0.00
T91_3dpa_300C_01-12_T_2-4-S	n/a	n/a	n/a	n/a	n/a	0.27	9.24	89.88	0.22	0.17	-0.01	0.75	-0.75	0.01	0.00
T91_3dpa_300C_01-12_T_2-5-S	n/a	n/a	n/a	n/a	n/a	0.29	9.33	89.74	0.23	0.18	0.01	0.83	-0.88	0.02	0.01

n/a = not applicable; short scans measure only the grain boundary concentrations, not the matrix concentrations

Table 5.12. Measured matrix and grain boundary concentrations from each line scan collected in T91 irradiated to 1 dpa at 400°C.

	Matrix Concentration (wt%)					**Grain Boundary Concentration (wt%)**					**Δ Concentration (wt%)**				
Scan ID	**Si**	**Cr**	**Fe**	**Ni**	**Cu**	**Si**	**Cr**	**Fe**	**Ni**	**Cu**	**Si**	**Cr**	**Fe**	**Ni**	**Cu**
T91_1dpa_400C_04-09_B_1-1-F	0.29	8.50	90.61	0.21	0.17	0.46	9.40	89.11	0.47	0.32	0.18	0.90	-1.49	0.26	0.15
T91_1dpa_400C_04-09_B_1-2-F	0.28	8.51	90.60	0.21	0.17	0.45	9.40	89.14	0.46	0.33	0.16	0.89	-1.47	0.25	0.16
T91_1dpa_400C_04-09_B_1-3-F	0.29	8.50	90.60	0.21	0.17	0.47	9.40	89.11	0.47	0.33	0.18	0.90	-1.50	0.26	0.15
T91_1dpa_400C_04-09_B_1-4-S	n/a	n/a	n/a	n/a	n/a	0.47	9.38	89.12	0.49	0.32	0.19	0.87	-1.49	0.27	0.15
T91_1dpa_400C_04-09_B_1-5-S	n/a	n/a	n/a	n/a	n/a	0.47	9.41	89.09	0.48	0.33	0.18	0.90	-1.52	0.27	0.16
T91_1dpa_400C_04-09_B_1-6-S	n/a	n/a	n/a	n/a	n/a	0.47	9.42	89.11	0.45	0.32	0.19	0.92	-1.50	0.24	0.15
T91_1dpa_400C_04-09_B_1-7-S	n/a	n/a	n/a	n/a	n/a	0.45	9.37	89.18	0.45	0.32	0.17	0.87	-1.43	0.24	0.15
T91_1dpa_400C_04-09_B_1-8-S	n/a	n/a	n/a	n/a	n/a	0.47	9.36	89.16	0.45	0.33	0.19	0.86	-1.44	0.24	0.15
T91_1dpa_400C_04-09_B_2-1-F	0.28	8.50	90.61	0.21	0.17	0.48	9.12	89.39	0.46	0.33	0.20	0.61	-1.22	0.24	0.16
T91_1dpa_400C_04-09_B_2-2-F	0.28	8.51	90.60	0.21	0.17	0.47	9.02	89.49	0.47	0.33	0.19	0.51	-1.12	0.25	0.15
T91_1dpa_400C_04-09_B_2-3-S	n/a	n/a	n/a	n/a	n/a	0.47	9.05	89.46	0.47	0.33	0.19	0.55	-1.15	0.25	0.15
T91_1dpa_400C_04-09_B_2-4-S	n/a	n/a	n/a	n/a	n/a	0.48	9.06	89.42	0.48	0.33	0.20	0.55	-1.18	0.26	0.16
T91_1dpa_400C_04-09_B_2-5-S	n/a	n/a	n/a	n/a	n/a	0.45	9.03	89.51	0.46	0.32	0.17	0.52	-1.09	0.24	0.15
T91_1dpa_400C_04-09_B_2-6-S	n/a	n/a	n/a	n/a	n/a	0.46	9.00	89.53	0.46	0.32	0.18	0.50	-1.08	0.25	0.15

n/a = not applicable; short scans measure only the grain boundary concentrations, not the matrix concentrations

Table 5.13. Measured matrix and grain boundary concentrations from each line scan collected in T91 irradiated to 3 dpa at 400°C.

	Matrix Concentration (wt%)					Grain Boundary Concentration (wt%)					Δ Concentration (wt%)				
Scan ID	**Si**	**Cr**	**Fe**	**Ni**	**Cu**	**Si**	**Cr**	**Fe**	**Ni**	**Cu**	**Si**	**Cr**	**Fe**	**Ni**	**Cu**
T91_3dpa_400C_12-07_M_1-1-F	0.27	8.57	90.56	0.20	0.16	0.61	10.28	87.94	0.65	0.27	0.34	1.71	-2.62	0.45	0.11
T91_3dpa_400C_12-07_M_1-2-F	0.27	8.55	90.52	0.19	0.17	0.62	10.20	87.85	0.71	0.30	0.35	1.65	-2.67	0.52	0.13
T91_3dpa_400C_12-07_M_2-1-F	0.27	8.55	90.52	0.21	0.16	0.47	9.82	88.74	0.44	0.24	0.20	1.27	-1.78	0.23	0.08
T91_3dpa_400C_12-07_M_2-2-F	0.28	8.50	90.51	0.19	0.17	0.49	9.83	88.59	0.46	0.26	0.21	1.33	-1.92	0.27	0.09
T91_3dpa_400C_12-07_M_2-3-F	0.27	8.53	90.57	0.20	0.16	0.51	9.83	88.69	0.45	0.23	0.24	1.30	-1.88	0.25	0.07
T91_3dpa_400C_12-07_M_3-1-F	0.27	8.55	90.52	0.20	0.17	0.58	10.12	87.97	0.67	0.36	0.31	1.57	-2.55	0.47	0.19
T91_3dpa_400C_12-07_M_3-2-F	0.28	8.51	90.58	0.21	0.15	0.57	10.14	88.04	0.64	0.32	0.29	1.63	-2.54	0.43	0.17

Table 5.14. Measured matrix and grain boundary concentrations from each line scan collected in T91 irradiated to 7 dpa at 400°C.

	Matrix Concentration (wt%)					**Grain Boundary Concentration (wt%)**					**Δ Concentration (wt%)**				
Scan ID	**Si**	**Cr**	**Fe**	**Ni**	**Cu**	**Si**	**Cr**	**Fe**	**Ni**	**Cu**	**Si**	**Cr**	**Fe**	**Ni**	**Cu**
T91_7dpa_400C_01-08_B_1-1-F	0.27	8.53	90.59	0.20	0.17	0.48	9.90	88.37	0.52	0.49	0.21	1.37	-2.22	0.32	0.32
T91_7dpa_400C_01-08_B_1-2-F	0.27	8.50	90.64	0.20	0.16	0.50	9.90	88.35	0.54	0.46	0.23	1.40	-2.29	0.34	0.30
T91_7dpa_400C_01-08_B_2-1-F	0.27	8.50	90.62	0.20	0.18	0.46	9.73	88.82	0.38	0.37	0.19	1.23	-1.80	0.18	0.19
T91_7dpa_400C_01-08_B_2-2-F	0.28	8.53	90.58	0.21	0.17	0.48	9.79	88.74	0.36	0.38	0.20	1.26	-1.84	0.15	0.21
T91_7dpa_400C_01-08_B_3-1-F	0.27	8.54	90.56	0.21	0.16	0.48	10.33	87.96	0.56	0.41	0.21	1.79	-2.60	0.35	0.25
T91_7dpa_400C_01-08_B_3-2-F	0.28	8.58	90.57	0.19	0.16	0.52	10.43	87.92	0.52	0.37	0.24	1.85	-2.65	0.33	0.21
T91_7dpa_400C_01-12_M_1-1-F	0.28	8.51	90.60	0.22	0.17	0.50	10.30	88.08	0.53	0.35	0.21	1.79	-2.52	0.32	0.18
T91_7dpa_400C_01-12_M_1-2-F	0.29	8.50	90.60	0.21	0.18	0.52	10.13	88.23	0.52	0.36	0.24	1.62	-2.37	0.30	0.19
T91_7dpa_400C_01-12_M_1-3-F	0.28	8.51	90.60	0.21	0.17	0.50	10.15	88.22	0.53	0.35	0.21	1.65	-2.38	0.31	0.18
T91_7dpa_400C_01-12_M_1-4-F	0.29	8.50	90.61	0.21	0.17	0.50	10.36	88.03	0.50	0.36	0.22	1.86	-2.57	0.29	0.19
T91_7dpa_400C_01-12_M_1-5-F	0.28	8.50	90.61	0.21	0.17	0.50	10.15	88.22	0.53	0.36	0.21	1.64	-2.38	0.32	0.18
T91_7dpa_400C_01-12_M_1-6-F	0.28	8.50	90.61	0.22	0.17	0.53	10.59	87.69	0.54	0.38	0.25	2.09	-2.91	0.33	0.21
T91_7dpa_400C_01-12_M_2-1-F	0.29	8.51	90.60	0.21	0.17	0.52	10.71	87.59	0.55	0.37	0.23	2.20	-3.01	0.33	0.20
T91_7dpa_400C_01-12_M_2-2-F	0.29	8.51	90.59	0.21	0.17	0.50	10.30	88.09	0.52	0.35	0.22	1.79	-2.51	0.30	0.18
T91_7dpa_400C_01-12_M_2-3-F	0.28	8.51	90.60	0.21	0.17	0.52	10.09	88.27	0.52	0.35	0.23	1.59	-2.33	0.31	0.18
T91_7dpa_400C_01-12_M_3-1-F	0.28	8.51	90.60	0.21	0.17	0.50	9.60	88.77	0.52	0.37	0.22	1.09	-1.83	0.31	0.19
T91_7dpa_400C_01-12_M_3-2-F	0.29	8.51	90.60	0.21	0.17	0.51	9.67	88.70	0.52	0.36	0.22	1.16	-1.91	0.31	0.19
T91_7dpa_400C_01-12_M_3-3-F	0.28	8.51	90.60	0.21	0.17	0.52	10.36	88.02	0.50	0.37	0.23	1.85	-2.59	0.29	0.19

Table 5.15. Measured matrix and grain boundary concentrations from each line scan collected in T91 irradiated to 10 dpa at 400°C.

	Matrix Concentration (wt%)					**Grain Boundary Concentration (wt%)**					**Δ Concentration (wt%)**				
Scan ID	**Si**	**Cr**	**Fe**	**Ni**	**Cu**	**Si**	**Cr**	**Fe**	**Ni**	**Cu**	**Si**	**Cr**	**Fe**	**Ni**	**Cu**
T91_10dpa_400C_01-08_M_1-1-F	0.30	8.51	90.59	0.21	0.18	0.39	9.69	89.22	0.40	0.27	0.09	1.18	-1.37	0.19	0.09
T91_10dpa_400C_01-08_M_1-2-F	0.29	8.49	90.58	0.22	0.18	0.44	9.51	89.36	0.40	0.26	0.15	1.02	-1.22	0.18	0.08
T91_10dpa_400C_01-08_M_1-3-F	0.29	8.50	90.27	0.21	0.18	0.45	9.86	88.84	0.36	0.29	0.16	1.36	-1.43	0.15	0.10
T91_10dpa_400C_01-08_M_2-1-F	0.30	8.50	90.58	0.20	0.18	0.41	9.44	89.62	0.38	0.21	0.11	0.94	-0.96	0.18	0.03
T91_10dpa_400C_01-08_M_2-2-F	0.30	8.51	90.58	0.22	0.18	0.46	9.33	89.66	0.41	0.24	0.16	0.82	-0.92	0.19	0.06
T91_10dpa_400C_01-08_M_2-3-F	0.30	8.50	90.58	0.21	0.17	0.42	9.39	89.63	0.42	0.19	0.12	0.89	-0.95	0.21	0.02
T91_10dpa_400C_01-08_T_3-1-F	0.30	8.49	90.58	0.21	0.18	0.47	9.08	89.93	0.42	0.24	0.17	0.59	-0.65	0.21	0.06
T91_10dpa_400C_01-08_T_3-2-F	0.29	8.50	90.57	0.21	0.18	0.43	9.08	89.87	0.37	0.28	0.14	0.58	-0.70	0.16	0.10
T91_10dpa_400C_01-08_T_3-3-F	0.30	8.51	90.56	0.12	0.17	0.45	9.01	89.99	0.29	0.20	0.15	0.50	-0.57	0.17	0.03
T91_10dpa_400C_01-08_T_4-1-F	0.30	8.49	90.59	0.20	0.18	0.46	9.48	89.47	0.51	0.24	0.16	0.99	-1.12	0.31	0.06
T91_10dpa_400C_01-08_T_4-2-F	0.29	8.51	90.59	0.20	0.17	0.52	9.49	89.56	0.42	0.20	0.23	0.98	-1.03	0.22	0.03
T91_10dpa_400C_01-08_T_4-3-F	0.31	8.51	90.59	0.20	0.18	0.43	9.65	89.39	0.32	0.22	0.12	1.14	-1.20	0.12	0.04
T91_10dpa_400C_01-08_T_5-1-F	0.30	8.49	90.58	0.21	0.18	0.54	9.24	89.77	0.54	0.31	0.24	0.75	-0.81	0.33	0.13
T91_10dpa_400C_01-08_T_5-2-F	0.30	8.51	90.59	0.20	0.19	0.46	9.18	89.87	0.45	0.31	0.16	0.67	-0.72	0.25	0.12
T91_10dpa_400C_01-08_T_5-3-F	0.31	8.50	90.58	0.21	0.17	0.49	9.21	89.79	0.40	0.24	0.18	0.71	-0.79	0.19	0.07

Table 5.16. Measured matrix and grain boundary concentrations from each line scan collected in T91 irradiated to 3 dpa at 450°C.

	Matrix Concentration (wt%)					**Grain Boundary Concentration (wt%)**					**Δ Concentration (wt%)**				
Scan ID	**Si**	**Cr**	**Fe**	**Ni**	**Cu**	**Si**	**Cr**	**Fe**	**Ni**	**Cu**	**Si**	**Cr**	**Fe**	**Ni**	**Cu**
T91_3dpa_450C_10-11_M_1-1-F	0.28	8.50	90.62	0.21	0.17	0.53	10.29	88.04	0.54	0.36	0.24	1.79	-2.57	0.32	0.19
T91_3dpa_450C_10-11_M_1-2-F	0.28	8.51	90.60	0.21	0.17	0.53	10.24	88.10	0.53	0.36	0.25	1.73	-2.51	0.32	0.18
T91_3dpa_450C_10-11_M_1-3-F	0.29	8.51	90.60	0.21	0.17	0.49	10.14	88.25	0.51	0.36	0.21	1.63	-2.35	0.30	0.19
T91_3dpa_450C_10-11_M_1-4-F	0.28	8.51	90.60	0.21	0.18	0.52	10.19	88.17	0.51	0.36	0.24	1.69	-2.44	0.29	0.19
T91_3dpa_450C_10-11_M_1-5-S	n/a	n/a	n/a	n/a	n/a	0.53	10.19	88.17	0.50	0.36	0.24	1.69	-2.44	0.29	0.19
T91_3dpa_450C_10-11_M_1-6-S	n/a	n/a	n/a	n/a	n/a	0.52	10.23	88.11	0.53	0.36	0.24	1.72	-2.49	0.32	0.19
T91_3dpa_450C_10-11_M_1-7-S	n/a	n/a	n/a	n/a	n/a	0.53	10.26	88.10	0.51	0.36	0.24	1.75	-2.50	0.30	0.18
T91_3dpa_450C_10-11_M_1-8-S	n/a	n/a	n/a	n/a	n/a	0.49	10.24	88.16	0.51	0.36	0.21	1.73	-2.44	0.30	0.18
T91_3dpa_450C_10-11_M_1-9-S	n/a	n/a	n/a	n/a	n/a	0.51	10.19	88.21	0.50	0.35	0.22	1.68	-2.39	0.29	0.18
T91_3dpa_450C_10-11_M_2-1-F	0.29	8.51	90.60	0.21	0.17	0.50	10.25	88.14	0.50	0.35	0.22	1.75	-2.46	0.29	0.18
T91_3dpa_450C_10-11_M_2-2-F	0.28	8.51	90.60	0.22	0.17	0.53	10.24	88.13	0.50	0.35	0.24	1.73	-2.47	0.29	0.18
T91_3dpa_450C_10-11_M_2-3-S	n/a	n/a	n/a	n/a	n/a	0.52	10.26	88.09	0.53	0.35	0.23	1.75	-2.51	0.31	0.18
T91_3dpa_450C_10-11_M_2-4-S	n/a	n/a	n/a	n/a	n/a	0.52	10.21	88.15	0.52	0.35	0.23	1.70	-2.45	0.31	0.18
T91_3dpa_450C_10-11_M_2-5-S	n/a	n/a	n/a	n/a	n/a	0.53	10.23	88.11	0.53	0.36	0.24	1.72	-2.49	0.32	0.19
T91_3dpa_450C_10-11_M_2-6-S	n/a	n/a	n/a	n/a	n/a	0.51	10.26	88.13	0.50	0.37	0.22	1.75	-2.48	0.28	0.19

n/a = not applicable; short scans measure only the grain boundary concentrations, not the matrix concentrations

Table 5.17. Measured matrix and grain boundary concentrations from each line scan collected in T91 irradiated to 3 dpa at 500°C.

	Matrix Concentration (wt%)					**Grain Boundary Concentration (wt%)**					**Δ Concentration (wt%)**				
Scan ID	**Si**	**Cr**	**Fe**	**Ni**	**Cu**	**Si**	**Cr**	**Fe**	**Ni**	**Cu**	**Si**	**Cr**	**Fe**	**Ni**	**Cu**
T91_3dpa_500C_07-08_B_1-1-F	0.26	8.55	90.59	0.19	0.16	0.51	9.75	88.82	0.46	0.19	0.25	1.20	-1.77	0.27	0.03
T91_3dpa_500C_07-08_B_1-2-F	0.25	8.52	90.63	0.21	0.17	0.52	9.70	88.80	0.50	0.22	0.27	1.18	-1.83	0.29	0.05
T91_3dpa_500C_07-08_T_2-1-F	0.27	8.56	90.58	0.20	0.16	0.44	9.95	88.79	0.42	0.16	0.17	1.39	-1.79	0.22	0.00
T91_3dpa_500C_07-08_T_2-2-F	0.26	8.54	90.61	0.19	0.16	0.45	9.95	88.74	0.42	0.18	0.19	1.41	-1.87	0.23	0.02
T91_3dpa_500C_07-08_T_2-3-F	0.26	8.58	90.56	0.18	0.18	0.46	10.04	88.48	0.48	0.21	0.20	1.46	-2.08	0.30	0.03
T91_3dpa_500C_07-08_T_2-4-F	0.26	8.54	90.59	0.19	0.19	0.49	10.01	88.55	0.47	0.20	0.23	1.47	-2.04	0.28	0.01

Table 5.18. Measured matrix and grain boundary concentrations from each line scan collected in T91 irradiated to 3 dpa at 600°C.

	Matrix Concentration (wt%)					**Grain Boundary Concentration (wt%)**					**Δ Concentration (wt%)**				
Scan ID	**Si**	**Cr**	**Fe**	**Ni**	**Cu**	**Si**	**Cr**	**Fe**	**Ni**	**Cu**	**Si**	**Cr**	**Fe**	**Ni**	**Cu**
T91_3dpa_600C_01-12_B_1-1-F	0.30	8.49	90.56	0.21	0.18	0.30	9.23	89.70	0.23	0.19	0.01	0.72	-0.90	0.02	0.01
T91_3dpa_600C_01-12_B_1-2-F	0.29	8.42	90.67	0.21	0.18	0.30	9.42	89.32	0.21	0.19	0.02	0.91	-1.27	0.00	0.02
T91_3dpa_600C_01-12_B_1-3-F	0.26	8.64	90.55	0.22	0.16	0.27	9.23	89.86	0.23	0.16	-0.01	0.71	-0.73	0.01	-0.01
T91_3dpa_600C_01-12_B_2-1-F	0.29	8.48	90.58	0.23	0.18	0.30	9.09	89.75	0.25	0.19	0.02	0.56	-0.84	0.03	0.02
T91_3dpa_600C_01-12_B_2-2-F	0.26	8.57	90.59	0.22	0.17	0.27	8.97	90.14	0.23	0.19	-0.01	0.44	-0.45	0.01	0.01
T91_3dpa_600C_01-12_B_2-3-S	n/a	n/a	n/a	n/a	n/a	0.25	8.97	90.10	0.21	0.17	-0.03	0.45	-0.49	-0.01	-0.01
T91_3dpa_600C_01-12_B_2-4-S	n/a	n/a	n/a	n/a	n/a	0.27	9.21	89.89	0.22	0.16	-0.01	0.68	-0.69	0.00	-0.01

n/a = not applicable; short scans measure only the grain boundary concentrations, not the matrix concentrations

Table 5.19. Measured matrix and grain boundary concentrations from each line scan collected in T91 irradiated to 3 dpa at 700°C.

	Matrix Concentration (wt%)					**Grain Boundary Concentration (wt%)**					**Δ Concentration (wt%)**				
Scan ID	**Si**	**Cr**	**Fe**	**Ni**	**Cu**	**Si**	**Cr**	**Fe**	**Ni**	**Cu**	**Si**	**Cr**	**Fe**	**Ni**	**Cu**
T91_3dpa_700C_05-12_MM_1-1-F	0.28	8.54	90.58	0.21	0.17	0.26	8.18	90.96	0.22	0.18	-0.01	-0.36	0.38	0.01	0.00
T91_3dpa_700C_05-12_MM_1-2-F	0.28	8.55	90.57	0.22	0.17	0.29	8.09	91.00	0.22	0.20	0.01	-0.46	0.44	0.00	0.04
T91_3dpa_700C_05-12_MM_1-3-S	n/a	n/a	n/a	n/a	n/a	0.35	8.34	90.66	0.24	0.19	0.07	-0.21	0.08	0.02	0.02
T91_3dpa_700C_05-12_MM_1-4-S	n/a	n/a	n/a	n/a	n/a	0.33	8.12	90.94	0.21	0.17	0.05	-0.42	0.37	0.00	0.00
T91_3dpa_700C_05-12_MM_2-1-F	0.30	8.50	90.57	0.22	0.18	0.33	8.20	90.81	0.25	0.18	0.02	-0.31	0.24	0.03	0.00
T91_3dpa_700C_05-12_MM_2-2-F	0.26	8.53	90.59	0.23	0.17	0.28	8.08	91.04	0.18	0.19	0.02	-0.44	0.45	-0.04	0.02
T91_3dpa_700C_05-12_MM_2-3-S	n/a	n/a	n/a	n/a	n/a	0.27	8.05	91.08	0.18	0.19	-0.01	-0.47	0.50	-0.03	0.01
T91_3dpa_700C_05-12_MM_2-4-S	n/a	n/a	n/a	n/a	n/a	0.38	7.93	91.06	0.22	0.19	0.10	-0.58	0.48	0.01	0.01
T91_3dpa_700C_05-12_MM_3-1-F	0.29	8.49	90.58	0.24	0.19	0.27	8.01	91.13	0.23	0.18	-0.02	-0.49	0.55	-0.01	-0.02
T91_3dpa_700C_05-12_MM_3-2-F	0.30	8.47	90.57	0.26	0.20	0.28	7.88	91.17	0.26	0.21	-0.02	-0.59	0.60	0.00	0.01

n/a = not applicable; short scans measure only the grain boundary concentrations, not the matrix concentrations

Table 5.20. Measured matrix and grain boundary concentrations from each line scan collected in 9Cr model alloy irradiated to 1 dpa at 400°C.

	Matrix Concentration (wt%)					Grain Boundary Concentration (wt%)					Δ Concentration (wt%)				
Scan ID	**Si**	**Cr**	**Fe**	**Ni**	**Cu**	**Si**	**Cr**	**Fe**	**Ni**	**Cu**	**Si**	**Cr**	**Fe**	**Ni**	**Cu**
9Cr_1dpa_400C_04-09_M_1-1-F	N.D.	9.05	90.95	N.D.	N.D.	N.D.	9.82	90.18	N.D.	N.D.	N.D.	0.77	-0.77	N.D.	N.D.
9Cr_1dpa_400C_04-09_M_1-2-F	N.D.	8.94	91.06	N.D.	N.D.	N.D.	9.65	90.35	N.D.	N.D.	N.D.	0.71	-0.71	N.D.	N.D.
9Cr_1dpa_400C_04-09_M_1-3-F	N.D.	8.99	91.01	N.D.	N.D.	N.D.	9.76	90.24	N.D.	N.D.	N.D.	0.77	-0.77	N.D.	N.D.
9Cr_1dpa_400C_04-09_M_2-1-F	N.D.	9.06	90.94	N.D.	N.D.	N.D.	9.06	90.94	N.D.	N.D.	N.D.	0.00	0.00	N.D.	N.D.
9Cr_1dpa_400C_04-09_M_2-2-F	N.D.	9.12	90.88	N.D.	N.D.	N.D.	9.58	90.42	N.D.	N.D.	N.D.	0.46	-0.46	N.D.	N.D.
9Cr_1dpa_400C_04-09_M_2-3-F	N.D.	8.96	91.04	N.D.	N.D.	N.D.	9.49	90.51	N.D.	N.D.	N.D.	0.53	-0.53	N.D.	N.D.
9Cr_1dpa_400C_04-09_M_3-1-F	N.D.	8.85	91.15	N.D.	N.D.	N.D.	9.52	90.48	N.D.	N.D.	N.D.	0.67	-0.67	N.D.	N.D.
9Cr_1dpa_400C_04-09_M_3-2-F	N.D.	9.01	90.99	N.D.	N.D.	N.D.	10.01	89.99	N.D.	N.D.	N.D.	1.00	-1.00	N.D.	N.D.
9Cr_1dpa_400C_04-09_M_3-3-F	N.D.	8.81	91.19	N.D.	N.D.	N.D.	9.36	90.64	N.D.	N.D.	N.D.	0.54	-0.54	N.D.	N.D.

N.D. = not detectable

Table 5.21. Measured matrix and grain boundary concentrations from each line scan collected in 9Cr model alloy irradiated to 3 dpa at 400°C.

	Matrix Concentration (wt%)					Grain Boundary Concentration (wt%)					Δ Concentration (wt%)				
Scan ID	**Si**	**Cr**	**Fe**	**Ni**	**Cu**	**Si**	**Cr**	**Fe**	**Ni**	**Cu**	**Si**	**Cr**	**Fe**	**Ni**	**Cu**
9Cr_3dpa_400C_01-12_B_1-1-F	N.D.	9.00	91.00	N.D.	N.D.	N.D.	9.72	90.28	N.D.	N.D.	N.D.	0.72	-0.72	N.D.	N.D.
9Cr_3dpa_400C_01-12_B_1-2-F	N.D.	9.01	90.99	N.D.	N.D.	N.D.	9.82	90.18	N.D.	N.D.	N.D.	0.82	-0.82	N.D.	N.D.
9Cr_3dpa_400C_01-12_B_1-3-F	N.D.	9.00	91.00	N.D.	N.D.	N.D.	9.80	90.20	N.D.	N.D.	N.D.	0.80	-0.80	N.D.	N.D.
9Cr_3dpa_400C_01-12_B_1-4-F	N.D.	9.00	91.00	N.D.	N.D.	N.D.	9.86	90.14	N.D.	N.D.	N.D.	0.86	-0.86	N.D.	N.D.
9Cr_3dpa_400C_01-12_B_1-5-S	n/a	n/a	n/a	n/a	n/a	N.D.	9.87	90.13	N.D.	N.D.	N.D.	0.87	-0.87	N.D.	N.D.
9Cr_3dpa_400C_01-12_B_1-6-S	n/a	n/a	n/a	n/a	n/a	N.D.	9.83	90.17	N.D.	N.D.	N.D.	0.83	-0.83	N.D.	N.D.
9Cr_3dpa_400C_01-12_B_1-7-S	n/a	n/a	n/a	n/a	n/a	N.D.	9.79	90.21	N.D.	N.D.	N.D.	0.79	-0.79	N.D.	N.D.
9Cr_3dpa_400C_01-12_B_1-8-S	n/a	n/a	n/a	n/a	n/a	N.D.	9.80	90.20	N.D.	N.D.	N.D.	0.80	-0.80	N.D.	N.D.
9Cr_3dpa_400C_01-12_B_1-9-S	n/a	n/a	n/a	n/a	n/a	N.D.	9.79	90.21	N.D.	N.D.	N.D.	0.79	-0.79	N.D.	N.D.
9Cr_3dpa_400C_01-12_B_2-1-F	N.D.	9.00	91.00	N.D.	N.D.	N.D.	9.72	90.28	N.D.	N.D.	N.D.	0.72	-0.72	N.D.	N.D.
9Cr_3dpa_400C_01-12_B_2-2-F	N.D.	9.00	91.00	N.D.	N.D.	N.D.	9.73	90.27	N.D.	N.D.	N.D.	0.73	-0.73	N.D.	N.D.
9Cr_3dpa_400C_01-12_B_2-3-S	n/a	n/a	n/a	n/a	n/a	N.D.	9.74	90.26	N.D.	N.D.	N.D.	0.74	-0.74	N.D.	N.D.
9Cr_3dpa_400C_01-12_B_2-4-S	n/a	n/a	n/a	n/a	n/a	N.D.	9.76	90.24	N.D.	N.D.	N.D.	0.77	-0.77	N.D.	N.D.
9Cr_3dpa_400C_01-12_B_2-5-S	n/a	n/a	n/a	n/a	n/a	N.D.	9.70	90.30	N.D.	N.D.	N.D.	0.70	-0.70	N.D.	N.D.
9Cr_3dpa_400C_01-12_B_2-6-S	n/a	n/a	n/a	n/a	n/a	N.D.	9.77	90.23	N.D.	N.D.	N.D.	0.77	-0.77	N.D.	N.D.

N.D. = not detectable

n/a = not applicable; short scans measure only the grain boundary concentrations, not the matrix concentrations

Table 5.22. Measured matrix and grain boundary concentrations from each line scan collected in 9Cr model alloy irradiated to 7 dpa at 400°C.

	Matrix Concentration (wt%)					**Grain Boundary Concentration (wt%)**					**Δ Concentration (wt%)**				
Scan ID	**Si**	**Cr**	**Fe**	**Ni**	**Cu**	**Si**	**Cr**	**Fe**	**Ni**	**Cu**	**Si**	**Cr**	**Fe**	**Ni**	**Cu**
9Cr_7dpa_400C_04-09_T_1-1-F	N.D.	9.01	90.99	N.D.	N.D.	N.D.	10.25	89.75	N.D.	N.D.	N.D.	1.25	-1.25	N.D.	N.D.
9Cr_7dpa_400C_04-09_T_1-2-F	N.D.	9.00	91.00	N.D.	N.D.	N.D.	10.32	89.68	N.D.	N.D.	N.D.	1.31	-1.31	N.D.	N.D.
9Cr_7dpa_400C_04-09_T_1-3-S	n/a	n/a	n/a	n/a	n/a	N.D.	10.30	89.70	N.D.	N.D.	N.D.	1.30	-1.30	N.D.	N.D.
9Cr_7dpa_400C_04-09_T_1-4-S	n/a	n/a	n/a	n/a	n/a	N.D.	10.31	89.69	N.D.	N.D.	N.D.	1.31	-1.31	N.D.	N.D.
9Cr_7dpa_400C_04-09_T_1-5-S	n/a	n/a	n/a	n/a	n/a	N.D.	10.31	89.69	N.D.	N.D.	N.D.	1.31	-1.31	N.D.	N.D.
9Cr_7dpa_400C_04-09_T_2-1-F	N.D.	8.99	91.01	N.D.	N.D.	N.D.	10.34	89.66	N.D.	N.D.	N.D.	1.34	-1.34	N.D.	N.D.
9Cr_7dpa_400C_04-09_T_2-2-F	N.D.	8.99	91.01	N.D.	N.D.	N.D.	10.34	89.66	N.D.	N.D.	N.D.	1.34	-1.34	N.D.	N.D.
9Cr_7dpa_400C_04-09_T_2-3-S	n/a	n/a	n/a	n/a	n/a	N.D.	10.31	89.69	N.D.	N.D.	N.D.	1.31	-1.31	N.D.	N.D.
9Cr_7dpa_400C_04-09_T_2-4-S	n/a	n/a	n/a	n/a	n/a	N.D.	10.55	89.45	N.D.	N.D.	N.D.	1.55	-1.55	N.D.	N.D.
9Cr_7dpa_400C_04-09_T_3-1-F	N.D.	9.00	91.00	N.D.	N.D.	N.D.	10.59	89.41	N.D.	N.D.	N.D.	1.59	-1.59	N.D.	N.D.
9Cr_7dpa_400C_04-09_T_3-2-F	N.D.	9.01	90.99	N.D.	N.D.	N.D.	10.59	89.41	N.D.	N.D.	N.D.	1.59	-1.59	N.D.	N.D.
9Cr_7dpa_400C_04-09_T_3-3-S	n/a	n/a	n/a	n/a	n/a	N.D.	10.55	89.45	N.D.	N.D.	N.D.	1.55	-1.55	N.D.	N.D.
9Cr_7dpa_400C_04-09_T_3-4-S	n/a	n/a	n/a	n/a	n/a	N.D.	10.56	89.44	N.D.	N.D.	N.D.	1.56	-1.56	N.D.	N.D.
9Cr_7dpa_400C_04-09_T_3-5-S	n/a	n/a	n/a	n/a	n/a	N.D.	10.52	89.48	N.D.	N.D.	N.D.	1.52	-1.52	N.D.	N.D.
9Cr_7dpa_400C_04-09_T_3-6-S	n/a	n/a	n/a	n/a	n/a	N.D.	10.61	89.39	N.D.	N.D.	N.D.	1.61	-1.61	N.D.	N.D.

N.D. = not detectable

n/a = not applicable; short scans measure only the grain boundary concentrations, not the matrix concentrations

Table 5.23. Measured matrix and grain boundary concentrations from each line scan collected in 9Cr model alloy irradiated to 10 dpa at 400°C.

	Matrix Concentration (wt%)					**Grain Boundary Concentration (wt%)**					**Δ Concentration (wt%)**				
Scan ID	**Si**	**Cr**	**Fe**	**Ni**	**Cu**	**Si**	**Cr**	**Fe**	**Ni**	**Cu**	**Si**	**Cr**	**Fe**	**Ni**	**Cu**
9Cr_10dpa_400C_01-12_T_1-1-F	N.D.	9.00	91.00	N.D.	N.D.	N.D.	10.79	89.21	N.D.	N.D.	N.D.	1.79	-1.79	N.D.	N.D.
9Cr_10dpa_400C_01-12_T_1-2-F	N.D.	8.99	91.01	N.D.	N.D.	N.D.	10.40	89.60	N.D.	N.D.	N.D.	1.40	-1.40	N.D.	N.D.
9Cr_10dpa_400C_01-12_T_1-3-F	N.D.	9.01	90.99	N.D.	N.D.	N.D.	10.30	89.70	N.D.	N.D.	N.D.	1.30	-1.30	N.D.	N.D.
9Cr_10dpa_400C_01-12_T_1-4-F	N.D.	9.00	91.00	N.D.	N.D.	N.D.	10.30	89.70	N.D.	N.D.	N.D.	1.30	-1.30	N.D.	N.D.
9Cr_10dpa_400C_01-12_T_1-5-S	n/a	n/a	n/a	n/a	n/a	N.D.	10.34	89.66	N.D.	N.D.	N.D.	1.34	-1.34	N.D.	N.D.
9Cr_10dpa_400C_01-12_T_1-6-S	n/a	n/a	n/a	n/a	n/a	N.D.	10.40	89.60	N.D.	N.D.	N.D.	1.40	-1.40	N.D.	N.D.
9Cr_10dpa_400C_01-12_T_1-7-S	n/a	n/a	n/a	n/a	n/a	N.D.	10.40	89.60	N.D.	N.D.	N.D.	1.40	-1.40	N.D.	N.D.
9Cr_10dpa_400C_01-12_T_1-8-S	n/a	n/a	n/a	n/a	n/a	N.D.	10.34	89.66	N.D.	N.D.	N.D.	1.34	-1.34	N.D.	N.D.
9Cr_10dpa_400C_01-12_T_2-1-F	N.D.	8.99	91.01	N.D.	N.D.	N.D.	10.66	89.34	N.D.	N.D.	N.D.	1.66	-1.66	N.D.	N.D.
9Cr_10dpa_400C_01-12_T_2-2-F	N.D.	9.00	91.00	N.D.	N.D.	N.D.	10.74	89.26	N.D.	N.D.	N.D.	1.74	-1.74	N.D.	N.D.
9Cr_10dpa_400C_01-12_T_2-3-S	n/a	n/a	n/a	n/a	n/a	N.D.	10.66	89.34	N.D.	N.D.	N.D.	1.66	-1.66	N.D.	N.D.
9Cr_10dpa_400C_01-12_T_2-4-S	n/a	n/a	n/a	n/a	n/a	N.D.	10.74	89.26	N.D.	N.D.	N.D.	1.74	-1.74	N.D.	N.D.
9Cr_10dpa_400C_01-12_T_2-5-S	n/a	n/a	n/a	n/a	n/a	N.D.	10.76	89.24	N.D.	N.D.	N.D.	1.76	-1.76	N.D.	N.D.
9Cr_10dpa_400C_01-12_T_2-6-S	n/a	n/a	n/a	n/a	n/a	N.D.	10.72	89.28	N.D.	N.D.	N.D.	1.72	-1.72	N.D.	N.D.

N.D. = not detectable

n/a = not applicable; short scans measure only the grain boundary concentrations, not the matrix concentrations

Table 5.24. Measured matrix and grain boundary concentrations from each line scan collected in HT9 irradiated to 3 dpa at 400°C.

	Matrix Concentration (wt%)					Grain Boundary Concentration (wt%)					Δ Concentration (wt%)				
Scan ID	**Si**	**Cr**	**Fe**	**Ni**	**Cu**	**Si**	**Cr**	**Fe**	**Ni**	**Cu**	**Si**	**Cr**	**Fe**	**Ni**	**Cu**
HT9_3dpa_400C_12-07_M_1-1-F	0.22	11.92	87.02	0.53	N.D.	0.27	12.57	85.77	1.11	N.D.	0.04	0.65	-1.26	0.59	N.D.
HT9_3dpa_400C_12-07_M_1-2-F	0.23	11.90	87.05	0.51	N.D.	0.27	12.59	85.66	1.19	N.D.	0.04	0.69	-1.39	0.68	N.D.
HT9_3dpa_400C_12-07_M_2-1-F	0.22	11.92	87.05	0.50	N.D.	0.26	12.46	85.86	1.12	N.D.	0.04	0.55	-1.19	0.62	N.D.
HT9_3dpa_400C_12-07_M_2-2-F	0.22	11.93	87.03	0.51	N.D.	0.26	12.68	85.73	1.04	N.D.	0.04	0.75	-1.30	0.53	N.D.
HT9_3dpa_400C_12-07_B_3-1-F	0.23	11.92	87.04	0.51	N.D.	0.26	12.66	85.68	1.10	N.D.	0.04	0.74	-1.36	0.59	N.D.
HT9_3dpa_400C_12-07_B_3-2-F	0.23	11.93	87.02	0.51	N.D.	0.26	12.68	85.71	1.05	N.D.	0.04	0.75	-1.31	0.54	N.D.
HT9_3dpa_400C_12-07_B_4-1-F	0.23	11.91	87.03	0.53	N.D.	0.26	12.67	85.66	1.11	N.D.	0.04	0.75	-1.36	0.59	N.D.
HT9_3dpa_400C_12-07_B_4-2-F	0.23	11.92	87.03	0.52	N.D.	0.26	12.57	85.81	1.07	N.D.	0.04	0.64	-1.22	0.55	N.D.

N.D. = not detectable

Table 5.25. Measured matrix and grain boundary concentrations from each line scan in HCM12A irradiated to 3 dpa at 400°C.

	Matrix Concentration (wt%)						Grain Boundary Concentration (wt%)						Δ Concentration (wt%)					
Scan ID	**Si**	**Cr**	**Fe**	**Ni**	**W**	**Cu**	**Si**	**Cr**	**Fe**	**Ni**	**W**	**Cu**	**Si**	**Cr**	**Fe**	**Ni**	**W**	**Cu**
HCM12A_3dpa_400C_12-07_M_1-1-F	0.27	11.00	85.28	0.41	1.92	1.13	0.32	11.73	82.83	0.55	1.87	2.70	0.05	0.73	-2.45	0.14	-0.05	1.58
HCM12A_3dpa_400C_12-07_M_1-2-F	0.27	10.96	85.24	0.39	1.86	1.28	0.29	11.54	82.13	0.60	2.21	3.23	0.02	0.59	-3.11	0.21	0.35	1.95
HCM12A_3dpa_400C_12-07_M_1-3-F	0.26	11.07	85.37	0.38	1.94	0.98	0.27	11.69	83.91	0.53	2.11	1.49	0.01	0.62	-1.46	0.15	0.17	0.51
HCM12A_3dpa_400C_12-07_M_2-1-F	0.27	11.09	85.42	0.37	1.89	0.96	0.35	12.19	83.29	0.43	2.21	1.53	0.08	1.10	-2.13	0.06	0.32	0.57
HCM12A_3dpa_400C_12-07_M_2-2-F	0.27	10.86	85.66	0.39	1.86	0.95	0.27	12.00	83.81	0.57	2.06	1.30	0.00	1.13	-1.85	0.18	0.19	0.35
HCM12A_3dpa_400C_12-07_M_2-3-F	0.28	10.83	85.68	0.40	1.88	0.93	0.35	11.89	83.76	0.52	2.17	1.30	0.08	1.06	-1.91	0.12	0.29	0.37
HCM12A_3dpa_400C_12-07_M_2-4-F	0.28	10.95	85.31	0.45	1.97	1.04	0.30	11.72	84.37	0.42	1.83	1.36	0.01	0.77	-0.95	-0.03	-0.13	0.33

Table 5.26. Average Δ concentration values and their standard deviations of the mean, taken over boundaries and conditions in T91.

Sample Designation	**Boundary (#) or condition (C) average?**	**Average Δ concentration (wt%) across all scans**					**Standard deviation of the mean (wt%)**				
		Si	**Cr**	**Fe**	**Ni**	**Cu**	**Si**	**Cr**	**Fe**	**Ni**	**Cu**
T91_UI	1	0.00	0.02	0.00	0.00	0.00	0.01	0.03	0.05	0.01	0.01
"	2	0.00	0.00	-0.02	0.00	0.00	0.01	0.02	0.02	0.01	0.01
"	3	0.00	-0.03	0.03	0.00	0.00	0.01	0.01	0.02	0.01	0.01
"	4	0.00	0.00	-0.01	0.00	0.00	0.01	0.03	0.05	0.01	0.01
"	C	0.00	0.00	0.00	0.00	0.00	0.01	0.03	0.04	0.01	0.01
T91_3dpa_300C_01-12	1	0.02	0.48	-0.51	0.02	-0.01	0.01	0.08	0.07	0.02	0.01
"	2	-0.01	0.72	-0.74	0.01	0.00	0.01	0.08	0.09	0.01	0.01
"	C	0.00	0.62	-0.63	0.02	0.00	0.02	0.15	0.14	0.01	0.01
T91_1dpa_400C_04-09	1	0.18	0.89	-1.48	0.25	0.15	0.01	0.02	0.03	0.01	0.01
"	2	0.19	0.54	-1.14	0.25	0.15	0.01	0.04	0.05	0.01	0.01
"	C	0.18	0.74	-1.33	0.25	0.15	0.01	0.18	0.18	0.01	0.01
T91_3dpa_400C_12-07	1	0.35	1.68	-2.65	0.49	0.12	0.01	0.04	0.04	0.05	0.01
"	2	0.22	1.30	-1.86	0.25	0.08	0.02	0.03	0.07	0.02	0.01
"	3	0.30	1.60	-2.55	0.45	0.18	0.01	0.04	0.01	0.03	0.01
"	C	0.28	1.49	-2.28	0.37	0.12	0.06	0.19	0.40	0.12	0.05
T91_7dpa_400C_01-08	1	0.22	1.39	-2.26	0.33	0.31	0.01	0.02	0.05	0.01	0.01
"	2	0.20	1.25	-1.82	0.17	0.20	0.01	0.02	0.03	0.02	0.01
"	3	0.23	1.82	-2.63	0.34	0.23	0.02	0.04	0.04	0.01	0.03
T91_7dpa_400C_01-12	1	0.22	1.77	-2.53	0.31	0.19	0.02	0.18	0.21	0.01	0.01
"	2	0.23	1.86	-2.62	0.32	0.19	0.01	0.31	0.35	0.02	0.01
"	3	0.22	1.37	-2.11	0.30	0.19	0.01	0.42	0.41	0.01	0.01

Table 5.26 – continued

Sample Designation	Boundary (#) or condition (C) average?	Average Δconcentration (wt%) across all scans					Standard deviation of the mean (wt%)				
		Si	Cr	Fe	Ni	Cu	Si	Cr	Fe	Ni	Cu
T91_7dpa_400C_01-12 (cont'd)	C	0.22	1.62	-2.37	0.30	0.21	0.02	0.32	0.35	0.05	0.04
T91_10dpa_400C_01-08	1	0.13	1.19	-1.34	0.17	0.09	0.04	0.17	0.11	0.02	0.01
"	2	0.13	0.88	-0.94	0.19	0.04	0.03	0.06	0.02	0.02	0.02
"	3	0.15	0.56	-0.64	0.18	0.06	0.02	0.05	0.07	0.03	0.04
"	4	0.17	1.04	-1.12	0.22	0.04	0.06	0.09	0.09	0.10	0.02
"	5	0.19	0.71	-0.77	0.26	0.11	0.04	0.04	0.05	0.07	0.03
"	C	0.16	0.87	-0.96	0.20	0.07	0.04	0.25	0.26	0.06	0.03
T91_3dpa_450C_10-11	1	0.23	1.71	-2.46	0.30	0.19	0.02	0.04	0.06	0.01	0.01
"	2	0.23	1.73	-2.47	0.30	0.18	0.01	0.02	0.02	0.02	0.01
"	C	0.23	1.72	-2.46	0.30	0.18	0.01	0.04	0.05	0.01	0.01
T91_3dpa_500C_07-08	1	0.26	1.19	-1.80	0.28	0.04	0.01	0.01	0.04	0.01	0.01
"	2	0.20	1.43	-1.95	0.26	0.02	0.02	0.04	0.14	0.04	0.01
"	C	0.22	1.35	-1.90	0.27	0.02	0.04	0.13	0.13	0.03	0.02
T91_3dpa_600C_01-12	1	0.01	0.78	-0.97	0.01	0.01	0.02	0.11	0.28	0.01	0.02
"	2	-0.01	0.53	-0.62	0.01	0.00	0.02	0.11	0.18	0.02	0.01
"	C	0.00	0.64	-0.77	0.01	0.00	0.02	0.17	0.28	0.01	0.01
T91_3dpa_700C_05-12	1	0.03	-0.36	0.32	0.01	-0.01	0.02	0.04	0.11	0.16	0.01
"	2	0.03	-0.45	0.42	-0.01	0.00	0.01	0.05	0.11	0.12	0.03
"	3	-0.02	-0.54	0.58	-0.01	-0.01	0.00	0.00	0.07	0.04	0.01
"	C	0.02	-0.43	0.41	0.00	-0.01	0.01	0.04	0.12	0.15	0.02

Table 5.27. Average Δ concentration values and their standard deviations of the mean, taken over boundaries and conditions in 9Cr model alloy.

Sample Designation	Boundary (#) or condition (C) average?	Average Δ concentration (wt%) across all scans					Standard deviation of the mean (wt%)				
		Si	Cr	Fe	Ni	Cu	Si	Cr	Fe	Ni	Cu
9Cr_UI	1	N.D.	0.00	0.00	N.D.	N.D.	N.D.	0.03	0.03	N.D.	N.D.
“	2	N.D.	-0.01	0.01	N.D.	N.D.	N.D.	0.02	0.02	N.D.	N.D.
“	C	N.D.	-0.01	0.01	N.D.	N.D.	N.D.	0.02	0.02	N.D.	N.D.
9Cr_1dpa_400C_04-09	1	N.D.	0.75	-0.75	N.D.	N.D.	N.D.	0.03	0.03	N.D.	N.D.
“	2	N.D.	0.33	-0.33	N.D.	N.D.	N.D.	0.29	0.29	N.D.	N.D.
“	3	N.D.	-0.74	0.74	N.D.	N.D.	N.D.	0.24	0.24	N.D.	N.D.
“	C	N.D.	0.61	-0.61	N.D.	N.D.	N.D.	0.28	0.28	N.D.	N.D.
9Cr_3dpa_400C_01-12	1	N.D.	0.81	-0.81	N.D.	N.D.	N.D.	0.05	0.05	N.D.	N.D.
“	2	N.D.	0.74	-0.74	N.D.	N.D.	N.D.	0.03	0.03	N.D.	N.D.
“	C	N.D.	0.78	-0.78	N.D.	N.D.	N.D.	0.05	0.05	N.D.	N.D.
9Cr_7dpa_400C_04-09	1	N.D.	1.29	-1.29	N.D.	N.D.	N.D.	N.D.	0.03	0.03	N.D.
“	2	N.D.	1.39	-1.39	N.D.	N.D.	N.D.	N.D.	0.11	0.11	N.D.
	3	N.D.	1.57	-1.57	N.D.	N.D.	N.D.	N.D.	0.03	0.03	N.D.
“	C	N.D.	1.43	-1.43	N.D.	N.D.	N.D.	0.14	0.14	N.D.	N.D.
9Cr_10dpa_400C_01-12	1	N.D.	1.41	-1.41	N.D.	N.D.	N.D.	0.16	0.16	N.D.	N.D.
“	2	N.D.	1.71	-1.71	N.D.	N.D.	N.D.	0.04	0.04	N.D.	N.D.
“	C	N.D.	1.54	-1.54	N.D.	N.D.	N.D.	0.20	0.20	N.D.	N.D.

N.D. = not detectable

Table 5.28. Average Δ concentration values and their standard deviations of the mean, taken over boundaries and conditions in HT9.

Sample Designation	**Boundary (#) or condition (C) average?**	**Average Δ concentration (wt%) across all scans**					**Standard deviation of the mean (wt%)**				
		Si	**Cr**	**Fe**	**Ni**	**Cu**	**Si**	**Cr**	**Fe**	**Ni**	**Cu**
HT9_UI	1	0.01	0.01	0.00	-0.04	N.D.	0.01	0.04	0.04	0.03	N.D.
“	2	0.00	0.02	-0.02	-0.01	N.D.	0.01	0.05	0.04	0.01	N.D.
“	C	0.00	0.01	-0.01	-0.03	N.D.	0.01	0.04	0.04	0.03	N.D.
HT9_3dpa_400C_12-07	1	0.04	0.67	-1.32	0.63	N.D.	0.01	0.03	0.09	0.06	N.D.
“	2	0.04	0.65	-1.25	0.57	N.D.	0.01	0.15	0.08	0.07	N.D.
“	3	0.04	0.74	-1.33	0.57	N.D.	0.01	0.01	0.03	0.04	N.D.
“	4	0.04	0.70	-1.29	0.57	N.D.	0.01	0.08	0.10	0.02	N.D.
“	C	0.04	0.69	-1.30	0.59	N.D.	0.01	0.07	0.07	0.05	N.D.

N.D. = not detectable

Table 5.29. Average Δ concentration values and their standard deviations of the mean, taken over boundaries and conditions in HCM12A.

Sample Designation	Boundary (#) or condition (C) average?	Average Δ concentration (wt%) across all scans						Standard deviation of the mean (wt%)					
		Si	Cr	Fe	Ni	W	Cu	Si	Cr	Fe	Ni	W	Cu
HCM12A_UI	1	0.02	0.10	-0.17	0.05	0.00	-0.01	0.02	0.05	0.02	0.01	0.14	0.11
“	2	-0.02	0.03	0.02	0.01	-0.09	0.05	0.02	0.02	0.02	0.02	0.02	0.02
“	3	-0.03	0.07	-0.15	0.02	0.01	0.08	0.01	0.02	0.02	0.02	0.02	0.02
“	C	-0.01	0.07	-0.10	0.03	-0.03	0.04	0.03	0.05	0.13	0.04	0.11	0.10
HCM12A_3dpa_400C_12-07	1	0.03	0.65	-2.34	0.17	0.15	1.34	0.02	0.08	0.83	0.03	0.20	0.75
“	2	0.04	1.01	-1.71	0.08	0.17	0.40	0.04	0.16	0.52	0.09	0.21	0.11
“	C	0.04	0.86	-1.98	0.12	0.16	0.81	0.03	0.23	0.69	0.08	0.19	0.67

Table 5.30. Microstructure measurements and sink strength calculations for alloy T91 as-received and irradiated at 400°C.

Alloy		**T91, 400°C**					
Dose (dpa)		**0**	**1**	**3**	**7**	**10**	**0-10**
Source of Data		Meas.	Meas.	Meas.	Meas.	Meas.	Range of Values Found in Literature [1], [11], [61], [72]
Grain Boundaries	Lath Length (10^{-6} m)	5.07	5.07	5.07	5.07	5.07	4.2-13.5
	Lath Width (10^{-6} m)	0.44	0.44	0.44	0.44	0.44	0.25-0.64
	d for Calculation (10^{-6} m)	1.49	1.49	1.49	1.49	1.49	--
	Sink Strength (10^{12} m^{-2})	10.76	10.76	10.76	10.76	10.76	--
Carbides	Diameter (10^{-6} m)	0.156	0.159	0.161	0.164	0.160	0.08-0.2
	Density (10^{20} m^{-3})	1.13	1.16	1.23	1.20	1.24	0.20-3.57
	Sink Strength (10^{12} m^{-2})	220.82	232.38	248.76	247.47	249.00	--
Disl. Line	Density (10^{14} m^{-2})	6.25	6.25	6.25	6.25	6.25	4.5-13.0
	Sink Strength (10^{12} m^{-2})	888	888	888	888	888	--
Disloc. Loops	Diameter (10^{-9} m)	0	15.7	28.5	31.8	49.0	11.3-55.7
	Density (10^{21} m^{-3})	0	3.41	9.10	13.9	14.0	2.0-17.8
	Sink Strength (10^{12} m^{-2})	0	673	3259	5567	8621	--
Total	Sink Strength (10^{12} m^{-2})	1120	1804	4407	6713	9769	--

Table 5.31. Microstructure measurements and sink strength calculations for 9Cr model alloy as-received and irradiated at 400°C.

Alloy		**9Cr Model, 400°C**				
Dose (dpa)		**0**	**1**	**3**	**7**	**10**
Grain Boundaries	Lath Length (10^{-6} m)	4.63	4.63	4.63	4.63	4.63
	Lath Width (10^{-6} m)	0.40	0.40	0.40	0.40	0.40
	d for Calculation (10^{-6} m)	1.36	1.36	1.36	1.36	1.36
	Sink Strength (10^{12} m^{-2})	12.96	12.96	12.96	12.96	12.96
Carbides	Diameter (10^{-6} m)	0.126	0.127	0.129	0.128	0.129
	Density (10^{20} m^{-3})	0.121	0.124	0.122	0.127	0.128
	Sink Strength (10^{12} m^{-2})	19.12	20.46	19.65	19.40	20.52
Disl. Line	Density (10^{14} m^{-2})	1.62	1.62	1.62	1.62	1.62
	Sink Strength (10^{12} m^{-2})	217	217	217	217	217
Disloc. Loops	Diameter (10^{-9} m)	0	13.2	26.7	33.5	40.6
	Density (10^{21} m^{-3})	0	1.57	4.32	5.87	6.02
	Sink Strength (10^{12} m^{-2})	0	260	1449	2472	3072
Total	Sink Strength (10^{12} m^{-2})	249	511	1699	2722	3510